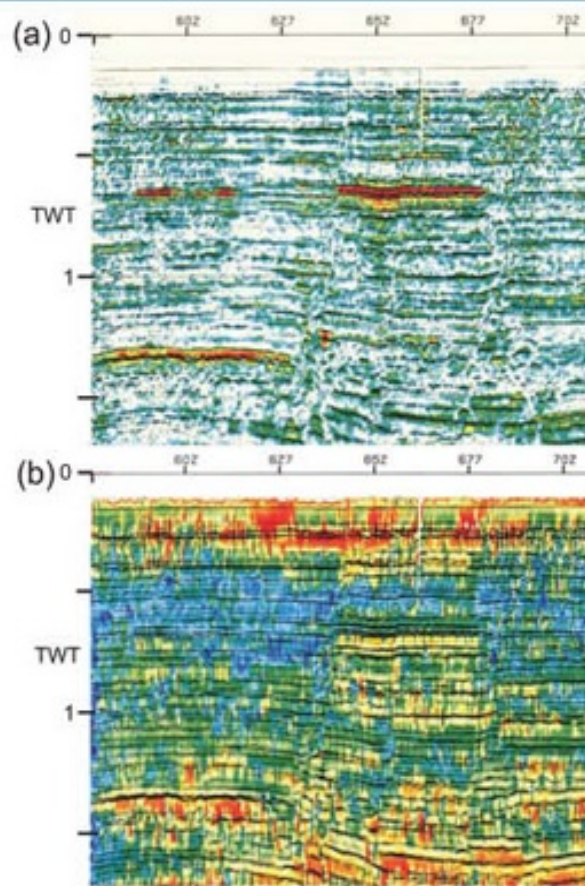
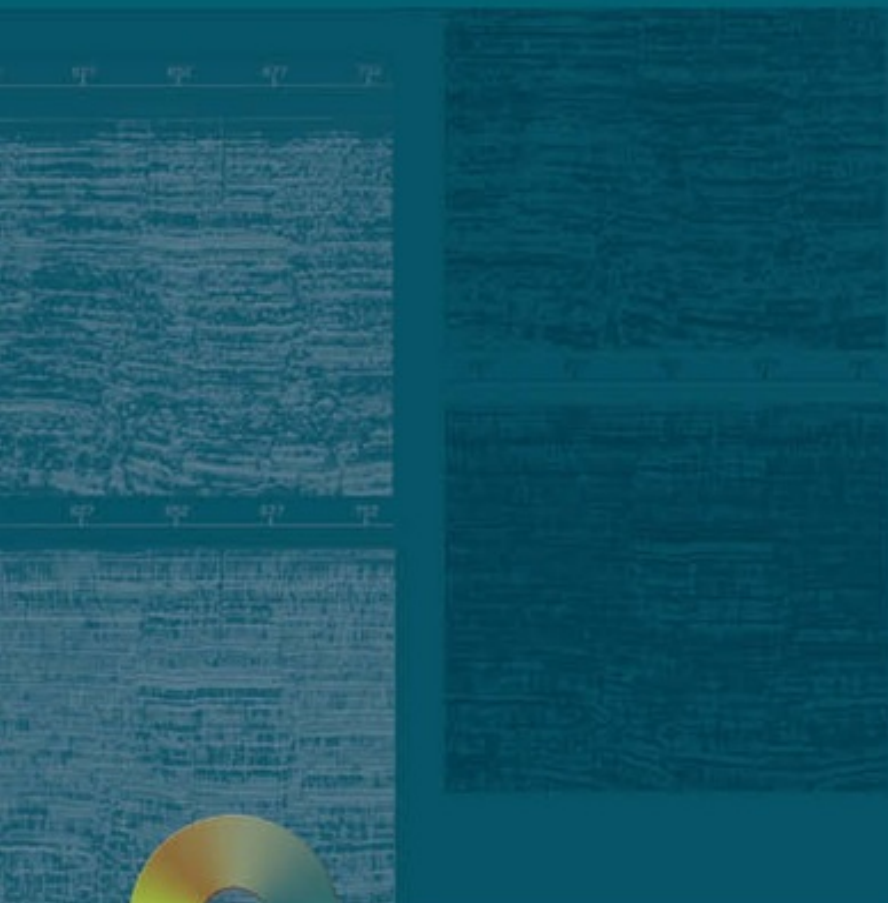


A Petroleum Geologist's Guide to Seismic Reflection



William Ashcroft

 WILEY-BLACKWELL

Contents

[Cover](#)

[Title Page](#)

[Copyright](#)

[Preface](#)

[Acknowledgements](#)

[Part I: Basic topics and 2D interpretation](#)

[Chapter 1: Introduction and overview](#)

[1.1 Exploration Geophysics in Petroleum Exploration](#)

[1.2 The Principle of Seismic Reflection Surveying](#)

[1.3 Overview of the Seismic Reflection Industry](#)

[1.4 A Brief History of Seismic Surveying](#)

[1.5 Societies, Books and Journals](#)

[Chapter 2: Geophysical signal description](#)

[2.1 Overview](#)

[2.2 Cosine Waves](#)

[2.3 Signals and Spectra](#)

[2.4 Periodic Waveforms: Fourier Series](#)

[2.5 Seismic Wavelets](#)

[2.6 Wavelet Characteristics: Time and Frequency Domains](#)

[2.7 Digitization of Signals](#)

[2.8 Fourier Description of Space-Dependent Quantities](#)

[Chapter 3: Data acquisition](#)

[3.1 General Points](#)

[3.2 Seismic Sources and Receivers](#)

[3.3 Static Corrections](#)

[3.4 Recording and Presentation of Data](#)

[3.5 Common Mid-Point \(CMP\) Shooting](#)

[3.6 The Attack on Noise](#)

[3.7 3D Surveys](#)

[Chapter 4: Seismic wave propagation](#)

[4.1 Introduction](#)

[4.2 P-wave](#)

[4.3 Controls on P-Wave Velocity](#)

[4.4 P-wave Waveforms](#)

[4.5 Shear Waves and Surface Waves](#)

[4.6 P-wave Attenuation](#)

[4.7 P-wave Transmission Paths](#)

[Chapter 5: The process of reflection](#)

[5.1 Introduction](#)

[5.2 Fresnel Zones](#)

[5.3 Fresnel Zones and the Seismic Reflection](#)

[5.4 Faults and Diffractions](#)

[5.5 Hyperbolae on Stacked Time Sections](#)

[5.6 The Reflection as a Summation of Hyperbolae](#)

[5.7 Resolution of the Seismic Reflection Method](#)

[5.8 Multiple Reflections: Common Modes](#)

[5.9 Multiples: the Scale of the Problem](#)

[Chapter 6: Velocity analysis, CMP stacking and post-stack migration](#)

[6.1 General Points](#)

[6.2 Definitions of Seismic Velocity: Well Data](#)

[6.3 Velocities from Seismic Data: \$V_{rms}\$](#)

[6.4 Velocities from Seismic Data: \$V_{stack}\$](#)

[6.5 Velocity Analysis](#)

[6.6 Errors in Seismic-Derived Velocities](#)

[6.7 Multiple Suppression by CMP Stacking](#)

[6.8 Stacking the Whole Section: A Make-or-Break Process](#)

[6.9 Some Stacking Refinements](#)

[6.10 Migration: The Fundamental Idea](#)

[6.11 Full-Waveform Migration](#)

[6.12 Migration example: 2D Section](#)

[Chapter 7: Interpretation of two-dimensional \(2D\) surveys for structure](#)

[7.1 Introduction](#)

[7.2 Linking well Geology to the Seismic Section](#)

[7.3 Choosing Reflections to Pick](#)

[7.4 Picking Reflections](#)

[7.5 Sideswipe](#)

[7.6 A Sideswipe Example: Fault Diffractions](#)

[7.7 Preparing Structure Maps in TWT](#)

[7.8 Time to Depth Conversion](#)

[7.9 Examples of Time-Depth Conversion](#)

[Part II: Seismic input to reservoir characterization](#)

[Chapter 8: Better images of the subsurface](#)

[8.1 Introduction](#)

[8.2 Reflection Point Dispersal, Conflicting Dips and DMO](#)

[8.3 Prestack Time Migration \(PSTM\)](#)

[8.4 Prestack Depth Migration \(PSDM\)](#)

[8.5 Anisotropy: the Ultimate Refinement in Velocity](#)

[8.6 Velocity-depth Ambiguity](#)

[8.7 Future Migration Technique: Kirchhoff or Wave](#)

[Extrapolation?](#)

[8.8 3D Migration](#)

[8.9 3D Seismic Interpretation](#)

[8.10 Growth and Impact of 3D Seismic Surveys](#)

[Chapter 9: Modifying the seismic waveform](#)

[9.1 Introduction](#)

[9.2 Testing an Electronic Filter: The Impulse Response](#)

[9.3 Digital Filters: Convolution](#)

[9.4 Cross-correlation and Auto-Correlation](#)

[9.5 Frequency Filtering by Convolution](#)

[9.6 The Seismogram As a Convolution](#)

[9.7 Deconvolution](#)

[9.8 Designing Deconvolution Operators](#)

[9.9 Predictive Deconvolution](#)

[9.10 Wavelet Processing](#)

[9.11 Frequency-domain Processing](#)

[9.12 Data Processing and the Fragility of Bandwidth](#)

[Chapter 10: Refining reservoir architecture from seismic data](#)

[10.1 Introduction: The Reservoir Model](#)

[10.2 Refining Reservoir Environment: Seismic Stratigraphy and Facies Analysis](#)

[10.3 Refining Reservoir Structure: Vertical Seismic Profiling \(VSP\)](#)

[10.4 Refining Reservoir Structure: Seismic Attributes](#)

[10.5 Seismic Forward Modelling](#)

[Chapter 11: Seismic input to mapping reservoir properties](#)

[11.1 Introduction](#)

[11.2 Reflection Amplitude](#)

[11.3 Acoustic Impedance \(AI\) Inversion](#)

[11.4 Amplitude Variation with Offset \(AVO\)](#)

[11.5 AVO Intercept and Gradient](#)

[11.6 Fluid Factor](#)

[11.7 AVO Inversion to Rock Properties \$\lambda\rho\$ and \$\mu\rho\$](#)

[11.8 AVO Inversion to P- and S-Wave Impedance](#)

[11.9 Elastic Impedance: AVO Made Easy?](#)

[11.10 Best Fluid Indicator?](#)

[11.11 Instantaneous Seismic Attributes](#)

[11.12 Usage of Seismic Attributes](#)

[11.13 Predicting Log Properties from Seismic Attributes](#)

[11.14 4C and 4D Surveys](#)

[Tutorial answers](#)

[References](#)

[Index](#)

A Petroleum Geologist's Guide to Seismic Reflection

William Ashcroft

 **WILEY-BLACKWELL**

A John Wiley & Sons, Ltd., Publication

This edition first published 2011, © 2011 by William Ashcroft

Blackwell Publishing was acquired by John Wiley & Sons in February 2007. Blackwell's publishing program has been merged with Wiley's global

Scientific, Technical and Medical business to form Wiley-Blackwell.

Registered office: John Wiley & Sons Ltd, The Atrium, Southern Gate, Chichester, West Sussex, PO19 8SQ, UK

Editorial offices: 9600 Garsington Road, Oxford, OX4 2DQ, UK

The Atrium, Southern Gate, Chichester, West Sussex, PO19 8SQ, UK

111 River Street, Hoboken, NJ 07030-5774, USA

For details of our global editorial offices, for customer services and for information about how to apply for permission to reuse the copyright material in this book please see our website at

www.wiley.com/wiley-blackwell

The right of the author to be identified as the author of this work has been asserted in accordance with the Copyright, Designs and Patents Act 1988.

All rights reserved. No part of this publication may be reproduced, stored in a retrieval system, or transmitted, in any form or by any means, electronic, mechanical, photocopying, recording or otherwise, except as permitted by the UK Copyright, Designs and Patents Act 1988, without the prior permission of the publisher.

Wiley also publishes its books in a variety of electronic formats. Some content that appears in print may not be available in electronic books.

Designations used by companies to distinguish their products are often claimed as trademarks. All brand names and product names used in this book are trade names, service marks, trademarks or registered trademarks of their respective owners. The publisher is not associated with any product or vendor mentioned in this book. This publication is designed to provide accurate and authoritative information in regard to the subject matter covered. It is sold on the understanding that the publisher is not engaged in rendering professional services. If professional advice or other expert assistance is required, the services of a competent professional should be sought.

Library of Congress Cataloguing-in-Publication Data

Ashcroft, W. A. (William A.)

A petroleum geologist's guide to seismic reflection / William Ashcroft.

p. cm.

Includes index.

ISBN 978-1-4443-3262-9 (cloth) – ISBN 978-1-4443-3263-6 (pbk.)

1. Seismic reflection method. 2. Petroleum—Prospecting. I. Title. II. Title: Guide to seismic reflection.

TN269.84.A84 2011

622'.1828—dc22

2010048040

A catalogue record for this book is available from the British Library.

This book is published in the following electronic formats: ePDF [ISBN: 9781444397857]; ePub
[ISBN: 9781444397864]

Preface

This book is written for anyone who wants to get quickly ‘up to speed’ on some aspect of reflection seismology as it affects the seismic interpreter. It is a development of course notes on seismic reflection interpretation which have been given to students on the MSc course in Petroleum Geology at Aberdeen University over many years, and thus it takes the form of a course manual rather than a systematic textbook. It can be used as a self-contained course for individual study or as the basis of a class programme. The notes were originally provided to make the subject more accessible to geology students, but this volume should also prove useful to others, such as petroleum engineers, who have to work in an integrated exploration or development team side by side with geophysicists and geologists. Much petroleum exploration and production is now driven by the seismic reflection survey technique, so that all team members need to know quite a lot about it.

Throughout this book, the way in which the subject matter is treated depends on its importance to the seismic interpreter. For example, in discussing data acquisition in the field, only the barest descriptions of seismic source and receiver hardware are given; the focus is on the geometry of survey layout and the maintenance of signal quality.

Geophysics uses the language of mathematics, which is like any other language – if you don't use it every day you soon forget it, so many people find the mathematics in geophysics a barrier to learning. The first rule for reading a maths-based topic might be summarized as ‘don't panic’! The second rule is to keep re-reading the bits you don't understand, with pencil and paper handy. The third rule is to read only twice over at any one time, then move on to rest your conscious brain and give its unconscious part time to work around it. That often works best while doing a practical tutorial of some sort – maybe something as simple as plotting a graph. Let your fingers help the learning!

The book is written with an eye to those points that students of the subject tend to find difficult, and it tries to provide insight through tutorial material of a practical nature. The tutorials aim to reinforce and deepen understanding of key topics and to provide the reader with a measure of feedback on progress. Some tutorials may only involve drawing simple diagrams, but many are computer-aided tutorials with graphics output to give insight into key steps in seismic data processing, or into the seismic response of some common geological scenarios. Other tutorials involve interpretation of seismic sections and associated well data. The reader is urged to complete the practical tutorials at the time they are encountered in the text. The main interpretation tutorials at the end of Chapter 7 can be done over a longer schedule.

There are two separate applications of the seismic reflection technique in the petroleum industry. The first is to determine subsurface geological structure as exactly as possible, by calculating the depth to key geological horizons and so delineate closed, possibly hydrocarbon-bearing structures and calculate their volume. The second application is to use seismic characteristics such as signal amplitude or frequency to determine subsurface properties such as porosity, or the presence of hydrocarbons in a reservoir rock, and to track variations in such properties away from well control.

Part I of this book covers fundamental topics such as data acquisition and the description of the seismic wavelet, together with structural interpretation from two-dimensional seismic sections. Part II deals with three-dimensional surveys and the seismic input to reservoir studies.

Dr. William Ashcroft,
Aboyne,
Royal Deeside,
Scotland

Acknowledgements

I am grateful for helpful comments on drafts of this work from Alan McGregor, Peter McAllister-Hall, Henry Allen, Stephen Spencer and Adrian Burrows.

Professor Jonathan Redfern, University of Manchester, helped the author to maintain focus on seismic facies. Seismic data for interpretation purposes was generously provided by WesternGeco and BP.

The open policy of the Society of Exploration Geophysicists towards the use of illustrative material from their publications has been a big help in preparing the work, and the ready contribution of similar material from the European Association of Geoscientists and Engineers, the Geological Society, the American Association of Petroleum Geologists and the Canadian Society of Exploration Geophysicists is gratefully acknowledged.

Part I

Basic Topics and 2D Interpretation

Chapter 1

Introduction and Overview

We should all be able to squint along seismic sections and grunt knowingly.

(Anstey, 1982)

1.1 Exploration Geophysics in Petroleum Exploration

Four geophysical survey techniques are commonly used in the exploration for petroleum: gravity surveys, aeromagnetic surveys, electromagnetic surveys and seismic surveys.

The first two are reconnaissance techniques designed to answer such questions as:

- Where are the sedimentary basins in an area?
- How deep are they (to ≈ 10 per cent accuracy)?
- What are the controlling structural features?

They provide low resolution data over a wide area comparatively cheaply.

Electromagnetic surveys have had a long history of application in the mining industries, but they have only recently been applied to petroleum exploration with the aim of directly detecting the presence of hydrocarbons in the subsurface.

Seismic surveys have a long history of use in petroleum exploration and are the primary tool for delineating subsurface structure and detecting the presence of hydrocarbons prior to drilling.

Seismic surveys can be of two types – refraction and reflection – depending on the mode of transmission of the seismic energy. The refraction technique is little used, because it again gives results of a reconnaissance nature. The main effort and expenditure is put into the reflection technique because it provides much more information, resolving structural detail down to scales of approximately 10 m and yielding full three-dimensional images of the subsurface. Where data quality is good, lithological and petrophysical data on subsurface rocks can also be derived from the seismic reflection data when this is integrated with information from wells.

In exploring a sedimentary basin, seismic reflection surveys are applied immediately after surface geological surveys and reconnaissance geophysical surveys have been made. The initial aim is to map out subsurface structure along two-dimensional cross-sections (2D surveys) in sufficient detail to map out the broad structure and stratigraphy of the basin and allow the siting of the first exploration wells. As promising leads are identified, intensive 3D surveys will be carried out to optimize the placement of wells and guide drilling. Finally, in the course of a field's history, repeated 3D surveys ('4D' surveys) may be undertaken to monitor the flushing of hydrocarbons from the reservoir.

1.2 The Principle of Seismic Reflection Surveying

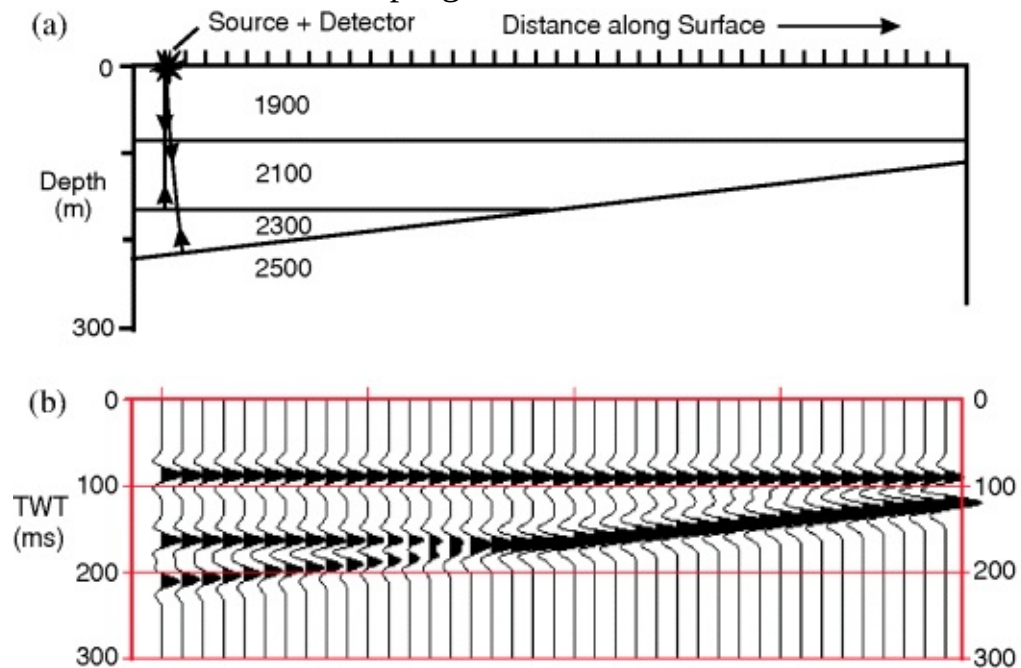
The principle is very simple: it is a form of echo-sounding. A sound pulse (compressional or P-

wave) generated by a powerful source at the surface (for example, an explosion) penetrates the rocks to depths of several kilometres and is reflected back as an echo from the interfaces between different rock types ([Figure 1.1](#)). The echoes are recorded at the surface on an array of sensitive receivers – geophones on land, hydrophones at sea. After initial processing of the data, one may regard the sound as having travelled down to and back from the interface along the same travel path (raypath) to a receiver located beside the shot ([Figure 1.1](#)). The raypath is at right angles to the interface, and for this reason it is called a normal-incidence reflection (‘normal’ in the sense of ‘at right angles to’). The reflective interfaces are usually bedding planes within a sedimentary sequence, but they may be low-angle faults or the sediment-basement interface.

Figure 1.1 Echo-sounding principle of the seismic reflection technique.

- a.** Sound from an explosive source is reflected from any surface which separates rocks with different sound velocities. Typical velocities are shown in m/s.
- b.** The reflected sound pulses build up an image of the strata scaled vertically in two-way time (TWT).

Section modelled in program *SYNTHSEC*.



The echoes are recorded at the surface as separate pulses of sound, and successive pulses may well overlap so that the final recording from a single receiver takes the form of an extended wave train several seconds in length. It is recorded digitally but can be displayed as an oscillographic trace – a seismogram or graph of receiver output versus time. The time is that taken for the sound to travel down to the reflector and back to the surface, so it is called the two-way time (TWT) or reflection time.

Many such seismograms are recorded from successive points along a survey line and displayed side-by-side on a large sheet of paper or on a computer screen with the TWT shown as increasing downwards ([Figure 1.1](#)). The zero of time is the time of firing the explosive shot, and this is measured to an accuracy of better than one thousandth of a second, i.e. 1 millisecond (1 ms). The reflected pulse from any one horizon may be readily followed by eye from trace to trace across the display. The whole bears a striking resemblance to a geological cross-section through the strata, as if it were a gigantic cliff face several kilometres high and tens of kilometres long, on which the strata were laid out for our inspection.

Possible oil-bearing structures may be recognized on such a display and their depth and amount of closure calculated from the observed reflection times, provided the velocity of propagation of seismic energy in the rocks above can be measured. Since the display so strongly resembles a geological section, but has a vertical dimension scaled in TWT, it is called a time-section.

In addition to the compressional wave (P-wave), two other types of seismic wave disturbance are produced by the source: shear waves and surface waves. Surface waves are a considerable source of interference in data acquired on land and will be considered in Chapter 3. Shear waves will be considered in the context of reservoir geophysics, where they have increasing application.

1.3 Overview of the Seismic Reflection Industry

The seismic reflection industry can be divided into three main sections: data acquisition, data processing and data interpretation. These incorporate not only areas of technique, but also of business activity and of employment:

- Data acquisition is a difficult operation on both land and sea. It requires a lot of skill and experience on the part of operating personnel and so, like much of the technically difficult operations in the oil business, is placed in the hands of specialist contractors. Firms such as Schlumberger Geco-Prakla, Western Geophysical, Petroleum Geo-Services (PGS) and Compagnie Generale de Geophysique (CGG) provide data acquisition and processing services and may also provide specialist interpretation of the results. However, most interpretation is handled by the client oil companies or specialist consultancies. The contractors may undertake to survey specific areas exclusively for oil-company clients – so-called proprietary surveys. They may also initiate non-proprietary or speculative surveys in areas which they think will be of interest, make interpretations of them and attempt to sell them to oil companies. Contractors are at the forefront of the research and development of new techniques in both acquisition and processing. They employ mostly physicists, geophysicists, engineers, computer scientists and mathematicians, with some geologists.
- Data processing is normally handled by the same contractors who carry out acquisition, with the addition of some smaller firms who may focus on particular advanced processing techniques. They all employ a similar mix of people.
- Data interpretation is mostly handled by the client oil companies, who employ both geophysicists and geologists as seismic interpreters. Most companies have moved away from workgroups based on skills ('Geology Department') to groups based on projects ('Tertiary Sand Plays') or based on assets such as individual fields ('Schiehallion team'). As a result, there is much more emphasis on the integration of geological/geophysical data with other data sets, such as those of the reservoir engineer, and all geoscientists have to know quite a lot about what the others in the group are doing.

The petroleum industry is by far the biggest spender on geophysical surveying, spending about five times the total spent on all other applications such as minerals, engineering and research. Most of the expenditure goes on seismic reflection surveys and the total length of profile surveyed in a year is well over one million miles. About a third of that is on land and two-thirds at sea.

1.4 A Brief History of Seismic Surveying

The earliest application of the seismic technique was inevitably a military one. In World War I, seismic receivers were used to locate the position of gun batteries by the seismic disturbance caused by their recoil. In the 1920s, there was considerable success in locating salt domes by the seismic refraction method, but the first usable reflection records were made in the mid-1920s, and by 1932 some 30 seismic reflection crews were working in the USA. An excellent account of the development of the technique is given in Sheriff & Geldart (1995) and much additional information is available in Lawyer *et al.* (2001).

Recordings were initially made directly onto paper records by photo-oscillographic techniques, with no subsequent processing of the data, and this continued unchanged until the next big step forward in the 1950s – magnetic tape recording. At this time, analogue processing of records was begun, together with compilation of the first time sections. Common mid-point (CMP) shooting was widely adopted in the early 1960s, and a few years later the processing of taped records had become so universal that a rapid switch to digital recording and processing was made. The result was a startling improvement in the quality of traditional seismic data and the development of new types of data processing and presentation, so that much more of the information contained in the seismic waveform could be put to use.

From the late 1980s, two further major advances in technique have been consolidated: the application of 3D seismic surveying and the concomitant move to interpretation on computer workstations – both made possible by the rise in computer power over the same period. These developments, together with an increasing emphasis on reservoir studies, have meant that the interpreter is now expected to be even more knowledgeable about signal processing than before, perhaps to the extent of carrying out some processing operations on his or her own workstation.

1.5 Societies, Books and Journals

The Society of Exploration Geophysicists (SEG) is the principal American body in the field and publishes *Geophysics* for more mathematical papers and *The Leading Edge* for more case-history style papers and chatty articles. In Europe, the European Association of Geoscientists and Engineers (EAGE) publishes two journals whose content is similar to those mentioned above: *Geophysical Prospecting* and *First Break*. Both *The Leading Edge* and *First Break* are very good for getting a ‘feel’ for the industry, with advertisements, company profiles and newsy articles. In addition, there are often geophysics-based articles in journals such as *Petroleum Geoscience* and *Journal of Petroleum Geology*.

A good introductory textbook is *An Introduction to Geophysical Exploration* (3rd edition, 2002) by P. Kearey, M. Brooks and I. Hill, published by Blackwell Science, of which about half is taken up with seismic surveying. The most comprehensive text on reflection seismology is *Exploration Seismology* (2nd edition, 1995) by R. E. Sheriff and L. P. Geldart, published by Cambridge University Press, with full mathematical treatment of all topics.

For data processing, the principal text is *Seismic Data Analysis* by O. Yilmaz (2nd edition, 2001), published by the SEG and for data interpretation *Interpretation of Three-Dimensional Seismic Data* by A. R. Brown (6th edition, 2004), published jointly by SEG and the American Association of Petroleum Geologists. A useful overview of interpretation is provided by *3D*

Seismic Interpretation by M. Bacon, R. Simm and T. Redshaw, published by Cambridge University Press in 2003.

Chapter 2

Geophysical Signal Description

2.1 Overview

A 'signal' is any physical measurement taken in the course of a geophysical survey and expressed as a graph of its variation with time or its variation with distance along ground surface or with depth down a borehole. Examples might include a seismogram expressing variation in ground motion with the passage of time at a fixed locality, or a gravity profile expressing variation of the Earth's gravity field along a survey line of traverse on the ground. In seismic recording, the combination of detector, signal amplifier and link to the final recording device is called a channel of information; in a typical survey, several thousand channels may be recorded.

The interpreter has to know about the mathematical description of signals for several reasons:

- First, the seismic section is not a natural phenomenon like a sedimentary succession exposed in a quarry face, but can be radically changed by a change in the methods of the data processing. The interpreter has to appreciate the essential elements of the processing sequence and their effects on the seismic signal in order to separate genuine geological information on the section from background 'noise', perhaps introduced by the processing.
- Second, the characteristics of the seismic waveform are being increasingly used to provide information on subsurface geological conditions, so the interpreter has to be aware of those characteristics and how they may be modified by passage through the earth.
- Third, the interpreter will be working at a computer workstation with the opportunity of doing some on-the-spot processing, so s/he has to feel comfortable with the basic concepts of signal description.
- Finally, the interpreter has to communicate with geophysicists as a member of an exploration or development team, so has to be comfortable with at least the basic vocabulary of the geophysicist.

The sinusoidal shape of a seismogram ([Figure 1.1](#)) suggests that its mathematical description might involve sines or cosines, and the main point of this chapter is to explore such a description. We are going to consider the cosine waveform initially, move on to repetitive or periodic waveforms in general, and then finally focus on the one-off pulse-type waveform that is created by an explosive seismic source (the seismic wavelet). We will finish by looking at the closely similar description of space-variant signals and the digitization of signals

2.2 Cosine Waves

In [Figure 2.1](#), a seismic wavefront advances from an explosive source. A small earth volume at P oscillates to and fro about its rest position as the wavefront passes by. This motion is complicated,

in that the particle's velocity is constantly changing – it is at its maximum as the particle passes through its rest position and is slowing down to zero at the extremities of the oscillation. We can simplify the motion by linking it to the steady rotation of a point R around a reference circle whose diameter is the maximum particle displacement about its rest position O ([Figure 2.2](#)). P is the projection of R vertically down or up on to the diameter so that, as R rotates at a steady rate round the circumference, P oscillates to and fro along the diameter of the circle.

Figure 2.1 Sound waves from an explosion cause earth particles at P to oscillate to and fro in the horizontal plane.

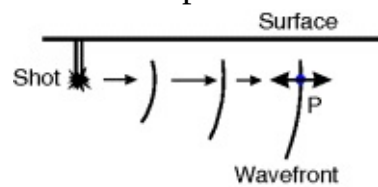
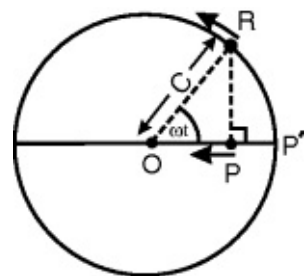


Figure 2.2 The oscillatory motion of P along the horizontal plane is linked to the steady circular motion of R about a reference circle. Time zero is taken when P is at P' and angle $\omega t = 0$.



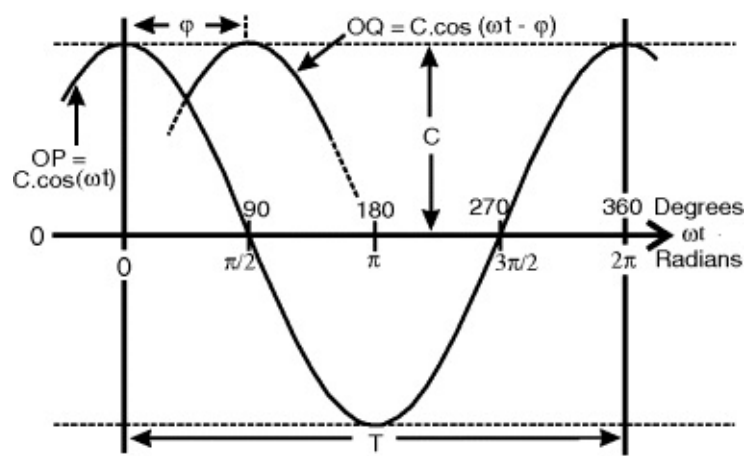
Reference point R rotates at a constant rate so that the angle ROP opens up at a constant rate measured in radians/sec and traditionally given the symbol ω (Greek omega). In [Figure 2.2](#), suppose we started to time the motion when the particle was at P', its maximum displacement, a distance C from its rest position. After t seconds have passed, the angle ROP has opened up to ωt radians and we can describe the displacement OP by the equation

$$(2.1) \quad OP = C \cdot \cos(\omega t)$$

ωt is called the phase angle.

The seismogram is a graph of earth motion against time. In this case, the graph will appear as shown in [Figure 2.3](#), the graph of the cosine of an angle plotted against the angle as the x -axis. When the angle $\omega t = 0$, displacement OP is a maximum (C) and as time increases, it falls to 0 when $\omega t = \pi/2$; it reaches $-C$ when $\omega t = \pi$; and it finally returns to C when $\omega t = 2\pi$ and one cycle of the reference circle has been completed. The horizontal axis of increasing angle is also one of increasing time, and we can re-scale angle (ωt) to time (t) by dividing by ω .

Figure 2.3 Oscillatory quantities OP and OQ plotted against angle ωt as defined in [Figure 2.2](#). T is the period, the time for one complete oscillation.



A particularly important time is the time for a complete oscillation (peak to peak in [Figure 2.3](#)). The angle swept out is 2π radians, so the time involved is $2\pi/\omega$ seconds. This time is called the period (T) of the oscillation.

$$(2.2) T = 2\pi/\omega$$

T is expressed as so many seconds per cycle (s/cycle).

A closely related quantity is the frequency (f) of the oscillation, i.e. the number of oscillations (cycles of the reference circle) that take place per second. For example, if the period of the oscillation is $1/7$ th of a second ($1/7$ s/cycle), it is clear that there must be 7 cycles/sec. Hence f is the inverse of T :-

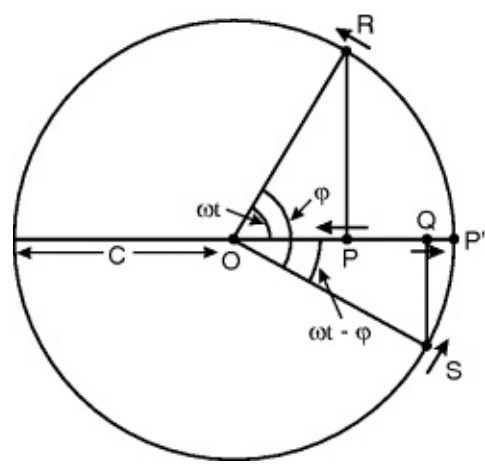
$$(2.3) f = 1/T = \omega/2\pi$$

So important is frequency that its unit of measurement (cycles/sec) is actually given a separate name – the Hertz (Hz for short). Heinrich Rudolf Hertz was a 19th century German physicist who first demonstrated experimentally the existence of the radio waves that had been predicted by Maxwell's theory of electricity and magnetism. Note that ω , the constant rate of rotation of the reference point, is also a measure of frequency; this is because if $f = \omega/2\pi$, then $\omega = 2\pi f$, a scaled-up version of f . This is called 'angular frequency'. Hence we can write the equation of the motion of particle P as:

$$(2.4) OP = C.\cos(2\pi ft)$$

Our description so far is for a special case, because we chose the start of time ($t = 0$) to be when P was at its maximum displacement P'. Suppose we keep that as the start of time, but also wish to describe another oscillation such as OQ in [Figure 2.4](#), which reaches its maximum amplitude at some time after the peak of OP, its reference point (S) on the circumference of the reference circle lagging behind R by an angle ϕ (Greek phi). Both R and S rotate at the same rate (ω) and are locked together a fixed angle (ϕ) apart. The angle ϕ is called the phase difference or phase shift, often just loosely referred to as 'phase' in the literature. In this case, where S lags behind R, we speak of OQ as having a negative phase shift or phase lag with respect to OP. Of course, it would be just as possible for OQ to have a positive phase shift or phase lead with respect to OP.

[Figure 2.4](#) A second horizontal oscillatory motion is represented by the distance OQ linked to point S on the reference circle. It lags behind OP by the phase shift angle ϕ .



How does the second oscillation plot as a time graph? It is clear from [Figure 2.4](#) that, as time goes on and the whole system rotates about the reference circle, OQ will reach its peak amplitude after a rotation of ϕ radians from the start of time (from $\omega t = 0$). The equivalent time waveform is shown in [Figure 2.3](#) with the peak delayed by an angle ϕ relative to the peak of OP , equivalent to a time delay of ϕ/ω seconds. From [Figure 2.3](#), it can be seen that the equation describing the waveform is now:

$$(2.5) \quad \begin{aligned} OQ &= C \cdot \cos(\omega t - \phi) \\ &= C \cdot \cos(2\pi f t - \phi) \end{aligned}$$

To conclude: only three quantities are required to describe a general cosine waveform: the peak amplitude C , the frequency f and the phase shift ϕ .

This is a good time to become more familiar with these basic quantities in Tutorial 2.1.

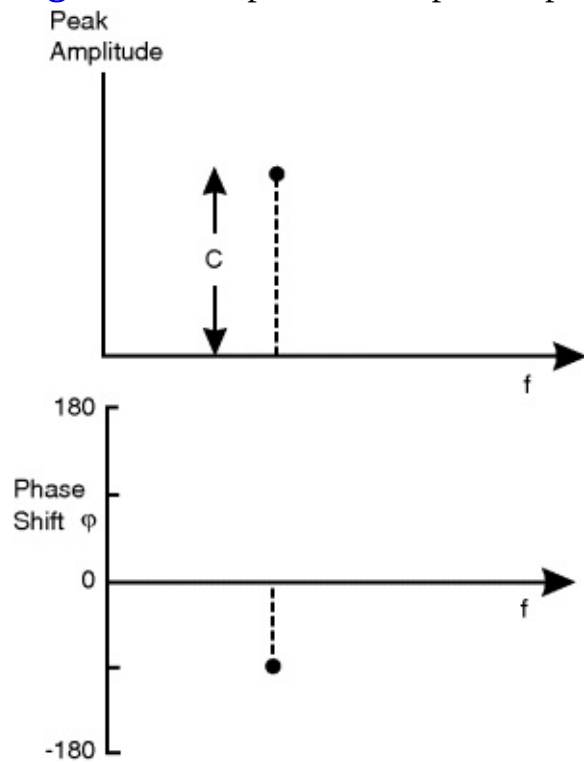
2.3 Signals and Spectra

So far, we have seen the cosine waveform plotted as a function of time, $f(t)$ where f is shorthand for ‘function of’, not frequency. A seismogram is a plot of the amplitude of earth motion plotted against time, and time plots are familiar to most people in the form of temperature records, sales charts, etc. They are commonly called time-series in those fields of application, rather than signals or waveforms, as we call them in seismology.

However, there is an alternative mode of plotting the same information that is not so familiar, in which the horizontal axis is an axis of frequency against which is plotted one of the other two key quantities – peak amplitude or phase shift. In common with other displays in physical science in which the horizontal axis is one of frequency, it is called a spectrum. We speak of working in the time domain or the frequency domain, depending on which description we are using – a waveform or a spectrum.

For any one waveform, two spectra are required: one plotting peak amplitude against frequency (amplitude spectrum); and one plotting phase shift against frequency (phase spectrum). For our cosine waveform, there is only one value of frequency, so the spectra are almost trivial and appear in [Figure 2.5](#). The amplitude spectrum consists of a single point plotted at the appropriate frequency f and raised C units above the frequency axis. To differentiate it from an ink spot or a dead fly on the paper, it has been attached to the frequency axis by a line. The phase spectrum also consists of a single point, negative in the case of the signal OQ and plotting at -90° (check the angle ϕ in [Figure 2.4](#)). Note that the phase spectrum is plotted between limits of $\pm 180^\circ$.

Figure 2.5 Amplitude and phase spectra of the cosine waveform OQ in [Figure 2.3](#).



Unlike time-domain plots, spectra are not familiar in everyday life, but they are bread and butter to the geophysicist and are widely used as a shorthand description of a waveform. They contain enough information to reconstruct the waveform exactly in the time domain – its amplitude, frequency and phase shift – and they will be used frequently throughout this book.

Quite often, a power spectrum is used instead of an amplitude spectrum. You will recall that the heating effect of an electric current c is proportional to c^2 ; in a similar way, a power spectrum is simply one where the square of the amplitude is plotted against frequency. Squaring the amplitude serves to emphasize the really important frequencies in a signal.

2.4 Periodic Waveforms: Fourier Series

So far, our signal description has a fundamental failing – our cosine wave has no beginning or end and goes on for ever, but the seismic impulse (wavelet) from an explosive source is very short-lived – less than a tenth of a second long ([Figure 1.1](#)). How do we progress from cosine wave to wavelet? We do it via an intermediate form – the periodic waveform. Such a waveform repeats itself over a regular period of time called the fundamental period, which has an associated fundamental frequency. The cosine wave itself is a periodic waveform of the very simplest type but, in general, periodic waveforms have a more complicated shape. Every human being has a built-in periodic waveform – the heartbeat – which has a fundamental period of about one second ([Figure 2.6](#)).

Figure 2.6 Periodic electrical signals associated with the beating of the human heart.



It turns out that periodic waveforms can be constructed in the following way. Take a cosine wave of frequency ω_1 and add to it further cosine waves whose frequencies are integer multiples of ω_1 . The base wave is called the fundamental and the others are called harmonics. As might be guessed, that term comes from the world of music. A musical note strikes the ear as a periodic waveform of air pressure, and its pitch is determined by its fundamental frequency. But when that note is played by a musical instrument, it is the harmonics that give the instrument its distinctive sound. A note played on a violin has much stronger harmonics than the same note played on a flute, so giving rise to the distinctive ‘zingy’ sound of the violin.

The harmonics making up the periodic waveform not only have their own frequencies ($\omega_1, 2\omega_1, 3\omega_1 \dots$ etc.) but also their own peak amplitudes ($C_1, C_2, C_3 \dots$ etc.) and their own phase shifts ($\phi_1, \phi_2, \phi_3 \dots$ etc.). The individual waveforms are summed together to form the composite periodic waveform as in the following expression:

$$f(t) = C_0 + C_1 \cos(\omega_1 t + \phi_1) + C_2 \cos(2\omega_1 t + \phi_2) + C_3 \cos(3\omega_1 t + \phi_3) \dots C_k \cos(k\omega_1 t + \phi_k)$$

or

$$(2.6) \quad f(t) = \sum C_n \cos(n\omega_1 t + \phi_n)$$

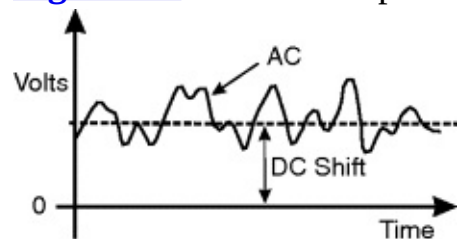
where $n = 0, 1, 2 \dots k$.

C_n and ϕ_n are respectively the peak amplitude and phase shift of the n th harmonic and ω_1 is the frequency of the fundamental. When $n = 1$, we have the fundamental component, when $n = 2$ we have the second harmonic, $n = 3$ we have the third harmonic, and so on. What about the case of $n = 0$? Then:

$$n\omega_1 t = 0$$

so there is no variation in the quantity with time and we have a constant term, C_0 , which simply shifts the general level of the waveform up or down from zero. In electrical signals, C_0 would represent a direct current (DC) component superimposed on an alternating current (AC) signal described by the rest of the series ([Figure 2.7](#)). It can also be described as the zero frequency component of the waveform, equivalent to its mean level. We can ignore it in seismology, because our instruments cannot record DC signals, so the mean amplitude of a seismogram is always zero.

Figure 2.7 AC and DC parts of an electrical signal.



The series of terms that are summed to form the periodic waveform is called a Fourier Series, named after the early 19th century French scientist Jean Baptiste Joseph Fourier, who first used this type of waveform description in dealing with pulses of heat.

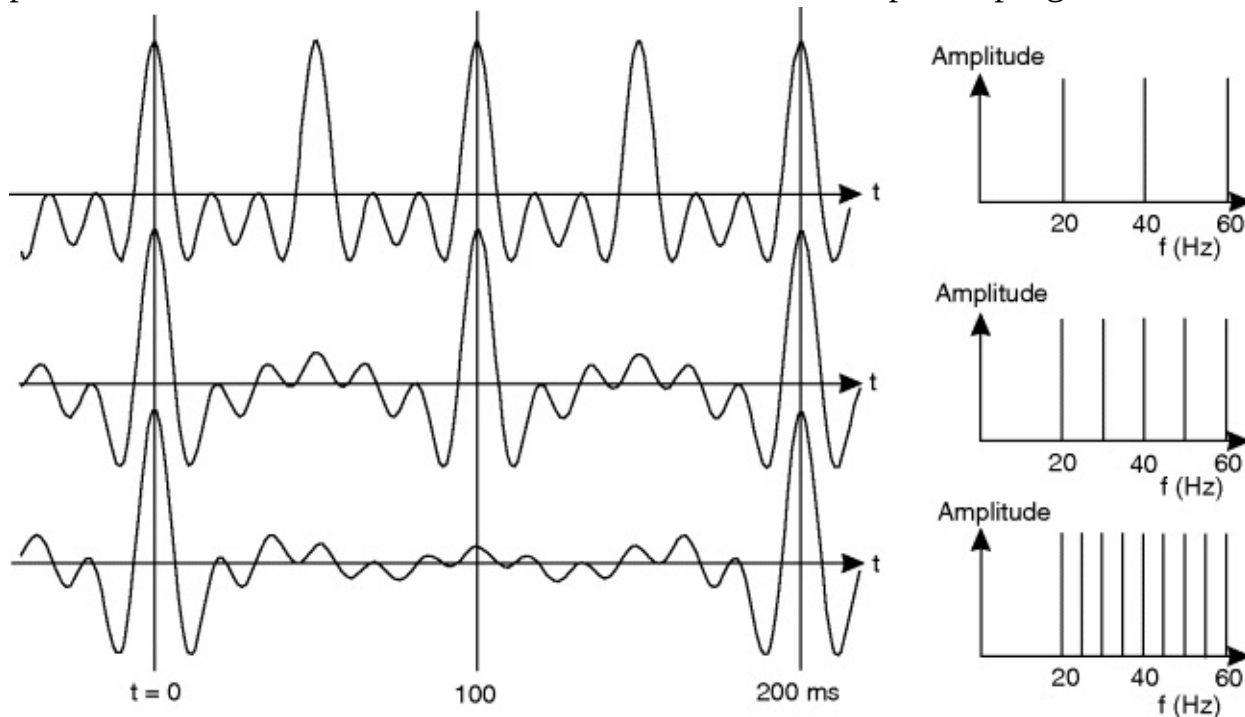
Tutorial 2.2 shows that it is quite straightforward to construct a periodic waveform by hand from a few component cosine waves.

2.5 Seismic Wavelets

We are now in a position to focus on describing the seismic wavelet itself – the one-off pulse of energy created by the explosive seismic source.

Suppose we take the spectra of Tutorial 2.2 and add more and more points at closer and closer intervals of frequency, but without exceeding the frequency limits of 20 and 60 Hz (Figure 2.8). You will recognize the top waveform in this figure as the one created in Tutorial 2.2. As the interval between frequency samples (δf) becomes less, so the interval of repetition (T) between the wavelets in the periodic waveform becomes greater. The waveform around $t = 0$ settles down to a fixed shape. Taking it to the limit, as $\delta f \rightarrow 0$, so $T \rightarrow \infty$ and we are left with an isolated wavelet about the $t = 0$ position, the wavelets at either side having disappeared to infinity. This remarkable development is also demonstrated in Tutorial 2.3 (with slightly different frequencies) using the program *FOURSYN*.

Figure 2.8 The effect of adding more Fourier components within a constant bandwidth of 20 to 60 Hz is to form a wavelet at $t = 0$, which becomes increasingly isolated from the others in the periodic waveform. See Tutorial 2.3. Waveforms developed in program *FOURSYN*.



In the frequency domain, the finite number of spectral components passes into a continuous distribution with an infinite number of frequencies between the limits of 20 and 60 Hz. The phase spectrum also becomes a continuous function of frequency. In the time domain, we are left with a single wavelet isolated at the time origin.

When it comes to the practical business of actually constructing a wavelet from its amplitude and phase spectra, we cannot take an infinite number of constituent cosinusoids, otherwise we would never finish the calculation! Instead, therefore, we take a finite number at specified frequencies, scaling each in amplitude according to the amplitude spectrum, setting the phase shifts according to the phase spectrum and then adding all the waveforms together (see Tutorial 2.3). In other words, we actually construct a periodic waveform consisting of widely separated wavelets (the separation increasing in proportion to the number of sinusoids used), and we use the waveform that plots around $t = 0$ as the time-domain description of the wavelet. We must be sure that we have sampled the spectrum closely enough so that it properly represents the continuous

variation in amplitude that it contains.

Although the component amplitudes must be scaled in proportion to the amplitude spectrum, the final waveform can be scaled to any convenient peak value. Since the process builds a waveform from its constituent sinusoids it is known as Fourier Synthesis. Tutorial 2.3 involves building waveforms in this way using the program *FOURSYN*.

The question naturally arises as to whether it is possible to work in the opposite sense, i.e. given a waveform, can it be broken down into its constituent cosine waves and so transformed into an amplitude spectrum and a phase spectrum? This is indeed possible, using a process in which we take samples of the waveform at closely spaced intervals of time and calculate values of the amplitude and phase shift at a specific frequency. Such a process can be repeated over a selection of separate frequencies to construct the complete spectra. Scaling of the waveform amplitudes is arbitrary and the final values of the amplitude spectrum can be normalized to a convenient peak value.

Since the process separates out a waveform into its constituent cosinusoids, it is also known as 'Fourier Analysis'. We speak of transforming the waveform from the time domain to the frequency domain. Unfortunately, there is no easy graphical way of demonstrating this process, as there is for the process of building a wavelet from its spectra using *FOURSYN*.

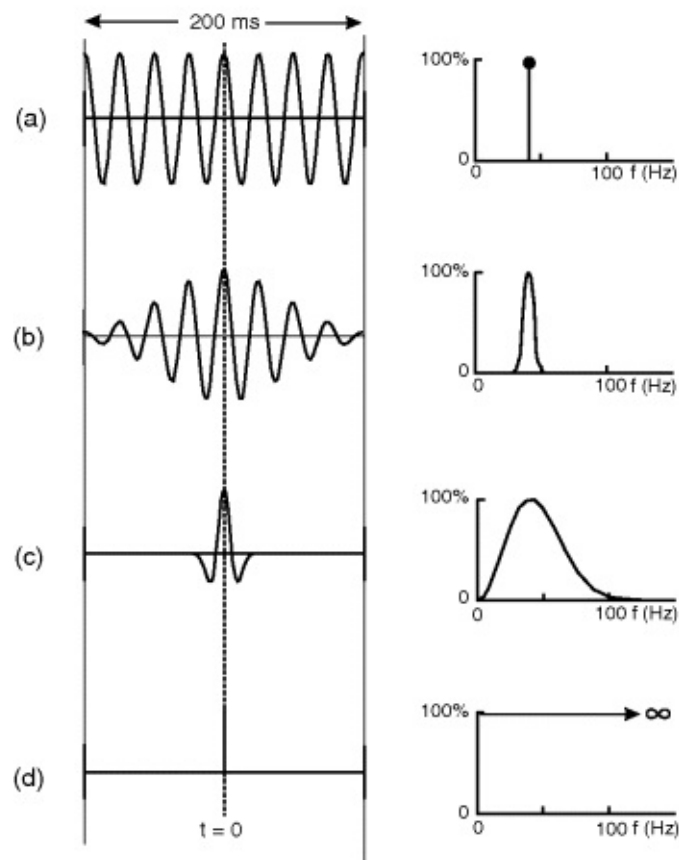
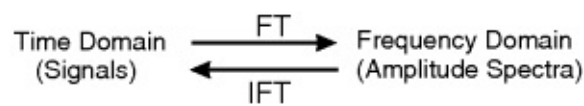
Fourier Analysis and Synthesis are part of a class of mathematical functions called Integral Transforms: Fourier Analysis is commonly called the Fourier Transform (FT) and Fourier Synthesis the Inverse Fourier Transform (IFT).

See how easy it is to construct signals from spectra using the program *FOURSYN* in Tutorial 2.3.

2.6 Wavelet Characteristics: Time and Frequency Domains

[Figure 2.9](#) illustrates the remarkable complementary nature of waveform descriptions in the time and frequency domains. Whatever is restricted in one domain is extended in the other. As the signal becomes more restricted in time, its spectrum broadens in frequency. Note especially that an infinitely short, spike-like impulse in the time domain will have an infinitely extended spectrum in the frequency domain. By analogy with the wide spectrum of white light, a signal of this sort is often called 'white'. Such an infinitely narrow spike waveform represents an ideal seismic signal in the sense of best resolving two closely-spaced reflective interfaces in the geological section. No matter how close are the interfaces, the two spikes would still be separated on the seismogram. Unfortunately, absorption of high frequencies in the earth is so severe that the actual seismic wavelet that is produced is very far from this ideal.

[Figure 2.9](#) Complementary nature of time and frequency domains; whatever is extended in one domain is compressed in the other. Waveforms developed in program *FOURSYN*.



A more typical seismic wavelet is the third one shown in [Figure 2.9](#). It is a Ricker wavelet, which has an amplitude spectrum defined by the equation:

$$(2.7) A(g) = g^2 \exp(-g^2)$$

where

A = amplitude

f = frequency

f_1 = modal frequency of spectrum (frequency of peak amplitude)

$g = f/f_1$

This particular spectrum was found to be typical of seismic wavelets experimentally observed in the classic early studies of Ricker (1953), and the wavelet is often used in calculating model seismograms from well data, partly because it is easily specified simply by its centre frequency (see Tutorial 2.4). The third wavelet in [Figure 2.9](#) is a Ricker wavelet of peak frequency 40 Hz, one in which there is zero phase shift between its constituent Fourier components, making it symmetrical about $t = 0$. Such zero-phase wavelets are highly desirable because they are the sharpest wavelets (they give the best resolution of close reflections) for any given amplitude spectrum (Schoenberger, 1974).

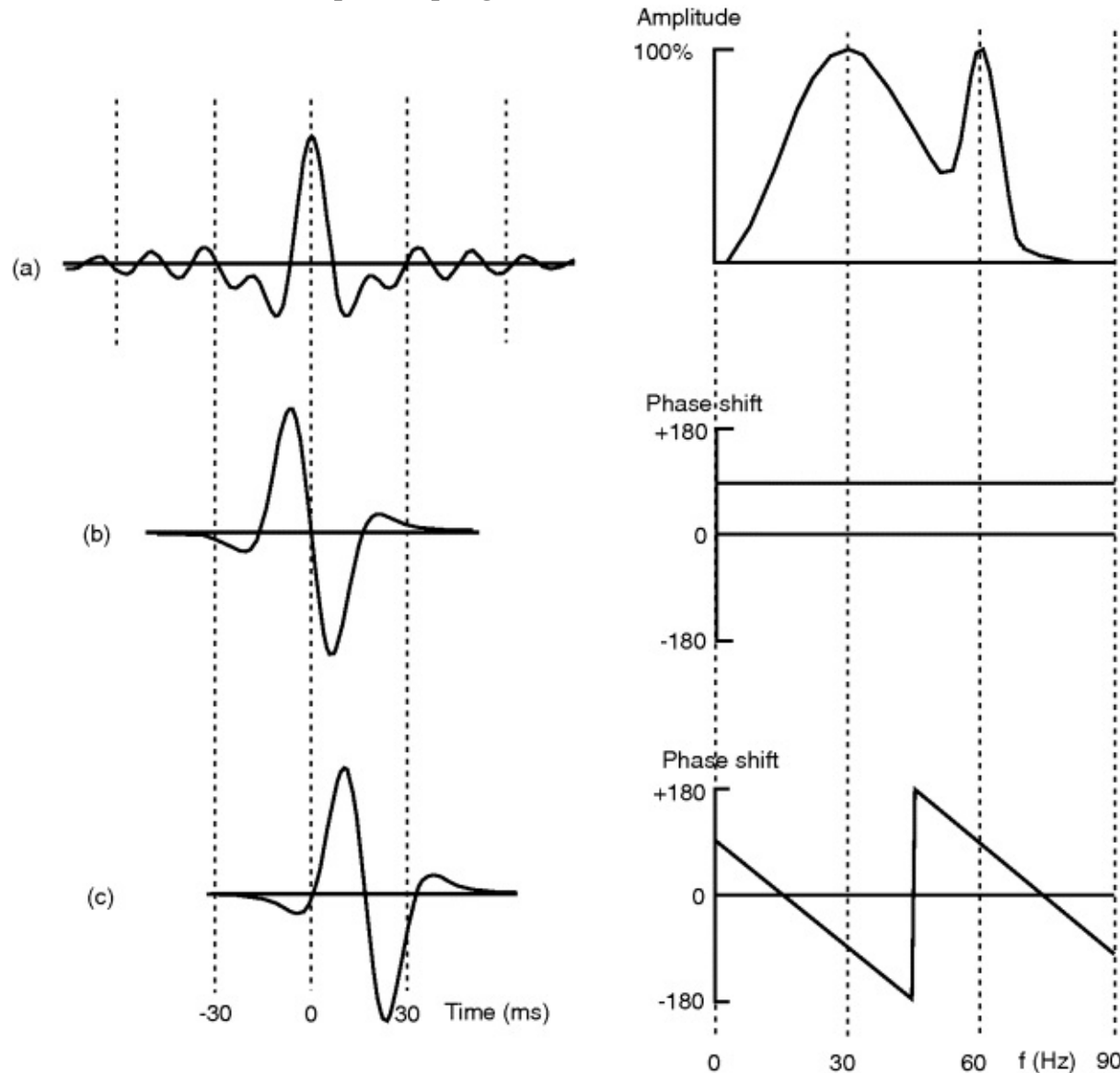
It is instructive to construct wavelets with varying phase and amplitude spectra. In [Figure 2.10](#), the basic wavelet is again a Ricker wavelet of peak frequency 30 Hz. In [Figure 2.10a](#), the amplitude spectrum has been modified by exaggerating frequencies around 60 Hz. Any such peak (or trough) in the amplitude spectrum introduces a ringing oscillation in the flanks of the wavelet, caused by the undue emphasis (or de-emphasis) of a particular band of frequencies – in this case,

around 60 Hz. Such a wavelet is highly undesirable because it complicates the reflection response from a geological interface.

Figure 2.10 Wavelet characteristics in time and frequency domains.

- a. Peaks or troughs in the amplitude spectrum cause ripples in the waveform.
- b. A uniform phase shift of $+90^\circ$ gives an asymmetrical wavelet.
- c. A linear negative shift in phase gives a delayed wavelet.

Waveforms developed in program *FOURSYN*.



[Figure 2.10b](#) shows the effect of a 90° phase lead on all components, giving rise to a wavelet with a characteristic peak/trough combination. [Figure 2.10c](#) demonstrates the importance of linear phase shift, which simply delays a wavelet without distorting it in any way. Any recording instrument (for example an amplifier) will inevitably introduce a phase shift in the seismic signal; it is therefore important that this should be linear to avoid distorting the wavelet. A linear phase shift also provides a convenient method of applying a precise time delay to a seismic trace in certain data processing operations. More detail on these topics is provided by means of Tutorial 2.4.

Bandwidth is the range of frequencies present in a wavelet. The wider the bandwidth in the frequency domain, the sharper the wavelet will be in the time domain – an expression of the complementary nature of the two domains ([Figure 2.9](#)). In order to separate closely spaced

reflections, it is desirable to have a narrow wavelet with a wide bandwidth. Bandwidth is fragile; it may be lost in data acquisition and may be both lost and recovered in data processing.

Bandwidth is generally defined numerically with reference to the power spectrum. It is the range of frequencies between the points in the spectrum at which the power has dropped to 50 per cent of its peak value. On the amplitude spectrum, the same points are those where the amplitude has dropped to about 70 per cent of its peak value.

Spectral amplitudes may be quoted as fractions or percentages of the peak value of the spectrum as described above, but equally well the decibel scale (db) is used. This is a logarithmic scale and thus allows large ratios to be expressed neatly as small numbers. If the amplitude at some frequency has fallen to a value A from a peak value A_{\max} the decibel value D_A of the ratio A/A_{\max} is expressed as:

$$(2.8) D_A = 20 \cdot \log_{10}(A/A_{\max})$$

Some typical values are:

Ratio (A/A_{\max})	db
1	0
1/2	-6
1/10	-20
1/100	-40
1/1000	-60

Where a ratio is greater than 1, the decibel figure will be positive. The decibel scale is widely used in the acquisition and processing areas of the seismic business, for example the overall amplification of the seismic receiver signal will be quoted as a (positive) db figure.

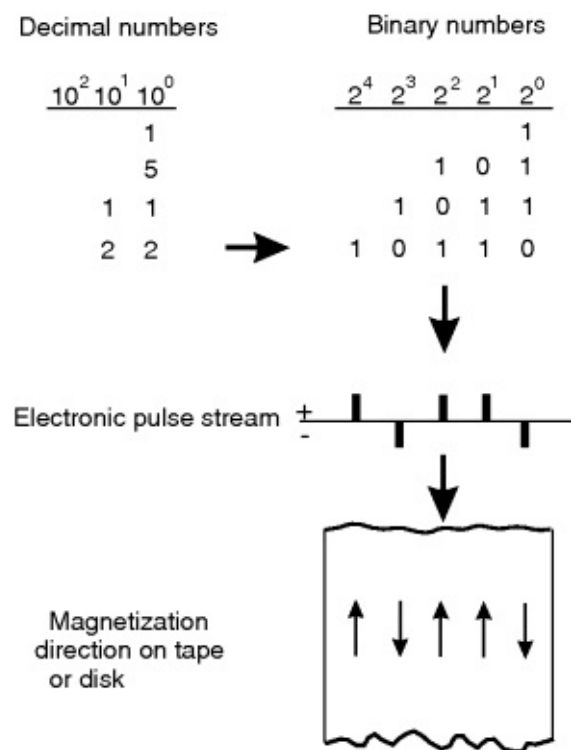
Polarity of the wavelet is defined as the sign of the numbers representing the maximum amplitude of a zero-phase waveform. If the waveform has a central peak represented by positive numbers, then the polarity of the waveform is positive and it will appear as a black peak on a conventional black and white seismic section. This definition was made by the Society of Exploration Geophysicists and is often referred to as SEG polarity (Sheriff, 2002). In practice, seismic sections are often produced with negative polarity, while for stratigraphic studies it is often useful to view (separately) sections of both polarities.

How do variations in amplitude and phase spectra affect the form of the seismic wavelet? Find out in Tutorial 2.4.

2.7 Digitization of Signals

The seismic waveform may be strongly affected by the method of recording the signal. An oscillographic record is an analogue of the variable voltage output of the geophone. Deflection of the trace on the record is analogous to voltage, both being continuously variable quantities. In a digital recording, the amplitude of the waveform is measured electronically at closely spaced intervals of time. The amplitudes are expressed as binary numbers, each number being recorded as a short sequence of electrical pulses marking the digits (ones and zeros) of the binary number code. In this form, the samples can be processed as numbers in a digital computer or stored on magnetic media or optically on CDs or DVDs ([Figure 2.11](#)).

Figure 2.11 Different ways of expressing and recording the decimal number 22.

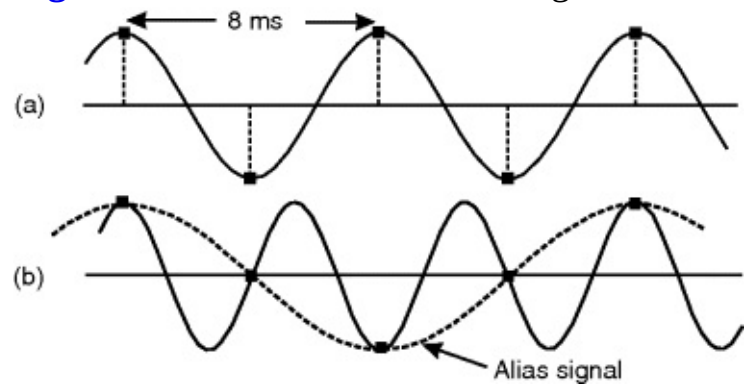


Measurement of the signal amplitudes is done by an electronic unit called an analogue-to-digital (A/D) convertor. The samples are measured at equally spaced sample intervals – generally 1, 2 or 4 ms for reflection seismic records. In the course of recording in the field, all seismic channels are sampled essentially simultaneously and the samples are recorded as a data block on magnetic tape or disk. Such interleaving of channels of information is called multiplexing, and one of the first tasks in later processing is to re-write each seismogram separately as a continuous string of numbers in a process known as de-multiplexing. If one wishes to see the seismogram as an oscillographic trace – say, for monitoring data quality in the field – it can be simply done by plotting the string of numbers as a graph against a time axis.

The Nyquist frequency (f_N) is the highest frequency that can be recorded at a particular sampling frequency (f_S). The waveform can just be adequately reconstructed if $f_S = 2f_N$ (Figure 2.12a). Typical values for deep seismic investigations are:

sampling period = 4 ms = sampling frequency of 250 Hz,
 so Nyquist frequency = 125 Hz.

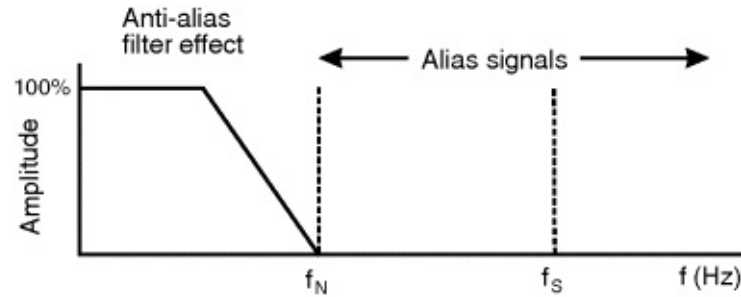
Figure 2.12 Creation of an alias signal.



When a signal is sampled whose frequency is greater than f_N , a spurious low-frequency signal is created as if the high-frequency signal were appearing under another name. For this reason, it is called an alias signal (Figure 2.12). To combat this unfortunate effect, the signal is passed through an analogue electronic filter before reaching the A/D convertor. This anti-alias filter sharply cuts

off frequencies higher than f_N ; indeed, it starts to cut signal amplitude at about $f_N/2$ (Figure 2.13). Hence, in the example quoted above ($f_N = 125$ Hz), frequencies above 62.5 Hz are progressively attenuated, typically at a rate of 72 db per octave, and the final bandwidth of the seismic data is $f_{low} - 62.5$ Hz, where f_{low} is the lowest frequency detected by the sensor. Inevitably, the anti-alias filter will introduce a phase shift into the signal, but this can be measured and compensated for during processing. Thus, the sample interval used in digitizing the signal defines the maximum bandwidth of the data and is one of the key parameters displayed on the seismic section label.

Figure 2.13 A spectral representation of aliasing.



2.8 Fourier Description of Space-Dependent Quantities

So far we have developed the Fourier description in the context of time-dependent quantities such as the output of a geophone at a fixed location. However, the description applies equally well to any quantity which varies cyclically against some other quantity instead of time. For example, we might measure variation of amplitude across a seismic section at a constant time, along a timeline on the section. As this line passes across the peaks and troughs of dipping reflections, we would find variations in amplitude: slow variations with gentle dip, fast variations with steep dip.

A graph of amplitude versus distance across the section would once again be of general sinusoidal form and would look like a seismogram, except that the variable is now distance instead of time. We could write an expression for the variation similar to the basic cosine wave formula given in equation (2.5) of this chapter, but with distance along the traverse, x , instead of time, t and a space-frequency, k instead of f :

$$(2.9) \quad f(x) = C \cdot \cos(2\pi kx + \varphi)$$

Instead of a periodic time T (seconds/cycle), we now have a periodic distance or wavelength λ (m/cycle) (Greek lambda). Just as frequency $f = 1/T$ cycles/sec, we can say that space-frequency $k = 1/\lambda$ cycles/m. Space-frequency is more often given the name wavenumber.

Data descriptions and processing operations developed on time-dependent data can be applied to space-dependent data as well. Frequency f and wavenumber k are used together in certain important types of seismic analysis and processing. We will not follow these out in any more detail, but will point them out from time to time as examples of f - k processing.

Finally, suppose a sinusoidal wave is travelling at a velocity V m/s and its frequency is f cycles/s (Hz). We can write:

$$(2.10) \quad \lambda = 1/k = V/f$$

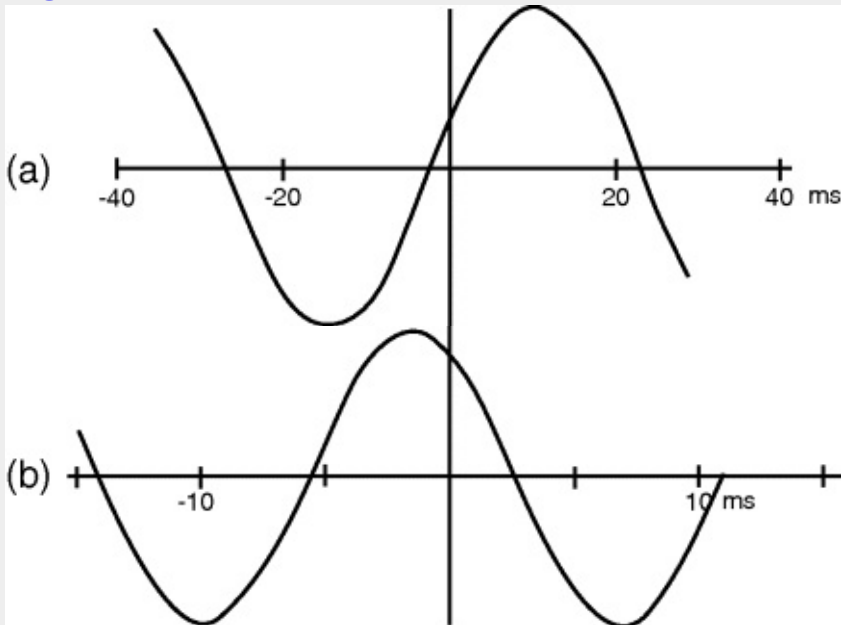
In 1 second, f cycles are spread over V metres, so the wavelength (the length of each cycle) is V/f metres.

Tutorials for Chapter 2

Tutorial 2.1

Purpose: To consolidate ideas of frequency and phase shift. For each of the cosine waveforms **a** and **b** in [Figure T2.1.1](#), measure the period, frequency and angular phase shift in degrees.

[Figure T2.1.1](#)



Tutorials 2.2

Purpose: To create a periodic waveform by Fourier summation as expressed in [equation \(2.6\)](#)

1. In [Figure T2.2.1](#), measure the amplitudes of the three waveforms at $t = 0$ (e.g. in mm).
2. Plot the sum of the three amplitudes at $t = 0$ in the space at the bottom of [Figure T2.2.1](#).
3. Repeat 1 and 2 above for the times marked by dotted lines and join the points with a smooth curve to form the summed waveform.
4. Complete the second half of the waveform by using symmetry.
5. Measure the frequencies of the three component waveforms.
6. Plot the spectra of the composite waveform on the axes shown in [Figure T2.2.2](#), using lines (or dots) to mark the spectral components.

[Figure T2.2.1](#)

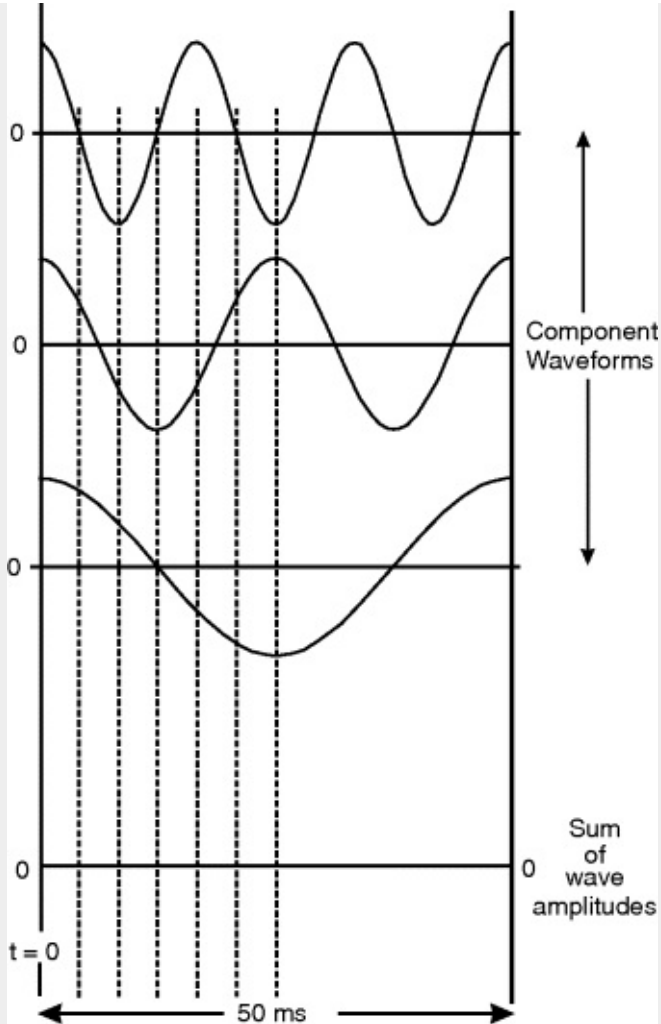
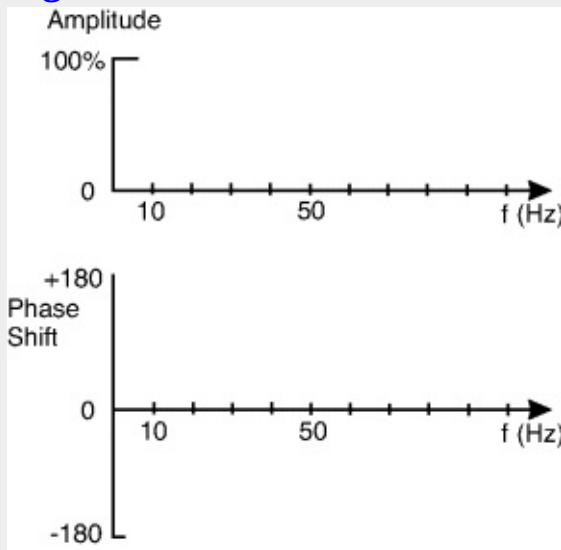


Figure T2.2.2



Tutorial 2.3

Purpose: To demonstrate the transition from periodic waveform to wavelet

1. Run the program *FOURSYN* and go through the Quick Start Tutorial under Help to check basic functionality.
2. Select Spectra/Generate/User-Defined/Parameters and set frequency increment to 8 Hz. Type in a title and click Check and Close.
3. Select Spectra/Generate/User-defined/Create, then read and OK the prompt.
4. In the amplitude spectrum, click on the following frequencies at the 100 per cent level: 32, 64 and 96 Hz, so we have a fundamental component of 32 Hz frequency with its 2nd and 3rd harmonics. Confirm the spectral frequencies chosen as listed in the Spectral Data window. Leave the phase spectrum as it is, i.e. zero phase shift on all spectral components.

5. Select Signal/Parameters and make the length 100 ms. Type a title then click Check and Close.
6. Select Signal/Draw and observe the periodic signal created by summing the three spectral components. Does the waveform have the same general shape (although a different period) as the summed waveform you obtained manually in Tutorial 2.2? Check that the period of the signal (T) is the same as the period of the fundamental component in the waveform. Select Signal/Parameters and make the length 400 ms, then re-draw the signal.
7. Click on the amplitude spectrum to add extra components to the spectrum halfway between those created so far, i.e. at 48 and 80 Hz. Make amplitudes the same, i.e. 100 per cent. Select Signal/Draw and observe the updated plot of components and signal. What is T for the new signal?
8. Again add extra spectral lines between those already there (i.e. at 40, 56, 72 and 88 Hz), re-draw the signal and measure T . *Save the spectrum* at this point – you will need it for the next tutorial. Give it some meaningful name like spec3296 (the extension .fdt for Fourier Data is added automatically). Perhaps take a print-out for your records.
9. Make up a table of Δf and T from your measurements: do the values support the conclusion that $T = 1/\Delta f$ (seconds)? So when $\Delta f \rightarrow 0$, $T \rightarrow ?$

Tutorial 2.4

Purpose: To answer the question: how do variations in amplitude and phase spectra affect the seismic wavelet?

Part I: *How do variations in the amplitude spectrum affect the wavelet?*

1. Start *FOURSYN*, select Spectra/Open and open the Fourier spectral data file spec3296.fdt saved from Tutorial 2.3.
2. Select Spectra/Draw: note zero phase shift on all components.
3. Set signal length to 200 ms and draw the signal (you can ignore a title). Since all components have zero phase shift, the wavelet is symmetrical and peaks at the $t = 0$ axis. It is not clear where the wavelet should be truncated, i.e. how much of the ripple waveform to either side should be included.
4. By clicking on the spectral lines, taper off the high frequency components in the amplitude spectrum with the following values: 96 Hz, 25%; 88 Hz, 50%; 80 Hz, 75% – then re-draw the signal. Has the annoying high-frequency ripple waveform gone? Has the width of the central wavelet changed?
5. To eliminate the residual low-frequency undulation in the waveform, taper off the low frequency components of the spectrum with the following values: 32 Hz, 50%; 40 Hz, 75% – and re-draw the signal. It is now an acceptable isolated wavelet and could be truncated at +20 and –20 ms.

Conclusion: Sharply truncating the amplitude spectrum leads to undue emphasis of frequencies at the truncation point. The spectrum should be smoothly tapered.

6. Select Spectra/Generate/Ricker/Parameters, set centre frequency to 64 Hz and spectrum sampling interval to 4 Hz and draw the spectrum. Note how well-tapered the ends are and how wide the bandwidth: it only drops to 50 per cent amplitude at 32 and 104 Hz.
7. Draw the signal – the Ricker wavelet. How does its width compare with the previous wavelet? Note the complete absence of any ripple because of the perfect cancellation of all spectral components to either side of the central wavelet. Another desirable quality to note is the ratio of positive peak amplitude to the negative troughs to either side. A geological interface would be marked by a single prominent peak on the seismic section.
8. Create a peak in the amplitude spectrum by setting, say, the 104 Hz component to 100%, draw the wavelet again and note the ripple waveform that has appeared. What is its frequency? Create a trough in the spectrum by reducing the 104 Hz component to zero. How is the wavelet affected?

Conclusion: Peaks and troughs in the amplitude spectrum are bad news, creating unwanted ripple-type noise in the wavelet.

Part II: *How do variations in the phase spectrum affect the wavelet?*

9. Keep the Ricker amplitude spectrum but set the phase to +180 on all components (*Tip: sweep the cursor along the phase spectrum at the +180 level while clicking the mouse furiously*). Each component is shifted by half a cycle (check [Figure 2.3](#)), so peaks become troughs and the wavelet is inverted. Note that a phase shift of -180° would have exactly the same effect. This explains why the phase shift axis on the phase spectrum is scaled between $\pm 180^\circ$. If the phase shift exceeds $+180^\circ$, say to $200 = 180 + 20$, it simply doubles back to be plotted at $-180 + 20 = -160^\circ$.
10. Set phase shift to $+90^\circ$ on all components so they are shifted by a quarter cycle to earlier time (check

[Figure 2.3](#)). The wavelet is now a peak/trough combination. A geological interface would now be represented by a peak accompanied by an equally prominent trough on the seismic section – a more complicated response than the zero-phase wavelet of paragraph 7 above.

Conclusion: Phase shifts in general lead to wavelets that are more complicated than the zero phase wavelet.

Chapter 3

Data Acquisition

3.1 General Points

The configuration shown in [Figure 1.1](#), where the source and receiver are at the same location, is not very practical because the receiver would be in danger of being blown up by the source! In practice, the receivers are laid out in a long line on the ground, typically as far as 3,000–4,000 m from the source (or towed on a long cable behind a ship), and the source is activated at one end of the line of receivers. The whole configuration moves up by one receiver interval (typically 20 m) for every new shot along the line of traverse. The data is recorded and then processed later to make it appear as if a source and a single receiver were coincident at each surface location, as in [Figure 1.1](#) (see Section 3.5).

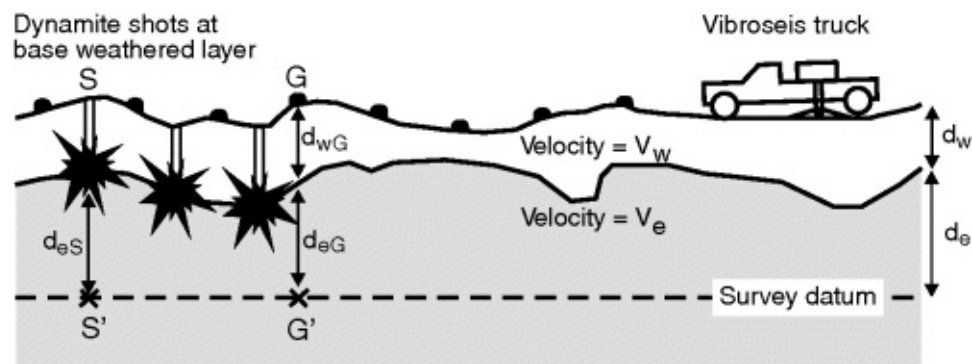
Although the basic layout and the recording instruments are the same in all environments, the types of source and receivers, and the problems of transport, access and sources of noise that may corrupt the data, are very different between land and sea operations. ‘Noise’ is a very general term that means any recorded signal that is not a reflection from a geological interface, and much of the effort in seismic data acquisition and processing is directed to maximizing the ratio of signal amplitude to noise amplitude – the signal/noise (S/N) ratio. The interpreter has to be aware of the possibilities of noise entering the data set while acquiring the data in the field, and also of fundamental limitations of the technique that arise from field procedures.

Data acquisition is a huge subject in itself, but well covered in textbooks such as Sheriff & Geldart (1995). In this review, we will focus on the common mid-point shooting method.

3.2 Seismic Sources and Receivers

The types of source and receivers used vary according to the field conditions. Dynamite is the traditional land source and is still much used. It gives a sharp pulse with a wide frequency bandwidth, and is the seismic source to which all new sources are compared. Charges vary from about 5 to 20 lbs. in weight and are detonated electrically in shallow boreholes drilled to the base of the weathered layer. The benefit of using dynamite is that it can be detonated below the energy-absorbing materials of the weathered layer, which preferentially attenuate the high frequencies of the seismic signal. ([Figure 3.1](#)). However, questions of safety and disturbance, security, political sensitivity and cost (including the shot-hole drilling) count against dynamite. In terms of useful (seismic) energy, it is very wasteful since most (approx. 98 per cent) of the energy produces heat by smashing up and compacting the surrounding earth (O'Brien, 1974). However dynamite is still the fall-back, go-anywhere seismic source and the only one that can be applied in really difficult terrain.

[Figure 3.1](#) Data acquisition on land. Dynamite shots are placed at the base of the weathered layer. The Vibroseis truck has to operate on the ground surface.



In the Vibroseis method on land, a truck-mounted hydraulic vibrator generates a long sinusoidal wave train that passes into the ground by means of a pad lowered beneath the truck (Figure 3.1). Later processing converts the long reflected wave trains into sharp wavelets. Although very convenient and environmentally acceptable, the vibrator suffers, like all surface sources, from the enormous loss of energy that takes place in the poorly-consolidated materials of the weathered zone which one finds immediately under the ground surface. Also, like all surface sources, it generates much more surface wave noise than a dynamite shot in a borehole. Even so, vibrators are the preferred land source and have even been successfully used as the source of energy in deep investigations of the earth's crust and mantle.

Marine operations require an easily repeatable source for continuous working, and an array of airguns is the standard source. An airgun is a steel cylinder ranging up to about 2,000 cubic inches in volume. The cylinder is pumped full of high-pressure air (2,000 psi) which is suddenly vented to the sea. The bubble of air expands until its internal pressure is less than that of the surrounding water, when it rapidly contracts, heats up and explodes once again, so a train of bubble pulses is produced instead of a single one. The period of repetition of the bubbles depends on the volume of the airgun (smaller airguns give shorter periods), and it is possible to choose an array of airguns of different sizes so that the bubble pulses largely cancel each other out while the first pulse is appropriately reinforced. In the water gun variety, the compressed air is used to blow out a packet of water at such high velocity that it leaves a cavity behind, which then implodes, leaving no bubble.

On land, the receivers are geophones, in which a coil, suspended on springs, bobs up and down in the vertical direction as the ground surface moves in response to the vertically travelling reflection wavefront. The coil windings cut the magnetic field of a permanent magnet, and the voltage induced across the coil terminals is proportional to the velocity of the ground motion. At sea, pressure-sensitive piezoelectric devices (hydrophones) are used to measure the varying water pressure as the P-wave passes.

Although they measure different physical quantities, the general shape of the waveform recorded by both devices is similar (see Chapter 4, Section 4.4). Apart from adequate sensitivity, their main requirements are a flat amplitude response and linear phase response over the working frequency range. The output from the receivers is passed through electronic amplifiers prior to digitization. The complete chain of recording instruments will inevitably introduce some phase shift into the recorded signal, but this can be measured and compensated for in the processing of the data. Final recording is done digitally on tape or disk (Chapter 2, Section 2.7).

3.3 Static Corrections

One of the many factors that make operations on land more complicated than operations at sea is the need to take account of variable near-surface conditions. There are two main difficulties: first, the presence of a weathered rock layer immediately below the surface, characterized by low velocity and rapid absorption of high-frequency energy; and second, topographic variation along the line of traverse.

The weathered layer, also known as the Low Velocity Layer (LVL) has different geological causes, depending on its location around the world. For example:

- in the tropics, it is commonly a layer of bauxite, the product of deep weathering on a variety of lithologies;
- in deserts, it may be dune sands;
- in glaciated areas of the temperate zone, it is typically glacial till.

Whatever the nature of the weathered layer, it is highly desirable to set the seismic source at its base to minimize the loss of high frequencies in the seismic wavelet. It is also essential to measure its thickness under each geophone station, because travel times from deep reflectors will be increased where the weathered layer thickens. Because of the low velocity of the layer (about 1,000 m/s), only a few metres' variation in thickness will cause time variations of several milliseconds between adjacent traces on the seismic section – enough to seriously degrade the continuity of reflections. Large variations in ground elevation along the survey line may also contribute to big variations in recorded TWT for deep reflections along the line of traverse, leading to false depth calculations.

The land situation is summarized in [Figure 3.1](#). A survey datum level is established just lower than the lowest topographic level in the survey area. Reflection times for the seismogram from shot S recorded at geophone G have to be reduced by the time taken to travel through the weathered layer and rock down to the survey datum level. Referring to [Figure 3.1](#), the total time correction applied to a dynamite seismogram is $(d_{eS} + d_{eG})/V_e + d_{wG}/V_w$. For Vibroseis data, a further correction will be made for the time spent in the weathered layer under the Vibroseis truck.

Time on the recorded seismogram is reduced by this amount, so that it appears as if sources and receivers were located on the datum level (S' and G' on [Figure 3.1](#)). Since the correction is fixed for all reflections on the seismogram, it is called a static correction to the data. It is determined by the field crew (hence 'crew static') and passed on to data processing staff for implementation.

When using dynamite, a geophone at the surface next to the shot point will record the uphole time through the weathered layer. If the shots are spaced closely enough and the weathered layer only varies slowly along the traverse, this may be enough to determine the weathered layer profile and correct the data. Alternatively, V_w , V_e and d_w may be determined from the first breaks on the reflection seismograms by employing a refraction interpretation. In the case of the vibrator source, a shallow refraction survey is carried out all the way along the line to determine these three quantities. Such corrections may still leave small time shifts between adjacent traces big enough to seriously detract from the continuity of reflections, but these can be tackled later as part of the data processing suite.

In marine surveying, the sediments immediately below the sea bed commonly show little lateral variation in thickness or velocity, so that generally static corrections are not made to the data.

3.4 Recording and Presentation of Data

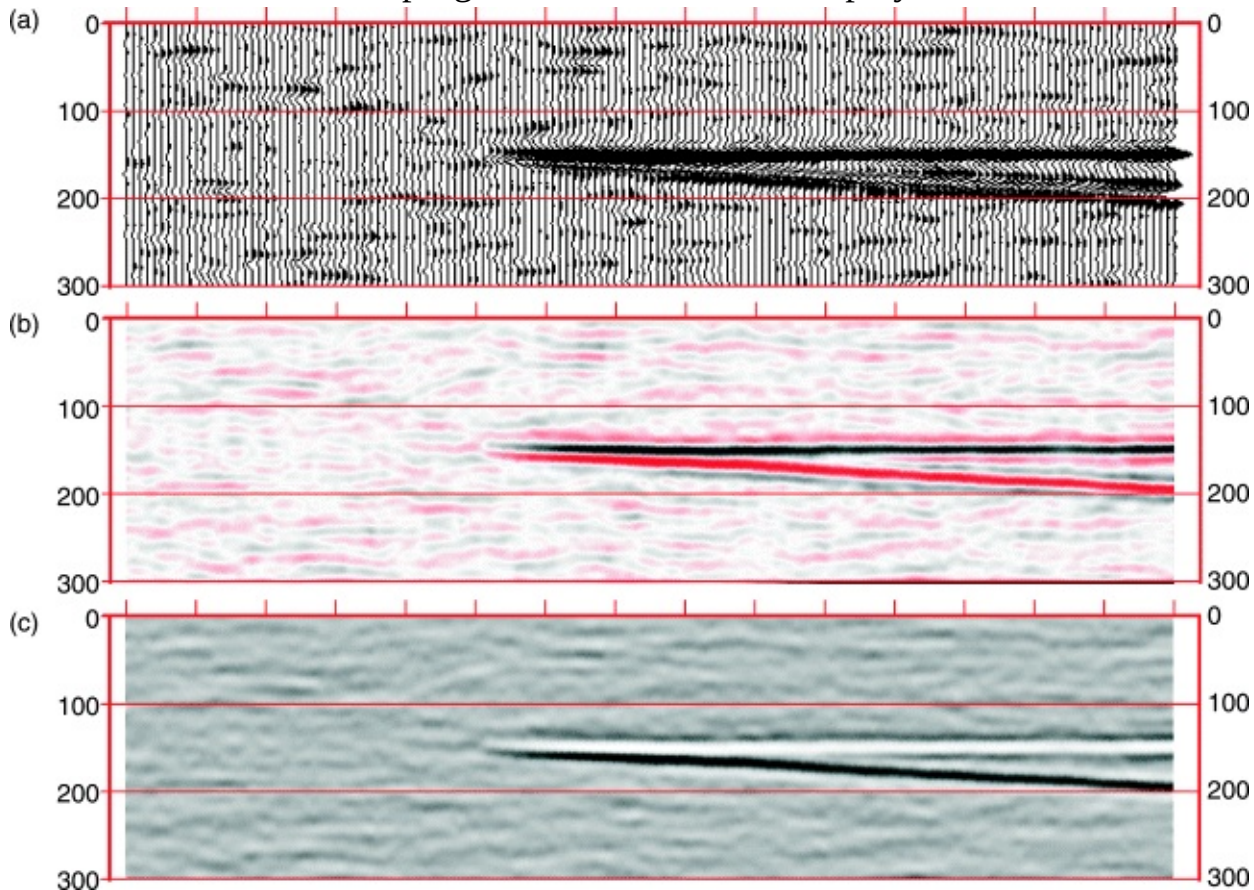
Analogue seismograms may be displayed in the field for quality control, but the data is digitized and recorded in digital form for later processing. A typical exploration seismogram may be recorded for six seconds TWT with data sampled at 4 ms intervals, so it is digitized into a string of 1,501 numbers, each number describing the amplitude of the waveform at an instant of time.

The way in which the data is presented can make a big difference to how it is perceived and interpreted. The time-honoured mode of presentation is a 'wiggle-trace' seismogram with peaks of positive amplitude shaded black, as in [Figures 1.1](#) and [3.2a](#). It can be created by plotting a graph of the digitized amplitude values against time. However, a seismic section can be treated as just a sheet of numbers, so can be displayed in a variety of ways, e.g. as colour contours, variable shades of grey, etc. ([Figure 3.2](#)). Individual seismic traces can no longer be distinguished, but colour adds a lot to the impact of the data presentation, especially in the recognition of subtle lateral changes along the section. Where the seismic data is used to investigate reservoir properties, colour displays are essential and, on modern workstations, the operator can change the display of the data easily. The image is built up by assigning a colour patch (called a picture element or pixel for short) to each sample of the seismic trace according to its amplitude. In [Figure 3.2b](#), high positive pixels are coloured black, pixels close to zero amplitude are white and high-amplitude negative pixels are red.

[Figure 3.2](#) A seismic section displayed in three different styles.

- a. Wiggle trace + variable area.
- b. Colour shades red-white-black.
- c. Grey shades intensity.

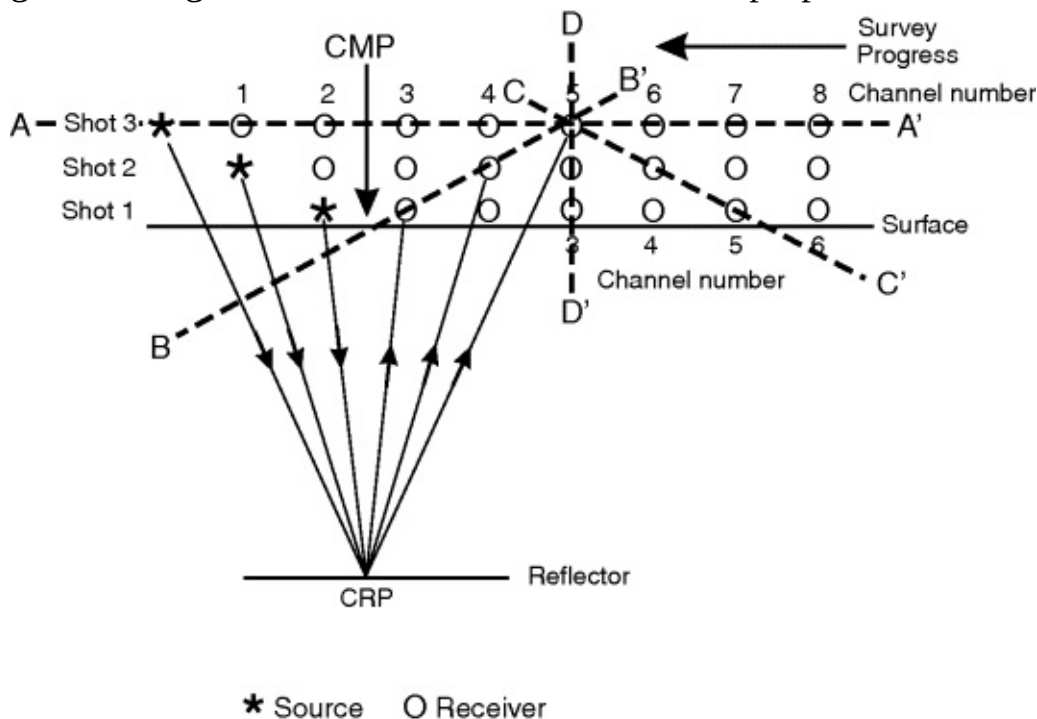
Sections modelled in program *SYNTHSEC* and displayed in *SEGYP2D*.



3.5 Common Mid-Point (CMP) Shooting

Two-dimensional data acquisition will be considered first, in which the object is to obtain individual time-sections scaled in the two dimensions of distance and TWT. The layout of a survey is similar on both land and sea ([Figure 3.3](#)). Shots are made at intervals of typically 25 m along straight lines, which are laid out on a grid and spaced according to the objective of the survey – 5 to 10 km for reconnaissance or as close as 200 m when detail is required over a prospect or field. Receivers are spaced at the same intervals as shots along the line. The linear array of receivers is called a geophone spread on land, or a hydrophone streamer or cable at sea.

[Figure 3.3](#) Shooting progress along a reflection seismic line. Successive shot-receiver positions are shown offset from ground surface for the sake of clarity. The recorded seismic traces are gathered together in different sets for different purposes.



At sea, the cable is towed along behind the shot boat and a shot is made every time the ship plus cable moves up by one survey interval. On land, move-up is achieved for each shot by switching geophone connections along a cable which is pre-laid on the ground ahead. At sea, the entire process is controlled by a computer system which continuously monitors the ship's position using GPS (Global Positioning System), steers the ship along the line and fires the shot at the correct location.

Analogue to digital conversion takes place close to the receivers and the digital signal is transmitted to the recorder by telemetry. In the recording truck or on the ship, the signals from the receivers are stored digitally for later processing. Each receiver is provided with its own channel through the system (cable, amplifier, digital recording), leading to the final seismogram. It is common nowadays to record several hundred channels simultaneously from one shot in 2D surveys or several thousand channels in 3D surveys.

In the course of data processing, the seismograms are assembled or gathered out of digital storage in several different combinations for different purposes, so it is important to relate these gathers to the field shooting configuration. In [Figure 3.3](#), the shot and receiver positions for three successive shots are shown. The basic field recording consists of all the seismograms recorded

from a single shot. Since the shot is the common factor, this assemblage of traces is called a Common Shot gather. The line A – A' in this figure indicates the set of receivers that record the Common Shot gather for shot 3. Each trace in the gather will contain a reflection from a different point on a subsurface reflector.

One particular reflection point in [Figure 3.3](#) is considered which forms a Common Reflection Point (CRP) for a group of seismograms culled from different Common Shot gathers. As the shot and cable move up together one interval at a time, successive shots provide reflections from this CRP on different recording channels: shot 1 on channel 1, shot 2 on channel 3, shot 3 on channel 5, etc. All these shot-receiver pairs have a Common Mid Point (CMP) – a unique location on the surface. The associated seismograms are named the CMP gather and, for reasons to be explained shortly, they constitute the most important assemblage of all.

Line B – B' in [Figure 3.3](#) identifies channels 1, 3, 5, 7... etc. that must be culled from successive shot gathers to form this particular CMP gather. But what about channels 2, 4, 6, 8... and so on? There will be another CRP adjacent to the one shown, but it will be positioned a half-interval to the right. That CRP will provide a reflection from shot 1 at channel 2, shot 2 at channel 4 and shot 3 at channel 6, etc. This CRP and the associated CMP is just half a survey interval from the first. Thus, a typical line with a shot and receiver interval of 25 m will generate CMPs spaced at intervals of 12.5 m. If there are n receivers in the hydrophone streamer or geophone spread, spaced at d metres, then each CMP gather will contain $n/2$ traces and the CMPs will be spaced $d/2$ metres apart.

Why is the CMP gather so important? Remember from [Figure 1.1](#) that we wish to record normal-incidence reflections, where the seismic energy travels straight down to the reflector and straight back up again to the surface. From [Figure 3.4](#), it is clear that the raypaths about the CMP vary in length with offset from the shot. The shortest ray at the shortest offset is nearly a normal-incidence ray and will have the minimum time, but reflections on the CMP gather increase in travel time as offset from the shot increases ([Figure 3.5a](#)). However, since we know the offset distance and can measure the seismic velocity down to the reflector, it is possible to correct all the traces to normal-incidence traces ([Figure 3.5b](#)) and finally add them together to form a single, enhanced normal-incidence trace ([Figure 3.5c](#)). The process is called CMP stacking, and this is a key step in data processing. The number of traces stacked together is called the fold of the gather. In [Figure 3.5](#), twelve-fold stacking is illustrated, less for the shallower reflections. Stacking clearly enhances the signal/noise ratio of the data, most evidently in the case of reflection 2, for which the signal/noise ratio in the original data was only 1 : 1. This and other important benefits of CMP stacking will be further explored in Chapter 6.

[Figure 3.4](#) Raypaths about a common mid-point (CMP) location, a fixed point on the seismic line, from a series of shots.

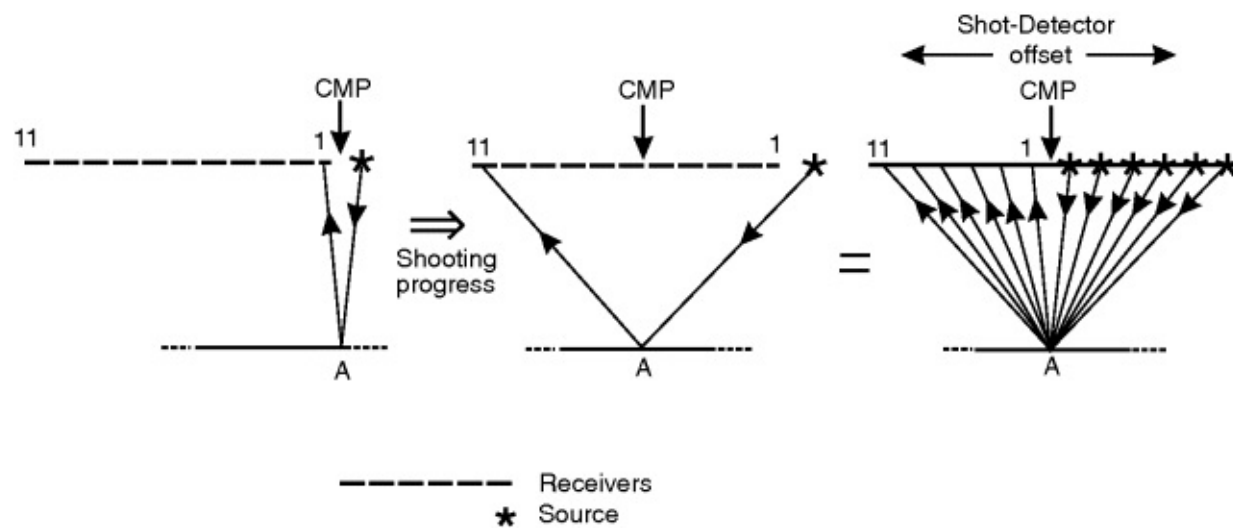
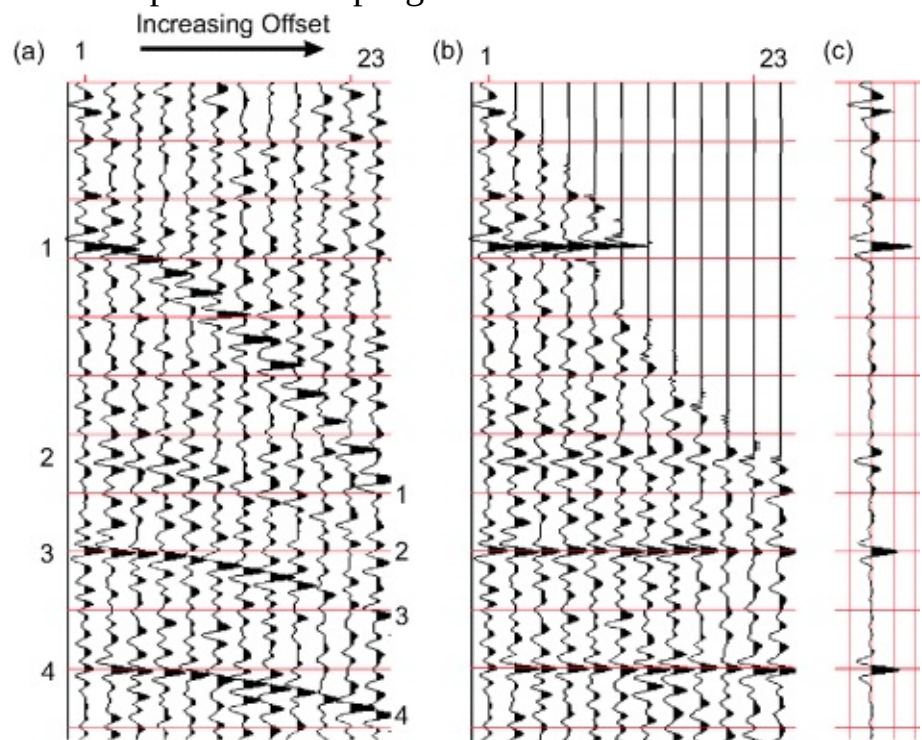


Figure 3.5

- a. The recorded CMP gather.
- b. Reflections on the CMP gather corrected for curvature (NMO correction).
- c. The reflections stacked (summed) across the gather to form a single composite trace with enhanced signal/noise ratio.

Data processed in program *NMOSTAK*.



In [Figure 3.3](#), line C – C' links the set of channels whose common factor is that their receivers are all at the same offset (range) from their respective shots so that they constitute a Common Offset gather. Line D – D' links channels whose common factor is that they are all recorded at the same receiver position, so they constitute a Common Receiver gather. Both gathers will feature in the appropriate contexts later.

3.6 The Attack on Noise

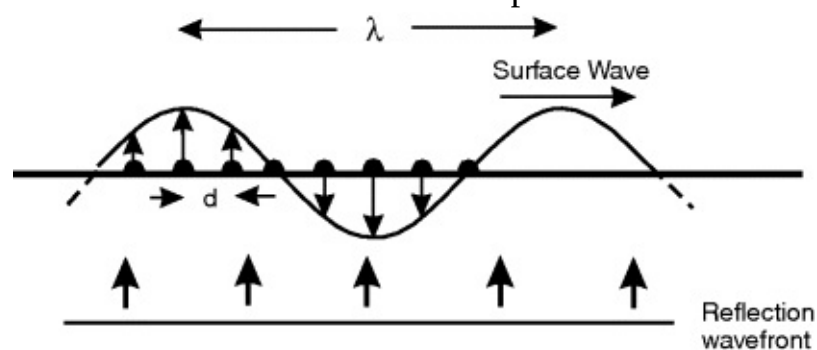
Noise is any disturbance on the seismic record which tends to obscure primary reflections from rock strata. It may be conveniently divided into two sorts – random noise and coherent (often

shot-generated) noise. Various antidotes to noise are employed, both during data acquisition and (especially) data processing. For the moment, we will look at some of the antidotes applied against noise during data acquisition.

Frequency filtering in earlier times was about all the data processing that was done and was performed during the recording operation in the field. Electronic filters were (and sometimes still are) employed to cut out noise frequencies that were substantially different from those contained in the signal. Wind noise, for example, is generally of a higher frequency than most of the seismic signal, so it may be eliminated with a high-cut filter. Low-frequency surface waves (5 to 20 Hz) are often treated with a low-cut filter. Nowadays the tendency is for the data to be recorded without filtering wherever possible (except for the anti-alias filter), and the filtering is applied digitally as part of the data processing.

Source and receiver arrays are employed against coherent noise passing horizontally along the length of the spread or streamer, such as surface waves on land or ship noise at sea. Often, such noise shows one dominant wavelength or a narrow range of wavelengths. In land work, it is usual practice to lay a small linear array of receivers along the spread spaced a distance d apart, such that the upwards part of the surface wave motion is cancelled by the downwards part ([Figure 3.6](#)). Wavelengths (λ) less than that shown will also be cancelled pretty well until $\lambda = d$ (or $d/2$, $d/3$, etc.), when peak output will occur. Wavelengths greater than $8d$ will show a progressively greater output as the receivers tend to move more in the same sense.

Figure 3.6 A surface wave travelling horizontally causes motion in opposite senses as it passes an in-line array of geophones, so the output of the array is zero, but a vertically travelling reflection wavefront causes maximum output.



Note that a reflection wavefront approaching the surface almost vertically will produce a large output from the array as it has a long apparent wavelength along the surface and so moves all geophones in the array up or down at about the same time. Similar thinking applies to the design of hydrophone groups at sea, where noise from the towing ship passes horizontally along the streamer. On land, it is common practice to arrange sources (e.g. shots, vibrators) in linear arrays as well, to help prevent the generation of noise in the direction of the geophone spread. A period of experimental shooting is generally required at the start of operations in a new prospect in order to assess noise characteristics and to optimize array spacing.

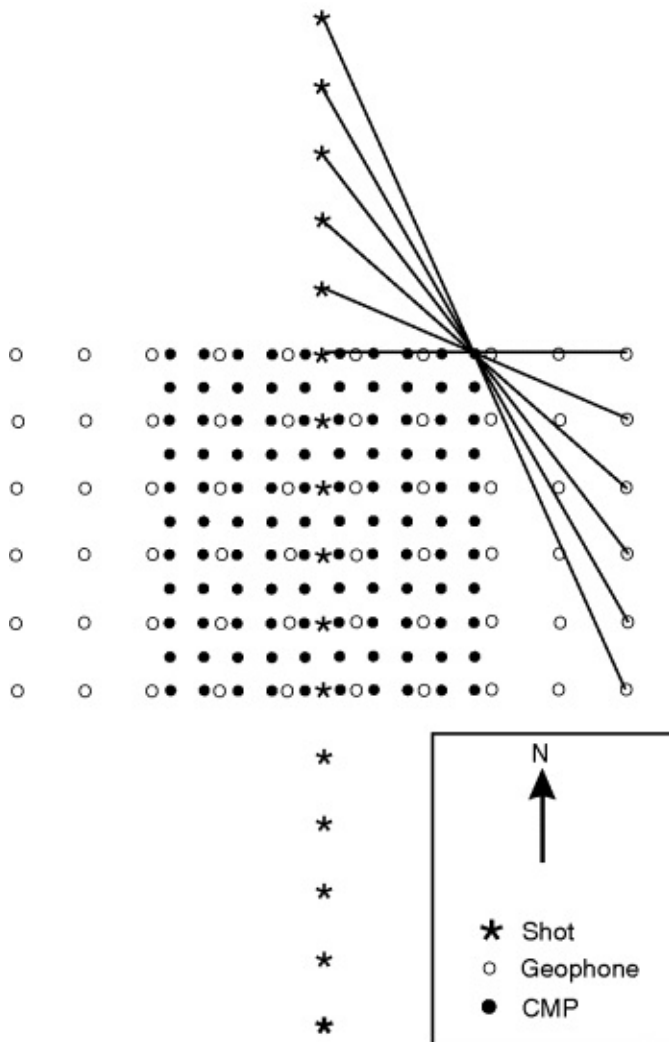
Vertical stacking is the summation of a number of records made from several shots fired sequentially at the same location. Surface sources invariably require stacking in this way to enhance the seismic signal which is weakened by passage through the energy-absorbing material of the near-surface layers. The stacking of records from N shots provides $N^{1/2}$ enhancement of signal/noise ratio over the recording made from one shot when noise is random.

3.7 3D Surveys

The object of shooting 3D surveys is to record reflections that come from out of the plane of the seismic line, so sources and receivers are not confined to working along a line but cover a swath of the ground surface.

On land, various shooting schemes may be used, which will vary according to terrain and access. Bee *et al.* (1994) is a good reference from which to get a feel for some of the problems associated with land 3D acquisition in a difficult environment. The most desirable procedure is to shoot a patch of CMP data from lines of shot points running at right angles to lines of receivers in the manner of [Figure 3.7](#). CMP points can be identified for a zone of coverage to either side of the shot point line, and CMP stacking will yield normal incidence traces for each of the points. Note that there is no requirement that all shots and receivers must be in a straight line to form a CMP stack; the only prerequisite is that the CMP should lie halfway between shot and receiver. Coverage over a wide area may be achieved by shooting many such patches side by side.

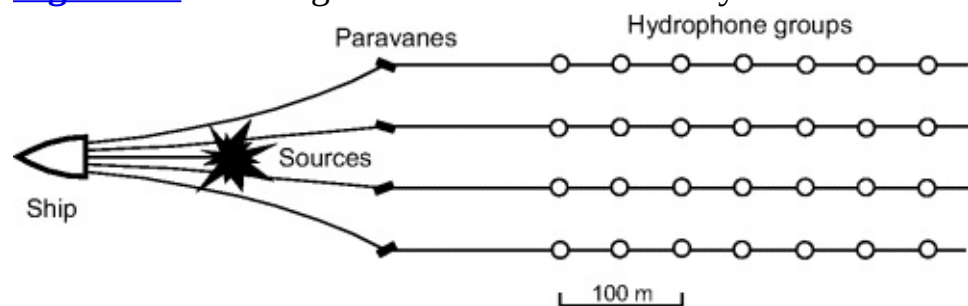
[Figure 3.7](#) 3D land survey. A single line of shots and six lines of geophones gives six-fold stacking on the patch of CMPs shown here. For one of the CMPs, the six shot-geophone pairs are indicated by the connecting lines.



At sea, the procedure is to tow several streamers behind the ship, kept in position by paravanes, with two airgun arrays firing alternately ([Figure 3.8](#)). On both land and sea, a matrix of CMP points is eventually created, covering a surface area at uniform density. Each point has assigned to it a single, stacked, normal incidence trace. When finally processed into a matrix of data points

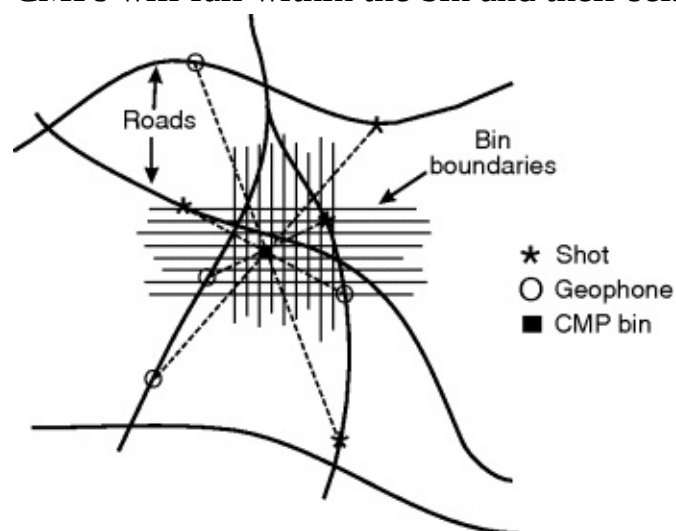
across the survey area, the data points aligned with the ship's course are called the inline data, and the data on lines at right angles to that are called the cross-line data.

Figure 3.8 Shooting marine 3D data. As many as 12 streamers may be deployed at once.



A major problem both on land and sea is that the sources and receivers may not lie exactly equidistant from the desired CMP. At sea, the hydrophone streamer is often curved or feathered, due to the action of currents across the line. On land, it may not be possible to arrange sources and receivers in an exact geometric relationship, for example where a Vibroseis party has to work along an existing system of tracks and roads (**Figure 3.9**).

Figure 3.9 3D land data acquired from shots and geophones distributed along a random network of tracks and roads. For each small bin area, a set of shot-geophone pairs can be identified whose CMPs will fall within the bin and their seismograms will form a CMP gather.



In both cases, the solution is to divide the area into sub-areas called cells or 'bins', perhaps 25 m square, and to stack up all the data for CMPs that fall within the bin. Since the survey coordinates of all locations are held on computer files, it is a straightforward matter to identify source-receiver pairs whose CMP lies within a particular bin and whose seismic trace may eventually be stacked at the bin location (**Figure 3.9**). The size of the bin has to be chosen well. If it is too big, then time differences between reflections on the constituent traces caused by the presence of dip on the reflector will destroy the high frequencies and reduce bandwidth. If the bin size is too small, only a few CMPs may be found within it and the fold of stacking may drop too low.

Binning the data in this fashion brings its own problems. The fold of coverage may vary considerably across the area, as some bins will be sparsely filled with traces while others are more densely filled, according to the distribution of shot-detector pairs. For example, in **Figure 3.9**, the fold of stacking will be dense through the middle of the area and sparser at the edges. Unequally weighted data of this sort may need special treatment in later stages of processing in order to

build the proper final waveform.

Chapter 4

Seismic Wave Propagation

4.1 Introduction

We are concerned with three types of seismic wave propagation: compressional waves (P-waves), shear waves (S-waves) and surface waves. In this chapter, we will look at wave propagation in the context of structural interpretation.

4.2 P-wave

The compressional or P-wave is the most important mode of propagation of the seismic disturbance for petroleum exploration. The 'P' is for Primary, a hangover from earthquake seismology, since the P-wave travels fastest of all and is always the first disturbance on an earthquake recording.

If a volume of material (solid, liquid or gas) is struck from one side, the initial compression is transmitted onwards from one set of particles to the next, somewhat in the manner shown in [Figure 4.1a](#). In this figure, the material is crudely modelled as a matrix of particles joined by springs. The initial compression will be transmitted onwards faster if the springs are stiff (incompressible) and the particles are light (low density) and thus easily moved. Hence, the velocity of propagation of the P-wave (V_p) will be proportional to the incompressibility (k) and inversely proportional to the density (ρ , Greek rho) of the substance. So:

$$V_p \propto k/\rho$$

Incompressibility is also called the bulk modulus of elasticity, defined as:

$$k = \Delta p / (\Delta v/v)$$

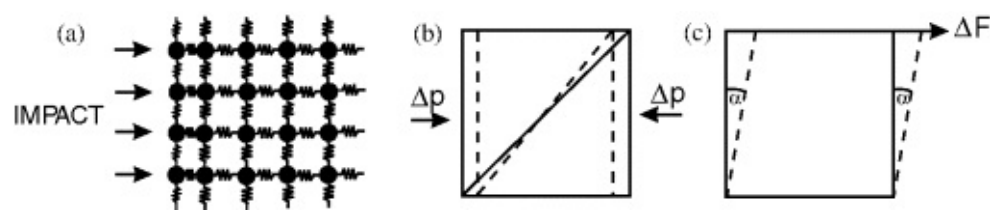
where Δp is the change in pressure that causes a fractional change in volume $\Delta v/v$ in rock of volume v ([Figure 4.1b](#)). Strong materials require a large Δp to induce a small $\Delta v/v$ so have a high k value. More detailed physical analysis shows that the exact relation for wave velocity in fluids is:

$$V_p = \sqrt{(k/\rho)}$$

(Sheriff & Geldart, 1995).

[Figure 4.1](#)

- a. A simplified model of elastic material consisting of particles joined by springs.
- b. A change in pressure (stress) causes a fractional change in volume (strain).
- c. A change in tangential force across the surface of a cube causes shear deformation of the cube with rotation of the side through a small angle.



The displacements and changes in pressure involved are exceedingly small. For example, a diver on the sea bed who happened to hear a reflected P-wave rising from the subsurface would have experienced a pressure change of only about 20×10^{-3} Pa or 3×10^{-6} p.s.i.

Solids are different from fluids in possessing shear strength – that is, they resist deformation induced by a force tangential to a surface within the material ([Figure 4.1c](#)). Liquids have zero shear strength. Shear deformation is characterized by rotation of the diagonal dimension of a rock volume and is present when a P-wave passes through a solid, even though the rock is only compressed or extended along one axis ([Figure 4.1b](#)). The shear strength of the rock is given the symbol μ (Greek mu) and expressed as the ratio $(\Delta FA/\tan \alpha)$, where A is the area of the surface over which the force acts ([Figure 4.1c](#)). If a big force per unit area gives rise to only a small rotation, the rock has high shear strength.

The resistance to shearing acts as an extra restoring force that tends to spring the material back to shape as the P-wave passes, so speeding it up. Hence, in solids, the shear modulus μ also enters into the equation for P-wave velocity:

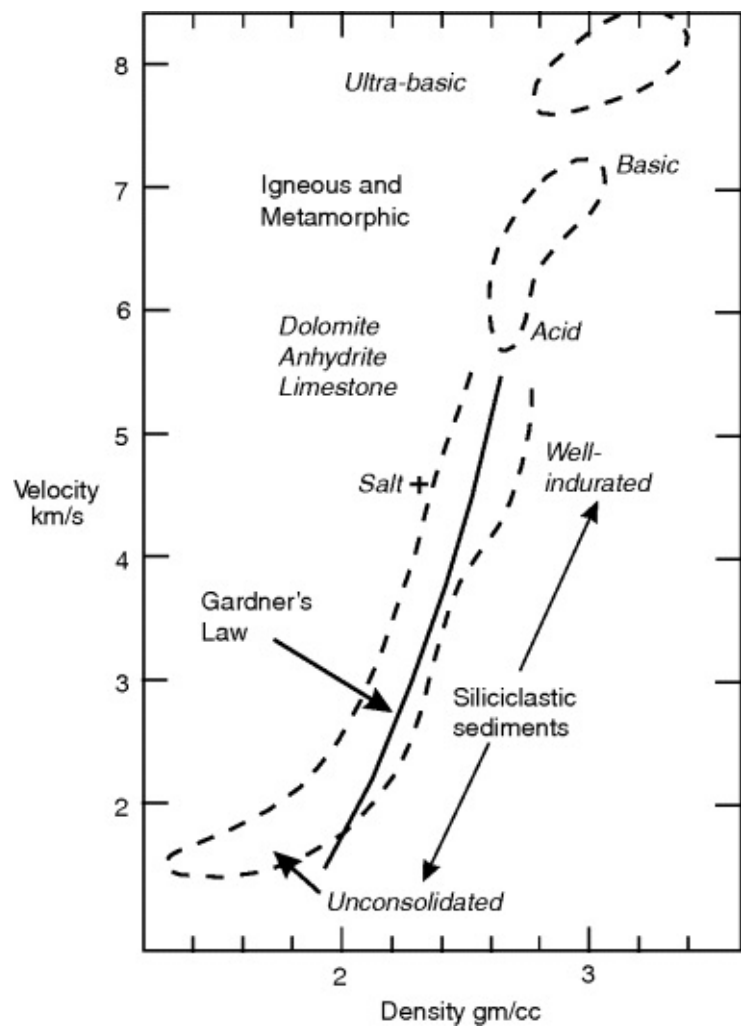
$$(4.1) \quad v_p = \sqrt{[(k + 4\mu/3)/\rho]}$$

(Sheriff & Geldart, 1995).

4.3 Controls on P-Wave Velocity

It is clear that any factor that tends to weaken a rock, making it more compressible or more susceptible to shearing, will reduce the velocity of propagation of the P-wave. It is no surprise, then, that the rocks that allow the highest P-wave velocity (6,000 to 8,000 m/s) are the strongest rocks – crystalline rocks such as granite or gneiss, in which the mineral grains form an interlocking mosaic of crystals bound together by strong intermolecular forces. Crystalline evaporites and carbonates also reach velocities as high as 6,000 m/s for the same reason. Sandstones and shales range from near water velocity when unconsolidated (1,500 m/s) to about 5,000 m/s, depending on their level of compaction and cementation, which can generally be related to age and depth of burial ([Figure 4.2](#)).

[Figure 4.2](#) An empirical plot of velocity versus density for all rock types compiled from Nafe & Drake (1963) and Birch (1961).



Note that velocity is inversely proportional to density in equation 4.1 – but this is for ideal materials. In real rocks, strength, measured by elastic moduli, varies over a much wider range than density, so it is strength that controls velocity. In general, the stronger rocks also happen to be the denser ones, so in practice density is found to rise with velocity (Figure 4.2). Empirical relationships have been established between velocity and density, of which the best known is Gardner's Law (Gardner *et al.*, 1974a) expressed as:

$$(4.2) \rho = kV^{1/4}$$

where $k = 0.31$ (ρ in gm/cm^3 and V in m/s) or $k = 0.23$ (ρ in gm/cm^3 and V in ft/s).

Porosity is found to be the single most important physical property to be correlated with sedimentary rock velocities. For clastic sediments, the empirical time-average equation or Wyllie equation (Wyllie *et al.*, 1958) works well: time in rock = time in grains + time in pores

$$\text{or } 1/V = (1 - \phi)/V_m + \phi/V_f$$

where

V_m = velocity of the rock matrix

V_f = velocity of the pore fluid

ϕ = fractional porosity

V = velocity of the rock

The relation is purely empirical and has no foundation in wave theory. The composition of grains clearly affects velocity, but it is not a major variable in siliciclastic sediments.

Grain bonding is important in determining a rock's strength and velocity. It is a function of compaction and cementation, which generally increase with depth of burial and age in clastic

sediments. Faust (1952, 1953) looked at velocities measured in wells and was able to show that the remarkably simple empirical relationship, $V = K(ZT)^{1/6}$ applied for clastic sediments. If Z is depth in feet and T is age in years, then V is in ft/s when $K = 125.3$. It is, of course, a great generalization and really applies well only to formations that have remained at their maximum depth of burial since deposition. If a formation has been uplifted, eroded and then buried under renewed sedimentation, it may well show velocities that are higher than the 'Faustian' norms for its final depth.

The presence of pore fluid pressure in a rock unit has an interesting effect on seismic velocity. The inter-grain pressure, or 'skeleton pressure' is the difference between the overburden pressure due to the weight of rock particles above and the pore fluid pressure, which is simply hydrostatic pressure for that depth if the pores are connected to the surface in the normal way. The fluid pressure effectively inflates the rock, decreasing the inter-grain forces which help to bind the rock together and so decreasing the elastic moduli and seismic velocity, compared to an 'empty' rock at similar confining pressure.

If the rock unit becomes sealed off from the rest of the sediment and continues to be compacted by an accumulating overburden, internal fluid pressure may rise well above normal hydrostatic level and the rock becomes over-pressured. The inter-grain pressure is thus decreased, the rock becomes weaker and both P-wave and S-wave velocities will be lower. If the fluid is gas and the formation is drilled in the shallow part of the section with only a short mud column in the well and so poor control of down-hole pressure, the well may blow out. High-resolution seismic surveys are now routinely carried out over platform sites to check for such shallow gas pockets, which are recognized primarily by sudden lateral variations in amplitude.

4.4 P-wave Waveforms

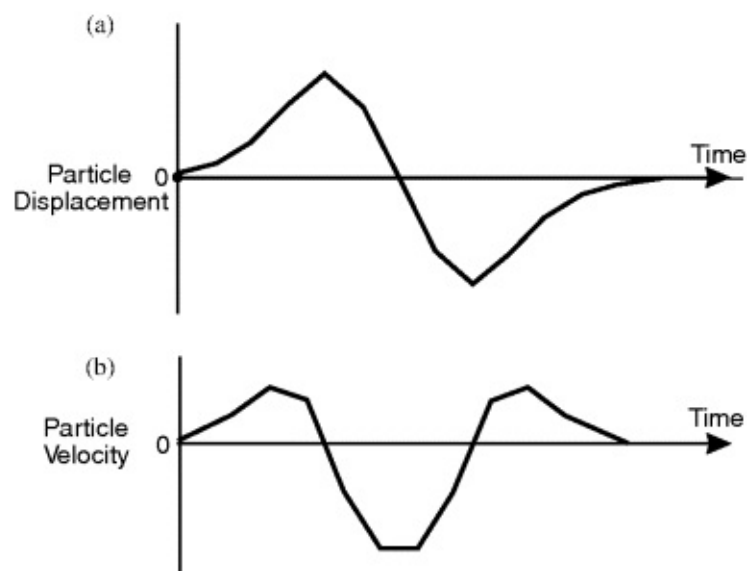
The simplest type of P-wave causes a particle to oscillate once to and fro about its rest position as the wave passes. It can be shown, by plotting successive positions of particle displacement, that the material develops a zone of compression, followed by a zone of extension, followed in turn by a second zone of compression. The manner in which these zones travel through the material as time passes can be shown on the computer screen using the program *PSWAVE* in Tutorial 4.1.

Start up program *PSWAVE* and have a look at the travelling waves in Tutorial 4.1.

If the material is rock and a geophone is being used to measure the passage of the P-wave, then the signal will be one of particle velocity, i.e. the rate of change with time of particle displacement ([Figure 4.3b](#)). The wavelet is a simple peak-trough-peak sequence, and such simple seismic wavelets have been recorded experimentally in the field, although not necessarily with the zero-phase property of [Figure 4.3b](#) (O'Brien, 1969; Ricker, 1953). It is clear from Tutorial 4.1 and [Figure 4.3b](#) that, if the medium is water, a hydrophone measuring pressure change as time goes by will generate a signal similar in shape to the velocity signal from a geophone.

[Figure 4.3](#)

- a. The time sequence of particle displacement associated with the travelling P-wave of Tutorial 4.1.
- b. The time sequence of particle velocity (rate of change of displacement).



4.5 Shear Waves and Surface Waves

In addition to P-waves, the shear deformation in solids leads to the generation of pure shear waves (S-waves). The particle motion is transverse to the direction of propagation (check Tutorial 4.1). The full analysis is more complex than for P-waves (see Sheriff & Geldart (1995) for a comprehensive account), but it leads to a simple equation for the velocity of propagation in an ideal isotropic solid:

$$(4.3) \quad V_s = [\mu/\rho]^{1/2}$$

The velocity of the S-wave is about half that of the P-wave in the same rock.

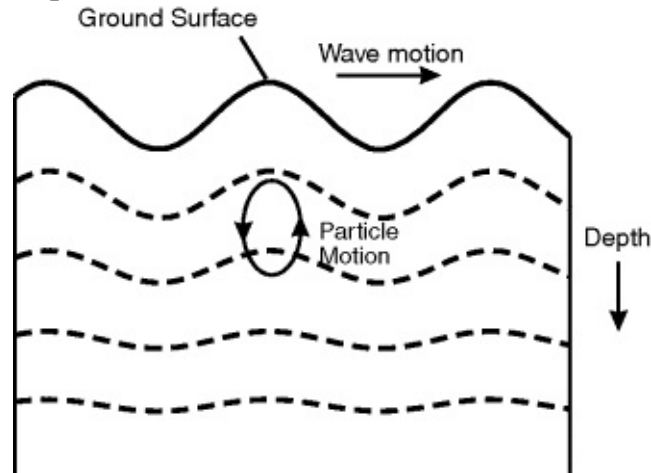
Polarization is common in S-waves – that is, particle motion may be constrained into one plane, which includes the line of propagation (SV for a wave polarized in the vertical plane, SH for the horizontal). Their velocity is only about half that of V_p and they are attenuated more rapidly in sediments than P-waves. They cannot be transmitted through water, which has zero shear strength, and, since particle motion is at right angles to the direction of propagation, they require different receivers from P-waves on land. In addition, they are more difficult and more expensive to generate on land and the time corrections for the weathered layer are greater and more difficult to measure than for P-waves. For these reasons, direct generation and recording of S-waves has not gone beyond the experimental stage in the petroleum industry. However some P-wave energy is converted to S-waves as it passes through the earth and forms the basis of survey techniques to be discussed in Part II of this book.

Surface waves, as their name implies, are found near the interfaces between different layered materials and they are a considerable nuisance in exploration seismology on land because they reach their greatest amplitude at the ground surface. Surface waves are the cause of ground tremors felt through the feet when heavy trucks pass close by, and they cause the structural damage from earthquakes.

Rayleigh waves are generally the most prominent and constitute most of the ground roll on seismic records. Particle motion is around an ellipse in the vertical plane ([Figure 4.4](#)), so it has a major vertical component just like the particle motion of a P-wave travelling vertically upwards from a reflection. Luckily, the velocity of Rayleigh waves is low, with a value of $0.92V_s$ in an ideal solid, so they are slow, low-frequency (c.10 Hz) waves moving horizontally across the

ground surface and are thus readily separated from the upwards travelling reflections by field and processing techniques.

Figure 4.4 Rayleigh wave motion: the amplitude is a maximum at the surface and dies away at depth.



4.6 P-wave Attenuation

As the P-wave spreads away from the source, two principal factors cause a fall-off in amplitude with distance, even in a homogeneous medium:

1. The energy is spread more thinly over the spherically-spreading wavefront. All frequencies are equally affected.
2. The energy of particle motion is dissipated into the rock as heat by inelastic processes such as internal friction and fluid flow in pore spaces temporarily deformed by the passage of the P-wave. This effect is frequency dependent, which leads to a loss of high frequencies, and it is a major limitation of the seismic technique.

4.6.1 Spherical Spreading

As the seismic wavefront spreads away from the source, it takes the approximate form of a sphere. 'Spherical spreading' is a term used to describe the enlarging of the wavefront and the corresponding drop in the amount of energy per unit area (the intensity) of the wavefront. Since area increases by the square of the distance travelled, intensity falls off inversely as the square of distance, while amplitude (proportional to the square root of intensity) falls off inversely as the distance.

An early step in processing is to correct the amplitude of the recorded reflections for spherical spreading by boosting amplitude in inverse proportion to distance travelled, i.e. by a factor of $1/VT$, where V is the velocity of propagation and T the two-way reflection time. In practice, the increase in velocity with depth in the earth means that the wavefront is no longer spherical, so it is better to scale amplitudes by $1/V^2T$ (Newman, 1973).

4.6.2 Frequency-dependent Attenuation

As a continuous sinusoidal wave passes through a rock, any small volume of the rock is taken through successive cycles of squeezing and stretching. During each cycle, a certain fixed fraction

of the energy in the waveform is lost as heat by internal friction. An everyday example of the same effect is the heating of a metal bar by repeated flexure. It seems intuitively likely that the same fraction of energy will be lost per cycle of deformation, no matter what the frequency of the Fourier component, and this is borne out by experiment.

The outstanding effect of frequency-dependent attenuation is the loss of bandwidth in the seismic signal. Since the high-frequency components of the waveform take the rock through more cycles of oscillation per km than the low-frequency components do, the high frequencies lose more energy than the low frequencies over the same travel path. It is this unfortunate fact of physics that determines the ultimate bandwidth of seismic data. Shallow reflections will have wide bandwidth – up to about 200 Hz in the first 0.5 seconds of TWT. At times greater than 3 seconds, bandwidth will have dropped to about 60 Hz. At the low-frequency end, bandwidth is limited by the nature of the recording devices, geophone or hydrophone, which do not record frequencies below about 5 Hz.

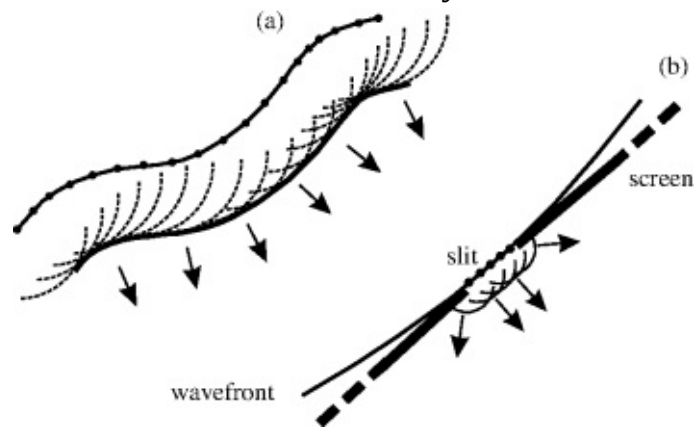
4.7 P-wave Transmission Paths

Just as in optics, we describe the passage of seismic energy through the ground by using the concepts of raypaths and wavefronts.

The wavefront is a snapshot of the position of the elastic deformation at a particular instant of time after the shot, showing it frozen in time after having travelled some distance from the source. In the 17th century, Christiaan Huygens postulated that innumerable secondary sources on a wavefront of light throw out energy, and that the new position of the wavefront is defined by the envelope of the secondary wavefronts so produced ([Figure 4.5a](#)). In this way he was able to explain the puzzling phenomenon of diffraction of light at a narrow slit, whereby light is observed not only to pass straight through, but also to be thrown off to the side ([Figure 4.5b](#)). Although Huygens was working with light waves, the same description applies to any wave-like transfer of energy, including seismic waves.

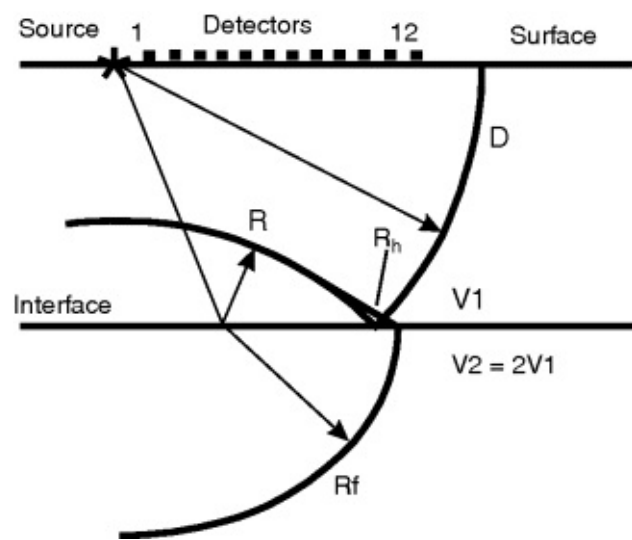
Figure 4.5 Huygens's Principle.

- a. Secondary sources on a wavefront throw energy forwards to form a new wavefront.
- b. Diffraction: secondary sources at the edge of a narrow slit throw energy off to the side.



The raypath is a trace of the path taken through the subsurface by the energy on a small piece of the wavefront, and it is always at right angles to its associated wavefront ([Figure 4.6](#)). Since they trace out the travel path from source to receiver, raypaths are especially useful as a basis for calculating travel times and associated depths in the subsurface.

Figure 4.6 The passage of seismic P-wavefronts from a shot above a single subsurface interface. Thick lines are wavefronts, arrowed lines are raypaths. D = Direct wave, R = reflected wave, R_f = refracted wave and R_h = head wave.



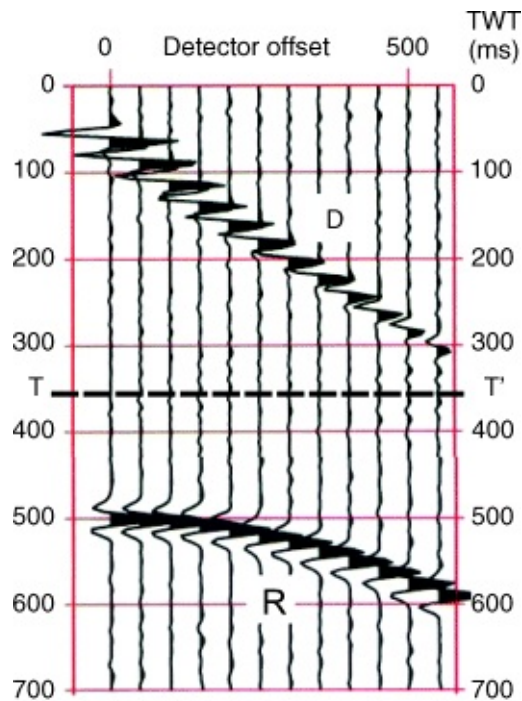
4.7.1 Wavefronts and Raypaths for a Single Interface

In [Figure 4.6](#), a single horizontal interface is shown between two rock layers of velocity V_1 and V_2 , where $V_2 > V_1$. Wavefronts are shown at an instant of time shortly after detonation of the shot at the surface. The Direct Wave (D) travels in the upper layer of rock at velocity V_1 and is the first disturbance recorded by receivers near the shot, having travelled directly from shot to receivers without reflection or refraction. In [Figure 4.6](#), it has just passed across the interface between the two rock types, and a Reflected Wave (R) is rising off the interface towards the surface. Energy has also passed through the interface into the lower layer, where it has travelled onwards some way at velocity V_2 and forms a Refracted Wave (R_f). Both the reflected and refracted wavefronts are generated by energy emitted from secondary sources on the interface, stimulated by the passage of the Direct Wave along the interface, as will be demonstrated in Tutorial 4.3.

[Figure 4.7](#) shows the seismograms that would be recorded from the spread of 12 geophones in [Figure 4.6](#). The horizontal dimension is distance from shot to geophone and the vertical dimension is time. The direct wave sweeps across the geophone spread at a steady rate determined by the velocity of the upper layer (V_1), travel time (T_x) and distance (X), being related simply by the equation:

$$(4.4) T_x = X/V_1$$

Figure 4.7 Idealized seismic recording of Direct (D) and reflected (R) waves from the detector spread of [Figure 4.6](#). T – T' = time at which wavefront positions shown in [Figure 4.6](#) are 'frozen'.



The reflected wave sweeps across the near-shot geophones very quickly, but then slows as the distance increases. It forms a characteristic hyperbola described by the equation:

$$(4.5) \quad (T_x)^2 = (T_0)^2 + (X/V_1)^2$$

where T_0 is the time at $X = 0$, the normal-incidence reflection time.

Get the feel of measurements of time, velocity and depth via Tutorial 4.2 before you go on.

As the refracted wave travels at speed through the lower medium, its upper boundary sweeps along the interface and soon moves well ahead of the direct and reflected wavefronts. As it travels, it stimulates secondary sources along the interface, which radiate upwards into the upper medium and generate yet another wavefront, the Head Wave, a plane wave which rises obliquely towards the surface (R_h in [Figure 4.6](#)). This forms the basis of the refraction method of seismic surveying which we will not consider further in this present volume.

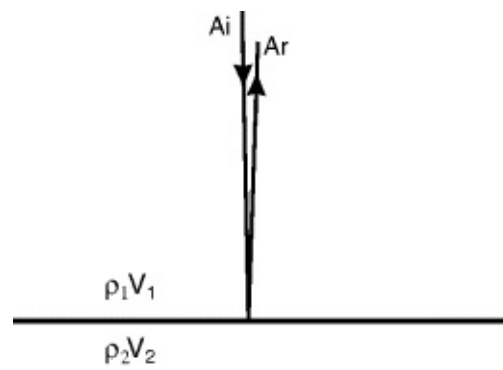
Now is the time to get the drawing compasses out and go through Tutorial 4.3. This takes the reader through a simple construction of the R and D wavefronts in [Figure 4.6](#) by using Huygens's principle.

4.7.2 Reflection Coefficient and Wavelet Polarity

Referring to [Figure 4.8](#), the amplitude of a normal-incidence reflection is determined by the contrast in Acoustic Impedance (product of density and velocity or ρV) across the interface. The reflection coefficient of the interface (R) is a measure of what fraction of the incident amplitude is reflected. It is given by the ratio of reflected to incident wavelet amplitude:

$$(4.6) \quad R = A_r/A_i = (\rho_2 V_2 - \rho_1 V_1)/(\rho_2 V_2 + \rho_1 V_1)$$

Figure 4.8 Normal-incidence reflection at the interface between two different rock types. ρV (density \times velocity) is the acoustic impedance of a rock.



The reflection coefficient is mostly determined by the contrast in velocities across the interface, because velocity varies over a range of about 2.5 : 1, whereas density varies only over a range of about 1.3 : 1. An excellent reflector, such as shale over limestone, can have a value of R of up to about 0.3. For an average shale over sandstone interface, R may be about 0.1 (see Tutorial 4.4). If the velocity drops across the interface, R is negative and the reflected wavelet has opposite polarity to the incident wavelet. Remembering the pressure waveform in Tutorial 4.1, if the wavelet travels down as the pressure sequence compression-rarefaction-compression, it is reflected back up as rarefaction-compression-rarefaction.

Get a feel for the size of reflection coefficients by using the well data in Tutorial 4.4.

In marine seismic surveys, a particularly important reversal of polarity occurs when the sea bed reflection travels up to the sea surface and is reflected back down again. At the surface, it meets an interface across which the velocity changes from high (in water) to low (in air), so what travels up as a positive wavelet goes back down as a negative one. It is reflected back up again a second time from the sea bed as a negative wavelet, and back down again as a positive one, a process repeated a number of times, with amplitude dropping each time until the reflection becomes undetectable. We shall study such multiple reflections in Chapter 5.

If the geophone is offset from the source, so that the incident raypath is oblique to the interface, some of the incident energy is converted to shear wave motion and both P- and S-waves are transmitted through and reflected from the interface, a process known as mode conversion of seismic energy. As a result, P-wave amplitude may vary considerably with source-detector offset, a phenomenon known as amplitude variation with offset or AVO, which we will pursue in much more detail in Part II of this book.

4.7.3 Ray-tracing in Seismic Modelling

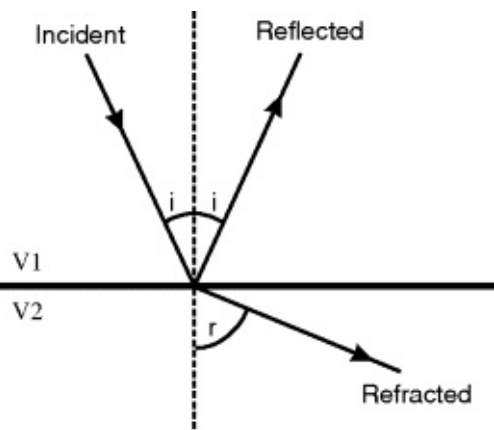
Raypaths are widely used to illustrate the geometry of seismic travel paths and to derive equations relating travel time to distance, such as [Equation \(4.5\)](#) above. The geometry of raypaths at a velocity interface is determined by Snell's Law of Reflection, which states that the angles of incidence and reflection of the raypaths on a reflector are equal – a principle familiar to every snooker player ([Figure 4.9](#))! If the angle of incidence is 0° , we are dealing with a normal-incidence reflection, as in [Figures 1.1](#) and [4.8](#). Equally important is Snell's Law of Refraction:

$$(4.7) \sin i / \sin r = V_1 / V_2$$

where i = angle of incidence on the interface and r = angle of refraction ([Figure 4.9](#)).

[Figure 4.9](#) At a velocity interface, Snell's law of Reflection states that incident and reflected

angles are identical. Snell's law of Refraction is that $\sin i / \sin r = V_1 / V_2$. For the case shown, $V_1 < V_2$.



Ray tracing is very often used in seismic modelling when a subsurface structure is set up and its geophysical expression is calculated. In reflection seismology, we might draw up a geological cross-section comprising several rock layers, assign velocities and densities to the layers and calculate the seismic trace that would be recorded at the surface from a normal-incidence reflection. By tracing out the passage of the seismic energy through the subsurface in the form of rays, we can measure the travel times from the length of the rays and the velocities assigned to the layers of the model. Reflection wavelets can then be plotted at the correct times on an artificial seismic section. You will see several examples of this type of forward modelling in later chapters.

Tutorials for Chapter 4

Tutorial 4.1

Purpose: To see the particle motion of P-waves and S-waves on screen

1. Run the program *PSWAVE*.
2. Click on Configure and set the path to your data folder. Accept other default settings.
3. Click on File and open the file *displace.sig* of particle displacements.
4. Click on *PWAVE*. Watch the red particles as they oscillate about the fixed starting position marked by the red line, demonstrating that there is no net translation of material, only of energy. Note the creation of travelling zones of compression and dilation in the wavefront. Select a faster speed to see the travelling wave best.
5. Click on *SWAVE*. The particles now oscillate in the vertical direction about their starting position. Displacements are now at right angles to the direction of travel and give rise to horizontally travelling zones of shear deformation.

Tutorial 4.2

Purpose: To make some basic seismic measurements of time, velocity and depth. Look at [Figure 4.7](#) on page 28.

1. Measure the velocity at which the direct wave passes across the line of receivers (time scale is one-way time for this).
2. Measure the T_0 value for the reflection, i.e. the reflection time at the geophone with zero offset from the shot which has recorded a normal-incidence reflection. Hence, calculate the depth to the reflector using the velocity measured in the overlying layer from 1 above.

Tip: Remember, reflection is a two-way travel path – down and up.

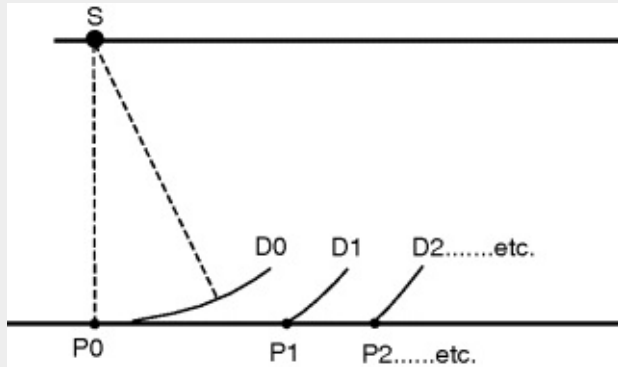
Tutorial 4.3

Purpose: to see how the reflection wavefront can be drawn by using Huygens's Principle. You will require a sheet of graph paper. Use the graph paper with the long axis as 'E-W'.

1. Draw a line along the length of the paper a few centimetres down from the top: this is ground surface. Draw another line parallel to the first, 5 cm below it, to represent a horizontal interface between two rock units. Towards the left, mark the source, S, on the surface.

2. **Direct wavefront:** with drawing compasses, draw an arc centred on S of radius 5 cm that just touches the interface; this represents a down-going direct wavefront D0. Draw small segments of arc, as shown in [Figure T4.3.1](#), to mark successive positions of the direct wavefront D1... D6 as it progresses at a steady rate through the medium. If the velocity is 1 cm per time unit, then each arc is greater in radius by 1 cm. For D6, show the whole D wavefront, i.e. make the D6 arc extend from the interface to the surface. The seven successive points at which the direct wave touches the interface will be referred to as P0 to P6, as in [Figure T4.3.1](#). Mark in extra points on the interface at $P0 + \frac{1}{4}$ and $P0 + \frac{1}{2}$.

[Figure T4.3.1](#)



3. **Reflected wavefront:** the objective is to construct the reflected wavefront at time D6. As the direct wave sweeps along the interface, it stimulates secondary sources along it at points such as P0 to P6, which emit circular secondary wavefronts that rise up and coalesce to form the reflected wave. Consider point P6: the direct wave has just arrived at that point on the interface, so no secondary wavefront has yet begun to develop. But at P5, energy started out one time unit before the D wave reached P6, so that energy has been rising up from P5 for one time unit. Draw a short segment of the circular wavefront centred on point P5 as it would be at time D6. Do the same for points P4, P3.... etc. Don't forget points $P0 + \frac{1}{4}$ and $P0 + \frac{1}{2}$ as well.

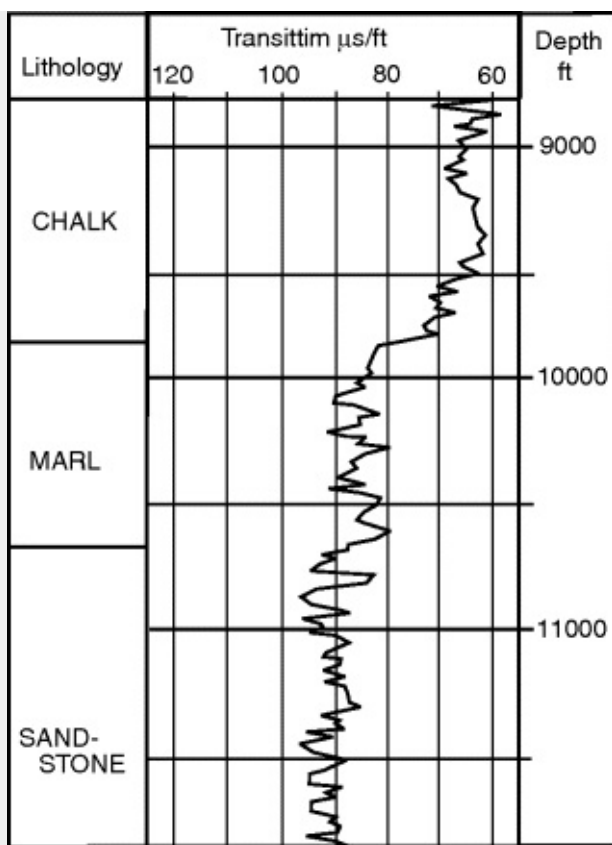
4. Draw in the envelope of the arcs to represent the final reflected wavefront at time D6. A good way to see the final picture is to colour both the direct and reflected wavefronts. Finally, if the reflector is regarded as a seismic mirror, there is a mirror image of the source at a distance below the reflector equal to the distance of the source above it. The reflected wavefront appears to come directly from this image source. Locate the position of the image source on the drawing and confirm with your compasses that the reflected wavefront is, indeed, an arc centred on the image source.

Tutorial 4.4

Purpose: to answer the question 'How big are typical reflection coefficients?'

[Figure T4.4.1](#) is a record of a sonic log measured in a well in the North Sea in a section through the base of the chalk, passing down into a marl and then a sandstone. The sonic log measures the P-wave velocity in the rock of the well-bore in great detail, and we will make use of the detail in constructing synthetic seismograms in later chapters. However, for this tutorial you can use the sonic log simply to give the average transit time of each geological unit by drawing a vertical line through the average position of the log at each of the three units.

[Figure T4.4.1](#)



For example, through the sandstone unit, the average reading of the log is about 91 microseconds per foot, so the rock velocity is $1/91$ ft per microsecond or $1/91 \times 1,000,000$ ft/sec. This gives a figure of 10,989 ft/sec = 3,349 m/s. Then carry on as follows:

1. Draw a mean line through the log for the marl and chalk intervals, read off the average transit time for the intervals and calculate velocities for those two intervals. Convert velocities to m/s so that you become familiar with both scales.
2. Use the velocities to calculate densities using Gardner's Law. For example, the sandstone unit will give a density of 2.36 gm/cm^3 .
3. Calculate acoustic impedance for all three units.
4. Calculate the reflection coefficients for the chalk/marl and marl/sandstone interfaces. Don't be surprised to find they are negative!

The chalk/marl reflection coefficient is big and the reflection would be a prominent event on any seismic section. The marl/sandstone coefficient is typical of modest reflections in a clastic sedimentary section. Note that the polarity of both reflections is negative.

Chapter 5

The Process of Reflection

5.1 Introduction

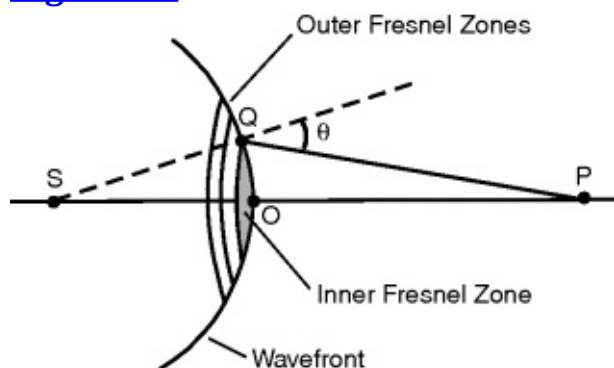
The use of raypath diagrams such as [Figures 4.8](#) and [4.9](#), while convenient, may convey the false impression that a reflection is generated by a small point on the reflector. However, we saw in Tutorial how the downgoing direct wave stimulated Huygens's secondary sources across a wide zone of the reflector to give rise to the reflected wavefront. In this chapter, we will explore that description of the reflection process and see how it affects what the interpreter sees on the seismic section. Huygens had not made a quantitative explanation of how secondary sources worked; it was to be some 140 years later, in 1818 that Fresnel worked out the process in detail. Although his concern at the time was to explain optical phenomena, the principles apply to any kind of wave transfer of energy.

5.2 Fresnel Zones

Referring to [Figure 5.1](#), Fresnel calculated the intensity of light at a point P some way from a source S of monochromatic light, supposing that the light had advanced as far as the wavefront shown. Energy from the secondary sources close to O on the advancing wavefront would all arrive at P in phase, because the path length is essentially the same. The area for which this is true forms a circular zone on the wavefront centred on O, called the inner Fresnel zone (IFZ). Further out along the wavefront, at points like Q, the path length will be longer, eventually becoming longer by half a wavelength ($\lambda/2$) so that the energy cancels out that which comes from the IFZ. The condition for cancellation is:

$$SQP = SOP + \lambda/2$$

Figure 5.1 Definition of the inner Fresnel zone.



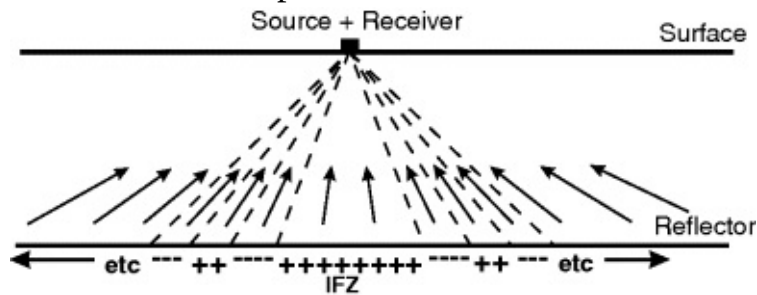
Thus, the area of reinforcement of energy in the IFZ is surrounded by a circular ring-shaped zone of cancellation. Further out again, there will be a circular zone where the path length is longer by a full wavelength, giving reinforcement once again of the energy from the IFZ. It is clear that a whole series of outer zones is present, which alternately cancel and reinforce energy from the IFZ.

Fresnel added up the contribution of all the zones to the light intensity at P and came up with the

5.4 Faults and Diffractions

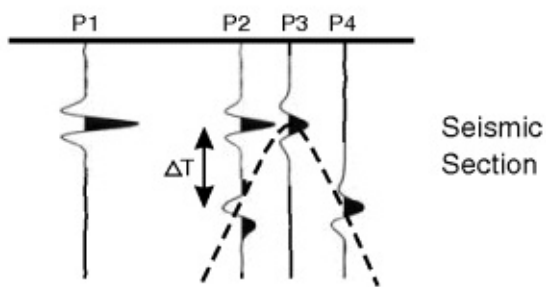
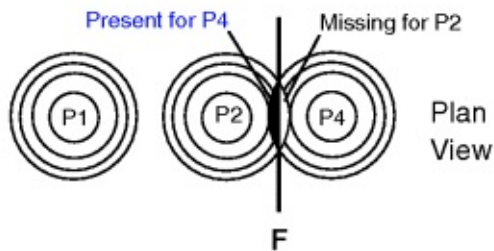
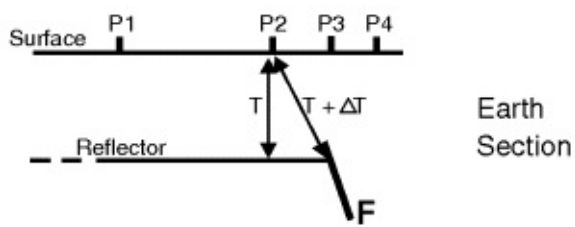
Alternate zones of cancellation and reinforcement may be visualized spread out across the reflector in the manner of [Figure 5.3](#). When the incident waveform is a wavelet, the build-up of energy due to the coherent radiation from the inner zone gives rise to the normal-incidence reflection wavelet. Energy from the outer zones is either in phase or out of phase, depending on the length of travel path. It all self-cancels at the receiver, so we see a dead trace after the initial wavelet. However, if the symmetry of the Fresnel zone system is upset (for example, if part of it is switched off by downthrow at a fault), then cancellation will not be complete and a second wavelet will appear on the recorded seismogram at a time later than the normal-incidence wavelet.

[Figure 5.3](#) Fresnel zones of reinforcement (+) and cancellation (-) developed on a reflector as the direct wave sweeps across it. IFZ = inner Fresnel zone. Zone widths are only schematic.



The most striking example of this arises at faults. In [Figure 5.4](#), at location P1, the full set of Fresnel zones is developed on the reflector and a single wavelet is recorded on the seismic section. At location P2, the zones adjacent to the IFZ are still unbroken, so, after the normal-incidence reflection, the seismogram will be as dead as usual, but only until time ΔT has passed, when part of the outer Fresnel zones will start to fall beyond the faulted edge of the reflector. Now the outermost zones can no longer self-cancel and a fault diffraction wavelet will appear on the trace as a result. This diffraction wavelet will lag behind the normal-incidence reflection wavelet by a time proportional to the extra length of the oblique 2-way travel path to the fault line (ΔT in [Figure 5.4](#)).

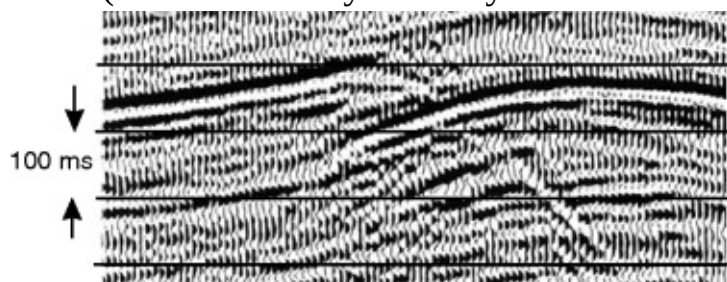
[Figure 5.4](#) Generation of a diffraction hyperbola at a fault (F). The concentric rings in plan view are a schematic representation of Fresnel zones on the surface of the reflector. Amplitudes are only approximate.



As the faulted edge of the reflector is progressively approached (P2 to P3 in [Figure 5.4](#)), the travel time of the diffracted wavelet will become less and less as the obliquity of the path decreases, until it merges with the normal incidence reflection when the shot is directly over the fault. The fault plane now divides the Fresnel zone system into two, so that the reflection wavelet is half its previous amplitude. As the shot-receiver pair continues to move over the ‘void’ (P3 to P4 in [Figure 5.4](#)), there is no inner zone reflection at all, but there is still some diffracted energy reaching the receiver, returned from parts of the outer Fresnel zone system on the upthrown side of the fault along increasingly oblique paths. The time of onset of this diffracted wavelet is again proportional to the raypath length to the faulted edge.

When the two-way times measured along the oblique travel paths to the faulted edge are plotted vertically below the surface points of observation (as they are in a CMP-stacked time section), they fall on a characteristic hyperbola (broken line in [Figure 5.4](#)). Such hyperbolae are commonly observed at faults on stacked, but unmigrated, time sections (e.g. [Figure 5.5](#)).

Figure 5.5 An unmigrated stacked time section showing a diffraction hyperbola generated at a fault. (Seismic data by courtesy of Western Geco).



The diffraction hyperbola is symmetrical across the central line of symmetry at the position of the fault, except in one respect: there is a change of polarity (or 180° phase shift) in the waveform from one side of the hyperbola to the other. The reason is that on one side (P2 in [Figure 5.4](#)), the

diffraction waveform is caused by *missing out* a portion of the Fresnel zone system from the total effect – whereas, on the other side (P4), the same portion of outer zone is the *only one present*. The two portions must be of opposite polarity in order to achieve the normal result of cancellation for a continuous reflector. This change of phase is difficult to see on most seismic sections, because the fault hyperbola is nearly always incomplete and interfered with by noise as in [Figure 5.5](#). In addition, fault drag tends to make the diffraction disappear under the upthrown side as in [Figure 5.5](#) (Hilterman, 1970).

5.5 Hyperbolae on Stacked Time Sections

We are now going to look at Fresnel diffraction and the creation of hyperbolae on stacked time sections from a slightly different, but very fruitful, point of view. Most people have looked down at a rocky coast and seen the phenomenon shown in [Figure 5.6](#), where a series of waves on the sea surface pass an isolated rock which acts approximately as a secondary point source, radiating diffracted energy in all directions about it.

[Figure 5.6](#) Water waves coming from top right strike a small reef which acts as a ‘point’ source of secondary radiation. The dark mass of rock in the foreground is about 10 m in width.



In the subsurface, we may imagine a small patch reef, much smaller than the inner Fresnel zone, acting in a similar way as the direct wave from the seismic source sweeps past it. It will act like an example of Huygens's secondary source, giving raypaths that diverge towards the surface and generate a hyperbolic event on the stacked time-section, as demonstrated in Tutorial 5.1.

Tutorial 5.1 is a simple demonstration of the expression of a small diffracting source on a seismic time section.

You can show that the TWT, T_x , for an oblique raypath to the scattering source is given by the equation:

$$(5.1) \quad (T_x)^2 = (T_0)^2 + 4X^2/V^2$$

where:

X = range from the symmetrical centre line of the hyperbola to the recording position

T_0 = minimum time on the hyperbola (TWT along the vertical path to the diffracting source at $X = 0$)

V = velocity down to the diffracting source.

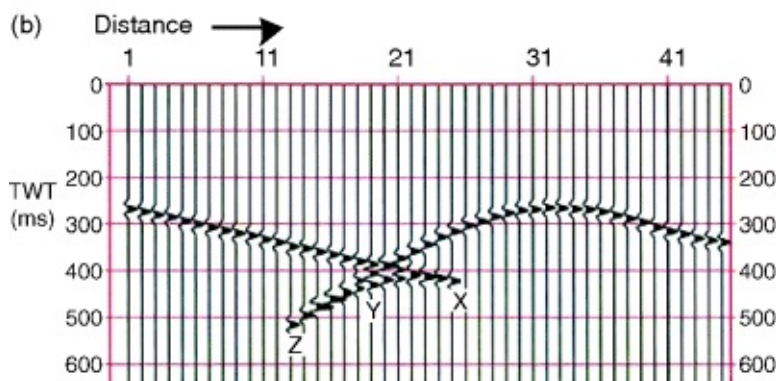
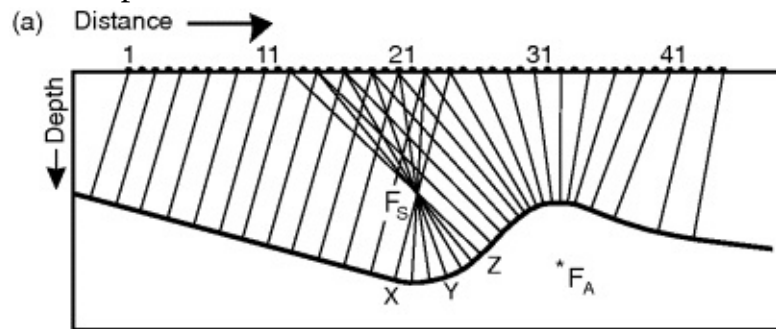
Tutorial 5.1 demonstrates that the point of minimum time on the hyperbola is located directly over the subsurface source (for uniform velocity or velocity a function of depth only). It is also evident from Tutorial 5.1 that sources which are shallow in the section will generate hyperbolae that are tight and sharply curved, while deep sources will generate much flatter hyperbolae. In marine surveys, it is not uncommon to see hyperbolae caused by seismic energy diffracted sideways through the water layer from wrecks or big rocks off to the side of the hydrophone streamer. Such a hyperbola can readily be recognized on account of its strong curvature caused by the low velocity of the water (1,500 m/s).

Apart from reflector discontinuities, there is another common source of hyperbolic seismic events on stacked sections. This is a buried focus – a point in the subsurface from which rays diverge towards the surface with the same geometry as in Tutorial 5.1. Both anticlines and synclines may generate such events ([Figure 5.7](#)). Remember that we plot the seismogram in the time-section vertically below its recording position on the surface. Thus, the seismograms from points X, Y, Z in [Figure 5.7](#) plot in the order Z, Y, X in the time section and form a characteristic cross-over ‘bow-tie’ event – a name which goes back to their appearance on black and white displays. Unlike fault diffraction hyperbolae, these events are limited in their extent across the time section and there will be no change in phase of the waveform from one limb to the other.

[Figure 5.7](#)

a. A model section of a reflector with normal-incidence ray-paths drawn. FA, FS are buried focal points of rays.

b. The CMP-stacked section observed over **a**, shown with twice the number of seismograms. Amplitudes are not exact.



The modern interpreter is very unlikely to see hyperbolae of any sort on the fully processed seismic section, because the key process called migration gets rid of them. However, they have a useful place in the interpretation of 2D data, as we shall see in Chapter 7, Section 7.6.

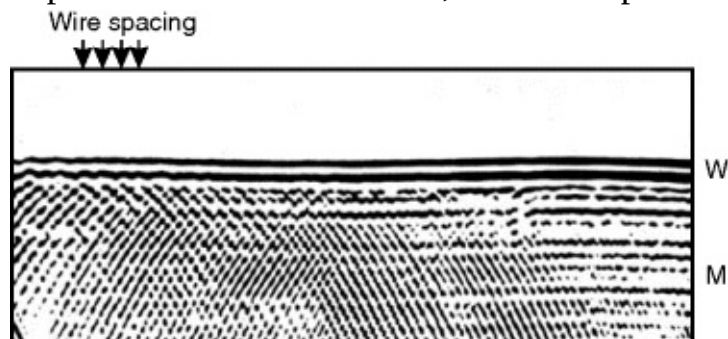
5.6 The Reflection as a Summation of Hyperbolae

Tutorial 5.1 developed the notion of diffraction of energy from a subsurface object (e.g. a small reef) which is much smaller than the inner Fresnel zone. This will give rise to a single diffraction hyperbola. Now imagine a reflector broken down into innumerable small diffracting areas, each smaller than the IFZ. Each one develops a hyperbola on the time section, and the continuous reflection that we actually see is the amalgam of the peaks of innumerable overlapping hyperbolae. The tails of the hyperbolae cancel each other out, so only a continuous reflection, generated by the amalgamated summits of the hyperbolae, is visible.

Gardner *et al.* (1974b) showed a fascinating illustration of this process from a modelling experiment using a physical model on the laboratory scale. They used a tank of water as the earth, with wires strung horizontally across the tank under the water to simulate diffracting sources. The wires were widely spaced at one side of the tank and were progressively more closely spaced across the tank until they formed an almost continuous sheet.

In order to scale the wavelengths to simulate real seismic conditions, Gardner *et al.* (1974b) used an ultrasonic source-receiver pair that moved across the water surface and emitted a wavelet at close intervals. Each recorded seismogram was then displayed on an oscilloscope screen, and eventually a composite section of all the traces was built up (Figure 5.8). They were able to show that, as the spacing between the sources decreased, the tails of the individual hyperbolae increasingly cancelled each other out, leaving only the single continuous reflection from the amalgam of the peaks and revealing multiple reflections below that were impossible to see where the wires were widely spaced (Figure 5.8). If a reflector surface is rough (in terms of wavelength) then, at each discontinuity, the hyperbolae tails will no longer cancel and they will reappear.

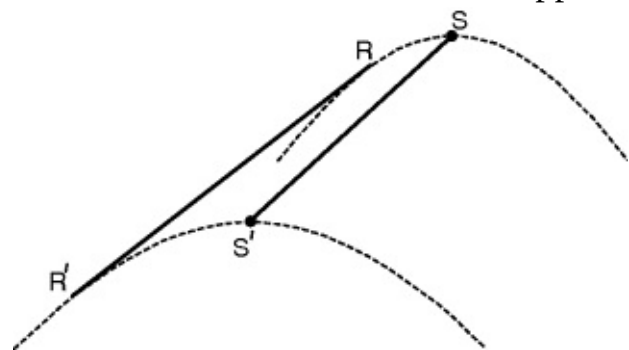
Figure 5.8 Diffraction hyperbolae from a sheet of wires recorded from a water tank ultrasonic experiment. W = wire sheet, M = multiple reflections. (After Gardner, French and Matzuk, 1974)



When the reflector is dipping, the hyperbolae are of unequal curvature, the shallowest being the most curved and narrow and the deepest being the broadest (as seen at the conclusion of Tutorial 5.1). The reflection seen on the time section is now the amalgam of the dipping flanks of the hyperbolae, with the rest of the hyperbolae overlapping and cancelling as before (Figure 5.9). The hyperbolic crests (if they could be seen) would still mark the true position of the diffracting sources, so it is clear that the reflector's position is misrepresented by the reflection on the stacked time section and it should be shifted some way off to the side in the up-dip direction. This sideways shift is traditionally given the rather grand name of 'migration' and is the final major step in the data processing sequence. Note that only dipping reflections need to be migrated.

Figure 5.9 The reflection R – R' from a dipping geological interface S – S' is formed from the envelope of the flanks of diffraction hyperbolae. Only reflection R – R' and the dotted hyperbolae

at the broken ends of S – S' will appear on the seismic section.



5.7 Resolution of the Seismic Reflection Method

To some extent, assessment of seismic resolution depends on how you define it. If we consider horizontal resolution, we might ask the question: how far apart do two small reefs have to be before we can see them as two distinct events on the seismic section? It is clear that rock units narrower than the first Fresnel zone will all appear as the same diffracting line or point sources, and their width cannot be measured. However, as the width of the target increases beyond that of the first Fresnel zone, the single diffraction hyperbola will split into two distinct events, each centred over an edge of the target. Thus, two small reefs lying inside the smallest inner Fresnel zone (determined by the highest frequencies present in the seismic signal) will not appear as separate entities. Splits or holes in the reflector smaller than the inner zone will be ‘healed over’ and invisible.

However, all this applies only to stacked, unmigrated seismic data. The process of migration not only relocates dipping reflections but causes a focusing of the image by reducing the effective Fresnel zone diameter to about half the dominant wavelength of the wavelet (Lindsey, 1989). For typical exploration conditions (wavelet mid-frequency = 30 Hz, velocity = 3000 m/s), the effective Fresnel zone diameter is 50 metres.

If we consider vertical resolution the question we should ask is: how thin a bed can we see in the sense of resolving its upper and lower surfaces separately? Referring to [Figure 5.10](#), the time interval between wavelets reflected by the top and bottom surfaces of a thin bed is

$$\sum_{k=1}^m n^k$$

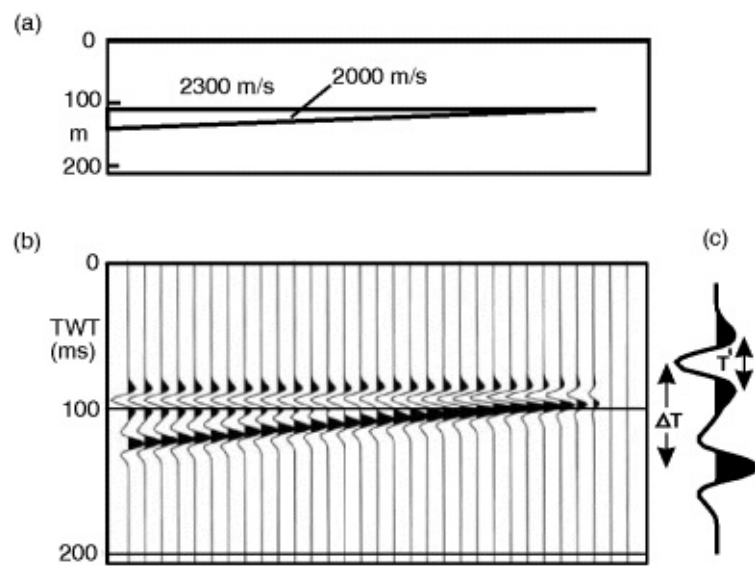
or

$$\Delta Z = \Delta T \cdot V / 2$$

where ΔZ = thickness and V = velocity of the bed.

[Figure 5.10](#)

- a. A geological section showing a thin sand encased in shale and pinching out.
- b. A model seismic section corresponding to a.
- c. Detail of the seismic trace from the thick end of the wedge in a. Data modelled in program *SYNTHSEC*.



If the wavelet has a simple zero-phase shape, the dominant period is defined by the separation T' shown on [Figure 5.10](#), so the dominant frequency is $f = 1/T'$. It is clear that, as the bed thins laterally, the reflections from top and bottom move together and constructively interfere to produce a high-amplitude event, before finally dying away as the bed pinches out completely. The high-amplitude event is often called a ‘tuned reflection’, in the sense that wavelet and bed thickness are matched to yield a large oscillation through constructive interference. Such tuning may cause local bright spots as beds wedge out below an erosional unconformity. Look back at [Figure 3.2a](#) (page 19) for a display of a reflection with an increase in amplitude caused by a stratum wedging out.

At tuning thickness the side-lobe of the upper wavelet reinforces the peak of the lower wavelet and maximum amplitude occurs, so:

$$\Delta T = T'/2$$

or

$$\Delta Z = \Delta T \cdot V/2 = T'V/4 = V/4f = \lambda/4.$$

For example, if $V = 3,000$ m/s, $T' = 20$ ms (a ‘50 Hz’ wavelet), then $\Delta Z = (0.020 \times 3000)/4 = 15$ m. A bed would therefore have to be greater than 15 m in thickness before two distinct reflections would be seen, one from the top and one from the base. However, it is clear from [Figure 5.10](#) that the presence of the bed would still be detectable (as a single event) well below tuning thickness (Widess, 1973). Once again, narrow wavelets of wide bandwidth at shallow depths are going to give the best resolution.

Studies of amplitude variation are often used to track changes in properties across a reservoir, and one of the many pitfalls that lie in wait for the interpreter is that false changes in amplitude may be caused by tuning in thin beds.

5.8 Multiple Reflections: Common Modes

Up to now, we have only considered primary reflections, in which the seismic energy travels directly from surface to reflector and back to surface. We would like the seismic section to contain only primary reflections, but one of the most serious problems in reflection seismology is the presence of multiple reflections generated by repeated reflection within the sedimentary sequence. These often remain the single biggest source of interference in the seismic section despite the best efforts of data processing to suppress them. This section and the next will

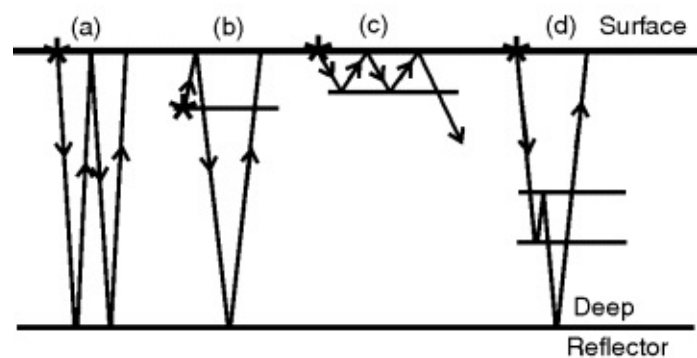
demonstrate how serious the problem is, but solutions will be discussed later.

Some common modes of multiple reflections are shown in [Figure 5.11](#).

Figure 5.11 Multiple reflections: some of the common modes.

- a. Surface multiple.
- b. Ghosting.
- c. Water reverberation.
- a. Peg-leg multiple.

★ Shot



Among the long-path multiples, the surface multiple is often the most troublesome because of the high reflection coefficients at the ground/air or water/air interfaces. It can be recognized by the following criteria:

1. It has twice the reflection time of some prominent shallow primary reflection which generates the multiple.
2. It has twice the dip of the associated primary.
3. It has reversed polarity compared to the associated primary, because the Earth's surface has a negative reflection coefficient as viewed from beneath (this may be tricky to see on the section).

An excellent example of surface multiples can be seen when interpreting the seismic data of Tutorial 7.3.

Short path multiples include peg-leg multiples, which are short-path reverberations within thin sedimentary units. They typically alter simple wavelets from deeper reflections to more complex forms. Two particularly troublesome forms of short path multiples are ghosting on land and water layer reverberation in shallow water. Ghosting commonly occurs with dynamite shots in boreholes, where energy reflected from the ground surface above the shot may follow the main wavelet down, giving rise to a noticeable low-amplitude reflection of reversed polarity which appears a short time ($2dw/V_w$) after every main event (dw is the depth of shot, V_w the weathered layer velocity).

The problem is much worse at sea, because the sea bed and water surface both have high reflection coefficients, so that the energy is partially trapped in the water layer and bangs up and down for several hundred milliseconds after the shot. As a result, in shallow water, each reflection is followed by a long reverberation and, in bad cases, the complete section may break down into a continuous sine wave and be virtually unusable. For a time, in the 1950s, it looked as if seismic work in shallow marine areas might be completely impossible because of water reverberation. Happily, data processing came to the rescue and the process of deconvolution now helps the wavelet to be simplified to the ideal zero-phase state.

5.9 Multiples: the Scale of the Problem

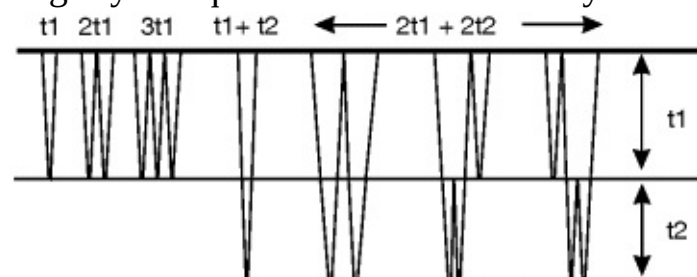
Even in a simple sequence of rock strata, the number of possible multiple paths rapidly reaches high numbers. It is useful to label reflections according to the number of two-way transit times spent in each layer, as defined in [Figure 5.12](#). If only one reflector is present, we get a primary at time t_1 and a series of intra-layer multiples at times $2t_1$, $3t_1$... etc. In theory, there can be an infinite number of these, but in practice they die away to insignificant amplitudes after only five or six unless there are exceptionally large reflection coefficients involved. If we limit the number of intra-layer bounces to a maximum of five and two reflectors are present, then two primaries and 28 multiples are generated. If three reflectors are present, there are three primaries and 152 multiples. In general, the total number of primaries plus multiples generated is:

$$\sum_{k=1}^m n^k$$

where n is the maximum number of intra-layer bounces and m the number of reflectors. For five intra-layer bounces and seven reflectors, a total of seven primaries and 97,648 multiples are generated!

Although many multiples are generated, most are irrelevant because their travel times fall far below the times of interest in an exploration survey and/or they are exceedingly low in amplitude. At the same time, the sheer multiplicity of raypaths means that certain multiples will be reinforced in amplitude by the simultaneous arrival of many low-amplitude wavelets. A simple example in [Figure 5.12](#) shows the three possible raypaths for seismic wavelets which pass through the first and second layers twice. Each wavelet will travel independently, but all three will arrive at the surface at the same time, $2t_1 + 2t_2$, so boosting the amplitude of the multiple reflection. Such reinforcement is an important factor in the persistence of certain multiples in the seismic section.

Figure 5.12 Some normal-incidence primary and multiple reflection paths. Raypaths are shown slightly oblique for the sake of clarity.



With so much potential for the creation of multiples, it is inevitable that some will fall into important parts of a seismic section covering a reservoir, and a lot of data processing is focused on their elimination.

In Tutorial 5.2, a simple geological model based on the stratigraphy of the northern North Sea is used to generate multiples across a reservoir interval using program *CMPGATHER*.

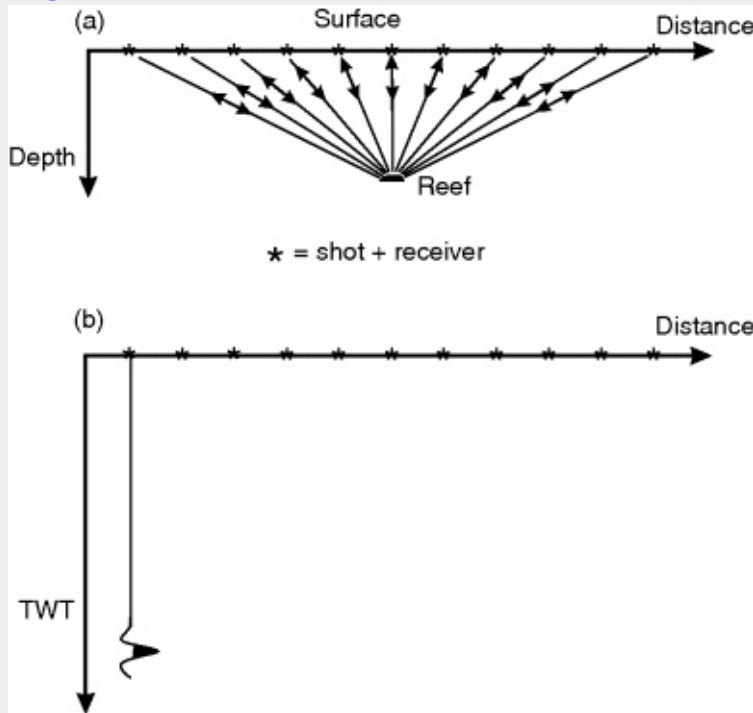
Tutorials for Chapter 5

Tutorial 5.1

Purpose: To show the seismic expression of a 'point' reflector.

In section **a** of [Figure T5.1.1](#), a small patch reef responds to seismic energy coming down from the surface shots by throwing back diffracted energy in all directions towards the surface. The TWT of the seismic arrivals at the surface will be proportional to the length of the raypath. Measure the lengths of the raypaths and plot a point at that distance *vertically* below the surface shot points in the time section **b**. For more realism, sketch a vertical seismic trace with a seismic wavelet at the plotted point.

Figure T5.1.1



As an image of a small reef, this leaves much to be desired! We would like to see a burst of energy under the reef's location on the seismic section, but the wavelets are spread over a characteristic curve – the diffraction hyperbola.

How would the shape of the hyperbola change in each of the following cases:

1. The reef is deeper?
2. The velocity changes smoothly across the diagram from high on the left to low on the right?

Tutorial 5.2

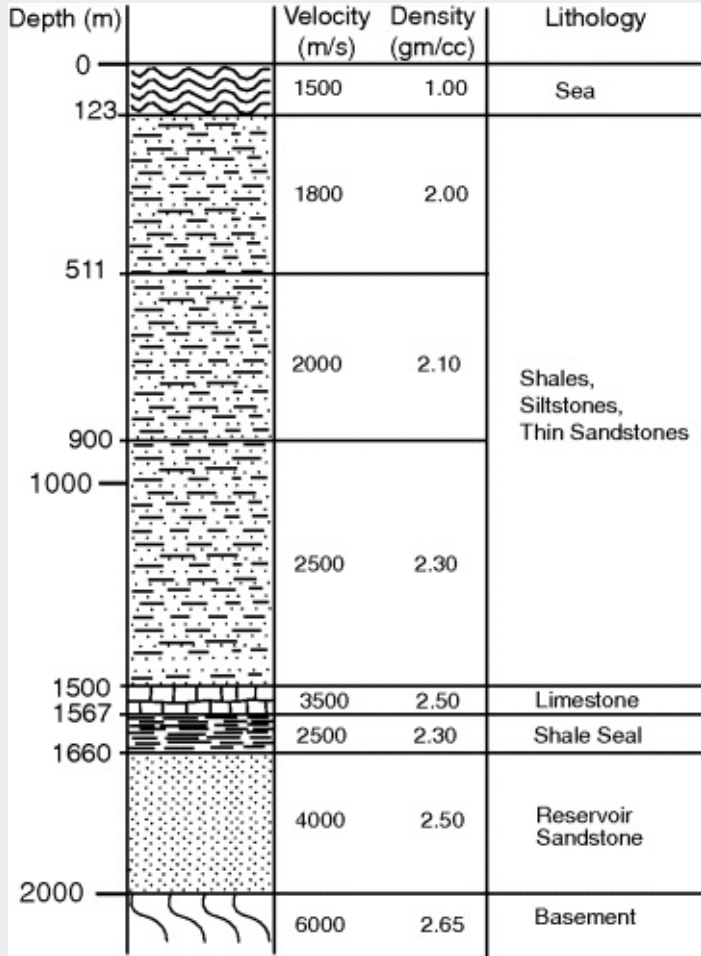
Purpose: to demonstrate how water-layer multiples may spoil a deep reservoir interval

The earth model BCU1.mod, which is supplied on the CD, is based on the stratigraphic section shown in [Figure T5.2.1](#). This section has some similarities to that found in the northern North Sea Basin, where the Brent Sands would be an analogue for the reservoir sandstone and the Base Cretaceous Unconformity would be an analogue for the limestone/shale interface. However, it is not intended as a rigorous model.

1. Start *CMPGATHER* and set the path to your data files via Configure on the menu.
2. Click on File/Open/Earth Model and open the geological model file BCU1.mod.
3. Click on File/Open/Wavelet and open the wavelet file rick2501.sig, a 25 Hz, zero-phase Ricker wavelet.
4. Click on Parameters and accept all settings. No multiples will be generated at this stage.
5. Click on Display and a tabulation of model parameters, velocities, times and reflection coefficients appears.
6. After noting the names of the two files that will hold the CMP gather, OK the prompt. The CMP gather will then appear in a panel on the left of the screen.
7. Pause at this point to tie reflections in the CMP gather to the stratigraphy. Note the top limestone event at zero-offset time of 1,464 ms, the top shale at 1,502 ms (why negative polarity?), the top reservoir sandstone at 1,577 ms and the reservoir interval extending to 1,799 ms. Take a print so that you have a note of the V_{rms} values for the primary reflections – you will use these in a later tutorial.
8. Click on Parameters again and set Multiples to 'On', then Display once more. Note that the CMP gather is filed under the same name but with 'M' for multiple added. All multiples with reflection coefficients greater than 0.004 are shown.
9. Take another print. Compare the two prints and note that every primary reflection now has several multiples

cascading down below it, generated by bounces within the water layer, each bounce adding the TWT through the water (164 ms). This is especially obvious in the case of the water bottom reflection itself at 164 ms, which generates multiples at 2×164 , 3×164 and 4×164 ms that alternate in polarity (why?). Identify the reservoir interval again and note how it is now badly affected by multiples spaced 164 ms below the primary reflections of top limestone and top shale. The basement interval, which should be reflection-free, is now occupied by multiples of substantial amplitude.

Figure T5.2.1



The two CMP gathers generated, one with and one without multiples, will be used in Chapter 6 (Tutorial 6.4), where CMP stacking will be shown to reduce the amplitude of the multiples, although not to eliminate them entirely.

Chapter 6

Velocity Analysis, CMP Stacking and Post-Stack Migration

6.1 General Points

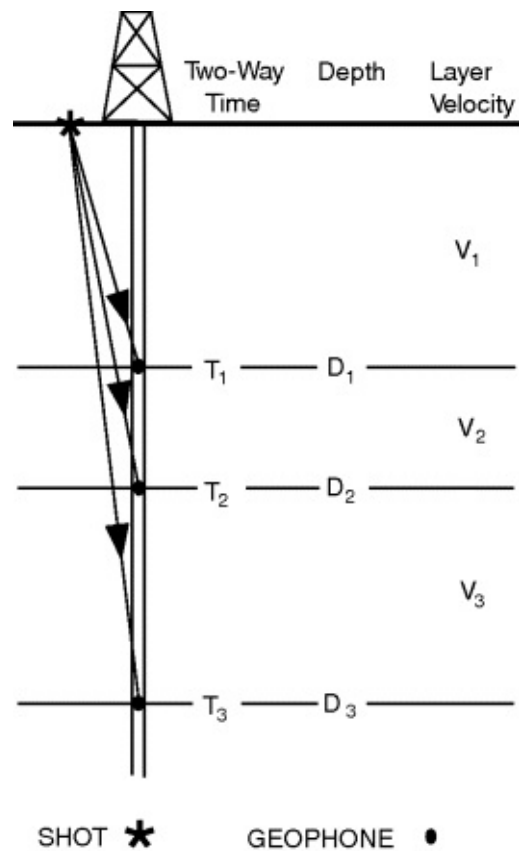
In this chapter we will look at three data processing steps which are particularly important in preparing the seismic data for structural interpretation – namely, velocity analysis, common mid-point (CMP) stacking and migration. All of these are make-or-break operations in the sense that, if they go badly wrong, the data may become impossible to interpret. Velocity analysis and CMP stacking are doubly important because they enable us to measure the velocity of propagation of seismic energy through the subsurface – the essential prerequisite for converting seismic time sections to geological depth sections.

Throughout this chapter, we will assume that CMP stacking results in a seismic trace that is the normal-incidence trace at the CMP location, which is strictly true only for flat geological strata. That was the state of the game for the first era of digital seismic processing, from about 1965 to 1980, but, since then, ever more sophisticated ways have been invented of dealing with the problem of steeply dipping strata and the associated problem of laterally variable velocity. For the moment, however, let us keep things simple and we can deal with the complications later.

6.2 Definitions of Seismic Velocity: Well Data

The topic of P-wave velocity was introduced in Chapter 4, but we now require more specific definitions of velocity. We use different definitions of velocity for different purposes and they are most easily explained (and often measured) with reference to a well, as indicated in [Figure 6.1](#).

[Figure 6.1](#) Velocity survey in a well.



The layered-earth model is commonly used as a starting point. The subsurface is divided into layers of variable thickness and uniform velocity $V_1, V_2 \dots$ etc. The layers will follow the main lithological units in the survey area, and reflections will be generated from the interfaces between layers where there is sufficient contrast in acoustic impedance. Layer velocities will vary considerably, depending on the lithologies of the layers, as mentioned in Chapter 4. Other key quantities in [Figure 6.1](#) are two-way (reflection) times (T) and depths to interfaces (D).

In most wells, a velocity survey will be carried out. In its simplest form, a specially constructed geophone is lowered down the well and positioned at the principal geological interfaces, while a shot is detonated at the surface. In this way, direct measurements of one-way time (OWT) and depth D can be made, enabling calculation of all the other quantities in [Figure 6.1](#).

Average velocity (V_a) is an important quantity and is simply defined as the depth to the reflector divided by the one-way travel time. In terms of [Figure 6.1](#) average velocity to the n th reflector is:

$$(6.1) V_{an} = 2D_n/T_n$$

For example, in Tutorial 6.1, average velocity to the top Permian reflector is:

$$3892/1.452 = 2680 \text{ m/s.}$$

Average velocity down to any reflector is a value which will vary across a survey area in response to variations in thickness and lithology in the section above. It has been much used for converting time maps to depth maps. As demonstrated in Tutorial 6.1, V_a increases slowly with depth.

Suppose we define the time taken for the seismic wavelet to pass through one layer as the interval time or transit time (t). Thus, for the n th layer:

$$t_n = (T_{n+1} - T_n)/2$$

Interval velocity or layer velocity (V_i) is the velocity at which the seismic energy passes through any one layer. Its value depends on the physical properties of the layer and it can be calculated for the n th layer in a well from a velocity survey as in [Figure 6.1](#):

$$(6.2) V_n = 2(D_n - D_{n-1})/(T_n - T_{n-1})$$

For example, in Tutorial 6.1, the Cretaceous interval velocity is:

$$2(1471 - 507)/(1.190 - 0.570) = 3110 \text{ m/s.}$$

If the depth interval occupied by the n th layer is $d_n = V_n t_n$, then average velocity down to the n th reflector can be defined as:

$$V_{\text{an}} = \frac{\text{sum}(\text{depth intervals})}{\text{sum}(\text{transit times})}$$

$$(6.3) \quad = \frac{\sum(V_i t_i)}{\sum(t_i)} \quad (i = 1, 2, \dots, n)$$

We define average velocity in this form in order to make comparison with the definition of another velocity later on.

Before going on, take the opportunity to get more familiar with these velocities by finishing parts 1 and 2 of Tutorial 6.1.

6.3 Velocities from Seismic Data: V_{rms}

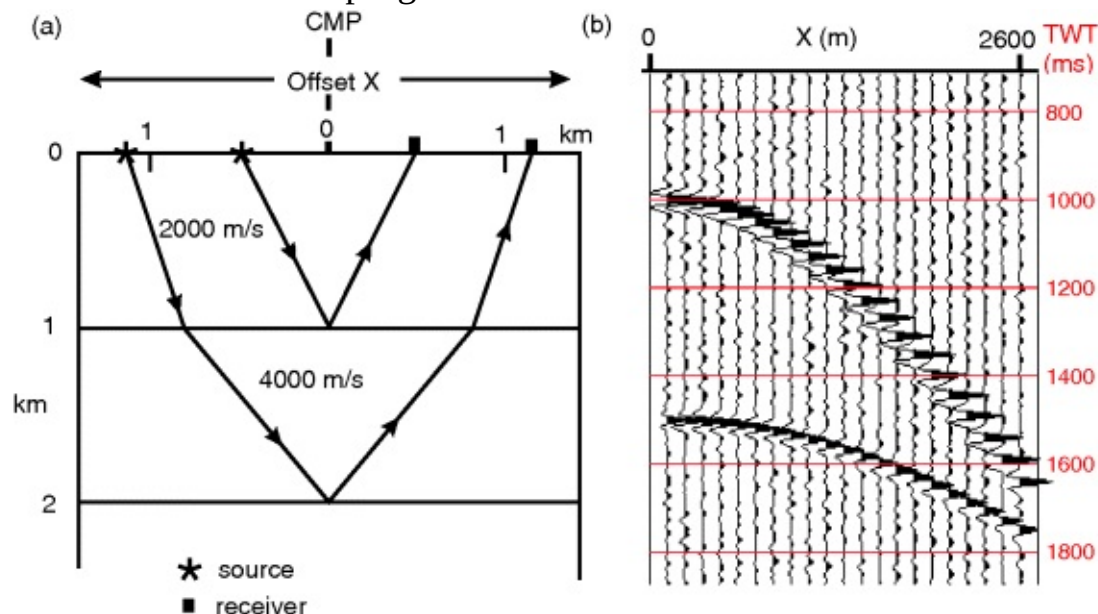
Average velocity, as defined in [equation \(6.1\)](#) above, applies to normal-incidence reflections where there is zero offset between source and receiver. But what of the case away from wells, where all we have are the travel times to seismic reflectors measured over oblique travel paths to receivers offset from the source?

The CMP gather is just such a set of seismic traces (see Chapter 3, Section 3.5). [Figures 6.2a](#) and [6.2b](#) show typical raypaths and a CMP gather of seismograms recorded from source-receiver pairs which are separated by a distance X about the CMP. If T_0 is the zero-offset reflection time (normal-incidence reflection), the simple reflection equation for no dip ([equation 4.5](#)) describes the reflection time T_x at an offset X :

Figure 6.2

- a.** An earth model with two reflectors and representative raypaths from shots to receivers offset about a common mid point (CMP).
- b.** A CMP gather of primary reflections generated from the section in **a**.

Data modelled in program *CMPGATHER*



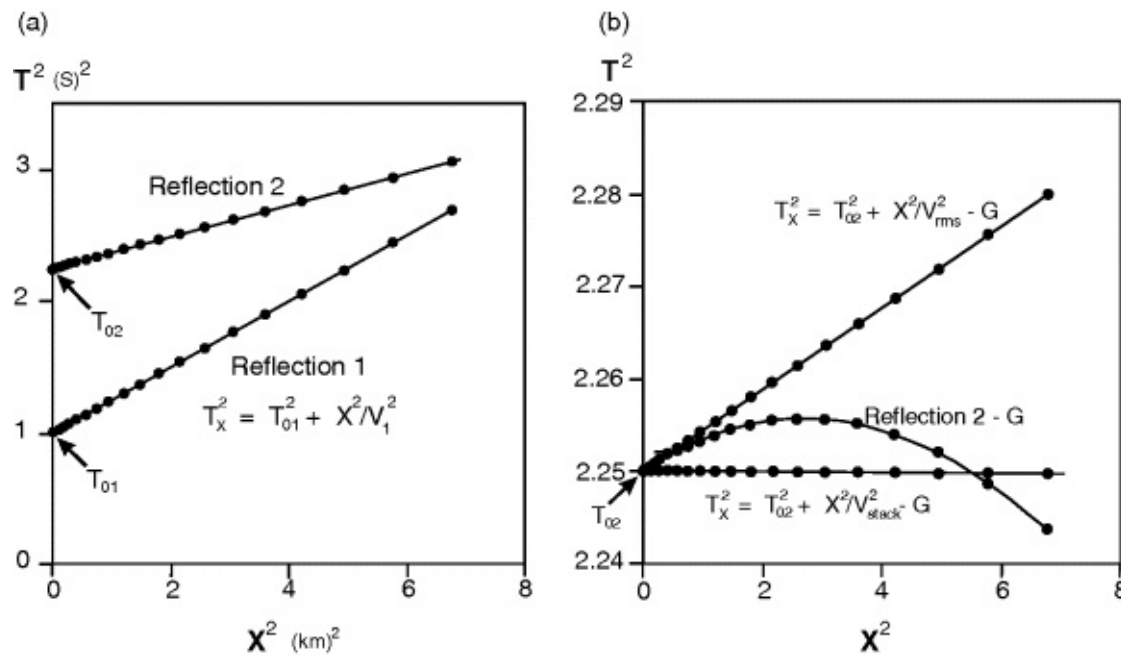
$$(6.4) \quad T_x^2 = T_0^2 + X^2/V^2$$

Plotting T^2 versus X^2 for times for Reflection 1 will give a straight line of slope $1/V_1^2$ and intercept T_{01}^2 (Figure 6.3a). However, refraction of raypaths in the layered earth will generally cause energy reflected from the second interface to spend a greater proportion of its total travel path in the lower (faster) layer (Figure 6.2a) and so travel at a higher velocity to the greater offsets. On the $T^2 - X^2$ plot (Figure 6.3), the line for Reflection 2 is thus not quite straight but droops to shorter times at greater offsets. In Figure 6.3b, a blown-up graph of times for Reflection 2 has been made by subtracting a linear gradient (G) from all times across the plot and using a suitably exaggerated time scale. Note that we can no longer draw a straight line through these travel times, so we cannot associate a single exact value of velocity with Reflection 2 as we could with Reflection 1.

Figure 6.3

a. T^2, X^2 plot for the two reflections in Figure 6.2.

b. Enlarged view of Reflection 2 from a with a linear gradient $G = X^2/V_{\text{stack}}^2$ subtracted. Travel times have also been plotted for two expressions which approximately describe the times of reflection 2. $V_{\text{stack}} = 2880$ m/s.



In a classic paper, Dix (1955) analysed this situation and showed that a single value of velocity could still be usefully derived. This is called the root-mean-square (rms) velocity, V_{rms} . On the $T^2 - X^2$ plot, the corresponding straight line is tangential to the curve of travel times at $X = 0$ (Figure 6.3b). The velocity takes its name from its definition in terms of transit times and the squares of interval velocities as:

$$V_{\text{rms}} = \left[\frac{\sum (v_i^2 \cdot t_i)}{\sum (t_i)} \right]^{\frac{1}{2}}$$

(6.5) ($i = 1, 2, \dots, n$)

Note the similarity to equation (6.3) for average velocity V_a , but now the velocity is weighted towards the higher velocities by taking the squares and is thus a few per cent higher than V_a in a typical section. For the section shown in Figure 6.2, V_{a2} is 2,667 m/s and $V_{\text{rms}2}$ is 6 per cent higher at 2,828 m/s.

In Figure 6.3b, travel times for Reflection 2 have been calculated from equation (6.4) (adjusted by gradient G), but using V_{rms} as the velocity. The resultant straight line is clearly tangential to

the travel-time plot at the origin as stated by Dix.

Why is V_{rms} important? In his 1955 paper, Dix showed that interval velocity V_i can be calculated from V_{rms} from the equation:

$$(6.6) \quad V_i = [(V_2^2 T_2 - V_1^2 T_1) / (T_2 - T_1)]^{1/2}$$

where V_1 , T_1 and V_2 , T_2 are V_{rms} and TWT values for the reflections at the top and bottom of a layer.

Once we have interval velocities, it is easy to calculate layer thicknesses (and so depths and average velocities) to key reflections on the seismic section. Thus we can acquire the same velocity information at a CMP location as we obtained from a well, provided we can measure V_{rms} from the CMP gather. The velocities so obtained are not as precise as those obtained at a well, but their big advantage is that they cover the whole area of a seismic survey.

A final word of warning: the velocities obtained from [equation \(6.8\)](#) (often called Dix velocities) apply exactly only to flat-lying strata. However, that does not stop them being used, even where dips are moderate, as a first approach to establishing the velocity structure of an area. In the next section, we will see how rapidly measurements of velocity can be made from the seismic data.

6.4 Velocities from Seismic Data: V_{stack}

You will recall, from [Figures 3.4](#) and [3.5](#) in Chapter 3, the general procedure involved in acquiring the data for CMP processing. Reflections in the raw CMP gather (e.g. [Figure 6.2b](#)) lie on hyperbolae which start at normal-incidence reflection time T_0 at offset $X = 0$ but which then curve down to greater travel times as the source-receiver offset increases and the raypaths become more oblique.

The amount of extra time due to obliquity of path compared to the normal-incidence trace is called the Normal Move-Out (NMO). So, using the notation of [equation \(6.4\)](#) again:

$$(6.7) \quad \begin{aligned} \text{NMO} &= T_x - T_0 \\ &= (T_0^2 + X^2/V^2)^{1/2} - T_0 \end{aligned}$$

For any sample down a trace in the CMP gather, we know T_0 and the offset X in [equation \(6.7\)](#). If we know V , we can calculate NMO sample by sample on each trace and shift the reflection backwards in time from the recorded time T_x to zero offset time T_0 . The reflection will no longer fall obliquely across the CMP gather on a hyperbola, but will run straight across it and can be stacked (summed) across the gather to form a single enhanced trace with a higher signal/noise ratio ([Figure 3.5b](#) and Tutorial 6.2).

Although we know T_0 and X in [equation \(6.7\)](#), velocity V is initially unknown. However, we can go through a process of trial and error to find the particular velocity that makes the best NMO correction for each reflection and stacks the reflection to a maximum amplitude. This velocity is called the stacking velocity, V_{stack} . All reflections in the CMP gather can be corrected for NMO and stacked, but each will have a different stacking velocity.

All will become clear if you go through the process of finding V_{stack} by trial and error for yourself right now in Tutorial 6.2, using program *NMOSTAK* and the CMP gather of [Figure 6.2b](#)

An approximate expression for NMO is:

$$(6.8) \text{ NMO} \approx X^2 / (2V_{\text{stack}}^2 \cdot T_0)$$

Thus, NMO is not just a function of X , but an inverse function of V_{stack} and T_0 , so that it decreases down the length of a seismogram as both V_{stack} and T_0 increase. It follows that deeper reflections show much less curvature than shallow ones ([Figure 6.2b](#)).

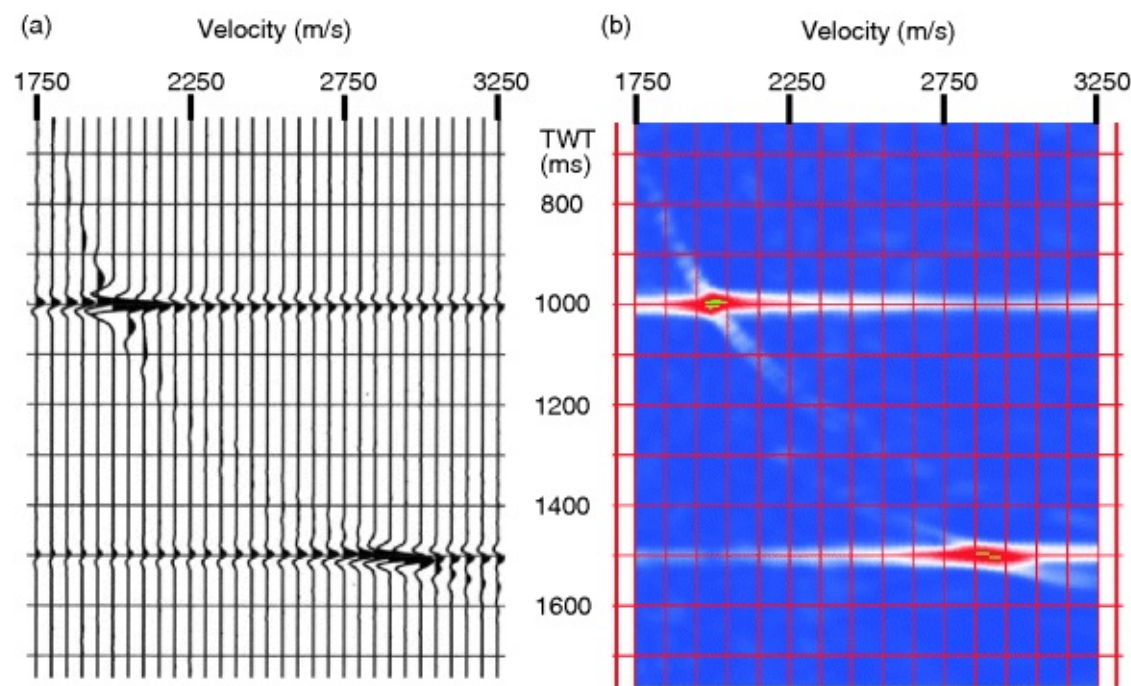
In the stacking process, the wavelet is amplified by a factor of the number of wavelets summed, i.e. 16-fold stacking will increase its amplitude 16 times. If random noise is present, then that will also increase. It will do so less than the reflection wavelet, however, because it does not stack coherently, and consequently the all-important signal/noise (S/N) ratio is improved. It turns out that if n traces are stacked, then S/N improves by a factor of \sqrt{n} , provided noise is random. For example, 16-fold stacking will enhance S/N by a factor of 4. Enhancement of S/N ratio is the first of three major benefits of CMP stacking.

6.5 Velocity Analysis

In Tutorial 6.2, the CMP gather was corrected using *only one* value of velocity for all T_0 values. As might be expected, this value properly corrects only one reflection and leaves the others over- or under-corrected. It is clear that we can keep trying trial stacks like this through a range of velocities until we have found the best stacking velocity for each reflection, and this is exactly the methodology adopted in Tutorial 6.2.

However, suppose we let the computer do all the repetitive work; let it step through a range of velocities from low to high and have it plot out a stacked trace for each velocity. [Figures 6.4a](#) and [6.4b](#) show the data from the CMP gather of [Figure 6.2b](#) treated in that way. The horizontal scale is now stacking velocity, ranging from low to high trial values, and the vertical scale is still normal-incidence TWT (T_0). It is now easy to see when a reflection stacks up to maximum amplitude and to read off the stacking velocity that best stacked the trace – so much quicker than the trial-and-error procedure of Tutorial 6.2! But we are still employing the same principle – getting the computer to do all the donkey work.

Figure 6.4 Velocity spectra derived from the CMP gather of [Figure 6.2b](#). In, (a) each trace is a stack of the gather after correction for NMO. In, (b) the same data is displayed as colour contours. Data displayed from program *VELSPEC*.



A table of TWT and V_{stack} can be built up for the principal reflections at the CMP location. If the squared amplitudes of the stacked trace are plotted, then signal troughs will contribute positive values and the high values can be shown more clearly on a colour plot, as in [Figure 6.4b](#).

One disadvantage of this presentation is that weak reflections will only give a weak ‘high’, which may be easily hidden by background noise; in actual practice, the quantity semblance is calculated across the traces within a moving window. Semblance is a measure of the similarity of traces giving a value between 1 (traces identical) and 0 (traces totally dissimilar), and is not so dependent on signal amplitude. The resultant display is very similar to [Figure 6.4b](#) and is interpreted in the same way (Neidell & Taner, 1971).

A display of this type is called a velocity spectrum, using ‘spectrum’ in a general way in the sense of a spread of values (Taner & Koehler, 1969). Since it is simply a sheet of numbers, it can be contoured or represented by coloured levels, as the squared amplitudes were in [Figure 6.4](#). Semblance ‘highs’ will develop wherever there is appreciable reflection energy and give spot determinations of V_{stack} and T_0 , between which linear interpolation may be made for intermediate travel times. The end product is a value of velocity for every T_0 down the CMP gather. Now it is possible to correct every reflection (indeed, every sample down a trace) with its own particular stacking velocity, so that the final stacked trace enhances every reflection wavelet. This was the end product achieved in Tutorial 6.2.

Take a break – try your hand at velocity analysis in Tutorial 6.3 before going on; you can then complete Tutorial 6.1.

6.6 Errors in Seismic-Derived Velocities

Although we measure V_{stack} from the seismic data, not V_{rms} , the difference between the two is very small for gently dipping strata. In the case of [Figure 6.3](#), for the second reflector, $V_{\text{rms}} = 2,828$ m/s and $V_{\text{stack}} = 2,880$ m/s, a difference of 1.8 per cent. If we plot travel times using V_{stack} in the travel time equation instead of V_{rms} , we get a straight line, which is a best fit line to the

curve of travel times for Reflection 2 ([Figure 6.3](#)). Stacking velocity is always a best fit velocity in that way; it is not fixed and calculable for a particular section like V_{rms} , but it will increase as the maximum source-receiver offset increases. For example, if the maximum offset of Reflection 2 in [Figure 6.2](#) is increased from 2,600 m to 3,600 m, then V_{stack} rises from 2,880 to 2,920 m/s.

Stacking velocity at short range (often called V_{nmo}) is close enough to V_{rms} to be used in calculating interval velocities ([equation \(6.6\)](#)), depths and V_a values, in a sort of reverse operation to the use of well data described in section 6.2 above. Strictly speaking, this procedure only applies to flat, isotropic layers with no lateral variation in velocity, but nevertheless it is always the first step in establishing the gross velocity structure of the subsurface. Thus the second great benefit of CMP stacking is that, away from well control, we can still derive usable velocities from the seismic data alone.

6.7 Multiple Suppression by CMP Stacking

In Chapter 5, Section 5.8, we saw that one of the most troublesome multiple reflections is the surface multiple. This will appear on the seismic section as a reflection with twice the TWT of some strong, shallow, primary reflection, so it may well interfere with deep primary reflections. However, the multiple has travelled only in the upper, low-velocity part of the geological section, so its NMO is greater than a primary reflection at the same travel time T_0 . Thus, when the primary is corrected for NMO, the multiple is still curved and, on stacking, its mis-aligned peaks and troughs effectively self-destruct (see Tutorial 6.4). Multiple suppression was one of the main reasons for the widespread adoption of the CMP technique in the 1960s (Mayne, 1962), and this constitutes the third major benefit of CMP stacking.

Remember the multiples you generated in Tutorial 5.3? See how CMP stacking helps to reduce them in Tutorial 6.4 and how they look in a velocity spectrum in Tutorial 6.5.

6.8 Stacking the Whole Section: A Make-or-Break Process

A velocity analysis is carried out on a CMP gather every 500 m or so along the section (depending on structural complexity) and, at intermediate CMPs, values of velocity are interpolated from the nearest velocity analyses. Now all CMP gathers along the entire seismic line can be corrected for NMO and stacked into enhanced normal-incidence traces. Initially these traces are plotted *vertically below* their CMP positions to form an unmigrated stacked time section.

CMP stacking is a make-or-break step in the data processing sequence. In the worst case, it would be possible to choose a range of velocities that would stack the multiples and destroy the primary reflections! Picking the wrong velocities can have a startlingly bad effect on data quality. Moreover, the velocities so derived will also be used later in further processing of the data (migration) and in the supremely important conversion from time to depth. So important is velocity analysis that it is never left entirely to the contractor. A company representative may carry out some velocity analyses independently, to monitor and maintain data quality in this crucial step.

The three principal benefits of CMP stacking can be summarized as:

1. Improvement in S/N ratio against random noise.
2. Suppression of surface multiples.
3. Measurement of the variation of velocity with time (and depth) in the subsurface.

6.9 Some Stacking Refinements

6.9.1 NMO Stretch

For shallow reflections at large offsets, NMO is very great and will lead to NMO stretch with severe distortion of the waveform at short TWT (Tutorial 6.2). The solution is simply to discard the early part of the traces and not incorporate them in the stack (trace muting). As a result, the fold of stack will not reach maximum until some way down the section, typically about 1,000 ms TWT with conventional geometries. The process also gets rid of the direct arrivals and shallow refracted energy.

6.9.2 Weighted Stacking

The inner traces of a CMP gather show very little NMO, so any reflection will stack up using almost any V_{stack} value in the NMO correction. In particular, a multiple reflection will still stack up on the near traces, even although it is being successfully cancelled on the outer traces. One solution is to give the inner traces a low weighting in the stack, effectively discarding the innermost (0 per cent weight) and progressively increasing the weighting at greater ranges. However, this makes it more awkward to scale the final stacked traces properly in amplitude. A better strategy is to anticipate the problem by modelling the multiples in the planning stage of the survey and to use a suitable offset between the source and the nearest receivers so that no near traces are recorded in the first place.

Where some of the traces are badly affected by noise, for example in a land party working along a road in the presence of traffic, the noisy trace might easily dominate the stack and render it useless. One solution is to assess the overall amplitude of the traces and assign weights that are inversely proportional to signal amplitude. The result is known as a diversity stack.

6.10 Migration: The Fundamental Idea

Migration is the name given to lateral repositioning of the reflection. It is an essential process in forming a coherent image of the geological cross-section. Some of the serious distortions that may occur in unmigrated time sections have already been discussed in sections 5.4 and 5.5 and in reference to [Figure 5.7](#).

For the present we will concentrate on two-dimensional seismic sections, where the survey has been designed with some prior knowledge of regional structure and the seismic lines have been shot at right angles to strike, so that we are looking at true dip sections. The seismic wavelet obtained from CMP stacking is plotted on the seismic time section vertically below the CMP location (point A, [Figure 6.5a](#)). However, that point is the true location of the reflector only where the reflector is flat. If the reflector dips, then the normal-incidence reflection point is off to the

side somewhere up-dip of the CMP location, so the wavelet should really be plotted over there (point C, [Figure 6.5a](#)). It is clear that the steeper the dip of the reflector, the further away is its true migrated position, and the horizontal shift X_m is given by:

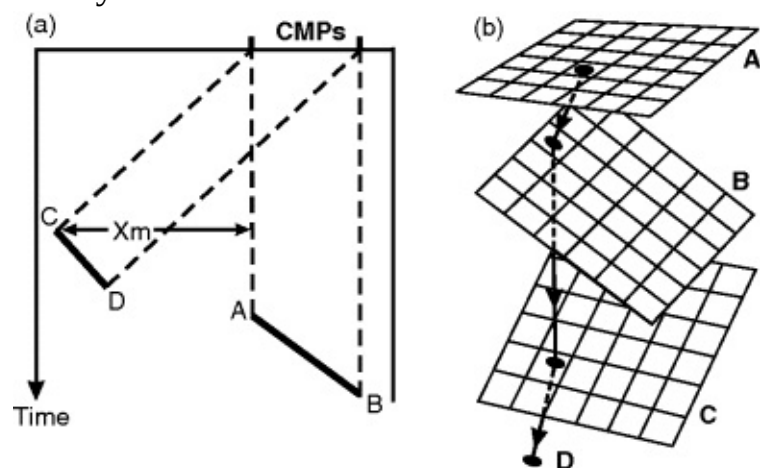
$$(6.9) \quad \begin{aligned} X_m &= 1/2 VT \sin \theta \\ &= 1/4 V^2 T (dT/dX) \end{aligned}$$

where V = velocity down to the reflector, T = TWT at the CMP location and dT/dX is the gradient of the reflection at the CMP location on the unmigrated time section. Note that the lateral shift is much greater for deep reflections, partly because T is greater, but also because it depends on the square of the (greater) velocity. [Figure 6.5](#) shows how migration shortens and steepens reflection segments as well as shifting them laterally.

Figure 6.5

a. A – B is a reflection segment of stacked, unmigrated data plotted vertically below the CMP positions; C – D is the true position of the reflection after migration.

b. Map migration. Starting from its angle of emergence at the surface (A), a ray can be traced through previously-migrated layer boundaries B and C to its reflection point at D, provided layer velocities are known.



6.10.1 Map Migration

If reflections are individually picked and timed on CMP-stacked data, they can be migrated to their true positions on a depth section by ray-tracing. The angle of emergence (α) of the raypath at the surface is given by:

$$(6.10) \quad \sin \alpha = (V/2)(dT/dX)$$

where V = velocity of the near-surface layer in m/s and dT/dX is the time gradient of the reflection across the section in s/m.

The ray is started off downwards from the surface at angle α and stops when the one-way travel time for that reflection has been used up. Once the first interface has been defined, the next reflection can be treated in the same way. Its ray may start off from the surface at a different angle and it will be refracted at the first interface in accordance with Snell's Law, again continuing downwards until its one-way time is used up. In this way, several interfaces may be established, working down from the top on a layer-by-layer basis.

If the layers all have the same strike but different dips, the process takes place in two dimensions in the plane of the dip section, as in Tutorial 6.6. More generally, though, working with 3D data, the angle and starting direction of a downgoing ray will be defined in three

dimensions. The ray can then be traced down through successive interfaces and a new set of properly located depth points can be established across the map area ([Figure 6.5b](#)). Since the process was originally used to convert an unmigrated time map into a migrated depth map, it is called map migration (Kleyn, 1983).

See migration by 2D ray-tracing in Tutorial 6.6. It's easy – half of it is done already.

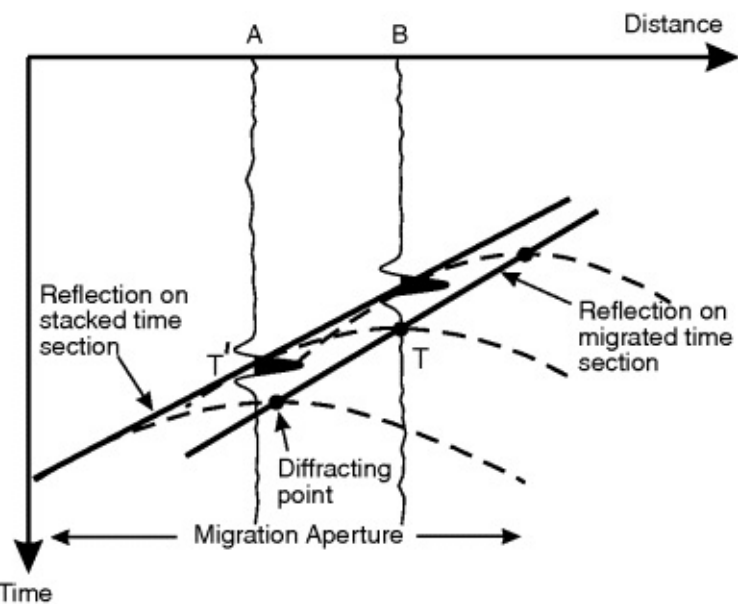
6.11 Full-Waveform Migration

If the geological structure becomes really complex, the CMP-stacked time section breaks down into a welter of criss-crossing hyperbolae and short, disjointed reflection segments which become near-impossible to unravel. Even in well-behaved, flattish sedimentary successions, some scattered energy may be present from faults that may obscure detailed features of stratigraphic interest and would be worth removing. What we need is a method of migrating the section sample by sample, so that the complete waveform is rebuilt at its new location. The goal is a section in which reflections are relocated laterally to their correct positions while retaining the full reflection waveform, and therefore the same density of information, as in the stacked time section.

6.11.1 Migration by Kirchhoff diffraction stack

This method of migration is the easiest to understand because it comes directly from the notion of the diffraction response of a point reflector developed in Chapter 5. Tutorial 5.1 demonstrates that the image of a small patch reef on an unmigrated seismic time section takes the form of a diffraction hyperbola spread out over a considerable width of the section. Unfortunately, it is nothing like the concentrated burst of energy under the location of the reef that we would like it to be. The Kirchhoff diffraction stack method reverses the scattering process of diffraction by seeking out all the samples positioned around the diffraction hyperbola and adding them up to form a composite waveform that is plotted at the summit location of the hyperbola ([Figure 6.6](#)). The distance over which the summation takes place is called the migration aperture, and this increases with the depth and dip of the reflector.

[Figure 6.6](#) Migration by Kirchhoff diffraction stack.



In [Figure 6.6](#), imagine the process moving down trace B sample by sample. At each sample, there are unique values of velocity and TWT which define a diffraction hyperbola ([equation 5.1](#)). The data values which are found on adjacent traces along the diffraction hyperbola are scaled appropriately and summed to form a new sample of the output migrated trace. In this way, the wavelet at T' on trace A is rebuilt at time T on the migrated version of trace B (not shown here). Note that the steeper the dip, the wider the migration aperture must be.

In effect, the calculation corrects the samples for the curvature of the hyperbola and adds them all together in a manner similar to NMO correction and stacking of CMP data. Newman (1990) showed that the process acts as a high-cut filter on the amplitude spectrum of the wavelet and shifts the phase by $+45^\circ$, and these effects must be corrected in processing to maintain the fidelity of the waveform. Schneider (1978) showed how the process was derived from the wave equation and pointed out its advantages over other methods, notably that steep dips up to 90° can be handled provided the migration aperture is wide enough.

Some further points are worth making:

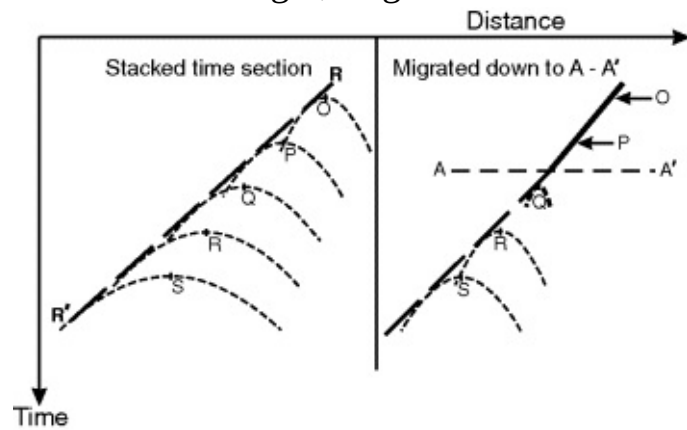
1. The diffraction curve is only strictly a hyperbola for uniform velocity. If velocity is some function of depth, then it is still hyperbolic enough, but rapid lateral variations in velocity cause the diffraction curve to become lop-sided (see Tutorial 5.1). This limitation of the Kirchhoff summation approach will be discussed more fully in Chapter 8.
2. High-amplitude bursts of noise will be smeared out into wavefront-like events, concave upwards, especially deep in the section where signal/noise ratio is low. Such events are often called migration smiles; they can be seen on any form of computer-migrated data.
3. The output section is still scaled in TWT. Times are now vertical times, i.e. they refer to points vertically below the surface observation points as long as V is a function of Z only. Thus a simple re-scaling to depth of the vertical dimension of the section may be carried out using the known velocity-depth relationship (but see Chapter 7, Section 7.8).

6.11.2 Migration by Wave Equation

The basic notion here is straightforward and is often described as the 'downward continuation' of the observed wavefield at the surface. Consider a time section with some diffractions on it, perhaps coalescing into a reflection segment ($R - R'$ in [Figure 6.7](#)). Suppose we could record our time section from shots and geophones buried at successively deeper levels in the subsurface. As

the recording level descends upon a diffracting source, the hyperbola becomes sharper and sharper and the tails fainter and fainter, until eventually it reduces to a single burst of energy when the recording level and the diffracting source coincide.

Figure 6.7 Migration by downward continuation of the wavefield. On the left, reflection R – R' is formed by the summation of the flanks of innumerable diffraction hyperbolae, of which five are shown. On the right, migration has reached the level A – A'.



On the right half of [Figure 6.7](#), migration has reached the level A– A' and hyperbolae O and P have been collapsed to points on the migrated reflection (solid line). Below A – A', the section is part-migrated, Q is shrunk almost to a point and R and S are much tighter. Of course, we cannot really make recordings underground in this fashion, but what we can do is to use the surface-recorded data as the starting point to back-calculate the configuration of the wavefield at greater depths and prior recording times.

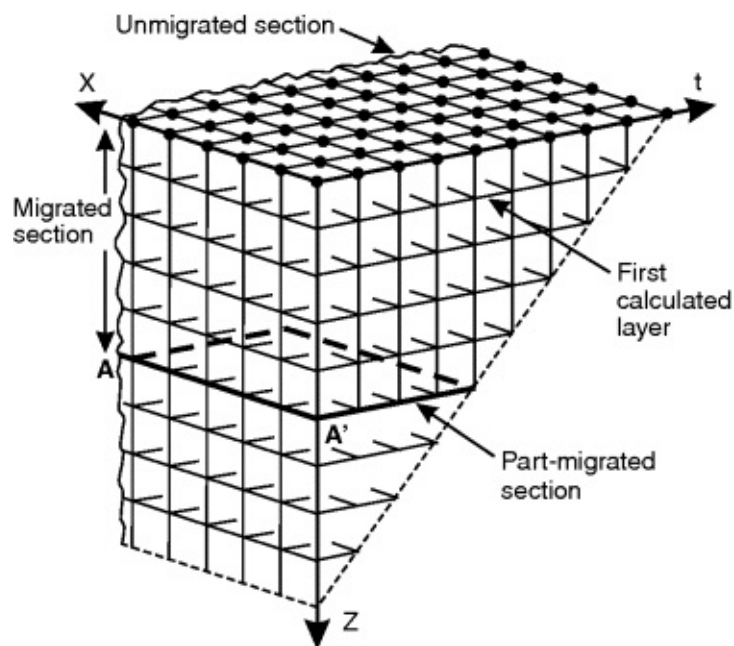
The basis of the calculation is the wave equation in its two-dimensional form:

$$(6.11) \quad \partial^2 S / \partial x^2 + \partial^2 S / \partial z^2 = (1/v^2) \partial^2 S / \partial t^2$$

Here S is the seismic data value, x is distance across the seismic section, t is time on the section and z is depth.

Discretely sampled S values may be thought of as lying on a 3D matrix of quantities in the 3D space of x , t , and z , and can be annotated as $S(x, t, z)$ ([Figure 6.8](#)). The surface-observed traces are the topmost layer – the $S(x, t, 0)$ values. Along each seismic trace, in the direction of increasing time, the finite difference in S values gives a measure of the rate of change of S with time ($\partial S / \partial t$), and the difference of differences gives the quantity $\partial^2 S / \partial t^2$. In a similar way, differences from trace to trace across the seismic section give a measure of $\partial^2 S / \partial x^2$. Substitution of these quantities into [equation \(6.11\)](#), together with a suitable velocity, gives a measure of $\partial^2 S / \partial z^2$. Although it is not possible to calculate data at other depths from this quantity alone, a modification of the wave equation does allow calculation of the next layer down from the surface (Claerbout, 1985).

Figure 6.8 Migration by downward continuation of the wavefield. A – A' is in a similar position to A – A' in [Figure 6.7](#).



Since we know the S values at the surface from the observed seismic section, we are able to calculate new S values at some small increment in depth and so calculate a new time section for that depth of observation. The process is repeated over and over again, each time generating a new layer of S values which represents the time section that would have been observed by a geophone spread and shots placed at the new depth.

Note how the deeper layers (back-calculated time sections) are diminished in time extent. For each layer, the new line of S values at zero time (e.g. $A - A'$ in [Figures 6.7](#) and [6.8](#)) represents an output line on the final display, which is built up line by line from the top down. Thus, in [Figure 6.7](#), the process has got some way down the section – the part above $A - A'$ is already migrated – and on [Figure 6.8](#) this is represented by the surface between $A - A'$ and the x -axis. The part below $A - A'$ in [Figure 6.7](#) is represented in [Figure 6.8](#) by the horizontal layer that includes $A - A'$.

Prior to performing the calculation, it is necessary to set up the appropriate velocity model. Usually stacking velocities are used, empirically reduced by a few per cent to approximate average velocities, and these give the best migrated result. (See Tutorial 6.1). The power of the process lies in the piecemeal nature of the finite-difference method, which can utilize lateral variations in velocity across the section much more easily than can be done in the diffraction stack.

As successive refinements have been made, both methods of migration – Kirchhoff diffraction stack and wave equation – have had their episodes of popularity. For reasons that will be amplified in Chapter 8, Section 8.7, wave equation methods have gained ascendancy in recent times. These two approaches to migration are the most commonly used, but human ingenuity does not stop there by any means. For example, remembering that, under the Fourier Transform, time transforms to frequency (f) and distance to wavenumber (k), yet another strategy is to transform the stacked time section from the time-distance domain to the frequency-wavenumber domain, carry out the migration there and then perform the inverse transform back to form a migrated time section. Such a technique is described as $f - k$ migration.

6.12 Migration example: 2D Section

The improvement in legibility of the section after migration is often dramatic. In [Figure 6.9](#), the

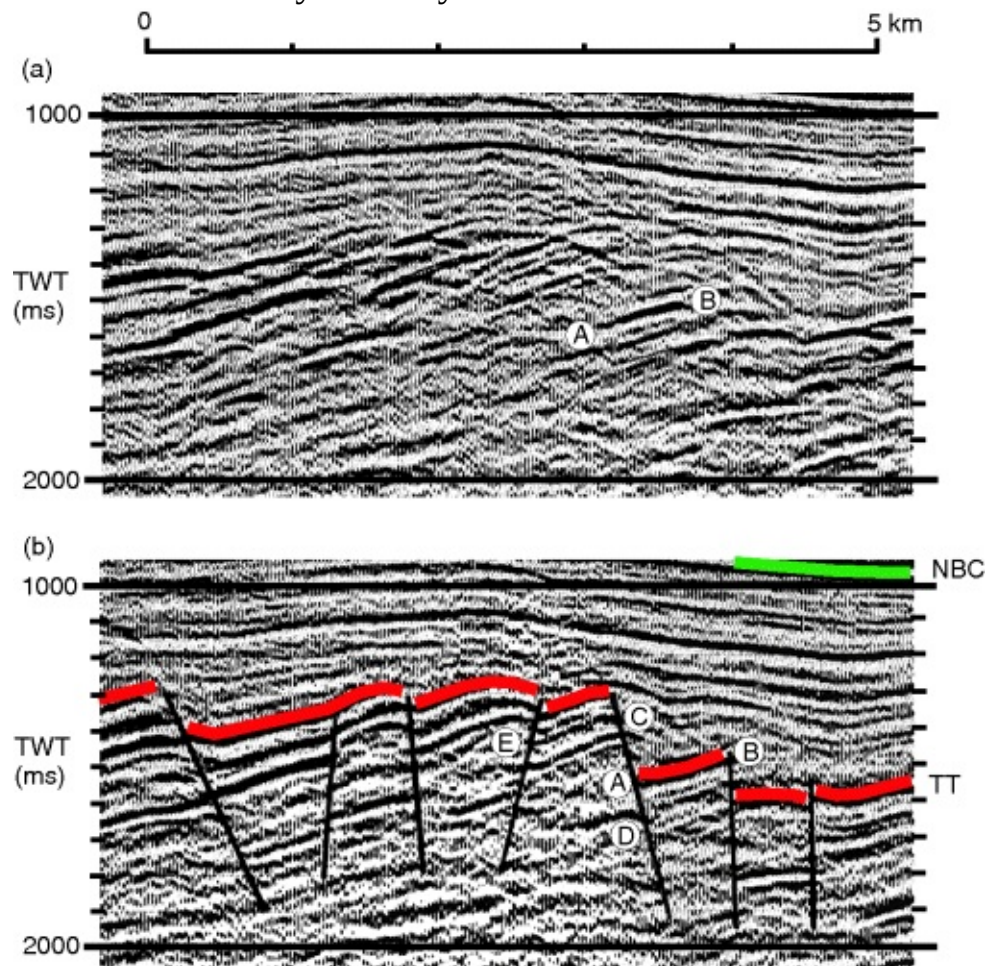
badly faulted sub-Jurassic succession is enhanced in two ways. First, reflections with dip have been shifted laterally to their proper locations (by about 300 m in the case of reflection segment A – B). Second, diffraction hyperbolae, evident in the stacked section as curved, convex-upward events which cross-cut structure and downgrade reflection character in a confusing way, have been almost completely eliminated. That is the result to be expected if the migration velocities are well chosen and the line is shot exactly at right angles to the faults.

Figure 6.9

a. Stacked, unmigrated time section.

b. Migrated version of a. The section is from the Inner Moray Firth area of the North Sea basin. NBC = Near base Cretaceous, TT = Top Trias.

Seismic data by courtesy of Western Geco



In this example, one of those conditions may not precisely apply because there are three points – C, D and E on the section – where some residual curvature can still be seen at the broken end of a reflection. How should this curvature be interpreted? Is it hyperbolic curvature improperly corrected because the velocity was too low? Is this fault plane not normal to the section? Or is it evidence of local compression within the fault system, caused by some strike-slip element in the fault displacement? Questions like this are typical of the dilemmas raised in 2D seismic interpretation and can only be resolved by a 3D survey. We are never completely content with any seismic section!

Tutorials for Chapter 6

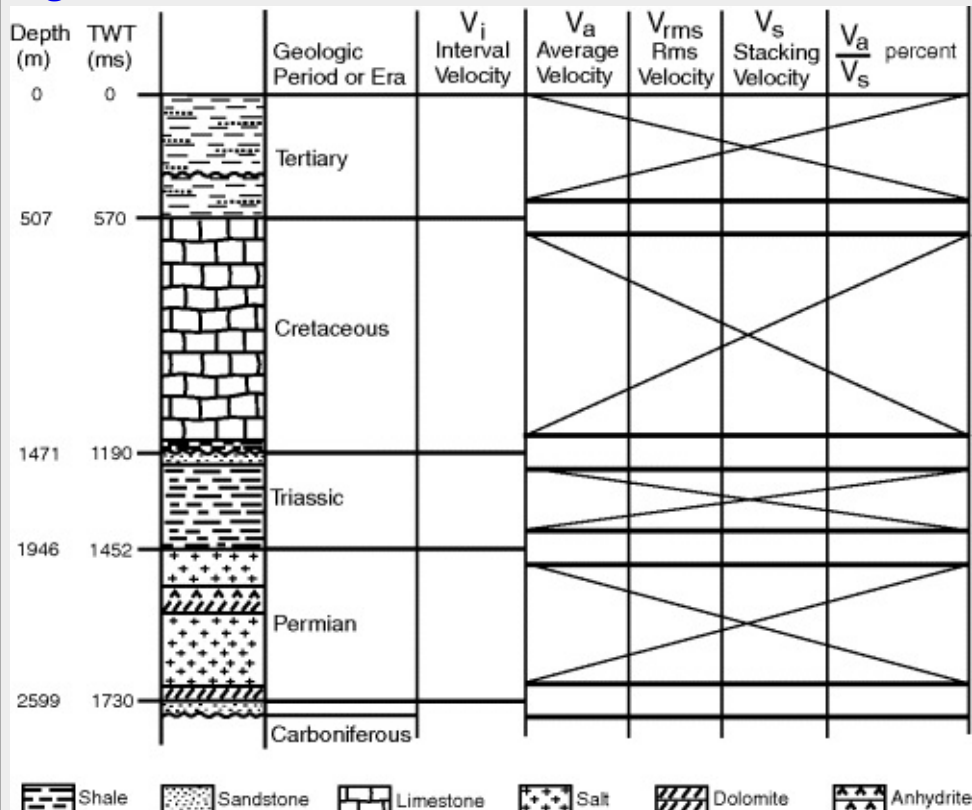
Tutorial 6.1

Purpose: To calculate velocities from a velocity survey and become familiar with typical values

The table in [Figure T6.1.1](#) shows data from a velocity survey in a well in the southern North Sea basin.

1. Calculate the interval velocities for the four named intervals and write them into the table. Do you think the interval velocities tie with lithology as discussed in Chapter 4, Section 4.3?
2. Calculate average velocity down to Top Chalk, Top Trias, Top Permian and Top Carboniferous and enter the values in the appropriate boxes in [Figure T6.1.1](#).
3. Write in V_{rms} for the Top Cretaceous. Calculate V_{rms} for the Top Triassic.
4. That's all for now, until you finish Tutorial 6.3 – then you can write in V_{rms} and V_{stack} for all four interfaces.
5. What is V_a as a percentage of V_{stack} at each interface?

Figure T6.1.1



Tips

- i. Always work in units of metres and seconds – velocities will then be in m/s.
- ii. The times here are two-way reflection times (TWT).

Tutorial 6.2

Purpose: To demonstrate NMO correction, CMP stacking and velocity analysis

1. Start up program *NMOSTAK*.
2. From the menu, select Help/Quick Start and follow out the tutorial, which uses the CMP gather shown in [Figure 6.2](#) as a data set.
3. Do you agree with the value of stacking velocity V_{stack} quoted in the caption of [Figure 6.3](#) ?
4. **NMO Stretch:** Notice that on the raw gather at maximum offset (2,400 m), the two reflections are separated by only about 120 ms, but, after both are corrected for NMO and run horizontally across the panel, the ends are separated by the difference in their zero-offset times (500 ms). Inevitably, the waveform has to be severely stretched at long offsets and cannot be incorporated in the stacked trace, so the stretched parts are simply turned off – the posh word is ‘muted’. This is done at an early stage in processing the seismic data after tests to find out where stretching becomes unacceptable. In *NMOSTAK*, an automatic process does the same job and gives an acceptable stacked trace.
5. **Improvement in signal/noise ratio (S/N):** In the data set in file fig6_2.cmp, only a small amount of random noise has been incorporated in the seismic signal. A much noisier version of the same gather appears in the file named fig6_2N.cmp, where $S/N \approx 1$ for Reflection 2. Open that file in *NMOSTAK* and process it to get the

stacked trace (**Tip:** just plug in the stacking velocities you found in 2 above). On the stacked trace, make a crude estimate of peak signal amplitude (e.g. distance from + peak to – peak in mm) and noise amplitude measured the same way. It helps to turn up Stacked Trace Amplitude in Settings. The ratio of the amplitudes is the signal/noise ratio (S/N). Is S/N for Reflection 2 approximately 4.58, its theoretical value? Why should it be 4.58 anyway? Check Section 6.4 in the text.

Tutorial 6.3

Purpose: To pick stacking velocities from a velocity spectrum

1. The velocity spectrum will be displayed by program *SEG2D*, so take a few minutes to go through the Quick Start tutorial in that program. Leave the program running for the display of other files generated in the tutorial.
2. The velocity spectrum itself is calculated by program *VELSPEC*, and for input we will use the same noisy CMP gather file as in Tutorial 6.2, but in the form of a SEG-Y file (fig6_2N.sgy), so you might like to remind yourself what it looks like by opening it in *SEG2D*. Accept default Display Settings and you will see a wiggle + variable area display of the two reflections. S/N ratio is about 1 for the deeper reflection. Click Go Back on the section window, but leave *SEG2D* running.
3. Start program *VELSPEC* and from the menu choose Help/Quick Start. That short tutorial uses the noisy CMP gather as input data (fig6_2N.sgy). The output file will be named VSfig6_2N.sgy (VS for Velocity Spectrum).
4. When *VELSPEC* is finished, open the file VSfig6_2N.sgy in *SEG2D*, accepting all default display settings. Note the two coloured spots showing semblance highs, one for each reflection. TWT and V_{stack} can be read directly off the screen at the centre of the coloured spots. (**Tip:** double the horizontal scale factor to estimate velocity more accurately). Do you get the same values for V_{stack} as in Tutorial 6.2? Note how powerful semblance is in pulling out coherent signal even in such noisy data.
5. The data set provided on the CD includes a CMP gather generated from the section illustrated in Tutorial 6.1 (file tut6_1.sgy). In *VELSPEC*, open that file and process for a semblance display. Measure the stacking velocity on the three deep reflections, enter the values into the tabulation in Tutorial 6.1 and so complete that tutorial.

Tutorial 6.4

Purpose: To demonstrate suppression of multiples by CMP stacking

You will recall that in Tutorial 5.2, you created a pair of CMP gathers from the geological model BCU1.mod – one without multiples (BCU1.cmp) and one with multiples (BCU1M.cmp). You should also have a list of the V_{rms} values for the seven reflections in the model. You can now stack these gathers in *NMOSTAK* and watch how the multiples behave on stacking.

1. In *NMOSTAK*, open the file BCU1.cmp and in the little Stacking Velocity window, enter the velocity of the first layer (water): 1,500 m/s. Apply Automute (via Settings) and Display. You will see the heavily muted sea-bed reflection at 164 ms. Start up T, V Picks from the menu and proceed down the gather, inserting the appropriate V_{rms} value for each reflection in turn. Don't miss the negative reflection at 1,500 ms. Finally, save the picks and obtain the stacked trace. It should be similar to the zero-offset trace. Print off the final picture.
2. Now open the file BCU1M.cmp and repeat the stacking process, once more printing the final picture.
3. Compare the two stacked traces. Between 0 and 1,400 ms, the multiples have largely self-cancelled except for the first sea-bed multiple at 328 ms. However, within the reservoir interval (1,580–1,800 ms) there is still significant multiple energy, with amplitudes as much as 25 per cent of the reflections that define the top and base of the reservoir. Further processing would be required to reduce these multiples.

Tutorial 6.5

Purpose: To show how multiples appear in a velocity spectrum

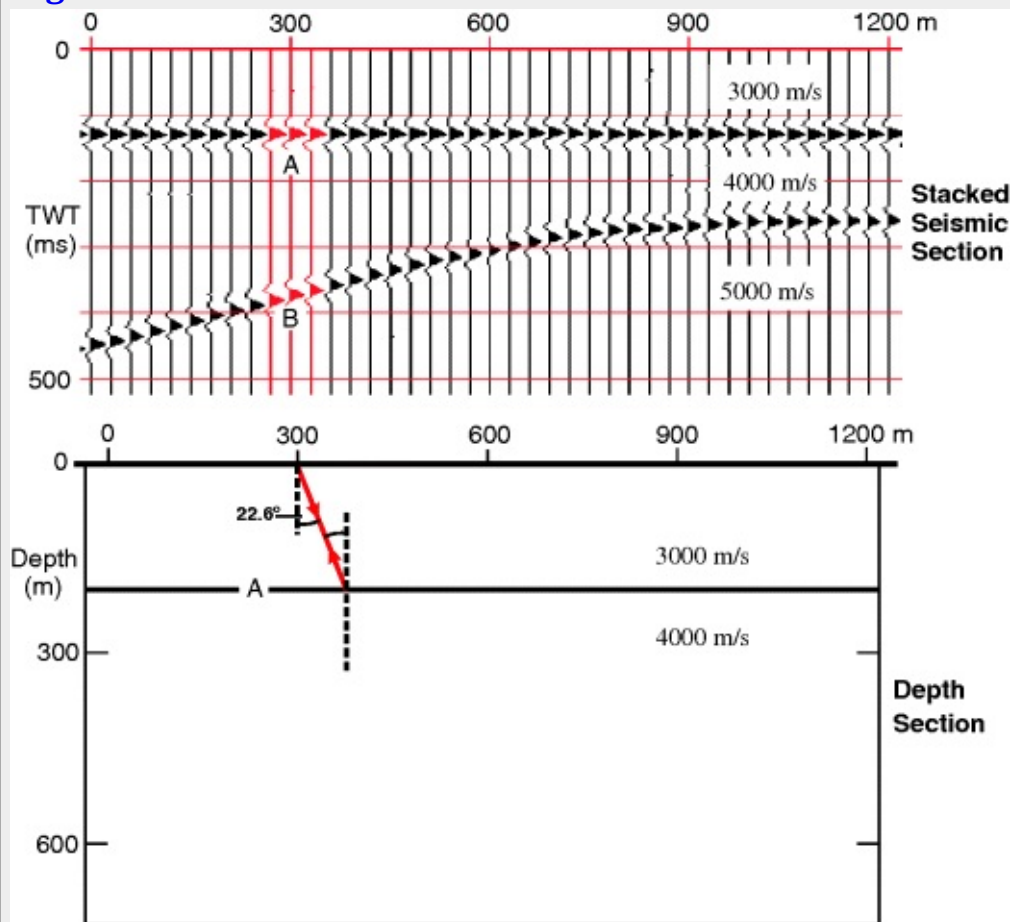
1. In program *VELSPEC*, open file BCU1M.sgy and process it for a semblance spectrum, displaying the spectrum in *SEG2D* as in Tutorial 6.3.
2. Note how the multiples cascade downwards through the plot from their associated primary reflections. The primary velocity picks should always be made on the highest velocities in the spectrum, even if they are not on features of the highest amplitude.

Tutorial 6.6

Purpose: To demonstrate migration by ray-tracing

In [Figure T6.6.1](#), the CMP spacing is 30 m. Reflection A requires no migration because it is flat. Its TWT is 0.130 s, so OWT = 0.065 s and depth = $3000 \times 0.065 = 195$ m. Migration of Reflection B is already partly done as described in Steps 1 and 2 below. You can complete it via Steps 3–5.

Figure T6.6.1



1. On the time section, two quantities have been measured at the 300 m location (centre of red traces):

i. The time of reflection B = 370 ms (call it T_2).

ii. The time gradient (dT/dX) of reflection B = 0.100 s in 13 trace intervals = $(0.100/390)$ s/m

2. Calculate the angle of emergence (α) of the ray at the 300 m surface location from:

$$\sin(\alpha) = (V/2)(dT/dX) = (3000/2)(0.100/390), \text{ so } \alpha = 22.6^\circ$$

In the depth section, the ray has been drawn from the surface point of emergence down to interface A. Measure or calculate the length of the ray travelled so far in layer 1, and so calculate the amount of travel time for that part of the path (call it t_1).

3. From Snell's Law of Refraction, calculate the angle at which the ray leaves the interface A travelling downwards.

4. The time spent by the ray in travelling through the second layer must be $(T_2/2) - t_1$. Calculate the length of the ray and complete drawing it down to the reflection point for Reflection B. Draw a short line there at right angles to the ray to represent a short segment of the reflector at the reflection point.

If all goes well, the (X, Z) coordinates of the reflection point should be (616, 588), so the true location of the reflection point is more than 300 m updip of the initial recorded position.

Chapter 7

Interpretation of Two-Dimensional (2D) Surveys For Structure

Of well ties, it is definitely true that ‘the devil is in the details’.

(White & Hu, 1998)

7.1 Introduction

Although the bulk of today's seismic data is shot in 3D mode, there are plenty of 2D surveys still being shot for reconnaissance purposes. The interpretation of both data sets has obvious similarities, but it is useful to consider 2D interpretation first, if only because the necessity of shooting 3D data becomes clearer as a consequence. Interpretation is carried out on a computer workstation, and even archived data preserved in the form of paper sections can be converted to digital form if required. For the purposes of this book, the interpretation tutorials are done on paper sections. However, for 2D data, the overall sequence of operations is much the same whether working on paper sections or at a computer.

Of the four tutorials at the end of this chapter, the first two take the reader through much of the detail of constructing a synthetic seismogram to match well data to seismic data. Readers who want to go straight to interpretation can skip the first two and go to Tutorials 7.3 and 7.4.

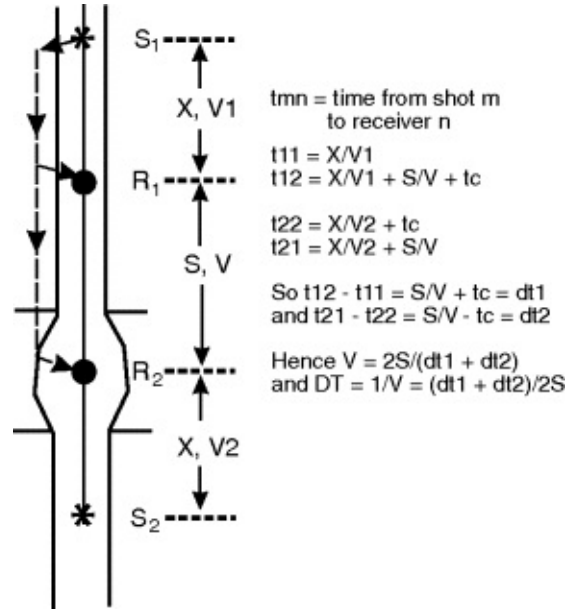
7.2 Linking well Geology to the Seismic Section

There are very few sedimentary basins that are totally unexplored nowadays, so nearly every seismic interpretation will start by making a link between well measurements and the seismic section. The key information required is recorded in the sonic log and in the velocity survey measured at the well.

7.2.1 Sonic Log or Continuous Velocity Log (CVL)

A logging sonde is a device lowered down a borehole on a cable to record the properties of the rock measured in the wall of the hole (Rider, 1996). In the sonic logging sonde ([Figure 7.1](#)), an ultrasonic pulse from the upper transmitter S_1 passes by refraction through the wall of the hole and is received at receiver positions R_1 and R_2 . A pulse from the lower transmitter S_2 is also recorded. The time interval in which the pulse travels between the receiver positions is recorded in each case (transit times dt_1 and dt_2) and the average of the two measurements is calculated to annul errors introduced by caving of the hole or tilting of the sonde. Since the distance between receivers is precisely known (generally 1 m), the velocity of the rock over that interval can be calculated. The measurement is repeated every 15 cm down the hole.

Figure 7.1 Sonic logging. The ultrasonic sources S_1 and S_2 are fired alternately and times to receivers R_1 and R_2 are measured and combined to yield the velocity V across the receiver interval S . The logged quantity DT is the transit time across the receiver interval expressed as microseconds/m. t_c is the extra time caused by cavitation.



The measurements of transit time are displayed as a continuous log scaled in units of $\mu\text{s}/\text{ft}$ or $\mu\text{s}/\text{m}$, but plotted with velocity increasing to the right on the log (check Tutorial 4.4). Because of the correction for caving, the log is often called a Bore Hole Compensated (BHC) sonic log and it is generally labelled DT in the list of logs for a well. It is best to use the version normally presented in the completion or composite log, where the gamma log, caliper log and lithological column are also shown, together with the sonic. Possible errors in the sonic log readings caused by poor hole conditions due to caving of the hole can then be assessed from the caliper log.

The main pitfall is that caving leads to a longer travel path through the drilling mud before the sonic pulse enters the rock, so that the true first arrival of the pulse is not recorded at sufficient strength to trigger the timing device and some later cycle is timed instead (this is called 'cycle-skipping'). A spurious long transit time will be recorded and an erroneous low velocity recorded. If caving has affected, say, 10 m of the hole, it could generate a spurious reflection in a synthetic seismogram. If deemed necessary, a section of good log from the same lithological unit can be spliced in from another well as a substitute for the damaged section, or the interval can be interpolated to remove the error.

7.2.2 Time-depth Plot

If all of the small transit times measured down a well are added together, the sum is a measure of the one-way travel time from top to bottom of the hole. Intermediate travel times are also available to any geological horizon of interest. The summation operation is described by the mathematical term 'integration', and the result is a set of integrated transit times (ITT) for the well. The results are commonly displayed in the form of a plot of one-way time vs. depth.

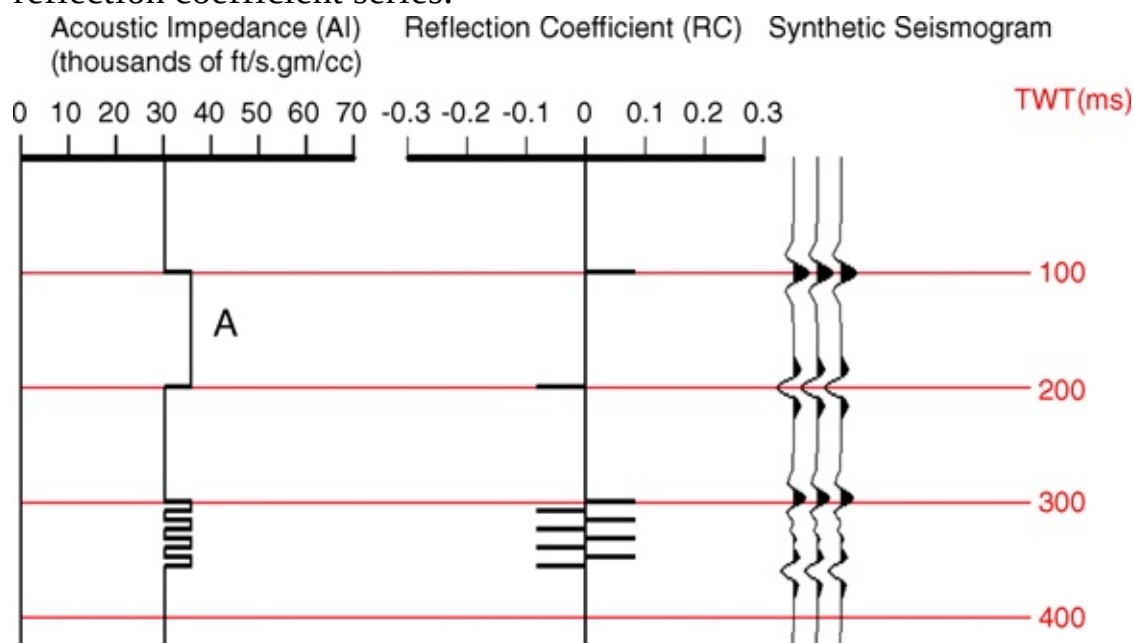
The process of measurement and integration of the transit times may introduce systematic errors into the one-way travel times, and these are assessed by carrying out a velocity survey (check-shot survey) as described in Chapter 6 (Figure 6.1). The travel times so obtained at several points in the well constitute a set of spot checks on the integrated times from the sonic log. The

two sets of times are compared and the integrated times adjusted where necessary, assuming a linear drift between checks. The velocity survey may be expanded to a full vertical seismic profile (VSP), for which a complete seismogram is recorded every 20 m down the well. That topic will be explored further in Part II of this book.

7.2.3 Making the Link: Synthetic Seismogram

The most common method of linking well data to seismic reflections is via generation of a synthetic seismogram. This is a model seismogram obtained by calculating a sequence of reflection coefficients down the well, from the sonic and density logs, and substituting a seismic wavelet for each reflection coefficient. The amplitude of the wavelet is made proportional to the reflection coefficient and its polarity is shown in accord with the sign of the reflection coefficient (Figure 7.2). It is essential to have the acoustic impedance (AI) log and reflection coefficient (RC) series plotted together with the synthetic seismogram, so that the detail of the stratigraphy can be correlated exactly with the seismic waveform. An increase in AI at the top of unit A (Figure 7.2) corresponds to a positive reflection coefficient of about 0.08 and gives a reflection of positive polarity (black peak – see Chapter 2, Section 2.6). Conversely, the base of unit A, where the AI drops, is marked by a negative reflection. Where the lithology is unchanging (in this idealized model), the AI is uniform and RC values are zero, so no reflections are generated. In Tutorial 7.1 you will deal with real log data and see that it is rather different from this.

Figure 7.2 Presentation of a synthetic seismogram with associated logs of acoustic impedance and reflection coefficient series.



The synthetic seismogram can be prepared to the same scale as the seismic data and overlaid on the section, whether on paper or computer screen, in order to correlate changes in geology directly with the occurrence of reflections on the seismic section (Tutorial 7.2). Needless to say, this procedure has its fair share of pitfalls, and more detail on the background and limitations of the synthetic seismogram is given in Chapter 10, Section 10.5.

Linari (2004) reports an alternative approach where the sonic log, carefully tied to check-shot times, is superimposed on a special version of the seismic section, where the reflections have been converted to show the velocity layering of the earth. Thus the well velocities of the sonic log can be tied directly to the seismic velocities of the section.

Let's ignore pitfalls for the moment; creating a synthetic seismogram is quite straightforward. Use program *SYNTH* to make a synthetic seismogram from some sonic log data in Tutorial 7.1.

7.3 Choosing Reflections to Pick

The approach to choosing which reflections to pick will vary according to the stage that the exploration programme has reached. In the rare event of there being no wells in the sedimentary basin, several prominent reflections should be chosen which delimit the top and base of the principal sedimentary sequences, defined according to the criteria of seismic stratigraphy (see Part II of this book). A tentative identification of the sedimentary units may be possible on the basis of seismic characteristics such as: interval velocity; number, frequency content and configuration of internal reflections; gross form of the unit; stratigraphic history as displayed by unconformities; and onlap and offlap relationships. All can be viewed from a background experience of adjacent or similar areas.

As a simple example, the Zechstein salt layer is readily identifiable on seismic sections of the southern North Sea basin on account of its pinch and swell geometry, the presence of internal diffractions or short reflections from broken anhydrite layers and its high interval velocity of about 4,500 m/s. Choosing the principal sequences in this way should ensure that they will also be the principal velocity units, which will assist the process of depth conversion later on. This should be checked via the displays of interval velocity.

Where well data is available, it is generally straightforward to pick out the main lithostratigraphical units of interest, which should also correspond to the main velocity units. Key marker reflections can then be identified by comparing a synthetic seismogram with the seismic section, as demonstrated in Tutorial 7.2.

This is the best time to carry out Tutorial 7.2, in which you can identify the three reflections which you will follow out across the seismic line of Tutorial 7.3.

7.4 Picking Reflections

On paper sections, the chosen reflections are followed out across the section by eye and marked in with (erasable!) coloured pencil (Tutorial 7.3). The human eye-brain combination is extremely good at seeing linearly connected patterns; evolution has clearly meant us to be seismic interpreters! Looking along the section at an oblique angle is remarkably effective in foreshortening the reflection and picking it out from noise. On the screen, the same effect can be achieved by squashing the display horizontally.

Essentially, the same method of interpretation is used on the screen of a workstation, but now the interpreter can take advantage of the automatic picking and marking processes provided by the software. However, the computerized picking process will fail if the data is poor or at a fault, or if the reflection divides into two. In such cases, the interpreter will have to step in and make the best pick manually before allowing auto-picking to carry on.

Continuity of the reflection event is the property used to carry it onwards. Where gaps occur due to poor data or faults, correlation of reflection patterns or the character of the event must be used

to carry the pick across the discontinuity. The 'character' may be some combination of wavelet amplitude, shape and frequency content that makes the reflection (or some sequence of reflections) recognizably different from other events in that part of the section. Across major breaks or zones of poor data, it is often a good plan to copy a window of data on one side of the fault and then superimpose it on the section on the other side, so directly comparing reflection patterns and seeking out similar sequences (Tutorial 7.3). All of the characteristics of seismic sequences as defined in the context of seismic stratigraphy may be brought into consideration in making correlations.

Where seismic lines intersect and paper sections are being interpreted, it is best directly to compare and transfer reflections to the new line by folding one section at the line of intersection and laying it on the other at the crossing point. Two sections can be juxtaposed in a similar way on the workstation screen. Care must be taken to ensure that the same event is being followed around grids of intersecting lines by carefully checking times at line intersections, because it is not difficult to miss-pick by a cycle. Times at intersections should agree to ± 2 ms or, in poor areas, to ± 10 ms.

It is important to realize that 2D migrated lines will only tie at their intersection if dips are gentle. If dips are appreciably large, then reflections on the dip sections will have been relocated in the up-dip direction, but those on the strike sections will be unaffected by migration and the two will no longer exactly tie at the intersection. Unmigrated lines will always tie exactly at their intersection.

Complications arise at faults, especially if the fault has been active during deposition so that the geological section changes drastically from one side of the fault to the other. In such a case, it may not be possible to recognize the same event across the fault on a dip line. The solution may be to loop around and follow it on a strike line parallel to the fault, until the fault dies out enough to make the correlation on another dip section, and then come back to the first line along another strike line. If only part of the stratigraphy is affected by the fault, a good technique is to make a copy of the interpreted side and lay it over the section on the uninterpreted side, looking for good correlation of some key reflection sequence. This is made rapid and easy on a workstation screen and the basic idea is demonstrated in Tutorial 7.3.

In 2D data, fault hyperbolae will only be properly collapsed if the line is at right angles to the fault; otherwise, a partially migrated diffraction hyperbola will droop off the ends of the broken reflection. This may result in reflections that slightly overlap, and the unaware interpreter may then mistakenly interpret a normal fault as a thrust. The fault plane is accurately located by joining the points where the hyperbola starts to bend down.

Another major difficulty occurs where reflections divide or merge laterally. Geological judgement has to be exercised to decide whether you are looking at an unconformity with erosional cut-off, or an expression of lateral sedimentary variation such as onlap. In all cases, it is extremely helpful to follow the reflection around a grid square of lines to check that it ties back to the starting point.

At all times, the interpreter has to be self-critical and aware of the many pitfalls in the data – for example, are multiples a problem on part of the sections? However, the biggest problem with 2D seismic interpretation is often the presence of sideswipe. This is explained in the following sections.

7.5 Sideswipe

In most of the diagrams drawn to represent the seismic reflection process, we have assumed that the line is shot parallel to dip (at right angles to strike), so that there is no component of dip across the plane of the section and all raypaths lie in the plane of the section. Now this is often the case, because the survey will be planned like this in the first place, but more commonly the structure will not have 2D elongation along a dominant strike direction, or the lines may have been shot obliquely to strike so that cross-dip is present. Over a cross-dipping reflection, stacking still works perfectly well, but the CMP raypaths will lie in a plane oblique to the vertical section and the common reflection point will lie off to one side of the line. If a vertical well were to be drilled on the seismic line, no interface would be encountered at the depth calculated for the reflection. Such reflections which come obliquely upwards from the side into the line of detectors are called sideswipe.

7.6 A Sideswipe Example: Fault Diffractions

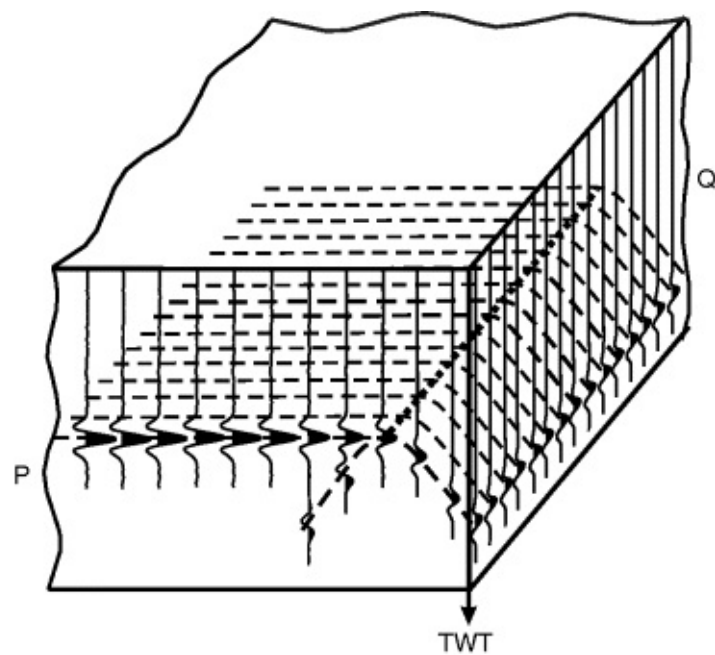
In badly faulted areas, a particular type of sideswipe occurs: diffraction hyperbolae. These may constitute a serious sideswipe problem, and as much as 50 per cent of the events seen on the lower parts of strike sections may be sideswipe of this type.

Suppose we look at many sections shot close together at right angles to a fault, as in [Figure 7.3](#). In a time-section 'universe', the fault diffraction event takes the shape of an elongated hyperbolic surface like the roof of a house, which is attached to the broken edge of the reflection along the crest of the roof ridge. A stacked section shot at right angles to the fault (section P) shows the diffraction hyperbola with its proper curvature. A stacked section shot parallel to the fault on the downthrow side (section Q) will only show a rather faint horizontal reflection where the tails of the hyperbolae intersect it, well below the TWT of the true reflection on section A. This is a perfect example of sideswipe. Any section shot obliquely to the fault will show an oblique section through the hyperbolic surface, i.e. a flattened version of the hyperbola. The true hyperbola will fit a theoretical curve calculated with the true average velocity (V) down to its summit time, but the flattened hyperbola will fit a curve calculated with a false high value of velocity (V'). You can show that the angle θ between the seismic line and the fault is given by:

$$(7.1) \cos \theta = V/V'$$

This can be very helpful in deciding on fault trends in a 2D survey.

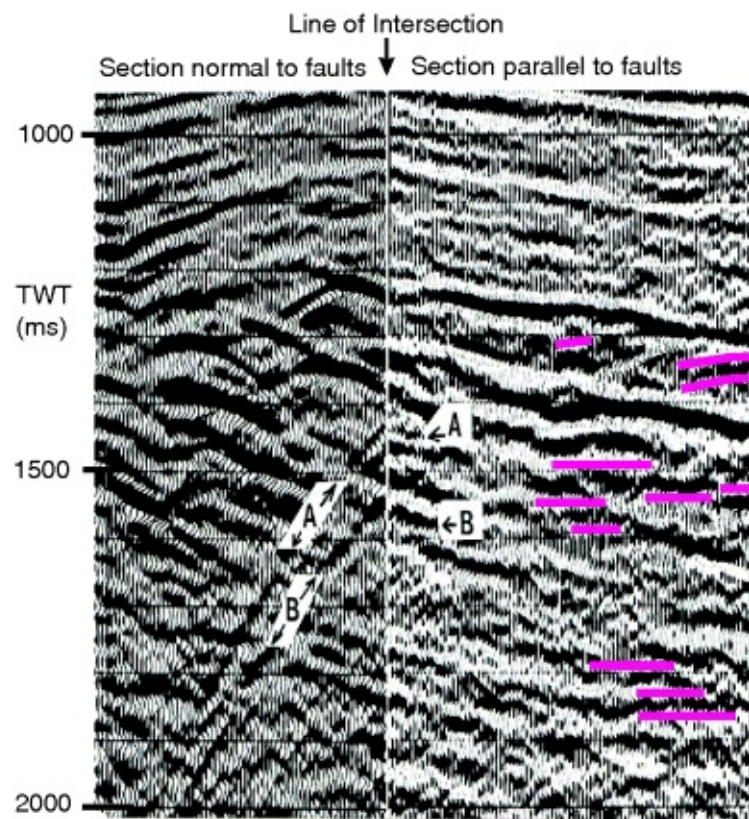
Figure 7.3 An example of sideswipe: a three-dimensional view of closely packed, unmigrated seismic sections shot perpendicular to the faulted edge of a reflector. Section P shows the full curvature of the fault hyperbola; section Q shows a flat reflector where the tails of the fault hyperbolae intersect it as sideswipe.



It is important to realize that the flat reflection in section Q ([Figure 7.3](#)) will be unchanged in its position if the stacked section is processed through 2D migration (remember, only dipping reflections are shifted in the plane of the section by migration). If a vertical well were drilled somewhere along section Q, it would not intersect a reflecting interface in the subsurface at the depth indicated by the TWT of the horizontal reflection.

The importance of such sideswipe in real data is illustrated in [Figure 7.4](#), which shows a section at right angles to a fault zone on the left hand side and a section parallel to the faulting on the right. The two sections are joined along the line of intersection in the same way as sections P and Q are joined in [Figure 7.3](#). Fault diffraction hyperbolae, labelled A and B on the dip section, can be readily linked to sub-horizontal events on the strike section that break the continuity of the genuine reflections there, which dip gently to the right as clearly shown in the upper, unfaulted part of the section. Other likely examples of sideswipe are marked in red.

Figure 7.4 Sideswipe from fault diffractions. Fault hyperbolae A and B appear on the left section, showing full curvature, and can be tied into sub-horizontal sideswipe events on the right section which are at variance with geological dip. Seismic data by courtesy of Western Geco



If a seismic stratigraphic interpretation were carried out, such events might be misinterpreted in places as prograding bedforms in the sedimentary sequence, for example between 1.3 and 1.4 s. It is probable that about 50 per cent of the visible seismic events in the lower part of this section is sideswipe. One of the most important consequences of 3D seismic surveying is that sideswipe of this sort is removed from the section by the process of 3D migration. However, the interpreter of 2D data should always be aware of its possible presence.

The rest of this chapter is about structural interpretation of reflection data and is best studied whilst periodically dipping into Tutorial 7.4, where you can interpret seismic data from the West Sole Field in the southern North Sea, all the way from measuring TWT to drawing a contoured depth map of the Rotliegend gas reservoir – and most of the calculations are already done!

7.7 Preparing Structure Maps in TWT

When the picking and marking out of reflections on the time section is complete, two-way travel times are measured at suitable intervals along the line and plotted on a base map – one map for each horizon of interest. In the workstation environment, the measurement of TWT and its plotting on base maps is done automatically. For paper sections, times can be measured on a digitizing table and recorded in a computer file, from which they may be plotted by computer on shot-point location maps. Times are estimated to the nearest ms.

Fault positions are also plotted and, if the fault plane dips appreciably and the throw is large, the width of the fault plane as seen in plan view should be displayed on the map. Faults are initially marked (as short lines, tick on the downthrow side) at right angles to the seismic line, since the actual angle at which they cross is not known, unless unmigrated data is available and a good fault hyperbola is visible.

To complete the structural map of a horizon, the first step is to connect up the faults with geometries that make the best structural sense. This is often one of the most difficult stages of a

2D interpretation, yet one of the most important, since the fault pattern will control the subsequent contouring of structures and thereby the estimation of structural closure and possible hydrocarbon trapping. The interpreter has to incorporate all of the background geological information on the likely structure that s/he can glean from personal experience, from interpretations of other surveys in related areas and from the knowledge base of structural geology.

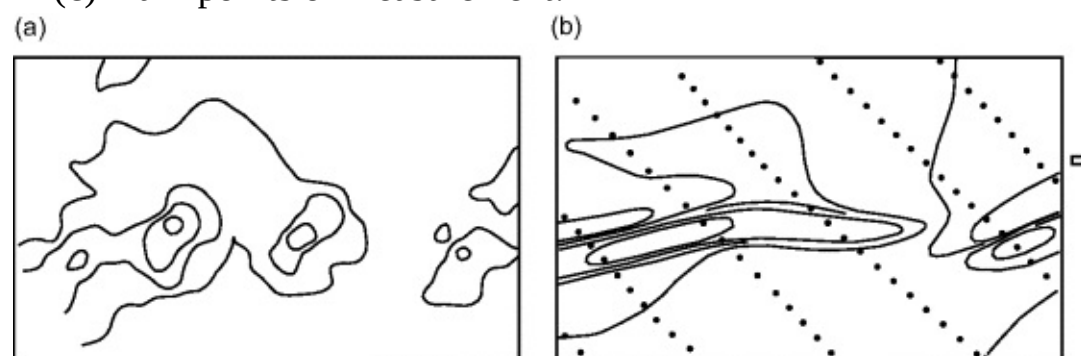
It is often helpful to window the horizon of interest on successive sections across the structure to bring the faulted zone of interest into close juxtaposition from line to line in one display and so help the process of connection (see [Figure T7.4.5](#) in Tutorial 7.4). Strike-slip faults are particularly difficult to interpret, because unrelated sedimentary sequences may be juxtaposed across them (Harding, 1985).

Finally, to display the structure of the horizon, contours of equal travel time (isochrons) are drawn on each of the surfaces that have been picked and timed. Each faulted block can be treated as a separate entity with its own set of contours, which will terminate on the bounding faults. With 2D data, drawing contours is a considerable art, as Tucker (1988) has pointed out. Major decisions about an exploration programme will hinge on the structure displayed on the contour map, so it is essential that the interpreter does some of it by hand, even if this means passing the bulk of the task on to someone else, e.g. a technical assistant or the person who wrote the contouring program on the computer system.

For 3D seismic surveys, where data points may be on a 12.5 m grid, computer contouring works well. For 2D surveys, a computer-contoured map may give an unsatisfactory rendering of the structure, depending on how big the structure is compared to line spacing. It is unlikely that useful auxiliary information like structural trends, which may be known to an interpreter, can be handled by the computer algorithm.

[Figure 7.5](#) is an example of a geophysical survey with rapid variation of the mapped quantity along widely spaced survey lines. In [Figure 7.5a](#), the computer program has simply connected high values on one line of data to the nearest high values on adjacent lines, giving a series of unconnected highs. In this case, however, float mapping and the shape of the magnetic anomaly strongly indicate that the cause is a basic dyke, so the interpreter is justified in manually connecting up the highs into an extensive linear feature that runs oblique to the survey lines ([Figure 7.5b](#)).

Figure 7.5 Portion of a ground magnetic survey contoured by computer (a) and by hand.(b) Dots in (c) mark points of measurement.



In contouring by hand, the interpreter should regard the surface being dealt with as a topographic surface right from the start, recognizing that the smaller TWT values indicate structural highs. It is sometimes helpful to start by quickly labelling some of the more prominent

highs and lows (e.g. with H and L), to get an early feel for what the surface is doing, and then to start drawing contours around a high at the intersection of two lines.

The contours are spaced by linear interpolation between times measured on the seismic lines and should be connected between the lines by as straight a path as possible, keeping the contour spacing constant or only slowly changing across the map between the seismic lines. Most people draw contours which wiggle around too much initially, but it is a good tactic to let this happen in a first pass and then come back over the map, endeavouring to straighten them out by asking to what extent each deviation is really required by the data. The drawing of fault lines and time contours is likely to contain major ambiguities, and the final picture may be one of several possible interpretations. The simplest interpretation that agrees with what is known of the geological structure is always to be preferred.

Time maps are often used as the first stage in the presentation of the interpretation of a seismic survey. If based on unmigrated stacked data, they are immutable in the sense that if the survey were re-shot in a hundred years time, the same travel times would be observed at the same surface locations. Time-migrated data is subject to more uncertainty, because the relocation of the data depends on the velocity chosen for the migration. Structure maps scaled in depth are the final goal of the interpretation, but they are different in kind from time maps because they have to pass through a further level of uncertainty – namely, our uncertain knowledge of the velocity structure of the earth.

In addition to maps showing structural surfaces, it may be useful for some purposes to prepare an isochron map, in which time intervals between the top and bottom of a sedimentary unit are plotted on the base map and contours of equal thickness in time are drawn. For example, where the exploration target is a sand unit pinching out up-dip, the feather-edge beyond which the unit does not exist is thus readily mapped out.

7.8 Time to Depth Conversion

Although time maps have the advantage of speedy preparation for a first look at structure, and are essential as a presentation of the raw data of a seismic survey, they have to be converted to depth for a proper assessment of possible hydrocarbon traps. This is often one of the most difficult parts of seismic interpretation and it is done by the optimum method, limited by time and cost, that will give usable results for the job in hand.

In principle, it is an easy calculation:

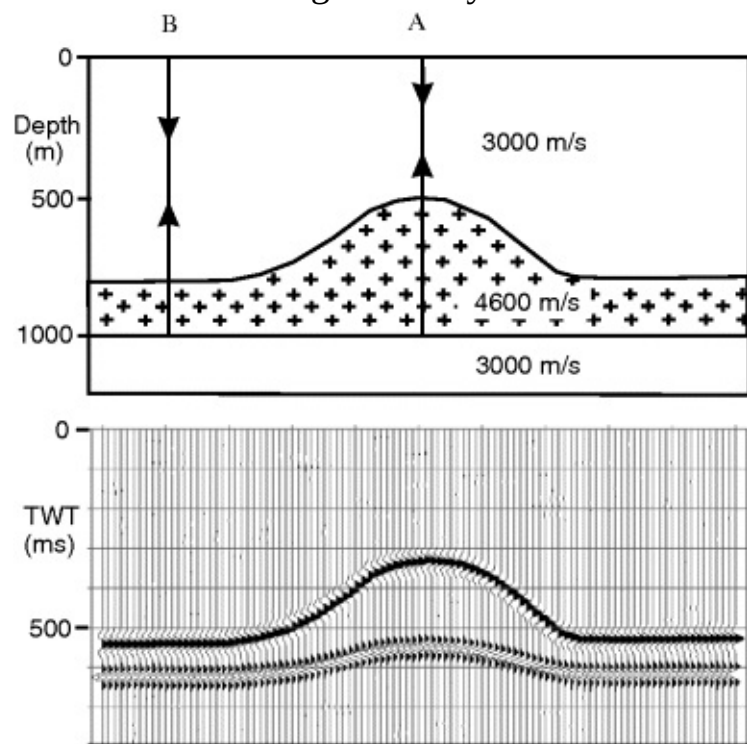
$$\text{depth} = V(T/2)$$

where T = two-way reflection time and V = a suitable velocity of propagation.

However, there is a major problem to be overcome. Seismic velocity from surface to target horizon is not constant; it generally increases by about a factor of two from top to bottom of the sedimentary column and it may well show rapid vertical and lateral variation at any level.

This point is illustrated in [Figure 7.6](#). Two-way travel times to a flat reflector under the salt will be less for a raypath through the centre of the salt swell than on the flanks because of the high velocity of the salt, so that a spurious structural high will appear under the salt, a phenomenon known as velocity 'pull-up'. A low-velocity overburden will cause the opposite effect – velocity 'push-down' – so that a genuine structural high may be converted to a flat horizon in terms of time.

Figure 7.6 Velocity pull-up under a salt swell. TWT to the flat base of the salt is less at A than at B because of the high velocity of the salt.



To overcome this problem requires that we have some way of describing the variation in seismic velocity in the subsurface, i.e. a velocity model of the earth. We have already considered one such model in Chapter 6 – the layered-earth model, in which the primary control on velocity is lithology. However, a secondary control within a layer of uniform lithology will be the depth to which it is buried. The deeper it is, the more it is compacted, and the greater is the likelihood of diagenetic effects like the filling of pore spaces with quartz or calcite. Both effects will strengthen the rock and raise its seismic velocity.

In this section, we will first look at some of the ways in which variation of velocity with depth can be handled, then we will consider some examples of depth conversion to illustrate different strategies. The discussion is based on the depth conversion of surveys where the structures are simple and the lateral variation in velocities across an area are not extreme. For 3D surveys with complex overburden (Gulf of Mexico sub-salt targets, etc.), depth conversion is more difficult. Time migration becomes inadequate and is performed only as an initial step, a complex velocity model is constructed and depth migration is carried out to obtain the final image of the structure (see Chapter 8).

7.8.1 Velocity as an Analytical Function of Depth

In many sedimentary basins, especially where the succession is dominated by alternations of sandstone and mudstone, velocity is found to be some relatively simple function of depth that can be expressed analytically (Marsden *et al.*, 1995).

A linear function of velocity with depth has often been used:

$$(7.2) \quad V(z) = V_0 + kz$$

where

$$V(z) = \text{velocity at depth } z$$

V_0 = velocity at the surface

k = velocity gradient with depth (k is constant for a given sedimentary sequence)

For example, typical values for the Tertiary of the North Sea are $V_0 = 1,700$ m/s and $k = 0.4$ m/s per m depth. So at a depth of 1,000 m, the velocity would be:

$$V(1000) = 1700 + 400 = 2100 \text{ m/s}$$

Note that we are discussing a spot velocity at a particular depth, not a velocity measured over an interval or an average velocity down from the surface.

The linear variation of velocity with depth is important and has a long history of usage in depth conversion in the seismic reflection technique. This is partly because both raypaths and wavefronts in the medium can be represented by simple circular arcs. A straightforward method of hand migration employing wavefront charts was generally based on this velocity model. The model may be combined with the 'layer cake' model, so that some or all of the layers are regarded as having a velocity gradient through them, rather than a constant velocity.

Kaufman (1953) lists many more velocity functions and formulae for calculating depth from reflection time. For example, for the linear increase in velocity with depth given above, the average velocity as a function of TWT is:

$$(7.3) V_a = V_0[\exp(kT/2) - 1]/(kT/2)$$

where T = TWT to the reflection whose depth is being calculated.

7.8.2 Time-depth Conversion Strategies

When the geological section contains no major lithological changes and has had a simple history of burial, time can readily be converted to depth by multiplying by the average velocity V_a down to each reflector:

$$D = V_a(T/2)$$

where T = TWT.

This method has the advantage that it can be easily computerized to handle large volumes of data. V_a may be calculated from interval velocities and well data and its lateral variation contoured across an area and combined with TWT at each surface location to produce a depth. The depths are then contoured to produce a structure map. The method is fast, and for that reason is used in Tutorial 7.4.

When the velocity can be modelled as a function of depth (as in [equation \(7.2\)](#)), a new V_a can be calculated (as in [equation \(7.3\)](#)) for each TWT prior to depth conversion. If control is good from wells and stacking velocities, it may be possible to contour k and V_0 in [equation \(7.2\)](#) across the area, so that at each location new values can be interpolated from the contours and used in the formula for V_a .

Very often the 'layer cake' approach is used, where the thickness of each interval between prominent reflections is calculated using the appropriate interval velocity and the observed reflection times from top and base. So, if TWT to the base of successive layers descending from the surface is $T_1, T_2, T_3 \dots$ etc., and the layer velocities are $V_1, V_2, V_3 \dots$ etc., the depth to the base of the 3rd layer is:

$$(7.4) D_3 = [(V_1 T_1 + V_2(T_2 - T_1) + V_3(T_3 - T_2)]/2$$

Depths may then be plotted onto base maps, faults inserted and contoured structure maps prepared. Extensive tracts of most sedimentary basins fall into this category and can be treated in a fairly straightforward manner. The error in the depths so calculated should be around two per cent with sparse well control (see Tutorial 7.4).

If sufficient well data is available, it may be possible to introduce more sophistication into the layer cake depth calculation, such as the use of an analytical velocity-depth function for a layer (e.g. the Tertiary in the North Sea) or a layer velocity which varies with the TWT to the middle of the layer. Much of the early reconnaissance data obtained from the southern North Sea basin was converted to depth in this way (Rockwell, 1967).

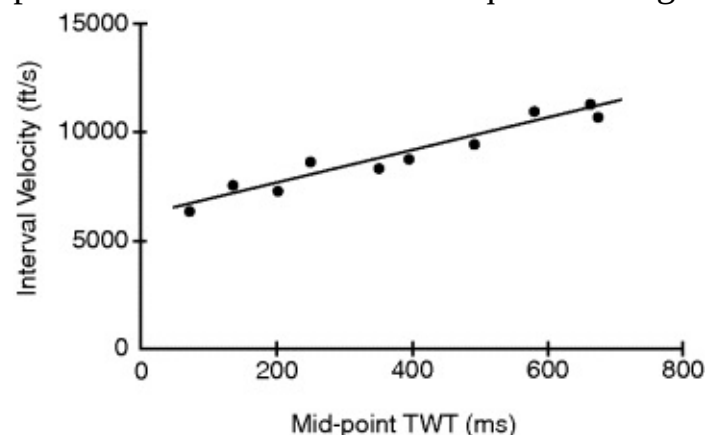
7.9 Examples of Time-Depth Conversion

Every conversion from time to depth is a one-off process to some extent, although based on the models described above. There is often a trade-off between degree of sophistication, time or expense involved and the required accuracy of the result. The following examples show some of the variations possible.

7.9.1 Southern North Sea: Rotliegend Sandstone Target

In this environment, several wells will typically be available and a number of intermediate layers will be picked above the target horizon, the Rotliegend sandstone. For each layer, a graph of interval velocity vs. TWT to the middle of the interval can be plotted from the well velocity surveys. [Figure 7.7](#) shows the graph for a Mesozoic interval measured at ten wells with a best least-squares line fitted. As might be expected, interval velocity increases as the layer is buried more deeply.

[Figure 7.7](#) Interval velocity of a geological formation measured in ten wells plotted against mid-point TWT with a best least-squares straight line fitted.



Starting with time-migrated data, times for each horizon are transferred from the 3D seismic interpretation software to a mapping package, where they are averaged on a regular grid over the survey area. Layer thicknesses are calculated from the mid-time values using an interval velocity calculated from the best-fit relationship ([Figure 7.7](#)). Finally, the thicknesses are summed to arrive at a depth to the Rotliegend sandstone. As explained in Chapter 8, image-ray corrections might have to be applied to fault locations in this situation to refine the structure.

7.9.2 Central North Sea: Paleocene Sands Target

Millar (1998) used a layer cake approach based on well control, but in a different way. The aim of the study was to assess the effect of variations of lithology on velocity within five layers of the Tertiary succession overlying possibly prospective sands of Paleocene age. The lateral variation of interval velocity was treated in a different way for each layer. For example, the variation in the Eocene layer was linked to a seismic attribute calculated for the Eocene interval from the 3D seismic data set. The value of the attribute at the well locations was found to have a linear variation against interval velocity measured at the wells. Thus, the attribute could be used to assess the variation in velocity between the wells all over the area of investigation at suitably closely spaced grid points.

A minor problem arises: the velocity at a well position calculated from the best fit line will not be quite the same as the velocity actually observed at the well, unless the line happens to run *exactly* through the well location. The wells can be reconciled to the calculated data by plotting the differences between well velocity and calculated velocity at the well locations and then drawing a contour map of velocity differences all across the area. Now at every grid point, a correction can be picked off the contour map of differences and applied to the calculated velocity value, so that grid values and well values are reconciled. The implicit rationale behind such a procedure is that the differences in velocity change slowly and smoothly across the area. We do not know this for sure, but we carry out the procedure anyway because it is the simplest scenario.

7.9.3 West Sole Field, southern North Sea

Tutorial 7.4 provides an opportunity of taking an interpretation right through from timing reflections to depth conversion. For this tutorial, it is assumed that there is no well control in the immediate neighbourhood of the prospect. Well data from similar stratigraphic successions elsewhere in the basin is available, as well as good quality velocity analyses. Depth conversion of times to the target Rotliegend Sandstone is carried out by using average velocity values, interpolated from a contoured map of average velocity at each point of time measurement.

The map is established from fairly sparse control points at which average velocity is calculated from the interval velocities of three layers: Jurassic and Triassic siliciclastic sediments and Zechstein evaporites. The first two layers are assigned interval velocities calculated from velocity analyses posted on the sections. The evaporite layer varies greatly in thickness according to the thickness of salt within it, but its interval velocity can be described as a function of the TWT interval through the layer and the (fixed) velocities of halite and dolomite. The depth subsequently measured at well locations agrees with the seismic depth to about two per cent – a good result considering that no well velocities were used. In this example, elements of layer cake and lithological control of velocity are combined to provide average velocities for depth conversion.

Tutorials for Chapter 7

Tutorial 7.1

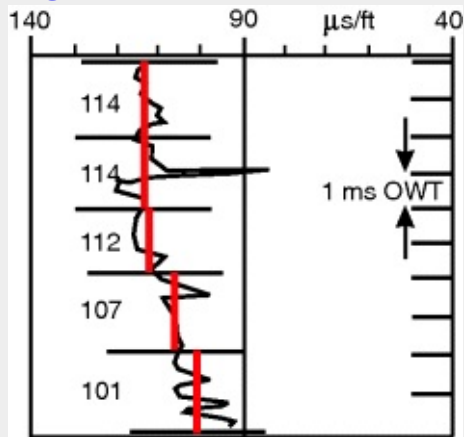
Purpose: To construct a synthetic seismogram from well-log data.

Time scales and sampling

The seismogram time scale is Two-Way Time (TWT), but the sonic log scale is One-Way Time (OWT) and the ticks

marking integrated transit-time are at 1 ms intervals of OWT. If a thin stratum is only 5 ms thick in OWT, the reflections from the top and bottom will be separated by 10 ms in TWT. It follows that if the reflection seismogram is sampled at 4 ms TWT, we must sample the sonic log at 2 ms OWT to maintain the same density of information ([Figure T7.1.1](#)).

Figure T7.1.1



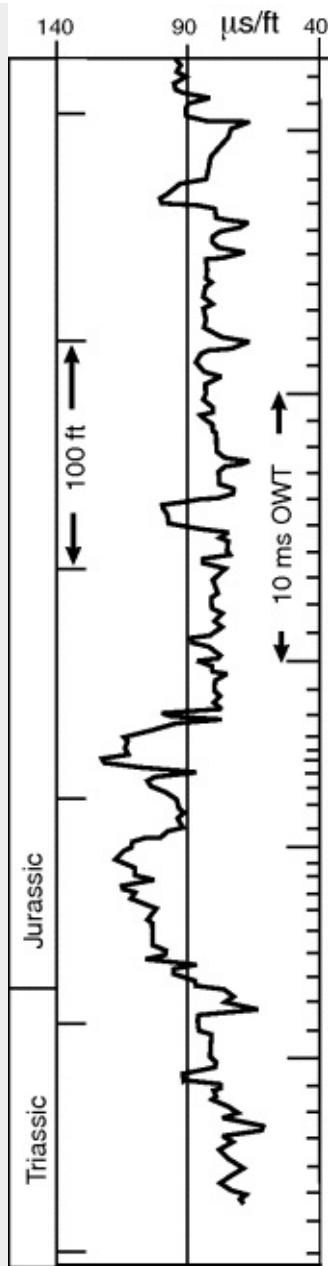
Data required

Two pieces of data are required – a digitized sonic log and a wavelet. The wavelet is easy – using program *FOURSYN*, make up a Ricker wavelet with centre frequency 20 Hz and phase shift of -45° , sampled at 4 ms. The well log we will use is only available as a paper chart recording, but it has been mostly digitized. You will complete the digitization as the first step in the tutorial. No density log is available, but Gardner's Law will be used to estimate densities from the velocities recorded in the sonic log.

Digitizing the sonic log

1. A portion of sonic log from well 12/28–3 appears in [Figure T7.1.2](#). On its right margin is a scale of ticks marking 1 ms intervals of OWT. Like all well logs, the vertical scale is in regular increments of depth. Thus, where the velocity of the rocks is low, the time lines crowd together, and where the velocity is high, they open apart.

Figure T7.1.2



On the log, draw short horizontal lines to divide it up into 2 ms intervals (see example in [Figure T7.1.1](#)). Within each interval, draw a short vertical line through the *average position of the log trace*, but ignoring any spikes.

2. Given the transit time scale across the top of the log, write in the transit time indicated by the vertical lines in step 1 above (check illustrated example). The log is scaled so 1 cm = 40 $\mu\text{s}/\text{ft}$. You should end up with 24 samples.

3. Using a suitable word processor, open the file 12-28-3A.sdt that you will find on the CD. Type in your readings of transit time at the end of the list. After each reading, type a space and a zero. If a density log were available, a density value could be substituted for the zero.

4. Scroll up to the top of the file and alter the fourth line to read 171, the new number of data points listed. Save the file as 12-28-3B.sdt and *make sure it is saved as a plain text file*. You have now completed the digitization of the well-log data.

Nowadays, all well logs are recorded digitally and will load into computer systems for generation of synthetic seismograms. However, although thousands of old well logs are still in analogue form, don't let that stop you from using them for synthetic seismograms. Digitization services are available from contractors, but for a one-off exercise you could digitize by hand or use a digitizing table if available.

Creating and displaying the synthetic seismogram

5. Run program *SYNTH*, open the digital well log file 12-28-3B.sdt and the 20 Hz Ricker wavelet, accept the default parameters and draw the display. Click on OK for the four messages that appear.

6. Inspecting the screen display, you will notice that the real earth is much more complicated than the simple model of [Figure 7.2](#). In this typical clastic sedimentary sequence, there are scarcely any places in the AI log where AI is constant for even a few readings, so the RC sequence is complex. Each spike in the RC sequence

represents a different reflection and each therefore generates a full wavelet in the final seismogram. The wavelets overlap and sum together to give the final seismic waveform, but it is often possible to see the effect of a particularly large RC (or a group of smaller RCs) on the final seismogram. For example, the step in AI at about 1,360 ms TWT gives two positive RC spikes which locally dominate the RC series and create an isolated wavelet fairly similar to the input Ricker wavelet.

7. Key stratigraphic markers in this data are the trough at 970 ms (base Cretaceous is at 1,000 ms), the aforementioned peak at 1,360 ms (near-Top Mid-Jurassic) and the peak at 1,470 ms (Top Trias).

8. Finally, to compare the synthetic seismogram with a seismic section (in Tutorial 7.2) we need to make an image now of one trace of the synthetic. In *SYNTH*, click on Parameters, set Trace Interval to 10, No. of Traces to 1, Trace Colour to Red, and re-draw. Click on OK for the four messages that appear. Press the 'Print Screen' key, which saves the image into the *Windows* Clipboard so that it can easily be pasted into *Windows Paint* or some other graphics-handling program. The seismogram can now be isolated and saved as a *Windows* bitmap image (read the file *paint.doc* on the CD to see how to do that in *Paint*).

Tutorial 7.2

Purpose: To compare a synthetic seismogram with seismic data at a well location

Before we start this tutorial, the synthetic seismogram has to be inserted into the seismic section observed at the well location in order to identify the marker reflections and start the process of picking them across the area of interest. This would normally be done using workstation software, but here we can easily do it by taking the image of the synthetic seismogram from Tutorial 7.1 and superimposing it on an image of the seismic section using the program *IMAGES* supplied on the CD. First, take a few moments to run the Quickstart Tutorial in *IMAGES* to get familiar with its basic controls.

1. Start program *IMAGES*, and for Image 1 open file *GMF31start.bmp* supplied on the CD. The location of well 12/28-3 is marked on the section. Open the image of the synthetic seismogram from Tutorial 7.1 as Image 2: it will appear in red on a white background.
2. On the Control Image 2 window, select Vertical Stretch/OK and click on Image 1 to stretch Image 2 until the time lines on both images match up. Be sure to select Cancel Stretch-Shrink/OK when they are matched.
3. The seismogram starts at 780 ms TWT, so shift it across the section so that it lies a little to the right of the well and the top line lies at 780 ms on the section. The prominent trough at 960 ms on the seismogram should match the trough in the seismic section at the same time. If it does not, check step 2 above.
4. Progressively shift the seismogram leftwards until it overlies the well.
5. Switch Image 2 Transparency to On. After minor adjustment of amplitudes using Horizontal Shrink, you can now check that the correspondence between peaks and troughs on seismogram and seismic section is very good, for example between 1,300 and 1,500 ms TWT. In fact, this is about as good as it gets. It might be slightly better if measured densities were used instead of those calculated from velocity. The three stratigraphic markers mentioned in Tutorial 7.1 can be reliably identified on the seismic section, and an interpreter would be justifiably confident about the starting point of an interpretation. This will be the starting point of the interpretation in Tutorial 7.3.
6. Note that the seismic section shows a broad peak between the two marker reflections where the synthetic seismogram shows two peaks close together. You will be able to see how that broad peak develops across the seismic section in Tutorial 7.3.

Tutorial 7.3

Purpose: To explore problems and solutions in the picking of reflections across a 2D seismic section that shows much structural and stratigraphic variation.

Materials

- i. Part of line *GMF31* across the Inner Moray Firth, UK North Sea as shown in [Figure T7.3.1](#) is presented in Sheets 1 to 5 ([Figures T7.3.3](#) to [7.3.7](#)). The data have been migrated. The vertical scale is 5 cm = 1,000 ms and the CMP spacing is 25 m. CMP numbers are marked along the top edge of the section. The data were acquired in 1976 and are of remarkably good quality for that era, as indicated by the good fit of the synthetic seismogram. However, lack of close velocity control has affected the quality of imaging in steep dip areas.

[Figure T7.3.1](#)

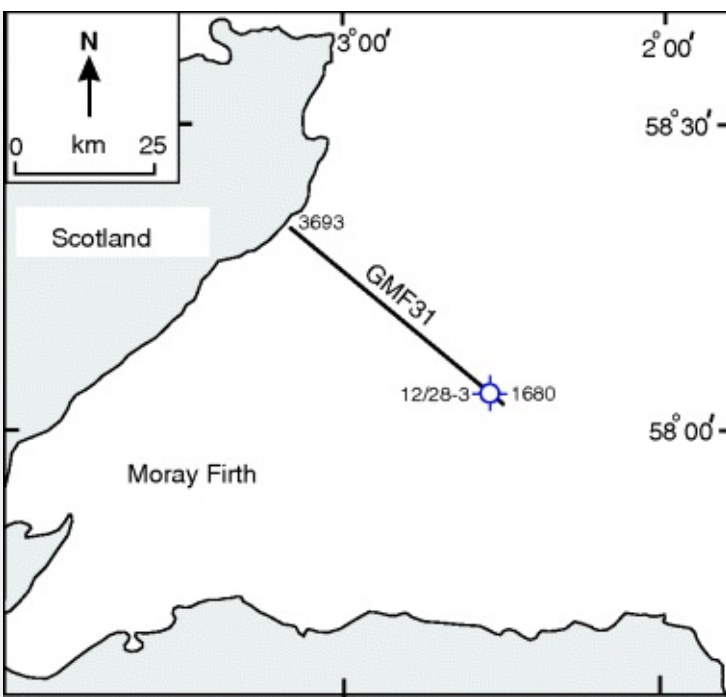


Figure T7.3.2 Seismic data by courtesy of Western Geco

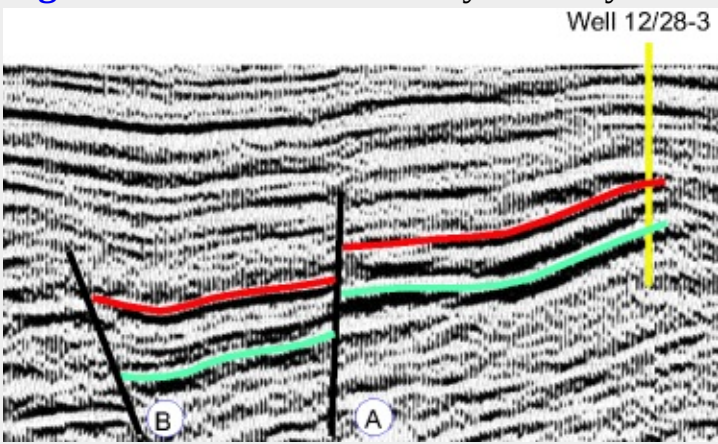


Figure T7.3.3 Seismic data by courtesy of Western Geco

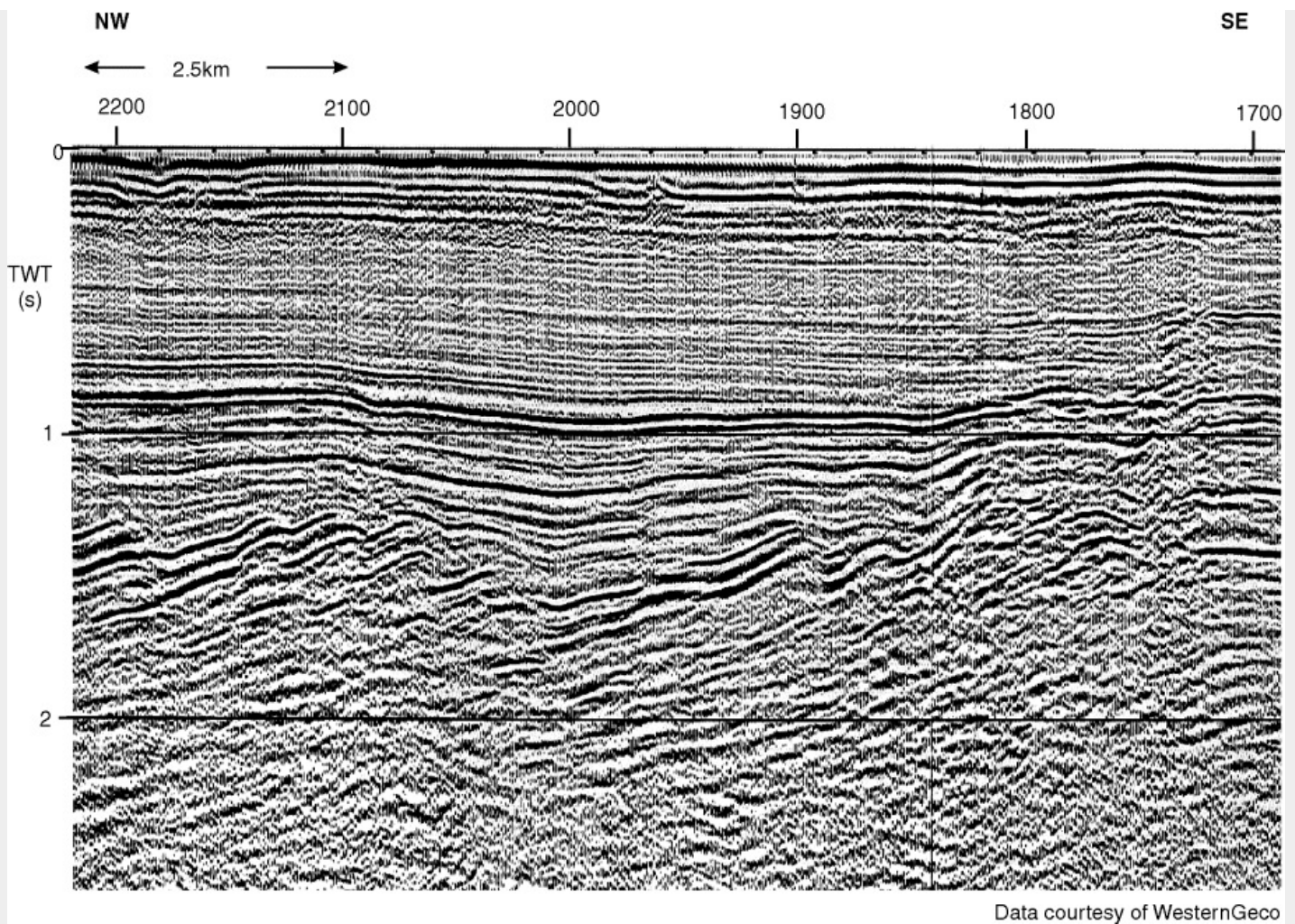


Figure T7.3.4 Seismic data by courtesy of Western Geco

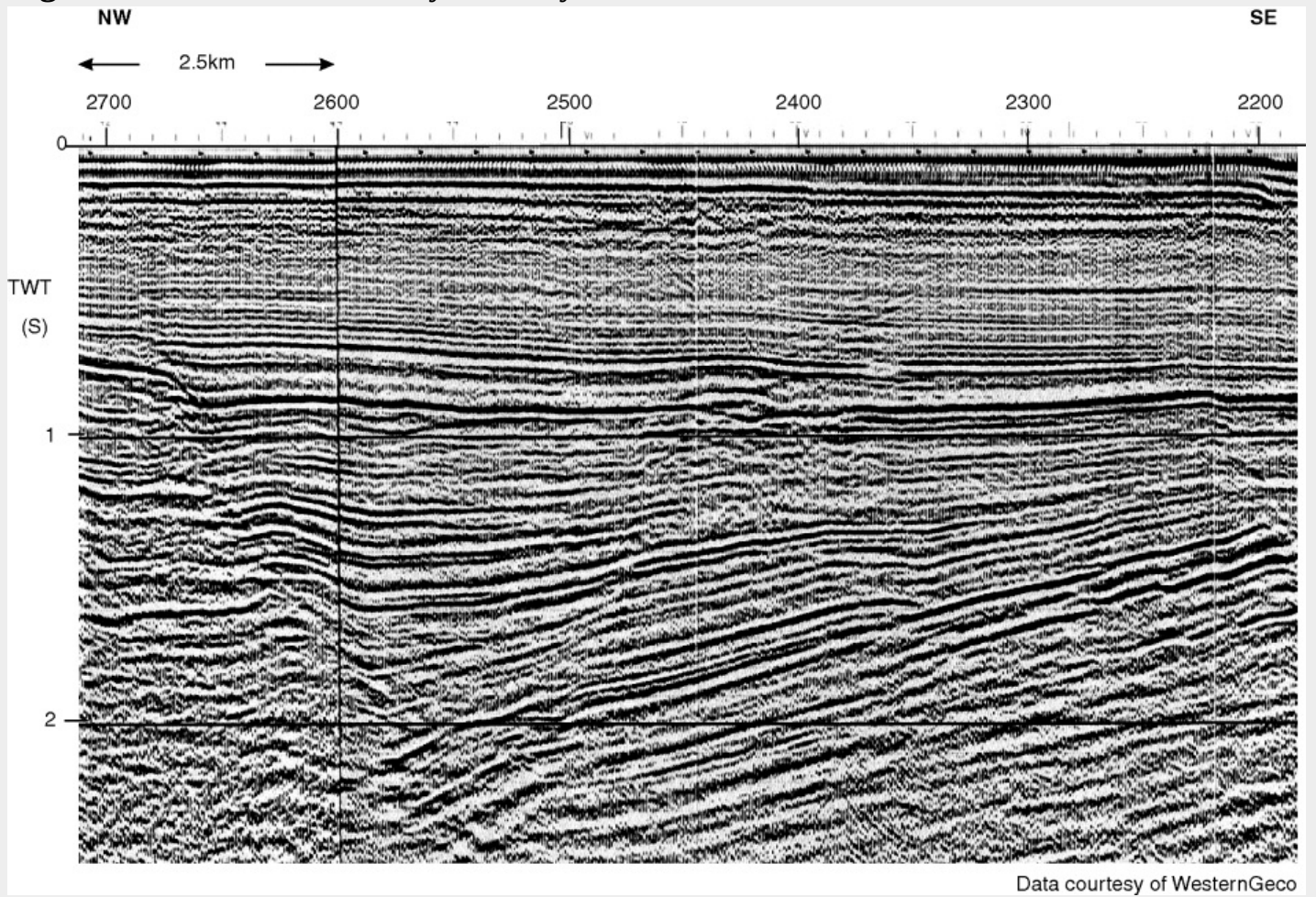
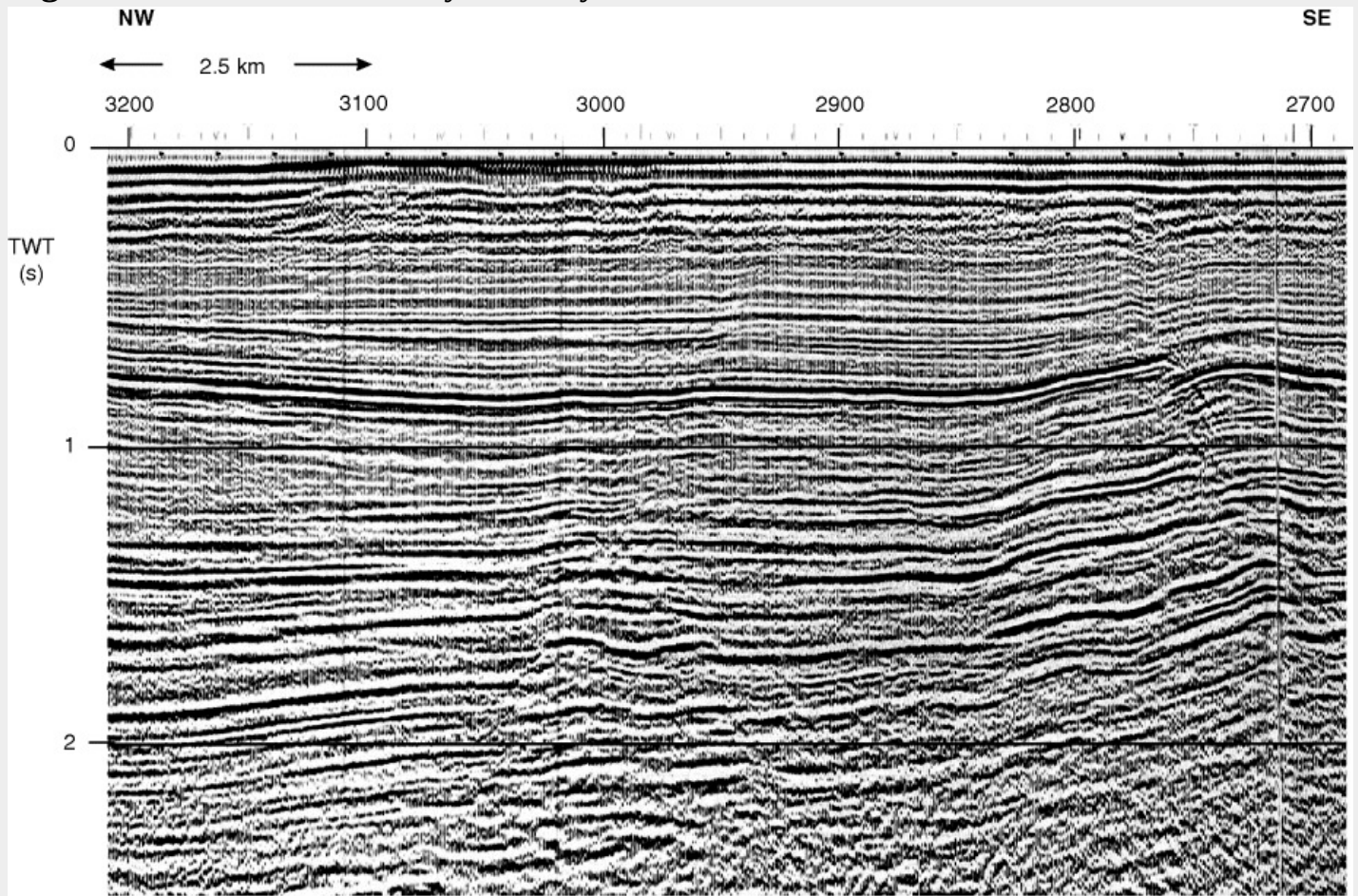
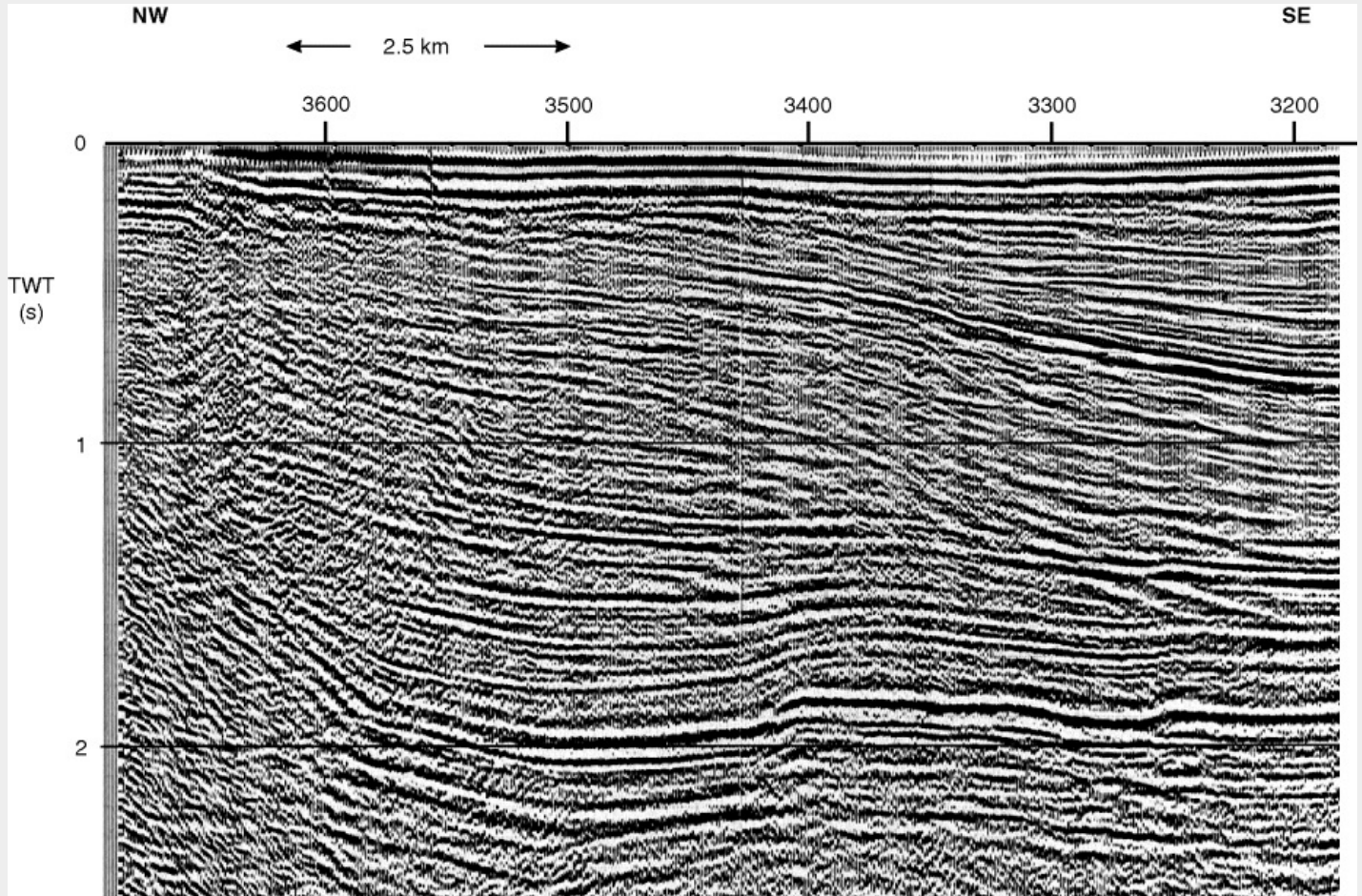


Figure T7.3.5 Seismic data by courtesy of Western Geco



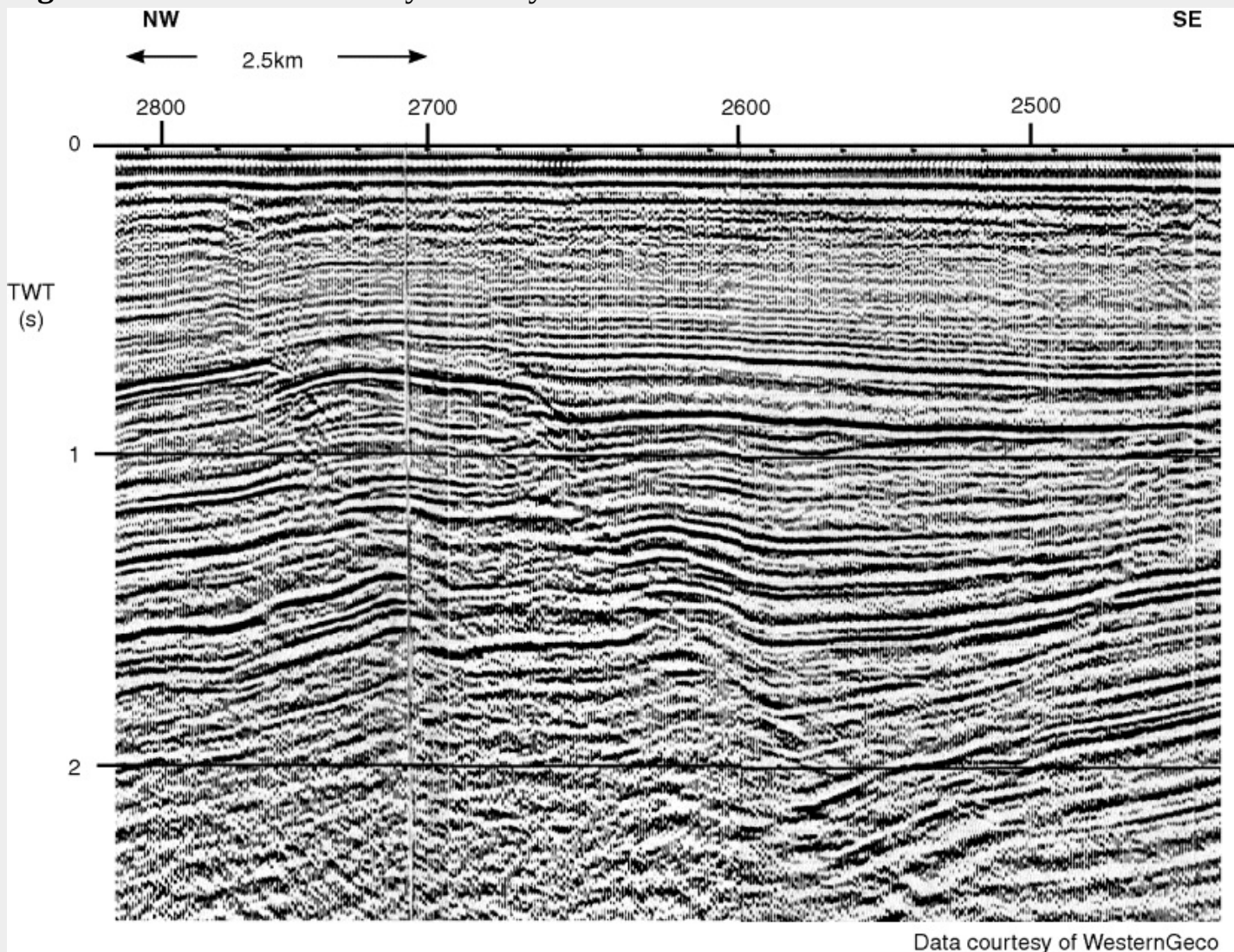
Data courtesy of WesternGeco

Figure T7.3.6 Seismic data by courtesy of Western Geco



Data courtesy of WesternGeco

Figure T7.3.7 Seismic data by courtesy of Western Geco



ii. The results from Tutorials 7.1 and 7.2, which identified three key reflections on GMF31 from the good match of a synthetic seismogram with the seismic data.

iii. Three coloured pencils, sharpened to fine points.

1. Starting off Start with Sheet 1 of the seismic data, identify the position of well 12/28-3 at CMP 1900 and draw a bold black vertical line down to 1,500 ms to mark the well bore. Colour the white trough at 950 ms which forms a good marker for a near-Base Cretaceous horizon. With different colours, also mark the trough above the peak at 1,350 ms (Top Mid Jurassic) and the trough above the peak at 1,450 ms (Top Trias). The latter two horizons are shown in [Figure T7.3.2](#). Make the coloured lines quite thin.

2. Picking away from the well We will pick the three reflections to the north-west of the well across all four sheets. The near-Base Cretaceous trough is uninterrupted and can easily be picked all the way across Sheet 1, but the other two events meet a discontinuity directly below CMP 1965 as shown in [Figure T7.3.2](#) (fault A). Several features which will recur many times across the section are displayed in this fragment of the section:

i. Fault A affects the strata for some way above the red reflection, but it dies out about 300 ms above it, where the displacement is taken up as a monocline. We conclude that on this fault, movement continued for some time into the Upper Jurassic.

ii. In the block between the two faults, the sediments thicken appreciably towards fault B. We must conclude that the fault was a growth fault in action in the Lower to Mid-Jurassic.

iii. In the same block between the faults, the broad peak between the two marker reflections has split into two separate peaks which diverge towards fault B as the sediment thickens. You may recall that the synthetic seismogram of tutorials 7.1 and 7.2 also showed two peaks at this level. As you pick the reflections across the rest of the section, be prepared to see sometimes one broad, diffuse peak or sometimes two distinct peaks at this stratigraphic level.

3. Faults The near Base Cretaceous reflection is straightforward across almost the whole section to about CMP 3450, apart from a couple of obvious fault displacements. The other two reflections pose questions in two areas

of difficulty: first, how to pick through the badly faulted area between CMPs 2000 and 2200 and, second, how to pick across the spectacular growth faults that cut the near-Base Cretaceous reflection at CMPs 2670 and 2760.

The approach in both cases is to recognize the characteristic reflection sequence from the Lower to Mid-Jurassic section that we first recognized at the well. It is probably easiest to jump across the faulted area to CMP 2200 and compare the sequence of strong reflections there at about 1,500 ms with the sequence at the well at about the same time. Then work backwards through about five other individual fault blocks to the deepest block at CMP 2000. The best line for the fault plane is generally indicated by the broken ends of reflections. Tensional tectonics clearly dominate the structure and all the faults are normal faults. When you have finished this section, compare your interpretation with that shown for the same section in [Figure 6.9 \(b\)](#).

Proceeding north-west from CMP 2200 on Sheet 2, there are a couple of relatively minor faults to insert: the one at CMP 2355 is at an angle to the section, so is not properly migrated. Use the crest of the diffraction hyperbola and reflection terminations below to pinpoint its position. You should be able to pick the two deeper reflections down to about CMP 2500, where the sequence has thickened a little and the two narrow peaks between the marker reflections have become very evident. You will probably be able to pick as far as CMP 2570.

4. Picking across the big growth faults Sheet 5 gives the best view of both faults together. It is not easy to see the characteristic reflection sequence of the Lower to Mid Jurassic section in the area between the two faults, where reflection quality is poor, but it can be seen in the area NW of CMP 2760. The sequence to be looked for is the version nearest to the faults on their south-east side, for example under CMP 2450, where you should have picked the top of the sequence at a time of 1,740 ms. You may be able to spot it in the section north-west of the faults by a careful comparison by eye, but on a workstation it would be possible to cut out a small window from the section at CMP 2450, drag it over to the other side of the faults and match it visually easily by sliding it up and down the sequence of reflections.

We can do exactly that by using the program *IMAGES* on the CD-ROM. Run the program and select Help/Quickstart Tutorial: the section NW of the fault is loaded as Image 1; the window of data extracted at CMP 2450, which contains the characteristic reflection sequence, is loaded as Image 2. Follow the Quickstart tutorial and you will see that the reflection sequence can be uniquely identified to the NW of the major faults. Mark the two reflections there on sheet 5, but refrain from picking them any further until the faults are sorted out. Notice that the reflection sequence has not changed from one side of the faults to the other, so they were not moving during sedimentation, in marked contrast to the Upper Jurassic sediments above.

5. Picking fault planes on the growth faults (Sheet 5) Start at CMP 2760 on the near-Base Cretaceous reflection and mark the fault break down the section, using truncations of reflections and the summits of partially migrated fault hyperbolae to locate the exact position of the fault plane down to about 1,800 ms. The hyperbolae are visible because the section is not at right angles to the faults (see Section 7.6). Moving upwards from the near-Base Cretaceous event at CMP 2760, there is probably fault disruption for about 200 ms before displacement passes up into a monocline.

Picking the other growth fault can be started at the near-Base Cretaceous reflection under CMP 2675, but the fault becomes less well defined at depth. Under CMP 2640 at about 1,300 ms, the strata have been folded against the fault plane, indicating some transcurrent motion on the fault at that stage of its movement. Bear in mind that better migration velocities might shift the broken ends up dip at that point. Further down there is little to guide the interpretation of the fault plane until the strong reflections under CMP 2580 at 2,100 ms and below. Don't miss the antithetic fault that breaks the characteristic Lower-Mid Jurassic sequence at about 1,900 ms under CMP 2500. You should be able to push through the interpretation in the wedge between this fault and the first of the growth faults to the north-west.

6. NW half of the section and basin margin (Sheet 4) The near-Base Cretaceous reflection dies out at about CMP 3450, but the Lower-Mid Jurassic sequence carries on to an abrupt termination at CMP 3600 at about 2 s TWT. This point marks the major fault that terminates the basin on its north-west side, and the best choice for the fault plane seems to be between there and the disruption of the shallow reflections under CMP 3650. The fault is the offshore continuation of the Helmsdale Fault, which outcrops along the coast to the south-west of the line (Hudson & Trewin, 2002). The near-Base Cretaceous reflection rises towards the fault and, if restored to its presumed depositional position of horizontal, it shows that the Helmsdale Fault was very active during deposition of the Upper Jurassic, allowing a thickening wedge of sediment to be deposited. The basin margin fault was also active during deposition of the Lower-Mid Jurassic interval, which thickens in time from 180 ms TWT at CMP 2750 to 290 ms at CMP 3500. Unfortunately, the velocity analyses are not numerous or detailed enough to give reliable interval velocities and so convert that observation into one of increased thickness.

Finally, Sheet 4 shows a fine example of surface multiples. Remember that the surface multiple has twice the travel time of its generating primary (check Chapter 5, Section 5.8). On sheet 4 at CMP 3410, measure TWT to

the near-Base Cretaceous reflection. Now look for a reflection at twice that time under the same CMP with a steeper dip than the others. Squint along that part of the section in a down-dip direction and you should see the multiple as a white trough breaking down through the rest of the reflections. Once you get your eye in, you will see plenty more multiples with the same dip breaking obliquely across the primaries, especially under CMP 3300.

Tutorial 7.4

Purpose: To show the necessity of time to depth conversion in the West Sole Field, UK southern North Sea

A Overview

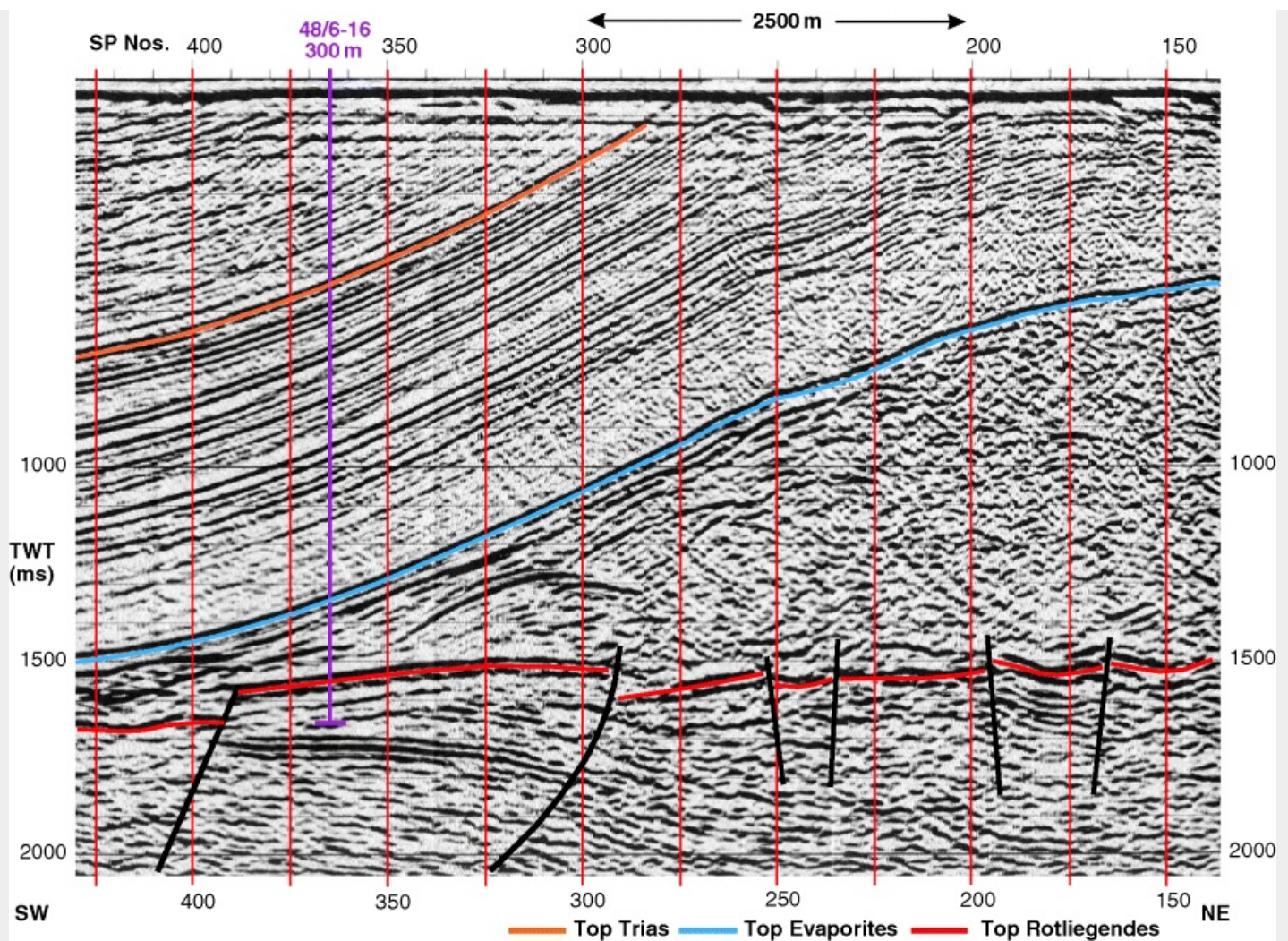
To keep this tutorial to a manageable size, we will assume that the exploration programme on the West Sole Field is at an early stage: only seven seismic sections are available and one well. Most of the TWT measurements have been made, but you will measure the remainder, contour the times to make a time map, convert times to depths, contour the depths to see the true structure and compare the depth from the seismic survey with that measured in wells.

B Setting the scene

i. Geology

[Figure T7.4.1](#) shows the location of the West Sole gas field in the southern North Sea Basin. The seven seismic lines shown will form the basis of the interpretation and TWT has been measured on most of them. You will measure times on part of lines 642A and 648. [Figure T7.4.2](#) shows part of the seismic section on line 628 and the location of well 48/6-16 projected onto the section from 300 metres away. Jurassic rocks, mostly shales, lie under thin sea bed sediments as far down as the orange reflection which marks the Top Trias. The Trias is lithologically varied in its upper part, with limestones and halite units interbedded with shales, giving the strong reflections evident on the section. Lower down, the Trias is more sandy. The blue reflection marks the top of the Permian Zechstein evaporite succession, comprising thick halite sandwiched between upper and lower successions of anhydrite, dolomite and limestone. At the well location, the prominent seismic trough at about 1,550 ms TWT marks the top of the Permian Rotliegend succession which is dominated by the Upper and Lower Leman Sandstone that forms the reservoir rock. In common with the many other fields of the Southern North Sea gas basin, the reservoir seal is formed by the overlying Zechstein evaporites and the source is the underlying coal-bearing Carboniferous. The base Permian is a sharp erosional unconformity very evident in [Figure T7.4.2](#) by the truncation of the underlying Carboniferous strata at about the total depth (TD) of the well, especially around SP 330.

[Figure T7.4.1](#)



ii. Geophysics

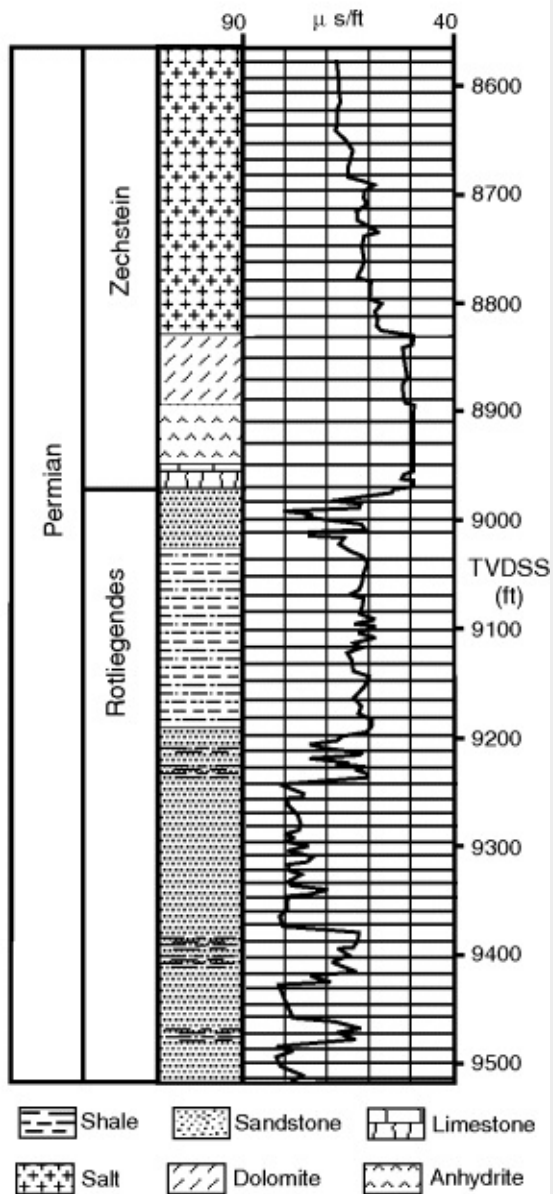
The polarity of the data is that an increase in acoustic impedance is marked by a black peak in the waveform (e.g. at the Trias/Evaporite reflection) and the data is of zero-phase form. On [Figure T7.4.2](#), note the horizontal multiples of the sea bed or shallow sediment layers in the first 300 ms of the section; these die out rapidly at depth. Note the strong reflections below the Top Evaporite blue marker; these are caused by the strong reflection coefficients of the halite/dolomite interfaces in this part of the section and they disappear further up the flank of the salt swell, presumably because the dolomite becomes disrupted by the flow of the salt. Occasional high-amplitude reflections within the salt swell may be attributed to broken rafts of dolomite.

[Figure T7.4.3](#) shows some detail of the stratigraphy of the top of the reservoir, together with the sonic log and OWT marks at 1 ms intervals. Exceptionally high velocities, up to about 6,000 m/s, are typical of the anhydrite-dolomite intervals of the Zechstein sequence. Velocities in the salt layer vary somewhat, depending on chemistry, but a fair average is about 4,500 m/s.

[Figure T7.4.3](#)

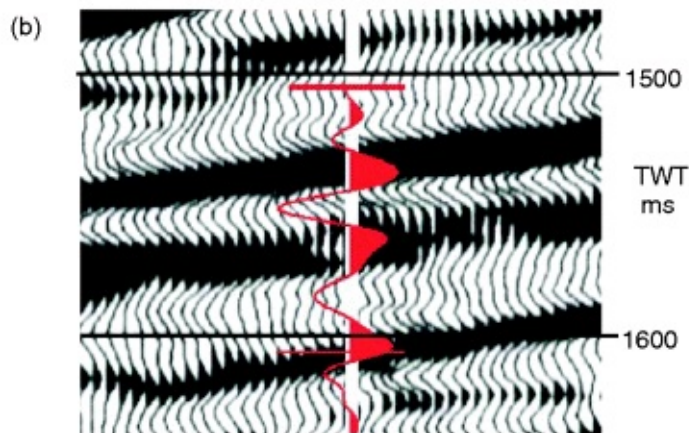
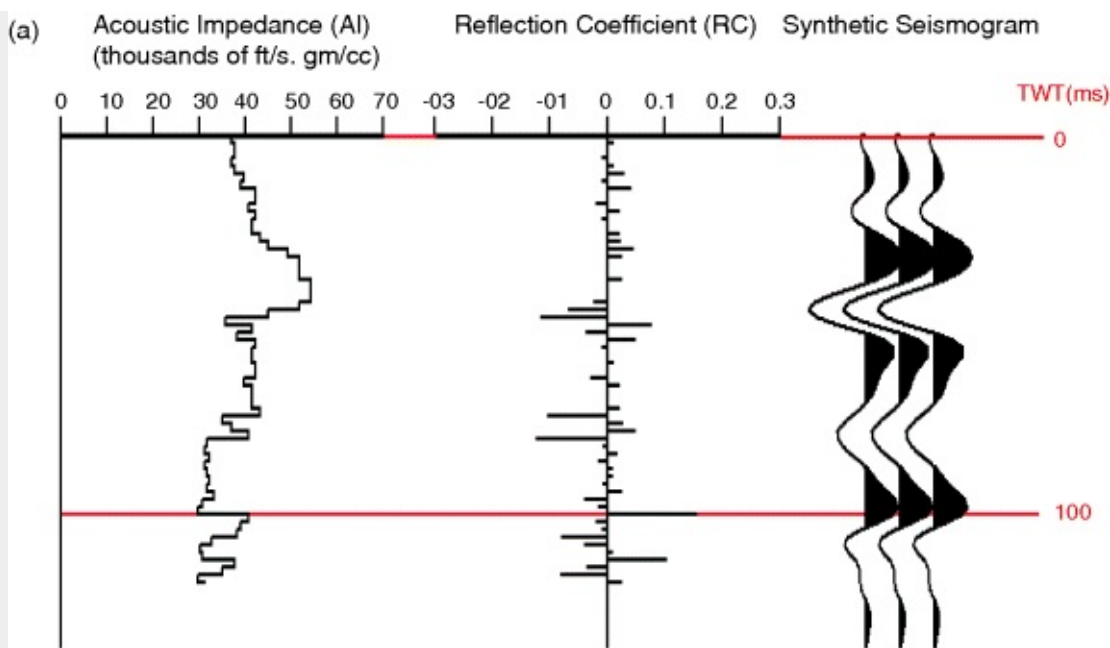
Sonic Log Data, Well 48/6-16

Horizontal lines at 1 ms
intervals OWT



[Figure T7.4.4](#) shows a synthetic seismogram derived from the data of [Figure T7.4.3](#). The distinctive trough in the waveform at 45 ms on the synthetic seismogram, equivalent to 1,550 ms on the seismic section ([Figure T7.4.4](#)), marks the top of the reservoir and is caused by the sudden drop in velocity from the Zechstein to the Rotliegend sequence. Moderate reflections within the Rotliegend sequence are caused by shalier intervals within the sandstone. The synthetic seismogram with a zero phase wavelet ties quite well to the seismic section.

[Figure T7.4.4](#) Seismic data by courtesy of BP



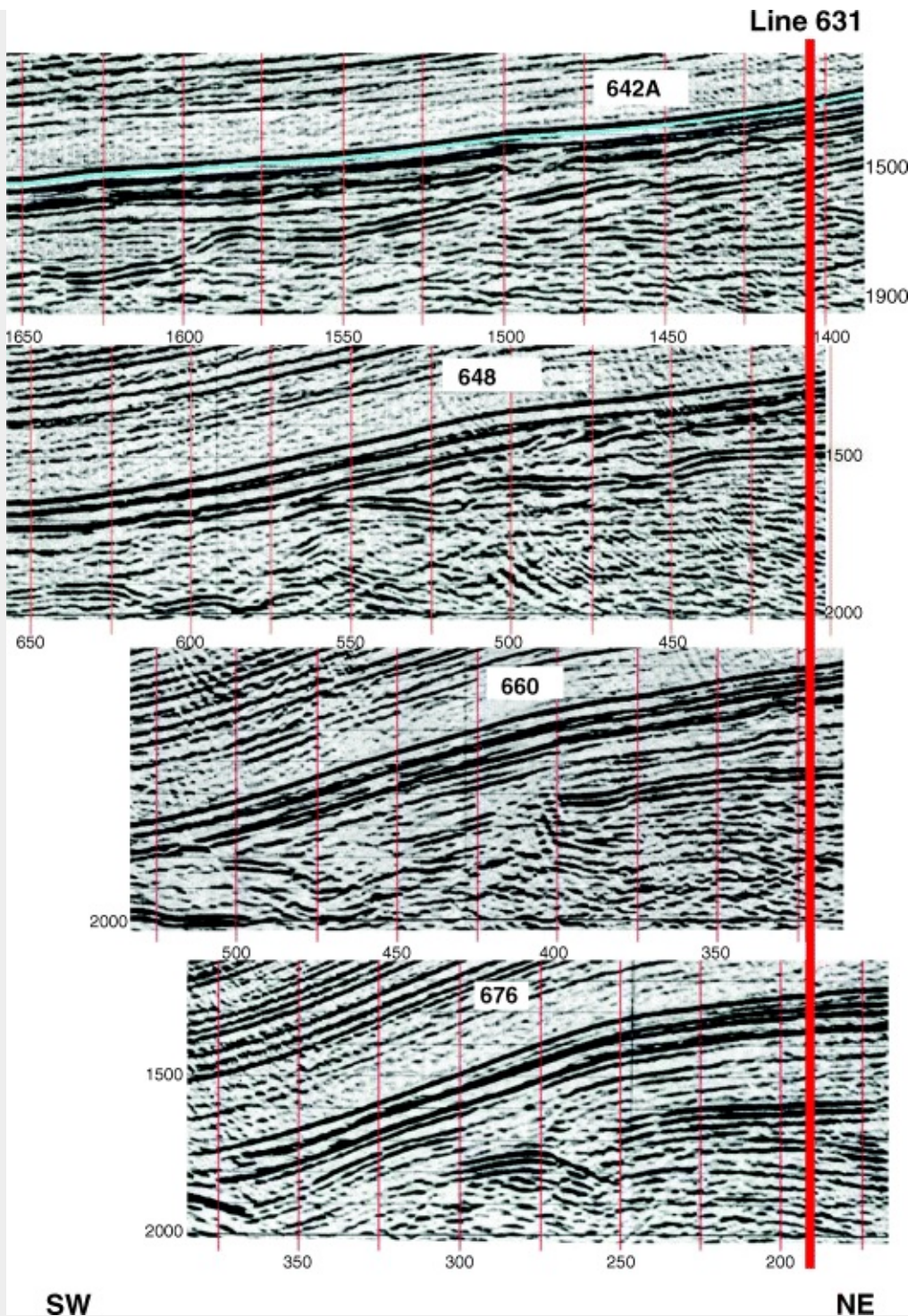
a. Synthetic seismogram generated from the well-log shown on Sheet 3.
 b. The fit of the synthetic seismogram (red) to observed data on line 628, close to well 48/6-16. The well location is offset 300 m SE of the seismic line. The prominent trough at 1550 ms TWT is the Top Rotliegend reflection. A 35 Hz zero-phase Ricker wavelet was used in the synthetic.

C Making a time map

1. Picking Top Rotliegend on lines 642A and 648.

- i. Four of the seismic sections are shown on [Figure T7.4.5](#), aligned with the cross-line 631 which ties them together. The Top Evaporite reflection is again marked in blue on line 642A and, by comparison with [Figure T7.4.2](#), you should have no difficulty in recognizing the distinctive trough of the Top Rotliegend 220 ms below the Top Evaporite at the intersection with line 631. Mark the trough with a distinctive colour all the way across the section. Mark in the two small faults that downthrow to the NE.

Figure T7.4.5 Seismic data by courtesy of BP



ii. Repeat for line 648 from the NE end at least as far as SP 550, but note that the two small faults throw in the opposite sense to those you picked on 642. Is it reasonable to connect the faults from one line to the other? To complete the presentation, colour the Rotliegend reflection on the NE halves of 660 and 676 as well and further south-west if you think it possible.

iii. On all four sections, note the long stretch of unfaulted Top Rotliegend reflection in the vicinity of line 631. On line 676, it ends abruptly against a major fault downthrowing SW. Mark in that fault on the section and find and mark the equivalent fault on lines 660 and 648.

iv. Have a go at picking the Top Rotliegend reflection to the SW of the major fault: it is possible, but it is not easy and is not worth wasting any time on.

2. Timing the Top Rotliegend reflection on lines 642A and 648.

You will have noticed that the SW half of lines 642A and 648 on [Figure T7.4.1](#) have no times marked – you have to measure the times, write the times on to [Figure T7.4.1](#) and complete the contour map of TWT. The program *MAPDIGIT* can be used to measure the times, so please take a couple of minutes to go through the Quickstart Tutorial if you have not used the program before.

i. In *MAPDIGIT/Configure*, type 642 for the project name. Open the file 642timing.bmp from the data set. At the SP locations marked by vertical red lines, measure travel times to the centre of the trough that marks

the Top Rotliegend. Repeat the procedure for line 648, working from the file 648timing.bmp. Since the process is very fast, on one of the lines repeat the measurement from scratch two more times (i.e. including reloading the file and re-calibration), so that you have three sets of times altogether from one line. Calculate the mean reading at each point and the average of the deviations of each reading from the mean, so you have some estimate of the error involved in timing reflections.

ii. Print out the two files of travel times and write the times on to [Figure T7.4.1](#) against the appropriate SP locations. Use ink, because you will be rubbing out a lot in drawing contours.

iii. Transfer the location of the faults marked on the sections to the map ([Figure T7.4.1](#)), e.g. the major fault, mentioned in Step 1(iii) above on line 676, lies directly under SP 250.

iv. Connect the major fault picked in Step 1(iii) across the three lines. If the fault line is projected further west on to line 642, is there any equivalent structural expression there?

v. Could one of the smaller faults mentioned in Step 1(ii) be considered a splay off the major fault?

3. Completing the contour map of TWT.

You are now in a position to complete the contour map of TWT on [Figure T7.4.1](#). Work in pencil, with a rubber handy. Contours can end abruptly on fault lines. The completed time map shows a steep slope on the south-west side trending NW–SE and falling away about 400 ms, but the structure flattens off to the north-east with only a meagre closure. Does it look promising as a potential hydrocarbon-bearing structure?

D Time to depth conversion

1. General strategy

The pinch-and-swell structure of the salt layer causes large variations in average velocity down to the reservoir across the whole area of the field. The TWT map has to be converted to depth in order to see the true structure of the field. The usual approach in this area would be to employ a detailed layer cake method involving measuring times on the Top Trias and Top Evaporite reflections, as well as the Top Rotliegend at all data points across the area. The times would be converted to thicknesses using a combination of well- and seismic-derived layer velocities. Depth to the Top Rotliegend is then simply the sum of the three thicknesses. A lot of timing is involved, and some way of coping with the lateral variation of interval velocity within each layer would have to be found.

In keeping with our assumption of an early stage in exploration and a limited data set, we will use a simple approach. At rather sparse control points, we will use seismic-derived layer velocities to calculate thicknesses of the first two layers down to the Top Evaporite reflection. The velocity control points have to be sparse because, although there are numerous velocity analyses along the lines, the velocity picks often do not correspond closely enough with formation boundaries to give good interval velocities. The thickness of the evaporite layer will be calculated from the known velocities of the evaporite lithologies (well data) and the TWT through the layer. From the total thickness of the three layers and the measured time to the Top Rotliegend, an average velocity can be calculated at each sparse data point and a contour map of average velocity drawn up. Each travel time on [Figure T7.4.1](#) can then be converted to depth by multiplication of the one-way time with the average velocity picked off by interpolation on the contour map at the location of the travel time observation.

2. Calculating average velocity.

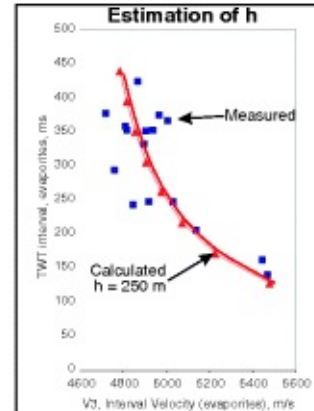
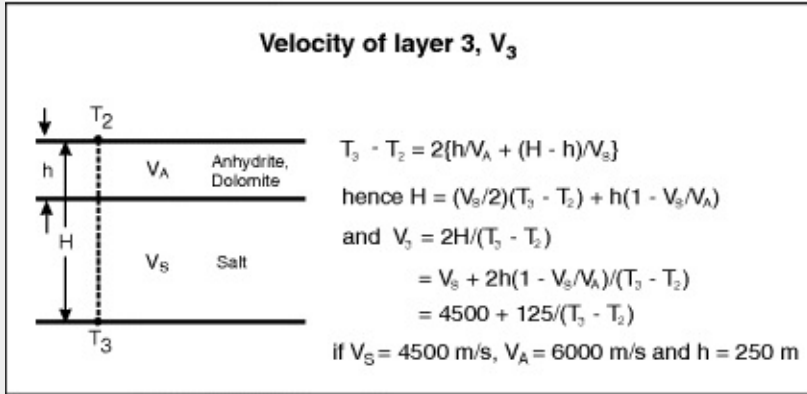
[Figure T7.4.6](#) is very busy, so let's take it bit by bit. It shows three panels. The top panel shows an example of the calculation of average velocity at SP 403 of line 631. The velocity analysis at that SP is given at the left, and we are interested in the columns labelled Time and V_{rms} (which is really stacking velocity). The time listed as 552 ms, with velocity 2,404 m/s, corresponds exactly to the Top Trias reflection on the seismic section, and these two values appear in the spreadsheet in the columns labelled T1 and V_{s1} . The values under T2 and V_{s2} are also taken from the velocity analysis tabulation and refer to the Top Evaporite reflection. From the explanatory formulae on the spreadsheet, you can follow the calculation of thickness of the first two layers (Z2 and Z3) as far as column L. Note that the velocities are corrected for dip if required. For migrated data, the geological dip of a reflecting interface, θ , is given by:

[Figure T7.4.6](#)

Velocity analysis
SP 403

TIME	V1	V2
8	1406	1416
43	1416	1838
124	1698	2325
314	2108	2598
488	2223	2518
552	2494	2957
629	2525	3267
749	2708	3518
837	2795	3444
989	2914	3496
1141	3828	3638
1279	3157	4117
1353	3241	4521
1428	3351	4457
1522	3482	5074
1627	3637	5477
1748	3614	5384
1944	3997	5245
2327	4228	5865
4883	4975	5865

	A	B	C	D	E	F	G	H	I	J	K	L	M	N	O	P
1	WEST SOLE FIELD: AVERAGE VELOCITY TO ROTLIEGENDES										#####					
2																
3	LOC.	Dip	T1	Vs1	T2	Vs2	T3	V1	Z1	Vs2c	V2	Z2	V3	Z3	D3	Va3
4																
5	Line 631															
6	SP 403	0.000	0.552	2404	1.279	3157	1.510	2404	664	3157	3626	1318	5042	582	2564	3396
7																
8	Stacking velocity, Layer 1, corrected for dip								V1 - Vs1*cos(dip)							
9	Thickness, Layer 1								Z1 = V1*T1/2							
10	Stacking velocity, Layer 2, corrected for dip								Vs2c = Vs2*cos(dip)							
11	Interval velocity, Layer 2								V2 = sqrt((Vs2c*Vs2c*T2 - V1*V1*T1)/(T2 - T1))							
12	Thickness, Layer 2								Z2 = V2*(T2-T1)/2							
13	Interval velocity, Layer 3 (calculated)								V3 = 4500 + 125/(T3 - T2)							
14	Thickness, Layer 3								Z3 = V3*(T3 - T2)/2							
15	Depth to Rotliegende								D3 = Z1 + Z2 + Z3							
16	Average velocity to Rotliegende								Va3 = 2* D3/T3							



$$\tan\theta = (V/2)(dT/dX)$$

where V is the velocity to the interface and dT/dX is the gradient of the reflection on the time-migrated section in s/m.

All that remains, then, is to calculate the thickness of the third layer, (Z_3), the evaporite layer. The panel at bottom left on [Figure T7.4.6](#) shows how the evaporite layer velocity, V_3 , depends on the ratio of velocities of the two constituent lithologies and the thickness h of the anhydrite/dolomite interval, which is assumed constant. The panel at bottom right shows how, as the salt thickness increases, V_3 will tend towards salt velocity and, as the salt thins, it tends towards anhydrite velocity. In the absence of well control, one way to estimate h is to calculate the theoretical variation of V_3 with TWT interval in the evaporite layer for a range of h values and compare those graphs with measured data obtained from velocity analyses. On [Figure T7.4.6](#), a value of 250 m was chosen for h .

3. Average velocity map.

Figure T7.4.7

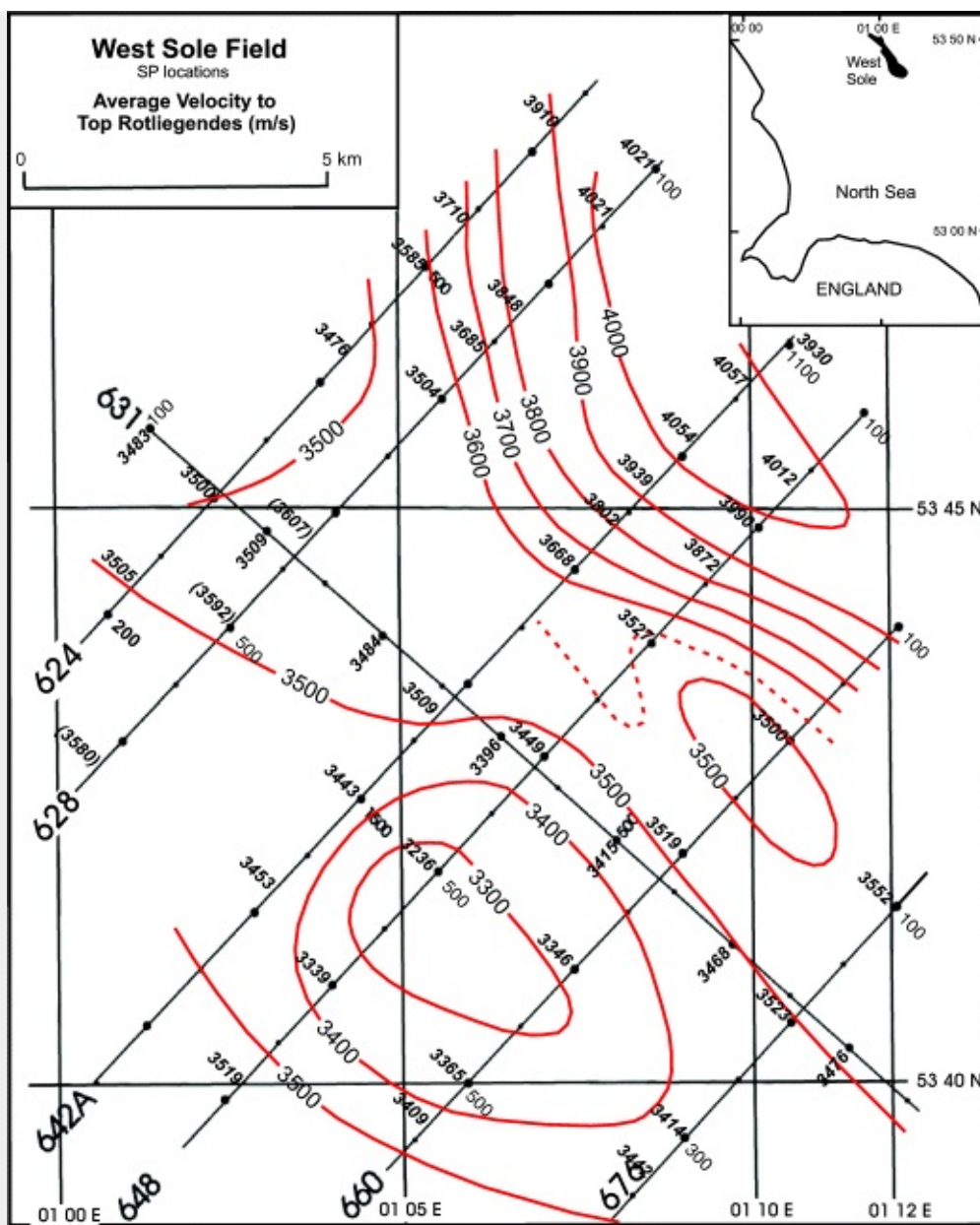
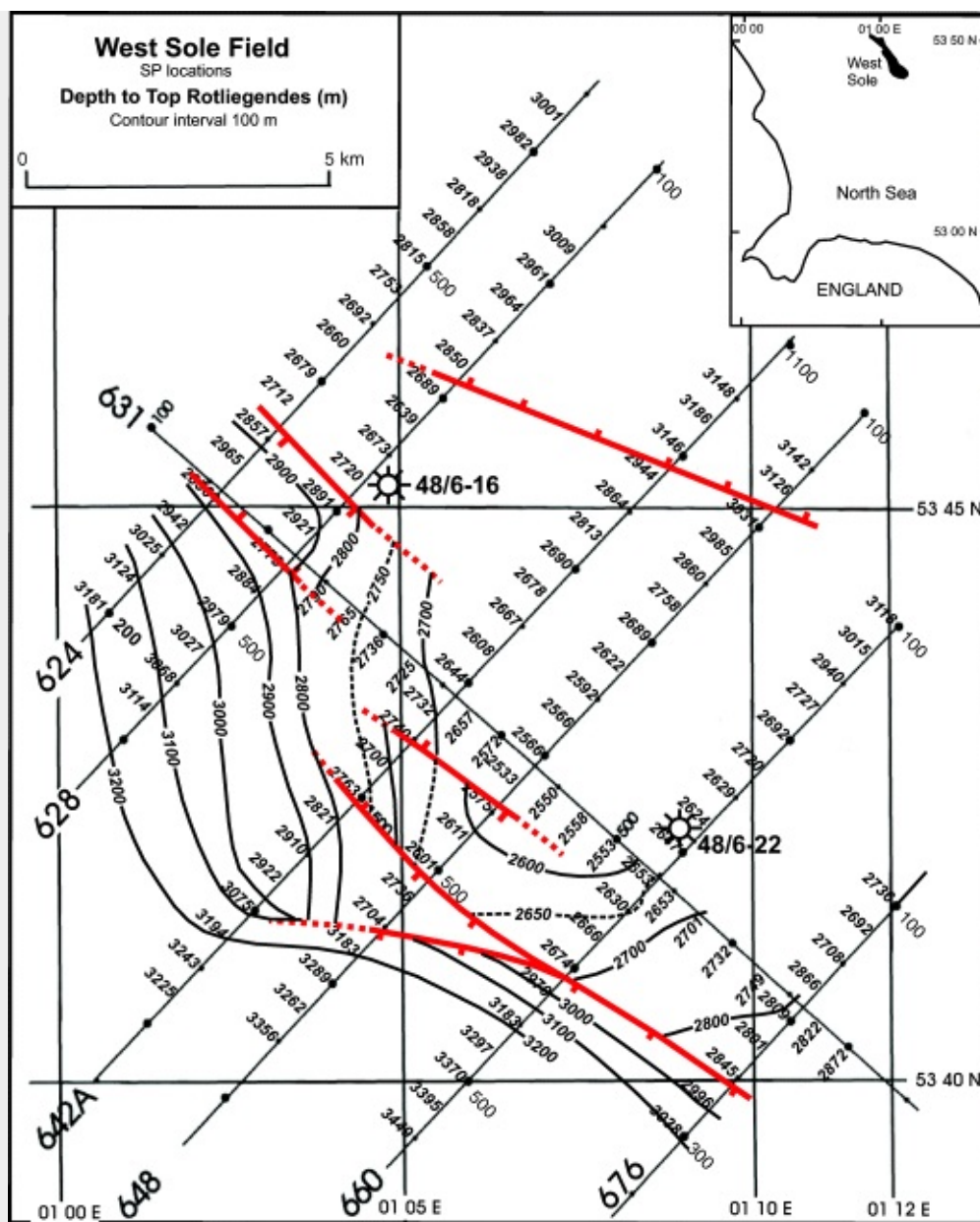


Figure T7.4.7 shows the average velocity values posted on the map and contoured. Contouring on rather sparse data like this has to be done with a 'broad brush' approach, quite justifiable for velocity in this area, where the overlying section is unfaulted and varies smoothly. The variations in velocity are reasonably consistent from line to line; only the south-west half of line 628 gave three values (shown in brackets on Figure T7.4.7) which seemed too high compared to those on lines 631 and 624 and were discounted. The contours vividly bring out the presence of the salt swell, with its crest trending NNW, forcing average velocity to rise over 4,000 m/s.

4. Contouring the depth map.

At each data point on the time map (Figure T7.4.1), a value of velocity was picked off the velocity map (Figure T7.4.7) by interpolating between contours and used to calculate depth. Depths have already been contoured to the south-west of line 631. Following your experience of contouring TWT in section C (Making a time map) step 3, above, you will not be surprised to see a long slope striking NW-SE which falls to the south-west at least 600 m from the summit of the structure. But where is the summit, exactly, and is there a corresponding slope closing off the structure to the north-east? Your task now is to draw contours across the rest of the map on Figure T7.4.8 and answer these key questions.

Figure T7.4.8



5. Epilogue: depth ties at wells?

Measured depths to Top Rotligend: Well 48/6-16 = 2763 m, Well 48/6-22 = 2685 m. Unfortunately, both wells are offset from the nearest seismic line by about 300 m, so we cannot get an exact tie. The contouring process introduces further uncertainties. Since the structure strikes at right angles to the seismic lines, probably the most reasonable course of action is to project the well location onto the nearest seismic line and interpolate a depth between the two nearest SPs. Do that now and estimate the percentage error in depth at each well. Any error must be caused either by errors in timing or in estimating velocity. Which do you think is the most important cause here, bearing in mind the estimate of timing error you made in section C (Making a time map) step 2, above?

Part II

Seismic Input to Reservoir Characterization

Chapter 8

Better Images of the Subsurface

The art of geophysics lies in finding the appropriate approximations.

(Thomsen, 2002)

8.1 Introduction

Two fundamental prerequisites for the seismic study of a hydrocarbon reservoir are:

1. that the reservoir-bounding reflectors are exactly located in the subsurface (the topic of this chapter);
2. that the reflections from rock interfaces are zero-phase wavelets free from noise (the topic of Chapter 9).

Two developments give better images of the subsurface structure than those considered in Part I: firstly, better migration of the data; and, secondly, the use of 3D data. There is a huge literature on migration, so no attempt will be made here to cover all the techniques that are available; we will stay with the two main-line approaches already introduced in Part I – Kirchhoff diffraction stack and wavefield continuation. We will concentrate on the two key developments in improved migration, namely the move from post-stack to prestack migration and the move from time migration to depth migration. The principles apply to 2D or 3D data equally well, but the chapter will finish by looking at the unique view of the subsurface provided by 3D data.

In Part I, we followed a simple route in constructing the migrated seismic section. The essential assumptions behind it were:

1. A set of CMP traces corrected for NMO and stacked together creates a trace of normal-incidence reflections.
2. Velocity varies vertically, but not horizontally, within the dimensions of a CMP gather.
3. The CMP-stacked time section can be migrated via the Kirchhoff method by stacking the data along symmetrical diffraction hyperbolae which are simply defined by the TWT to the summit and the velocity down to that TWT ([Equation 5.1](#)).

Where the strata are horizontal or dip gently (say, less than five degrees) and velocity varies only with depth, an acceptable image of the strata will be produced. However, where there is appreciable structure and dips increase, the migrated image of the subsurface will become blurred and distorted for two reasons:

1. The traces in a CMP gather no longer share a common reflection point but come from an extended area of the dipping reflector. We call this ‘reflection point dispersal’.
2. The velocity down to the reflector varies rapidly across the section, leading to distortion of the diffraction hyperbola.

In spite of these limitations, reflection sections were routinely processed in this fashion for about the first 15 years of digital processing. For example, the sections to be interpreted in Tutorial were

constructed on this basis.

8.2 Reflection Point Dispersal, Conflicting Dips and DMO

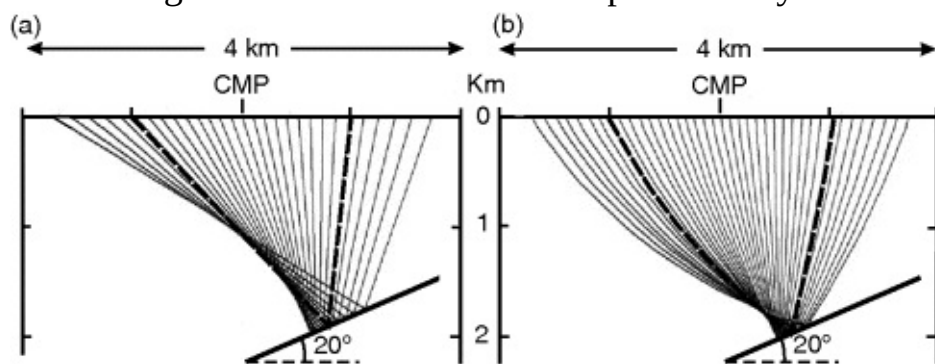
A very simple geometrical construction will show how the reflection points for a CMP gather become displaced across a dipping reflector (Tutorial 8.1).

Give yourself a nasty surprise when you see the severity of reflection point dispersal in Tutorial 8.1.

Given the results of Tutorial 8.1, you may well wonder that CMP stacking ever worked in anything but horizontal strata! However, you will also notice that reflection point dispersal increases rapidly as the offset/depth ratio increases, so it is worse at long offsets and shallow depths. For many exploration scenarios where depth is about the same as maximum offset, dispersal is not excessive, at least at moderate dips. Also, the general increase in velocity with depth causes curvature of the raypaths, fortunately in such a way as to reduce dispersal, although not to eliminate it ([Figure 8.1](#)). The influence of both these factors helped to keep CMP stacking going as a robust process.

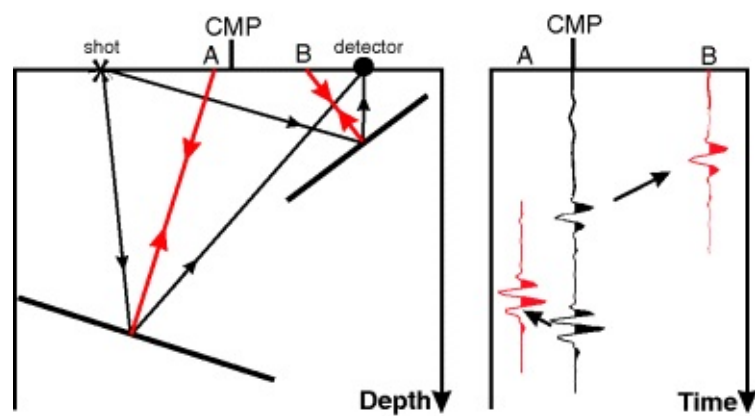
Figure 8.1

- a. The set of raypaths of a CMP gather for the case of uniform velocity. Reflection point dispersal is much reduced when maximum offset = depth (broken lines).
- b. Same reflector geometry as a, but velocity increases with depth and raypaths are curved causing a further reduction in the spread of rays.



A related problem is that of conflicting dips within the CMP gather. [Figure 8.2](#) shows the problem. A single raw trace from a CMP gather is shown in black. It contains two reflections – one from a steeply-dipping shallow reflector, the other from a deeper reflector of opposite dip. As usual, we correct the trace for NMO and plot it vertically below the CMP position. Unfortunately the NMO correction simply shifts the reflection wavelets to lesser times along the trace; what we really want is to reposition the wavelets to plot vertically below adjacent CMPs A and B at the times of true zero-offset reflections.

[Figure 8.2](#) Application of NMO correction, followed by DMO correction, re-builds recorded traces (black) at the correct locations and times for zero-offset reflections (red). The horizontal scale on the time section is double that on the depth section.



Until the late 1990s, this job was done by the Dip Move-Out (DMO) correction, an extra procedure applied after NMO. It takes the trace apart, sample by sample, and distributes the samples around elliptical wavefront-like arcs, curving upwards to each side of the recorded trace. A coherent new waveform will build up, where the arcs from many CMPs merge together at the appropriate CMP location off to the side. Since an element of migration is involved, the process is also known as Prestack Partial Migration. (Deregowski, 1982; 1986; Yilmaz & Claerbout, 1980).

The creation of true zero-offset traces by the DMO correction brings two important benefits:

1. Much crisper velocity spectra, and so better velocity analysis.
2. More accurate migration, especially of steeply dipping reflections, e.g. reflections from fault planes and the steep sides of salt diapirs.

8.3 Prestack Time Migration (PSTM)

A processing path through DMO and post-stack migration was widely used through the 1980s and 1990s, and enabled the expensive processing stage of migration to be confined to a one-pass operation at the end of the processing sequence. However, DMO always had limitations concerned with steep dips and lateral variations in velocity (Al-Yahya, 1989). From the earliest days of digital processing (e.g. Gardner *et al.*, 1974b), it was recognized that the best course would be prestack migration, i.e. migrate the data before stacking and then stack the migrated data as a final step. Through the latter half of the 1990s, two factors worked to encourage prestack migration:

1. Computing costs fell as super-computers were built from arrays of cheap processors.
2. Exploration moved into areas with challenging seismic targets, such as the sub-salt structures in the Gulf of Mexico.

As a result, prestack migration has overtaken DMO and is now the preferred approach in creating the best image of the subsurface (Dragoet, 2005). It is most easily explained as Kirchhoff migration of common-offset sections, so we will start with those.

8.3.1 Common-offset Sections and the Cheops Pyramid

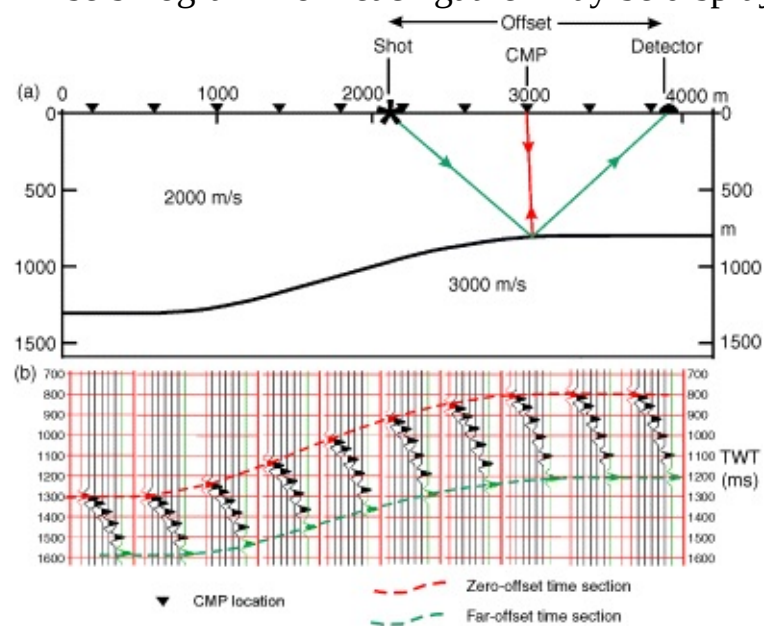
Let's go back to the basic shooting layout of a seismic line in the field. In [Figure 3.3](#), if we call the trace recorded from shot 1 to channel 5 the 1–5 trace, then the traces 1–5, 2–5, 3–5, etc. have, as a common factor, the offset from shot to detector, which is the same distance for each trace. If we gather those traces out of the recorded data set, they constitute a common offset gather and, if we display the traces across a section under their CMP locations, we create a common-offset time section.

[Figure 8.3](#) shows a set of model CMP gathers recorded across a simple geological section. For the sake of clarity, only seven channels are shown in each CMP gather rather than the 240 that might be recorded in practice. Any set of traces with a common offset may be taken out of the CMP gathers and displayed as a one-fold time section. For example, in [Figure 8.3](#), the red traces could be displayed on their own as a zero-offset section. The green traces could be displayed as another common-offset section, but this time the offset is not zero but 2,000 m.

Figure 8.3

a. Depth section with raypaths for zero offset (red) and far-offset (green) seismograms in a CMP gather.

b. A selection of CMP gathers across the section in **a**. For any particular offset, one seismogram from each gather may be displayed at the CMP to form a common-offset section.



How should such sections be migrated? Recall that the basis of Kirchhoff migration of zero-offset data is the diffraction hyperbola – we find data samples spread around the hyperbola on a zero-offset time section, apply appropriate scaling and phase shift and then plot the sum of the samples at the time of the hyperbola's summit (see Chapter 6, Section 6.11). So what is the equivalent summation path for common-offset data? Referring to [Figure 8.4](#), two-way time across a diffraction point for a constant shot-detector offset is given by:

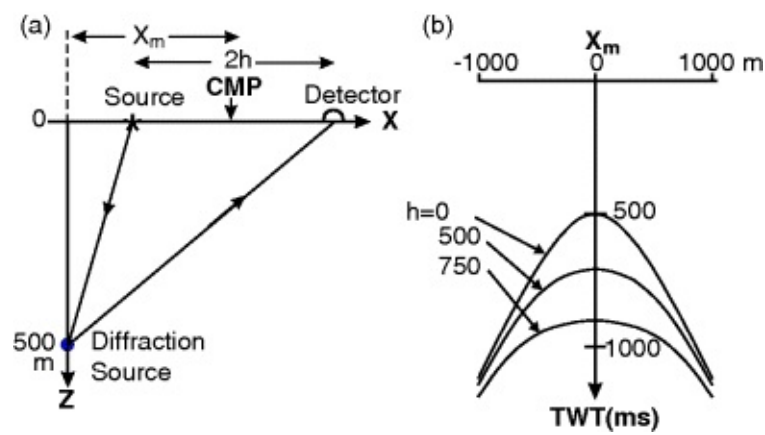
$$(8.1) T_x = [(T_0/2)^2 + (X_m - h)^2/V^2]^{1/2} + [(T_0/2)^2 + (X_m + h)^2/V^2]^{1/2}$$

where X_m = distance to the CMP from a point vertically above the diffractor and $2h$ = shot-detector offset.

Figure 8.4

a. A source and detector with a constant offset $2h$ move across a buried diffractor. X_m is the mid-point range from the diffractor.

b. Diffraction curves for three constant offsets calculated for velocity = 2,000 m/s. The curve is a hyperbola only for $h = 0$.



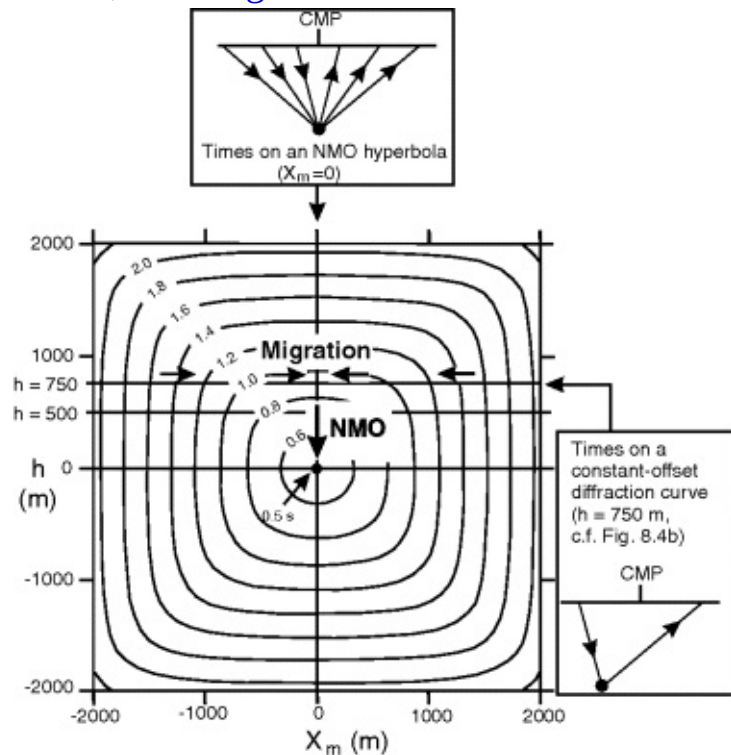
Examples of such curves are shown in [Figure 8.4b](#) for three different half-offsets: $h = 0$, 500 and 750 m. When $h = 0$ in [Equation \(8.1\)](#), the time equation reduces to the simple zero-offset hyperbola:

$$T_x^2 = T_0^2 + 4X_m^2/V^2$$

As the offset $2h$ increases, the shape of the diffraction curve departs more and more from the hyperbola, becoming flatter over the top ([Figure 8.4b](#)). This curve now defines the path to be followed across a common-offset section when summing the data samples in the process of Kirchhoff migration.

For a particular diffraction point, T_0 and V are constants in [Equation \(8.1\)](#), so T_x now depends on the two quantities X_m and h and can be mapped out as a variable across the plane defined by X_m and h axes. Such a map appears in [Figure 8.5](#), where the T_x values are shown by contours. The times form a pyramid-shaped surface, which is often dubbed the ‘Cheops Pyramid’ after the biggest of the three Great Pyramids of Giza in Egypt.

Figure 8.5 Shot-receiver travel times for a diffraction point as a function of half-offset, h and horizontal distance from diffraction point to CMP, X_m . Velocity = 2,000 m/s, depth to diffractor = 500 m, as in [Figure 8.4b](#).



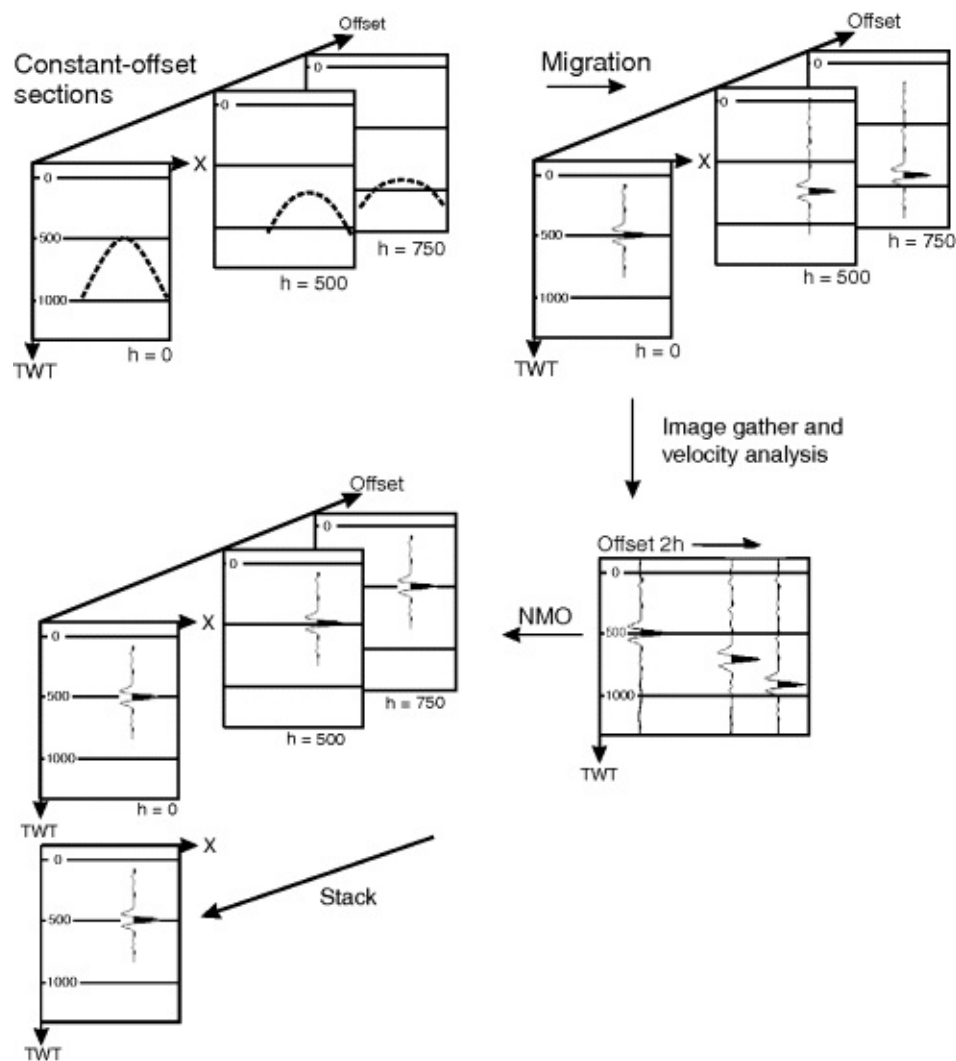
Now the time curves displayed on [Figure 8.4b](#) are the times that occur along horizontal lines in

[Figure 8.5](#), where h is some fixed amount such as 500 or 750 m. Along the horizontal line through the centre, $h = 0$ and only X_m varies, the condition for the familiar zero-offset diffraction response. Along the vertical line through the centre, $X_m = 0$, but h varies – just the conditions for a CMP Gather – so the times once again lie on a NMO hyperbola. Migration of the data from a common-offset traverse over a diffractor now takes the form indicated by arrows on [Figure 8.5](#) – summation along the flattened hyperbola, followed by NMO correction to bring the summed data to the summit of the pyramid.

8.3.2 PSTM and Image Gathers

[Figure 8.6](#) summarizes the process of prestack time migration for the case of a single diffraction point. We know that whatever works for that will work equally well to migrate any reflection, since a reflection is the sum of innumerable diffraction points. The three diffraction curves from [Figure 8.4b](#) are shown as they might appear on three separate constant-offset sections, one a zero-offset section and the other two with half-offsets, h , of 500 and 750 metres. Migration by Kirchhoff diffraction summation condenses the data to a burst of energy at the diffraction point on all sections. After migration, each diffraction image appears at the time of the summit of its diffraction curve, a different time for each image. Thus, in [Figure 8.5](#), the times lie on the vertical line through the pyramid where $X_m = 0$. The NMO correction will bring all the images up to the summit time of the pyramid, the zero-offset reflection time for the diffractor ([Figure 8.5](#)).

[Figure 8.6](#) Generalized processing sequence in prestack time migration (PSTM) for the case of a single diffractor.



One of the benefits of migration by Kirchhoff summation is the opportunity to perform velocity analysis between migration and stacking. [Figure 8.6](#) shows how traces for the same surface CMP location, but with different offsets, can be taken out of the migrated sections and presented as a gather suitable for velocity analysis, usually described as an image gather. The traces are all generated from the same subsurface reflection point, so they can also be called a Common Reflection Point (CRP) gather. The basic concept was first published in 1974 by Gardner *et al.* (1974b), but it was to be another 20 years before computer capability advanced enough for the industry to adopt it economically.

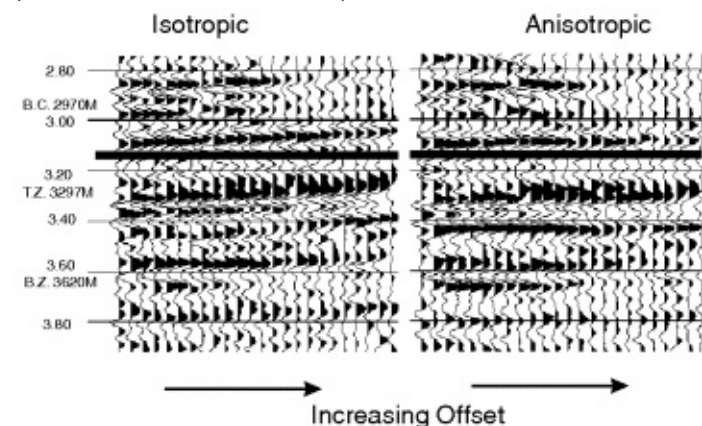
In [Figure 8.6](#), the image gather is ready for NMO correction to be applied. When that is done, the diffraction images should lie on a flat line running across the gather, just as they would on a conventional velocity analysis (see [Figure 3.5](#) and Tutorial 6.2). If necessary, the migration velocity can be fine-tuned at this point and the data re-migrated. When all reflections in the image gather are flat, the data can be stacked into a single trace and the traces finally displayed as a stacked migrated section. Alternatively, you can view the process as a final stacking of one-fold migrated sections as in [Figure 8.6](#).

Of course, we need to have reasonably good velocities in order to migrate the data in the first place, and those velocities will be acquired from well data and by conventional velocity analysis of the CMP data, possibly optimized by the use of DMO correction. The image gathers can then be used to fine-tune the velocities in areas of complex structure. [Figure 8.7](#) shows how an initial assumption of isotropic velocity in the geological section gave image gathers with anomalously short times at long offsets (times here converted to depth), but use of anisotropic velocity

flattened the events in the image gather. As a result, well ties to the seismic data were greatly improved (Hawkins *et al.*, 2001).

Figure 8.7 Image gathers corrected for NMO. On the left, the assumption of isotropy has made the correction velocity too low, so the reflections are over-corrected. Using anisotropic velocity flattens the image gather.

(From Hawkins *et al.*, 2001)



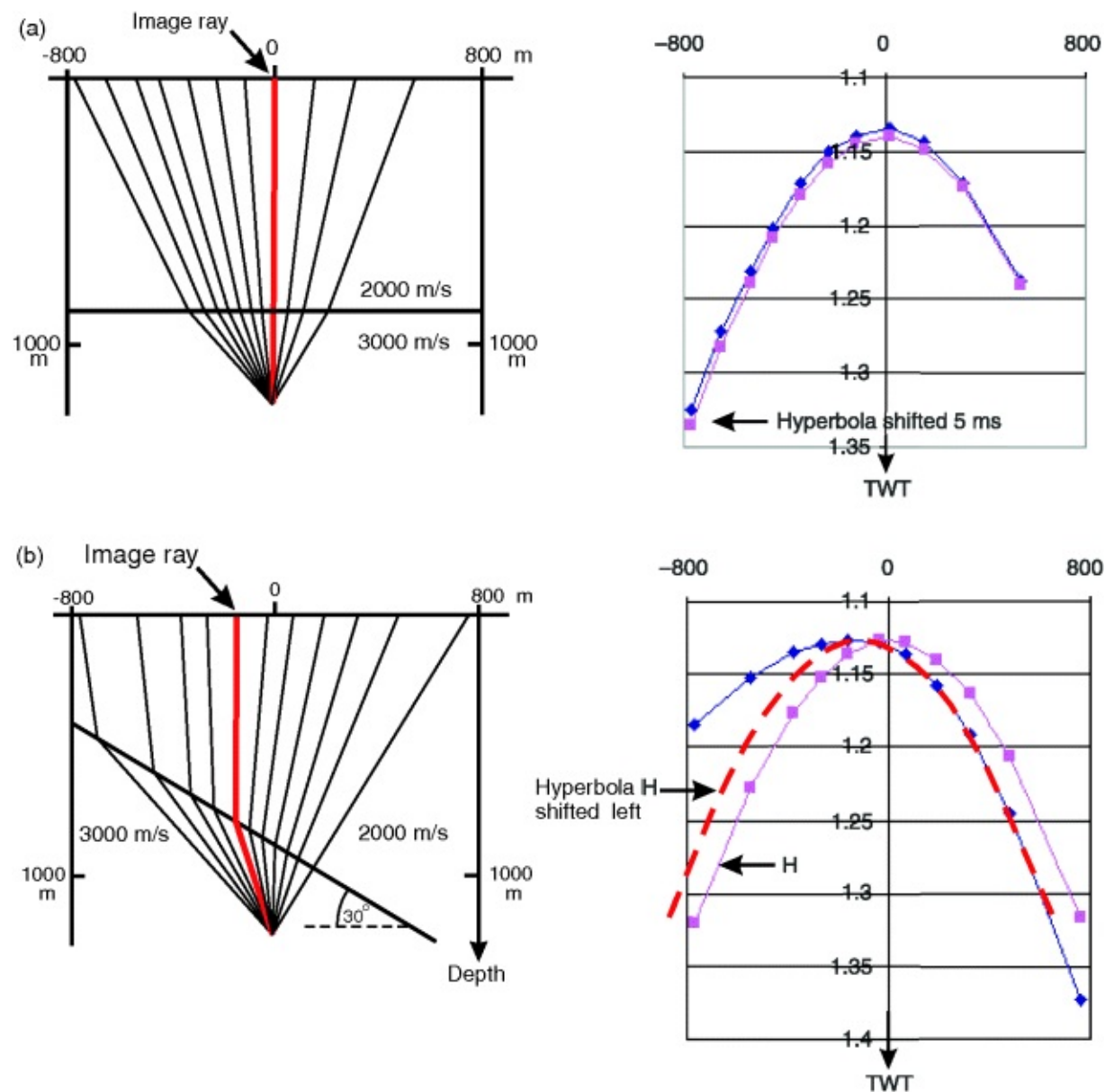
8.3.3 The Limitations of PSTM: Lateral Variations in Velocity

In Section 8.1, lateral variation in velocity was identified as the second disturbing factor in the creation of an accurate subsurface image. It will occur as soon as dip appears in the section, or from lateral facies variation, or from structural juxtaposition of units of different velocities. Once again, we need only consider what happens to the migrated image of a single diffractor, since reflections are made up of many such images. In [Figure 8.8a](#), the strata are flat, velocity varies only with depth and the ray-traced diffraction curve (in black) is almost indistinguishable from the hyperbola (in red) calculated for a uniform average velocity down to the diffractor. Time migration will provide a good subsurface image. Note the presence of the ray that emerges vertically at the surface, corresponding to the summit of the hyperbola. This is given a special name – the ‘image ray’.

Figure 8.8 Ray-path diagrams and diffraction curves for an earth model:

- a. with no lateral variation in velocity;
- b. with such variation.

Black curves are diffraction curves derived from ray-tracing. Red curves are simple hyperbolae calculated with rms velocity and with the same summit time as the black.



In [Figure 8.8b](#), a dipping interface separates two layers of different velocity. The average velocity down to diffraction points will vary across the section, from high on the left to low on the right. The times to the diffractor now lie on a distorted hyperbola, whose summit is displaced up-dip from the true position of the diffractor. Time migration will proceed trace by trace across the section, using summation along a simple hyperbola.

On some trace to the left of the diffractor position, migration will proceed through summation along the red, shifted hyperbola in [Figure 8.8b](#). The shifted hyperbola coincides with enough of the diffraction curve to produce some sort of image, but image quality would be a lot better if summation could be done over the black diffraction curve. The image is placed at the summit of the shifted hyperbola so, although a usable image may be achieved, it is actually mis-located. One again, the image ray emerges vertically at the surface over the crest of the hyperbola, but now it is displaced over 100 metres away from the true subsurface position of the diffractor!

To summarize, there are two problems with time migration where the structure and velocity varies laterally:

1. The migrated waveform is not well reconstructed. It has a poorer S/N ratio than it might ideally have and also has a distorted wavelet shape.
2. The migrated image is in the wrong place.

Not for the first time in reflection seismology, it seems that just when we think we have solved

one problem, yet another pops up!

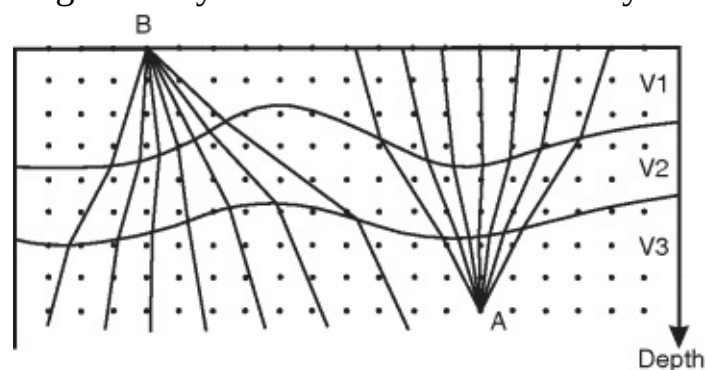
Can time migration really be that bad? Complete the worked example in Tutorial 8.2 and see how tracing the image ray through the flank of a salt diapir reveals gross mis-location of faults in the reservoir below, after time migration.

8.4 Prestack Depth Migration (PSDM)

Somehow, we have to take account of the lateral variation in velocity in our migration scheme. Instead of summing the seismic data amplitudes over a hyperbola, we must sum over a ray-traced diffraction curve like the black curve in [Figure 8.8b](#). Obviously, we need to have a velocity-depth model to carry out the ray-tracing – so, not for the first time in seismology, it seems we need to know the answer before we can work it out! The starting point will be an initial depth section, prepared by picking reflections on the time-migrated section and converting to depth using a combination of well-derived and seismic-derived velocities. A commonly used approach to constructing the initial velocity-depth model is described in the next section (8.4.1).

Imagine a grid of points placed over the depth section, as shown schematically in [Figure 8.9](#). We treat each grid point as if it were a diffractor with particular X, Z coordinates (e.g. point A in [Figure 8.9](#)). At each point, ray-tracing through the depth section to the surface will give us the shape of the diffraction curve as a set of T, X values. Next, we go to the common-offset section, seek out the seismic data amplitudes at those T, X points (the black curve in [Figure 8.8b](#) on a zero-offset section) and sum them in the usual way of Kirchhoff migration, weighting the samples in the summation according to the length of ray and its angle of emergence at the surface. Now we can capture all the relevant data values around the summation curve, so the waveform is properly formed and the S/N ratio is better. Finally, we place the sum not at the crest of the diffraction curve, but at the (X, Z) position of the diffractor on the depth section.

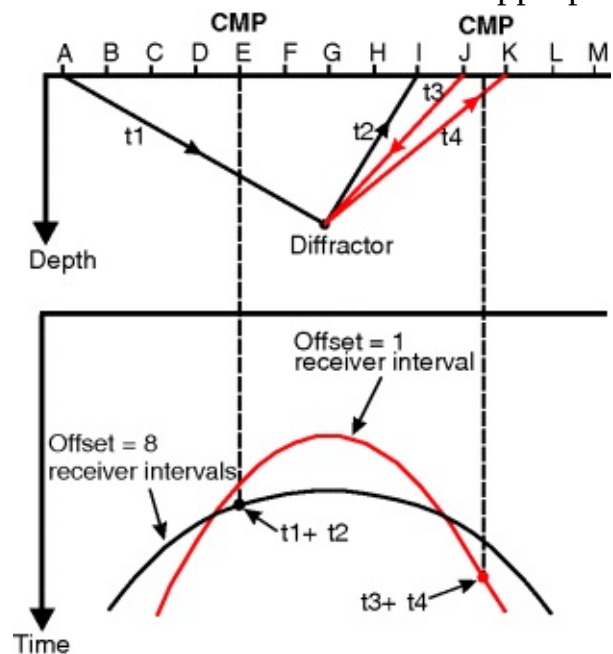
Figure 8.9 Ray-tracing through a velocity-depth section to establish diffraction curves for depth migration by the Kirchhoff method. Layer velocity V_2 is greater than both V_1 and V_3 .



Ray-tracing is computationally intensive, in that a ray must join every surface recording point to every subsurface grid point within the aperture of the migration ([Figure 8.10](#)). Even in the sparse grid of [Figure 8.9](#), with a spacing of roughly 500 m, this means tracing approximately 1,500 rays. What we really need is a grid spaced at the survey trace interval, perhaps as close as 12.5 m. Two short cuts are thus made to lessen the computational load. First, diffraction curves are calculated by ray tracing for rather widely spaced grid points (say, 50 m), and the times are interpolated between those down to a finer grid spaced at the survey trace interval. Second, if the rays from a surface point like B in [Figure 8.9](#) are traced downwards, they will provide times from the surface point to interpolated grid points at all deeper levels in a single pass (Gray, 1986). In contrast, the

set of rays traced upwards from a point such as A in [Figure 8.9](#) provides times from A to the surface level only.

Figure 8.10 When one-way times from a diffractor to all receiver points on the surface have been found by ray-tracing, the two-way diffraction curve for any common-offset section can be constructed from the sums of appropriate one-way times.



The improvement in depth-migrated sections over time-migrated sections is especially striking in places like the Gulf of Mexico or the southern North Sea, where mobile salt gives rapid lateral variations in velocity. [Figure 8.11](#) shows an example where major improvement in the image of the salt base and the sub-salt area is evident. Note also the general increase in resolution and clarity of reflections, even above the salt, when the data are depth-migrated. [Figure 8.12](#) shows a spectacular example of the improved subsurface imaging provided by prestack depth migration.

Figure 8.11

- a. 2D prestack time migration.
- b. 2D prestack depth migration.

(From Ratcliff et al., 1994)

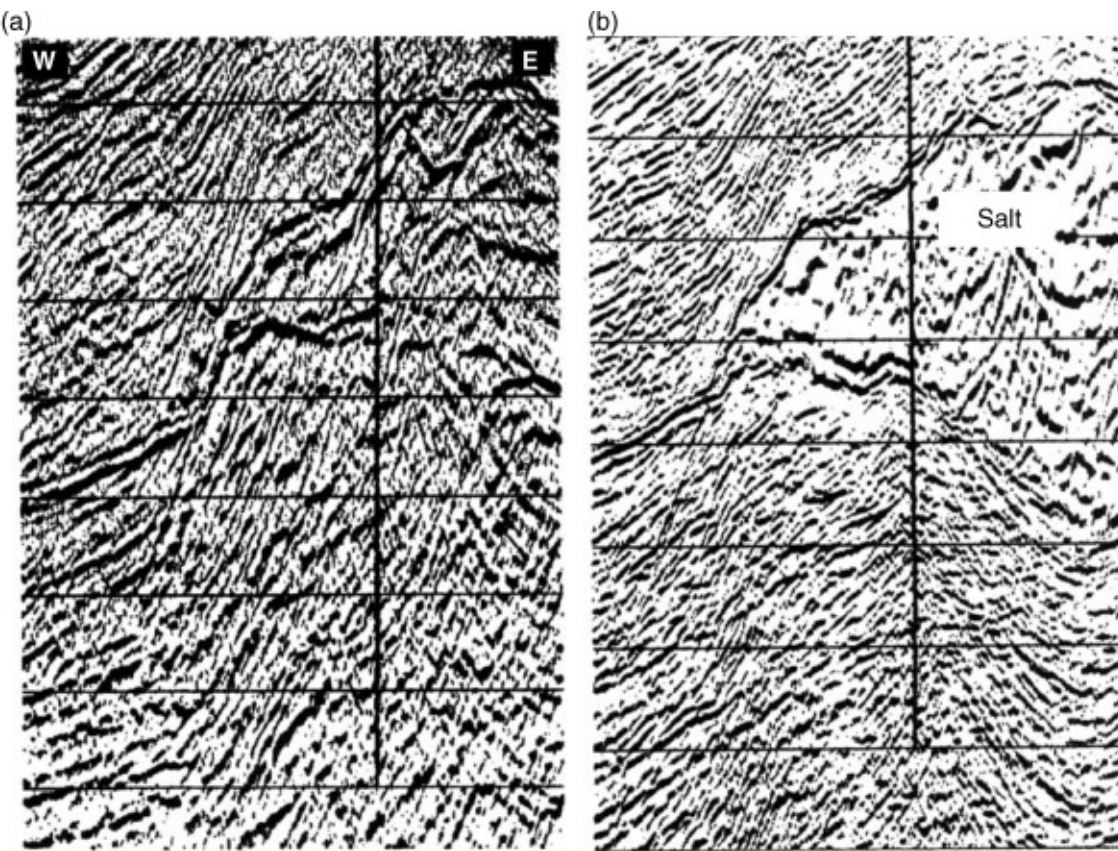
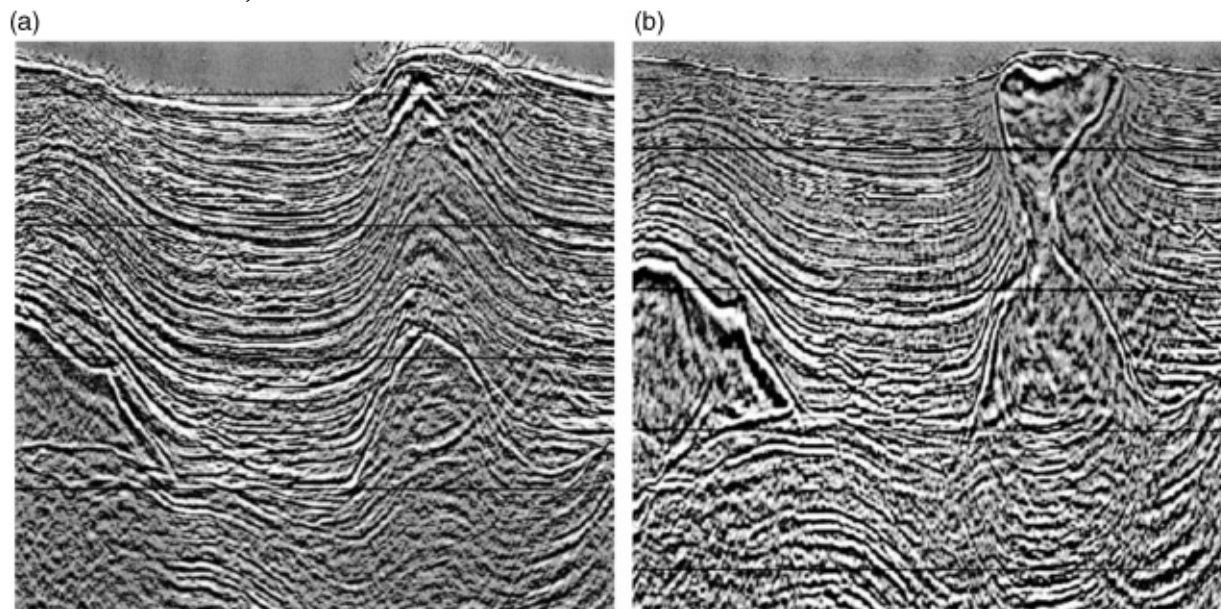


Figure 8.12

a. 3D prestack time migration.

b. 3D prestack depth migration. The emergence of the hour-glass salt diapir in **b** is a most remarkable feature.

From Albertin et al., 2001



8.3.4 Velocity-depth Model Based on Layers

In Tutorial (interpretation of West Sole data), a very simple velocity-depth model was used to convert time to depth. Average velocity from the surface to the target horizon was established from velocity analyses at sparse control points and smoothed by contouring (see [Figure T7.4.7](#) in Tutorial 7.4). However, in order to carry out ray-tracing of the type shown in [Figure 8.9](#), a much more detailed velocity-depth structure is required. One of the commonest strategies is a top-down,

layer-by-layer approach employing image ray tracing (Yilmaz, 2001).

The ideal starting point is a prestack time-migrated section on which key horizons have been picked and timed. Prestack image gathers will be available which refer to true CRPs in the subsurface ([Figure 8.6](#)). Velocity analysis of these gathers can be made at closely spaced intervals (≈ 500 m) along the section, and rms velocities at the times of the key horizons can be picked from the analyses. Some smoothing of the rms velocities along horizons may be done.

The next step is to calculate layer velocities between the picked horizons by means of the Dix equation ([Equation 6.6](#)). With all layer velocities and horizon times now available, conversion to depth may be done by image-ray tracing (map-migration) to take account of the lateral shifts inherent in time migration, a process carried out layer by layer from the top down (see Tutorial 8.2). Image-ray tracing can be extended to three dimensions as shown in [Figure 6.5b](#), but now the ray starts down at right angles to the surface. The final result is a velocity-depth model with all the picked horizons defined in depth, ready for diffraction-point ray-tracing and Kirchhoff PSDM.

After migration, traces created at one particular location can be selected out of the one-fold depth-migrated sections and assembled into image gathers as in the case of PSTM ([Figure 8.6](#)). However, in PSDM they are now scaled vertically in depth instead of time. If the velocity model is accurate, reflections on the gathers should be flat. If velocity was too low, the reflections at long offsets will be too shallow, so the reflections in the image gather will curve upwards (check [Figure 8.7](#) again). If the velocity is too high, the reflections in the image gather will curve downwards. Deviations from flatness (residual move-out or RMO) can be used to adjust velocities in the initial depth section. It is, of course, essential to make such adjustments layer by layer from the top down, because RMO on gathers from a deep layer could be caused by poorly chosen velocities anywhere in the section above it. Migration is repeated with the updated velocities until no further improvement appears.

8.3.5 Velocity-depth Model Based on Tomography

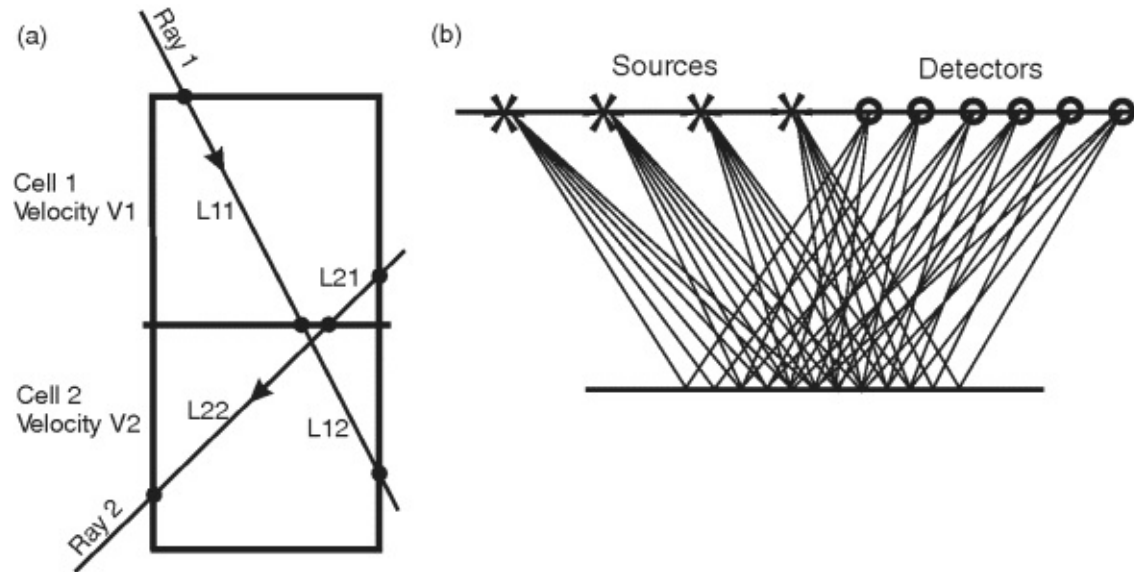
The word tomography comes from the Greek word *tomos*, which means a section. In medicine, Computer Aided Tomography (CAT) scans using X-rays are used to build up sections of the human body, and the same principle can be applied in seismology to build up velocity sections (or 3D volumes) of the subsurface. The basic idea is straightforward: wave energy is fired through the object of study along a variety of raypaths, and some property of the wave is recorded at the end of the travel path. By analyzing variations in the measured property, we can map out the distribution of some feature within the object.

In seismic applications, the property that is recorded is the travel time from source to receiver, and the feature that is mapped is the seismic velocity within the volume traversed by the rays. To analyze the results, the earth is divided into rectangular cells. In [Figure 8.13a](#), a very simple example is shown which consists of only two cells. The travel time along any raypath is the sum of times through the cells traversed by the ray, and a travel time equation can be written for each ray in terms of the distance traversed within each cell and the cell velocity. If the coordinates of the cells and of the source and receiver of the ray are known, the distance travelled within each cell can be calculated. Since the travel times are measured directly, the only unknowns in the travel time equations are the cell velocities. A collection of simultaneous equations is formed, and these can be solved for the velocities of the cells.

[Figure 8.13](#)

a. Principle of seismic tomography.

b. Even a modest set of surface sources and detectors provides a multitude of ray-paths for tomographical analysis – and this only in two dimensions.



In the simple example of [Figure 8.13a](#), lengths L_{ij} of the i th ray in the j th cell are known and travel times t_i are measured. Two simultaneous travel time equations can be set up:

$$t_1 = L_{11}/V_1 + L_{12}/V_2$$

$$t_2 = L_{21}/V_1 + L_{22}/V_2$$

which can be solved for the unknown cell velocities V_1 and V_2 .

Needless to say, complications arise in practice, notably that seismic raypaths are not straight, unlike X-ray paths through the body, and the number of simultaneous equations to be solved is enormous, since we can make use of the very large number of raypaths available in the course of surface seismic surveys ([Figure 8.13b](#)). Lines & Newrick (2004) include many references in an informative review of the topic.

Seismic applications of tomography include Vertical Seismic Profiling and well-to-well (crosswell) studies. For the large-scale velocity-depth model of the earth to be used in depth migration, we can make use of the very large number of raypaths available from surface seismic surveys ([Figure 8.13b](#)).

Tomography has proved particularly useful where there are no major velocity layers but simply an increase in velocity with depth caused by compaction in a clastic sequence, for example in the Gulf of Mexico (Fliedner *et al.*, 2002). However, it can also be usefully applied in layer-by-layer velocity modelling when a layer shows rapid velocity variations which are not expressed as reflection events. Such a hybrid approach has proved very useful in the southern North Sea Basin, where the Cretaceous Chalk layer often shows rapid velocity variations both horizontally and vertically (Whitfield *et al.*, 2008, Jones *et al.*, 2007).

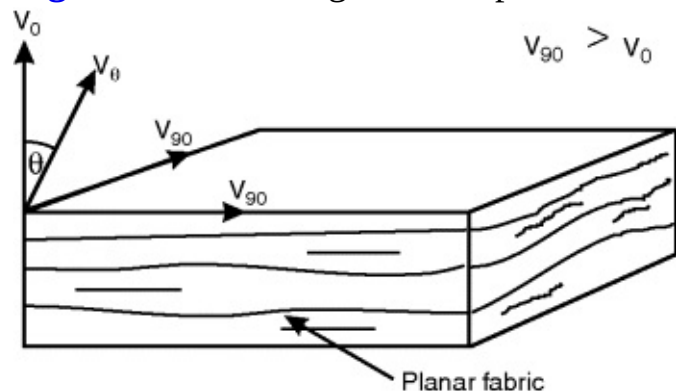
8.5 Anisotropy: the Ultimate Refinement in Velocity

You will be glad to know that we have reached the last refinement in building better subsurface images. A rock is said to be isotropic as regards velocity, if the velocity is the same no matter in what direction it is measured (from the Greek *iso*, equal and *tropos*, turn). That has been the assumption behind all the usage of velocity so far. In an anisotropic rock, the velocity varies with

the direction of measurement through the rock.

A rock with a distinct planar fabric, such as shale, will generally show velocity anisotropy, as the velocity measured parallel to the planar fabric is higher than that measured perpendicular to the fabric ([Figure 8.14](#)). The normal to the plane of the fabric is the polar axis, and this type of anisotropy is named polar anisotropy or Vertical Transverse Isotropy (VTI). A common measure of anisotropy is the ratio $(V_{90} - V_0)/V_{90}$ expressed as a percentage, where the subscripts refer to the angle of raypath relative to the polar axis ([Figure 8.14](#)).

Figure 8.14 Defining terms in polar anisotropy of velocity.



In flat-lying sediments, a planar fabric may develop parallel to bedding planes, so that the velocity measured in the horizontal direction will be higher than in the vertical, typically by about 10–20 per cent (Thomsen, 1986, Wang, 2002). Such anisotropy of velocity may also occur in a sequence of thin-bedded sediments, even if the individual beds are isotropic. Where beds are dipping, the polar axis may be tilted.

How does anisotropy of velocity affect the subsurface image? Referring to [Figure 8.9](#) and supposing the second layer to be anisotropic, with the polar axis roughly vertical, then rays passing obliquely through this layer will travel at higher velocities than vertical rays and the shape of the summation curve in Kirchhoff migration will differ from the isotropic case of uniform velocity. If the data is processed isotropically and migration velocities are adjusted to achieve a sharp image, then it will be at the wrong depth. If it is processed isotropically to give the correct depth, then the image will be poorly focused and fuzzy. Only anisotropic processing using correct velocities on oblique raypaths will give a sharp image at the correct depth (Alkhalifa *et al.*, 1996).

Anisotropic processing was a latecomer to the seismic scene for a variety of reasons (Peng & Steenson, 2001):

1. It is difficult to see the main controlling factors in the exact mathematical description.
2. Anisotropy may only affect one formation in a sedimentary sequence, and only to a small degree. The effect on much data may be very small.
3. It is difficult to detect. For example, it is not apparent in standard velocity analyses.
4. Its main effect (depth mis-ties) was often disguised in the general uncertainty of depth calculations. However, serious mis-ties of seismic to well data of up to 300 m may be found where thick anisotropic sections occur.

Why are the mathematics so intractable? You will recall from Chapter 4 that the velocity of an isotropic rock depends on two elastic constants – the bulk modulus (stiffness) k and the shear modulus μ . In an anisotropic rock, the elastic constants depend on direction. For example, the shear modulus measured parallel to the planar fabric is different from the shear modulus

measured across the fabric. For polar anisotropy, there are five independent constants to be considered, leading to complex expressions for velocity that make it impossible to see the important controls.

Thomsen (1986) showed that, because anisotropy is generally weak, simplifications could be made. He encapsulated several elastic constants into just two new parameters – ε and δ – with which velocity for a ray at an angle θ to the polar axis could be written:

$$(8.2) V_{\theta} = V_0[1 + \delta \sin^2 \theta \cos^2 \theta + \varepsilon \sin^4 \theta]$$

with the angle θ defined as in [Figure 8.14](#). When $\theta = 0$, $V_{\theta} = V_0$. When $\theta = 90^\circ$, $V_{\theta} = V_0 [1 + \varepsilon]$, hence $\varepsilon = (V_{\theta} - V_0)/V_0$, the conventional measure of anisotropy. The δ parameter is especially important because it also occurs in another important finding. A CMP gather from an anisotropic formation looks quite normal, with reflections following hyperbolic paths, but now the short-offset stacking velocity is given by the equation:

$$(8.3) V_{\text{nmo}} = V_0(1 + \delta)$$

Any velocity model made on this basis, for example by calculating Dix-type interval velocities, will end up with velocities that are too high. They will thus give seismic depths that are too deep – a strong indication of anisotropy in the section above (Thomsen, 2002).

How does anisotropy affect time migration? You will recall from Section 4.7.1 in Chapter 4 that a reflection on a CMP gather from the base of a single layer of uniform velocity V will lie on a hyperbola exactly described by the equation:

$$T_x^2 = T_0^2[1 + R^2]$$

where $R = X/T_0V$ and $T_0 =$ zero-offset TWT.

When the layer is anisotropic, the reflection deviates from a hyperbola especially at long offsets and the travel-time equation requires an extra term. Alkhalifah & Tsvankin (1995) succeeded in reducing the inevitable complications down to a single extra parameter η (Greek eta), which is defined in terms of the Thomsen parameters for the layer as:

$$(8.4) \eta = (\varepsilon - \delta)/(1 + 2\delta)$$

The time equation for the reflection on the CMP gather becomes:

$$(8.5) T_x^2 = T_0^2[1 + R^2/(1 + \eta)]$$

Velocity analysis is more complicated, because we have to find not just the variation of velocity with time, but also the variation of η . However, when that is done, we have all we need both to stack the data and to perform time migration, for example by Kirchhoff diffraction stack along a diffraction curve defined in accord with the revised offset travel time.

How does anisotropy affect depth migration? To carry out ray-tracing in the manner of [Figure 8.9](#), we need to calculate V_{θ} values from [Equation \(8.2\)](#), so now we require δ and V_0 , the velocity in the direction of the anisotropy axis, the vertical direction in flat-lying strata. Velocity analysis is no help, because [Equation \(8.3\)](#) shows that we cannot separate out the V_0 and δ terms from the observed V_{nmo} value (short-offset stacking velocity). Instead, we must make use of well data.

We are not going to follow out anisotropic migration in any more detail in this book. It is fair to say that when you need it, nothing else will do, a point that is well illustrated in the context of PSDM by a paper by Hawkins *et al.* (2001). The goal of that project, in the southern North Sea basin, was to improve ties to wells at the Zechstein level, where seismic depths after isotropic PSDM were as much as 300 m too deep. The anisotropic formation was the Cretaceous chalk and

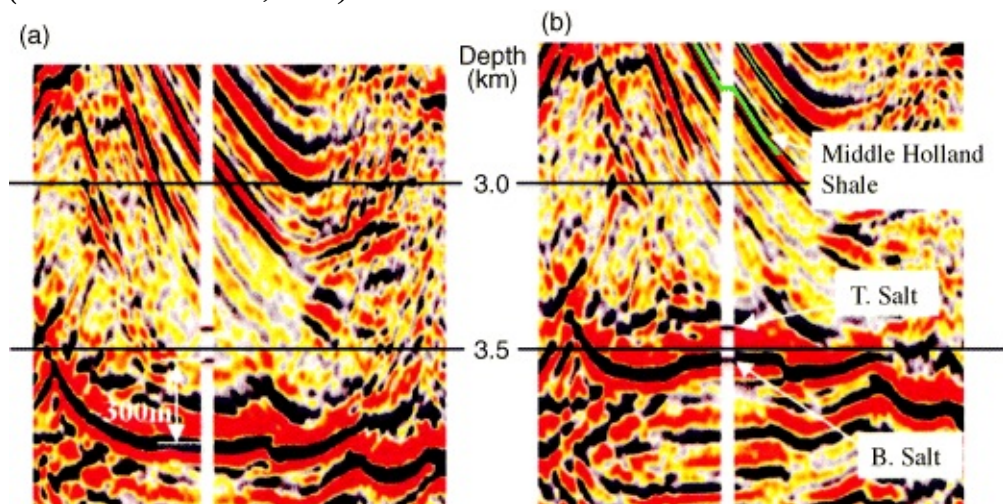
the anisotropy seemed to be controlled by depth even where the beds were dipping. Not only were depth mis-ties eliminated ([Figure 8.15](#)), but details of the subsurface image, such as fault locations, were significantly improved by anisotropic migration.

Figure 8.15 Data from the southern basin of the North Sea.

a. PSDM using isotropic velocities.

b. PSDM using anisotropic velocities in the Chalk section (above the section shown). The white line marks a well. The mis-tie at Base Salt level in a is 300 m.

(From Hawkins et al., 2001)



8.6 Velocity-depth Ambiguity

Are we now home and dry with a correct geological depth section of the subsurface structure? Not necessarily! All we ever measure is TWT on the unmigrated time section, and in depth migration we juggle velocity and depth to satisfy the time measurements. Suppose we check the travel times generated by our interpreted earth model against observed TWT and find they are the same, so the fractional error in time is zero. Lines (1993) showed by analysis of a single layer that, in the case of *zero offset data*, the fractional error in time (dT/T) is related to the fractional errors in depth Z and velocity V by the equation:

$$dT/T = dZ/Z - dV/V$$

So we can easily get zero error in time by a combination of wrong velocities and wrong depths.

Methods of velocity analysis, of course, depend on analyzing variable-offset data. How do we know any final section is 'the truth'? One standard of truth is the unmigrated raw time section, which would look exactly the same if we came back a hundred years later and shot the same survey. Thus, one ultimate check is to use ray-tracing on the final depth-migrated section to generate reflection times (by zero-offset rays, as in [Figure 5.7](#), or by constant-offset rays) and compare them to the original unmigrated data. If the reflections tie all the way down the section, we can be more confident that it represents reality. The ultimate standard of truth, of course, is to drill a well and tie to depths measured down the well.

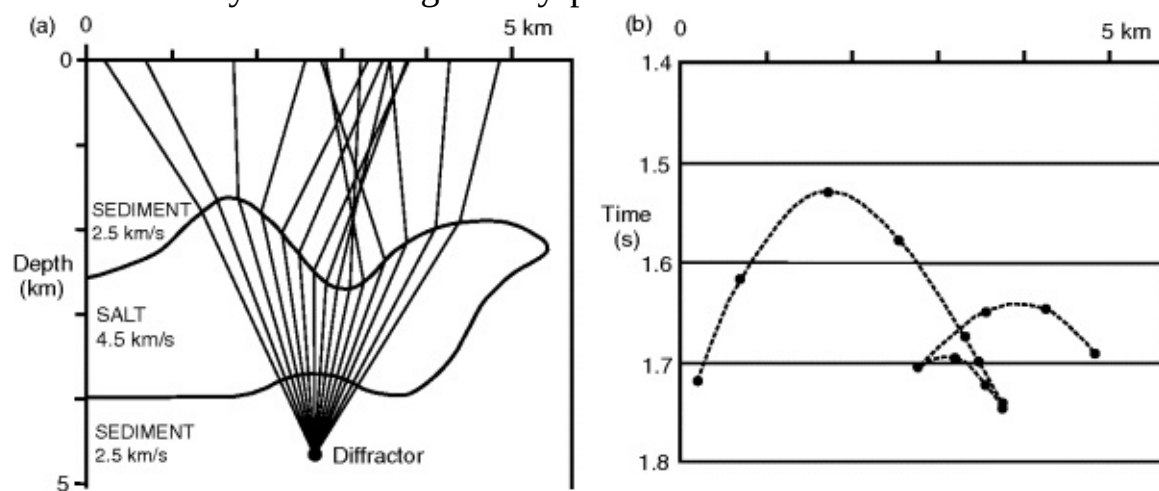
8.7 Future Migration Technique: Kirchhoff or Wave Extrapolation?

Throughout this book, the emphasis has been on Kirchhoff migration because it ties back to the notion of the reflection as an amalgam of diffraction hyperbolae and facilitates an intuitive grasp of the process. It has long been the commonest method throughout the industry, because of its cheapness compared to wave extrapolation, especially in 3D, and because it enables adjustments to be easily made to the velocity model of the earth through residual move-out analysis on common-image gathers.

Computer advances since about 2000 have enabled reductions in the cost and time of the calculations and made wave extrapolation quite feasible as a routine tool in 3D processing. The method makes use of the full wavefield that may develop through complex structure, not just the first arrivals determined by ray-tracing. In [Figure 8.16a](#), rays have been traced from a diffractor at depth to the surface through a salt body similar to those found in the Gulf of Mexico. The rays follow multiple paths, so the travel times ([Figure 8.16b](#)) now fall on three separate hyperbolae, which makes it difficult to define the summation path in Kirchhoff migration. However, since the recorded wavefield at the surface captures every structural detail, that detail will be incorporated in the structure finally delineated at depth in the course of migration by wavefield extrapolation.

Figure 8.16

- a. Raypaths from a diffractor up to the surface through a salt body.
- b. One-way times along the ray-paths shown in a.

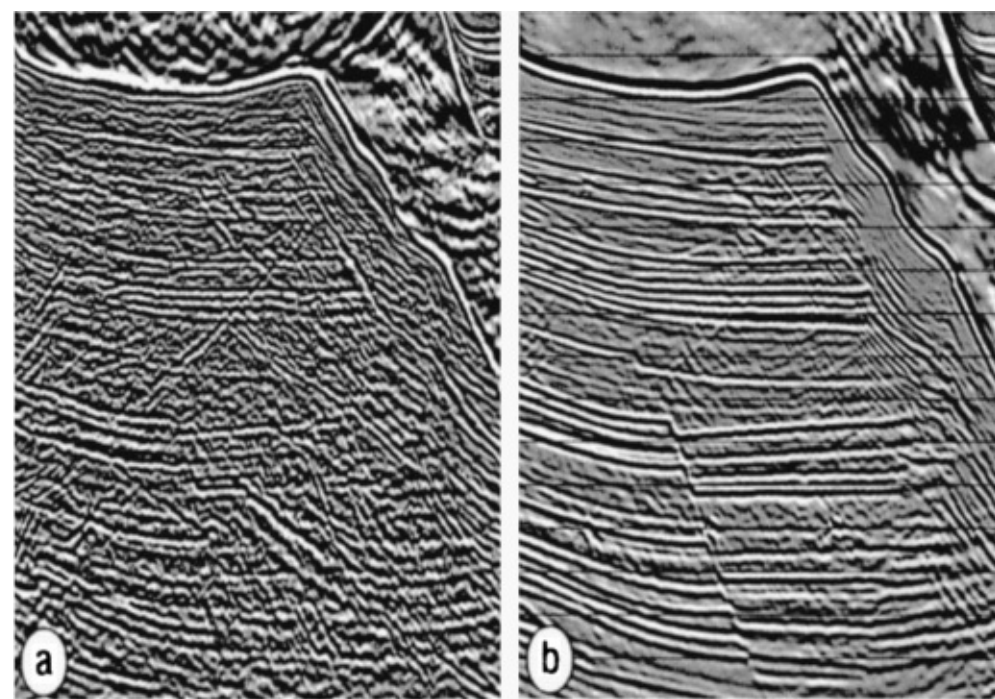


Pharez *et al.* (2005) discuss the pros and cons of the two approaches, pointing out that residual move-out information can now be derived to update the velocity model even in wave extrapolation. They give several examples, from different seismic environments, where migration by wave extrapolation seems to clarify the section better than Kirchhoff migration. This is especially so in sub-salt structures ([Figure 8.17](#)). It looks as if wave extrapolation will be the preferred method in the future.

Figure 8.17

- a. Kirchhoff migration of a test set of synthetic seismic data (Sigsbee A model).
- b. Migration of the same data by wavefield extrapolation.

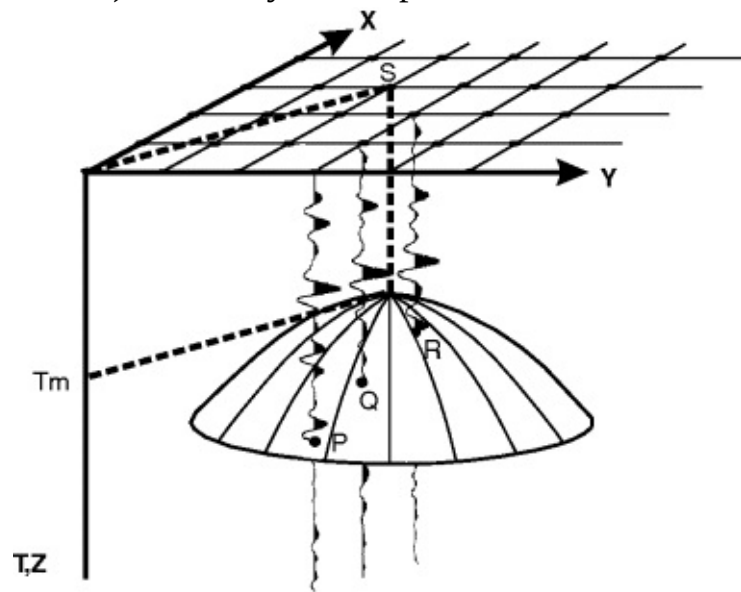
From Pharez *et al.*, 2005



8.8 3D Migration

All methods of migration discussed and illustrated so far for 2D sections can be extended to 3D. The simplest and cheapest is post-stack time migration of CMP-stacked, zero-offset traces. The traces are acquired by shooting over a survey area in the manner of [Figures 3.7](#) or [3.8](#). Thus they are no longer confined to a section, but form a data volume of traces referenced to a grid of surface locations ([Figure 8.18](#)).

Figure 8.18 Kirchhoff migration of 3D CMP-stacked data. Data samples found over the surface of the search hyperboloid are scaled, summed and plotted at time T_m on a new migrated trace (not shown) vertically below point S.



In Kirchhoff migration, the summation of data samples is no longer over a hyperbolic time-curve in two dimensions, but has to be done over a 3D time-surface called a hyperboloid, shaped rather like an umbrella and generated by rotating the 2D hyperbola about its vertical axis. Like the 2D hyperbola, only the summit time (T_m in [Figure 8.18](#)) and the velocity down to that time are

required to generate the hyperboloid. Data samples which fall on the surface of the hyperboloid (like P, Q and R in [Figure 8.18](#)) are suitably scaled and summed, and the sum is plotted at the time and location of the crest of the hyperboloid to form one sample of a new trace located at S. The process is repeated for the next hyperboloid, one sample interval deeper, and calculated with a new value of T_m and a new velocity, until the entire migrated trace has been built up sample by sample at S. Finally, the entire procedure is repeated at every grid point until a new volume of migrated traces has been formed.

To build up a new trace at every grid location of the survey clearly demands a very large amount of computation. In 3D prestack depth migration, the computational load is even heavier. The summation time-surface is no longer a simple hyperboloid defined by its summit time and velocity; now, a pseudo-hyperboloid surface has to be defined by 3D ray-tracing through the velocity model of the earth (imagine [Figure 8.9](#) or [Figure 8.16](#) with an added third dimension!). Migration by wave extrapolation can also be extended to three dimensions, again with a heavy computational cost.

8.9 3D Seismic Interpretation

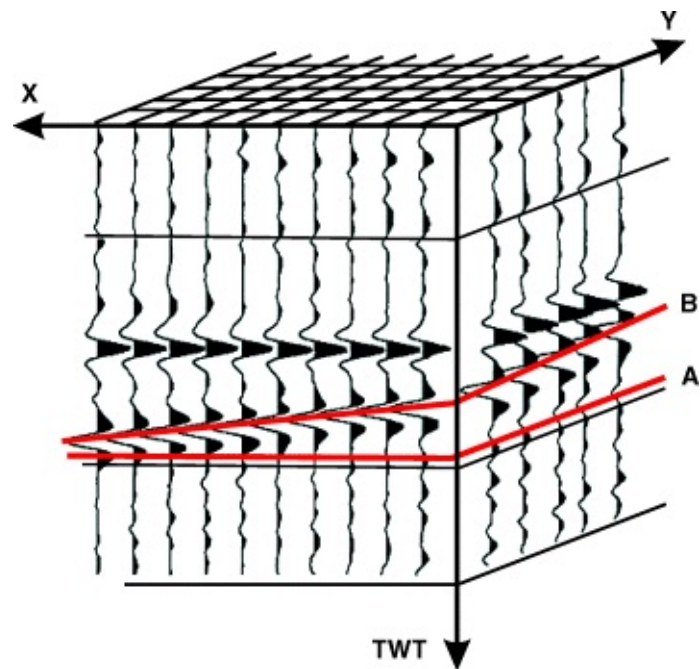
Needless to say, whole books have been written about the interpretation of 3D seismic data (Brown, 2004, Bacon *et al.*, 2003). In this section, we will simply take a quick look at basic structural interpretation; other aspects of 3D interpretation will be followed up in Chapters 10 and 11.

You will recall from Chapter 7 that the two big problems with the interpretation of 2D seismic sections are the presence of sideswipe and the low density of information, which makes contouring structures and connecting faults on structural maps problematic. Sideswipe is completely eliminated by 3D migration, there are no ‘sides’ any more and reflection energy from all around the recording location is drawn into the point of summation at the summit of the hyperboloid. But the truly revolutionary aspect of 3D data is the opportunity to create horizontal sections through the 3D data volume. Since the grid spacing of the survey is the same as the trace spacing in a 2D section, the information is displayed at the same high density and geological features can be mapped across the survey area at the same high resolution.

Time-slices are horizontal sections taken parallel to a time plane. The amplitude of the seismic signal at the same TWT on each trace is plotted out on a map at the coordinates of the trace location ([Figure 8.19](#)). Geologists are comfortable with time-slices because they give the same view of structure as that displayed in a geological map. Reflections now form ‘outcropping’ bands running across the map, displaying arcuate forms or closures around structures and discontinuities across faults (Tutorial 8.3).

Take a look at some 3D data in Tutorial 8.3 and see how a time-slice is essentially a subsurface geological map.

[Figure 8.19](#) A 3D seismic data volume. A is a time-slice and B is a horizon slice.



A horizon slice is formed by mapping out the amplitude of the seismic signal along a particular reflection that has been picked across the area (Figure 8.19). It enables the interpreter to focus on a particular stratigraphic level in the subsurface and to map variations in the seismic response that may relate to variations in rock properties at that level, such as porosity or fluid content.

Vertical sections are now possible in any orientation through the data, for example along a zig-zag course across the map area, linking a set of wells to enhance the process of stratigraphic correlation from well to well. In-line sections are in the direction of the original receiver lines in the field, cross-line sections at right angles to that.

Choosing the reflections to pick is done with the aid of synthetic seismograms at well locations, as before, and some convenient feature of the waveform (peak, trough or zero-crossing) is digitally marked in the data set and on screen. The high spatial density of the 3D data allows much of the picking of the reflections to be done automatically by the computer program.

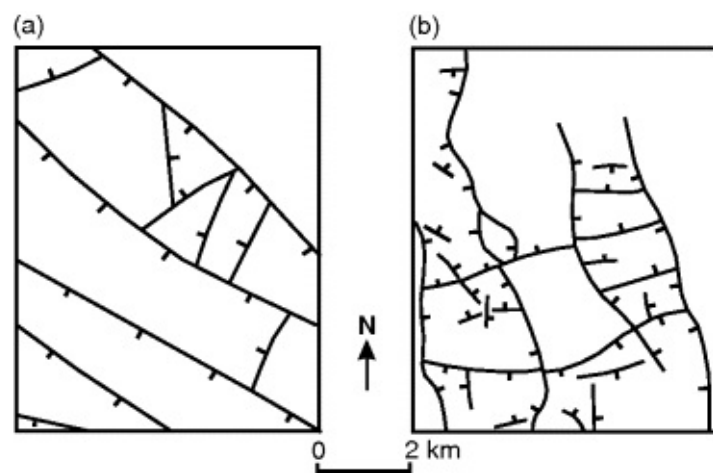
Initially, the process will be closely monitored by the interpreter on a number of 'seed' lines, and it may be necessary to pick the horizon through areas of poor data manually. It is normal practice to pick about every 10th line semi-manually and then to let the autopicking process fill in the areas between. Herron (2000) points out some of the problems and pitfalls that may arise in the course of this process. The old bottlenecks in manual interpretation, like measuring TWT and plotting up and contouring time and depth maps, are now bypassed. Conversion to depth is dramatically improved by the greater density of velocity analyses available, and contouring of structural surfaces can now be reliably done automatically.

The old uncertainties about the trend of faults in 2D data are gone. Indeed, one of the striking differences between 2D and 3D seismic structure maps is the huge increase in the number of faults recognized in 3D data (Figure 8.20). Faults are often so numerous that automatic methods of detection have had to be developed to speed up interpretation. We will see more on that and other topics in 3D interpretation in Chapters 10 and 11.

Figure 8.20

- a.** Faults interpreted from 2D unmigrated data, 1969.
- b.** The same area, but interpreted from 3D migrated data, 1988.

(After Nestvold, 1991)

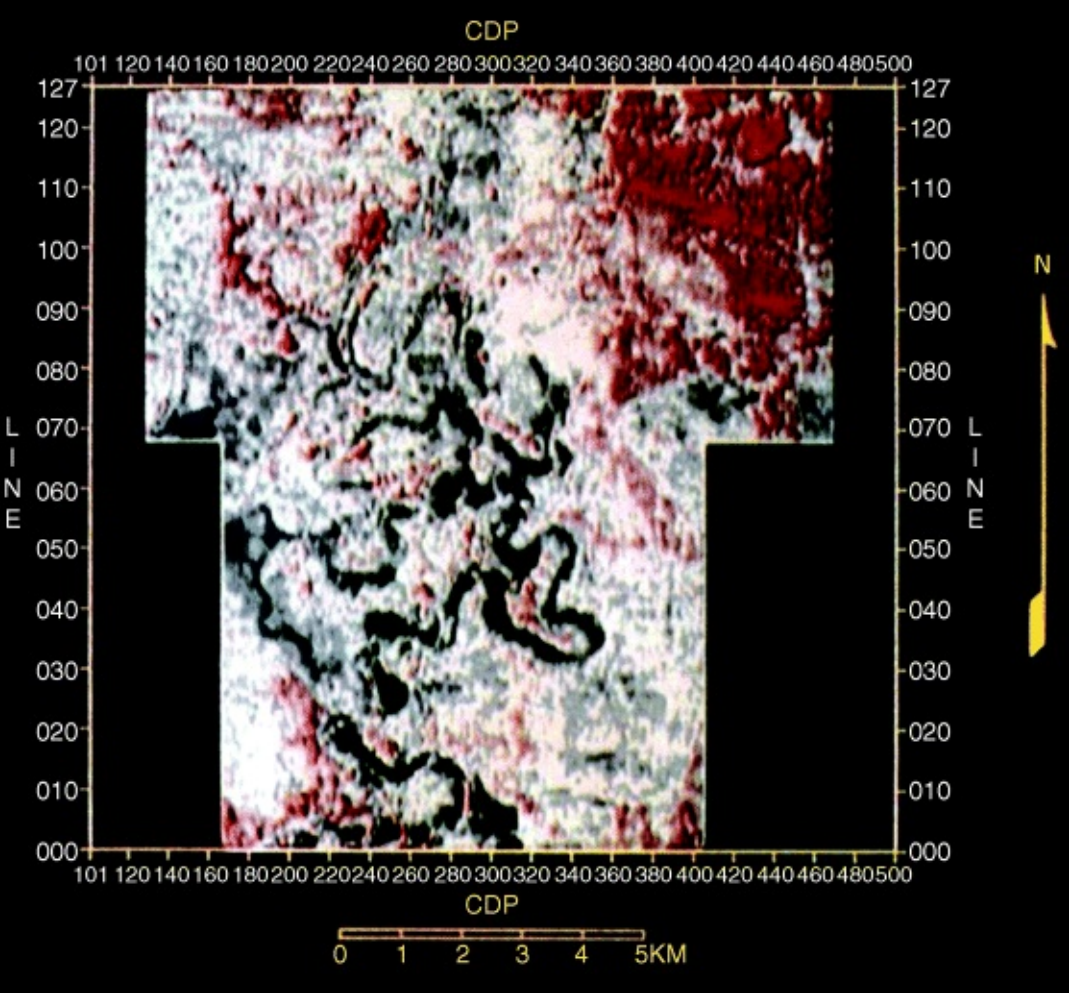


8.10 Growth and Impact of 3D Seismic Surveys

The history of 3D seismic surveying provides a classic example of how our scientific view of the world is defined by the available technology. The first surveys were done in the late 1960s by Esso (Walton, 1972), but without on-screen computer graphics to facilitate interpretation (not to mention the high costs), there was little take-up by the industry for the next ten years. By the early 1980s, computer advances had allowed spectacular subsurface images to be displayed, which showed that the unique mapping property of 3D data could reveal hitherto inaccessible exploration targets. [Figure 8.21](#) shows a shallow time-slice in flat-lying Tertiary sediments from an early 3D survey in the Gulf of Thailand (Brown *et al.*, 1981). This striking image can only be interpreted as the buried meander belt of an ancient river system, a possible exploration target in a deeper section and quite impossible to detect from widely-spaced 2D sections.

Figure 8.21 A shallow time-slice in flat-lying Tertiary sediments from a 3D survey in the Gulf of Thailand. From Brown *et al.*, 1981.

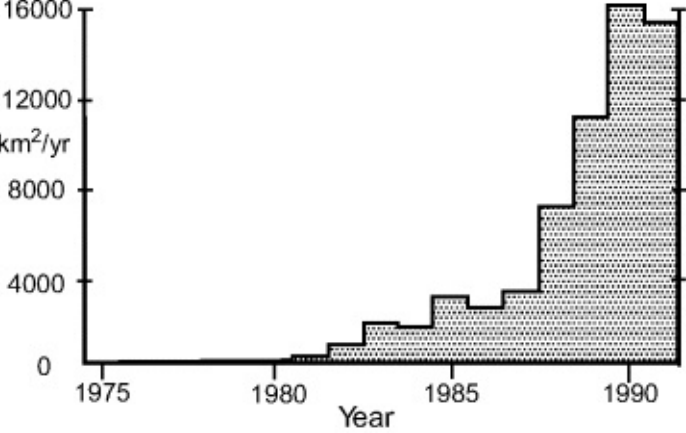
(Reproduced with the permission of the European Association of Geoscientists and Engineers (EAGE))



Images such as that in [Figure 8.21](#) helped to persuade the industry at that time that 3D seismic surveying was worthwhile. However, it was not until about 1987–88 that 3D surveys finally went into exponential growth ([Figure 8.22](#)). The bulk of seismic surveying is now carried out in 3D, although there will always be a place for 2D surveys in the very early assessment of a frontier area of exploration.

Figure 8.22 Growth in usage of 3D surveys by Shell, 1975–91, marine and land, excluding North America.

After Nestvold, 1991

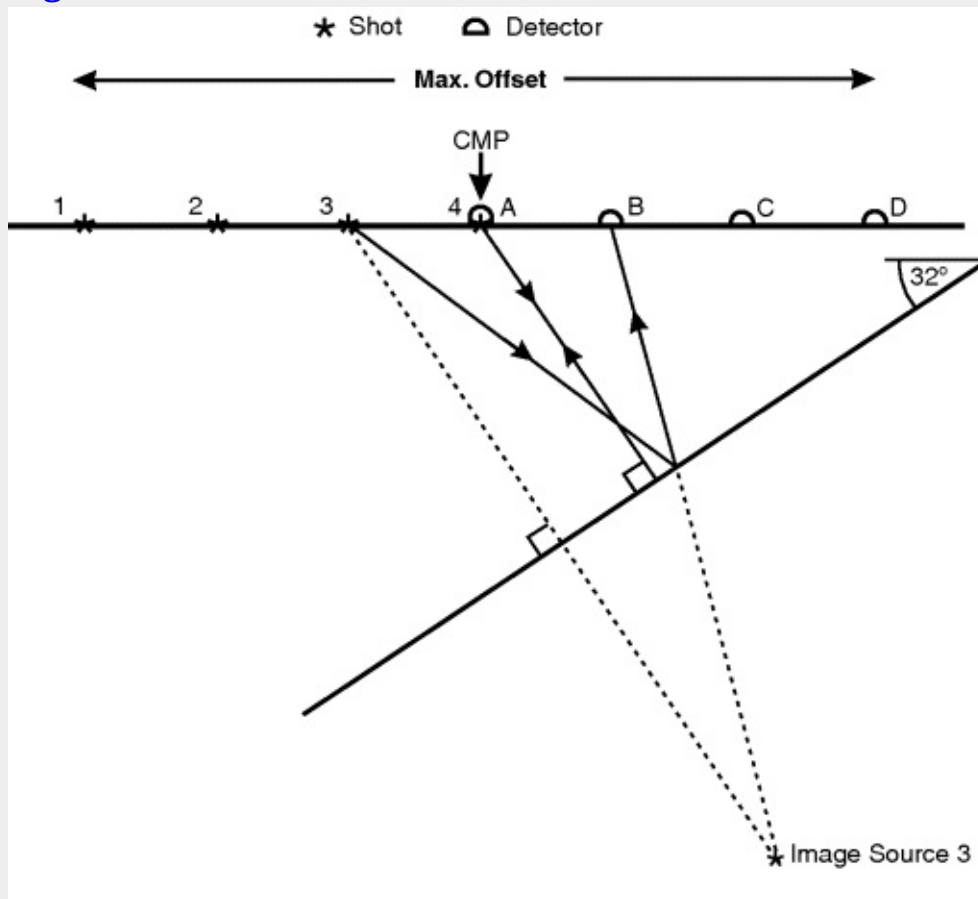


Tutorials for Chapter 8
Tutorial 8.1

Purpose: To show reflection point dispersal of CMP raypaths from a dipping reflector

1. Note the construction used on [Figure T8.1.1](#) to locate the raypath from 3 to B. Use the same construction to find the image sources for shots 2 and 1 and draw the complete raypaths 2–C and 1–D. The reflection points are spread over a surprisingly large area up-dip from the point of normal incidence.

Figure T8.1.1



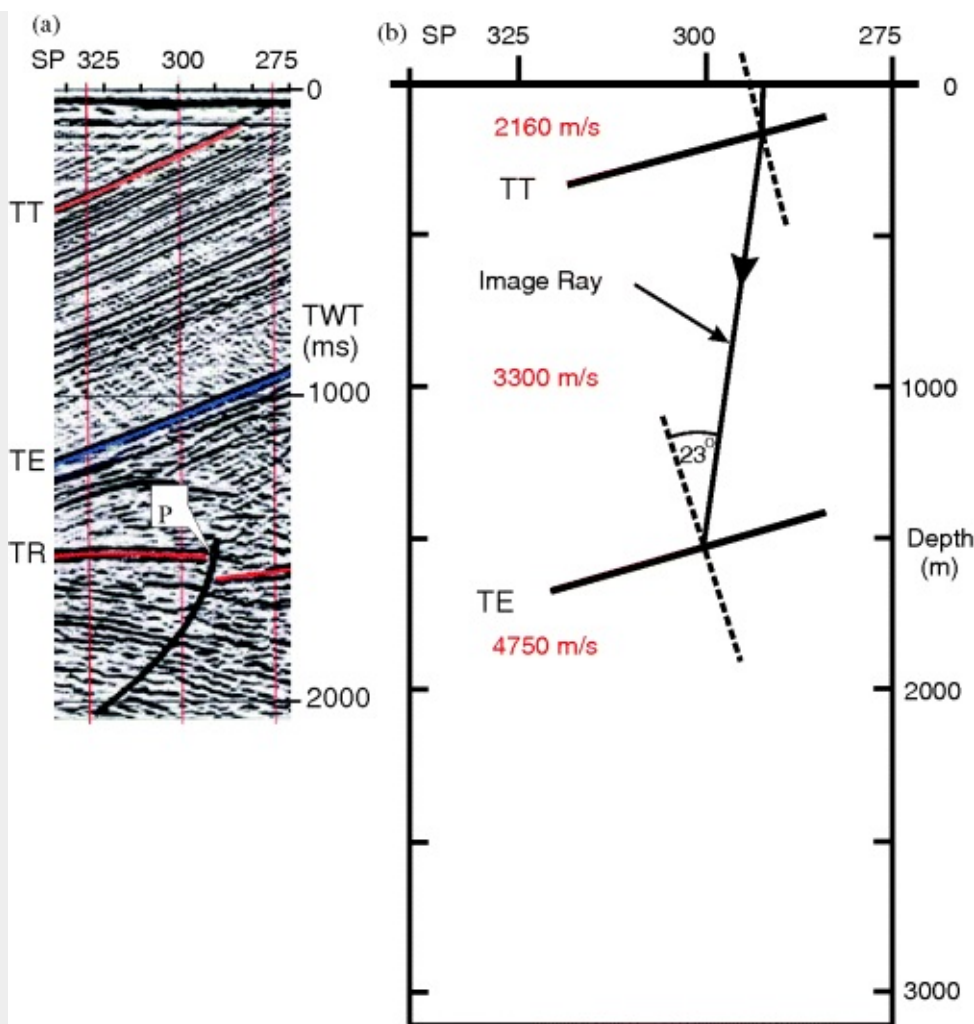
2. How does dispersal change as maximum offset decreases?

Tutorial 8.2

Purpose: Image ray-tracing to find the lateral mis-location in time migration

[Figure T8.2.1](#) shows a small portion of a section across the West Sole gas field, southern North Sea, which was displayed in [Figure T7.4.2](#) of Tutorial 7.4. TT = Top Trias, TE = Top Evaporites, TR = Top Rotliegend.

Figure T8.2.1 Seismic data by courtesy of BP



We start with the following measurements from the time section under SP292:

TWT in seconds for the three horizons of interest: TT = 0.160, TE = 1.020, TR = 1.509. In addition, the time slope (dT/dX) on the TT horizon = 0.100/400 s/m.

[Figure T8.2.1](#) shows part of the construction of an image ray from the surface down to point P in a. The image ray emerges at the surface vertically above P at SP292 on the migrated section, so the construction starts there by drawing the ray vertically down from the surface to its intersection with TT at a depth of $(0.160 \times 2160)/2 = 173$ m.

The construction down to TE continues as follows:

1. Calculate the dip of TT, α , from $\tan \alpha = (V/2)/(dT/dX) = (2160/2) \times (0.100/400) = 0.27$. Hence $\alpha = 15^\circ$. The ray is refracted at TT with angle of incidence = 15° , hence angle of refraction = 23° , from Snell's Law of Refraction (see [Figure 4.9](#)). The length of ray from TT to TE = $(1.020 - 0.160) \times (3300/2) = 1419$ m. The dip of TE = dip of TT.
2. Now you can complete the raypath down to TR. Given the angle of incidence on TE as shown (23°) and the layer velocities, calculate the angle of refraction from Snell's Law, lay off the new direction of the ray and draw its continuation below the interface.
3. Calculate the remaining ray length from the time interval (TR - TE) and the layer velocity, and so complete the ray to P. The end of the ray is the true position of P. Measure the horizontal mis-location of the fault in metres from its time-migrated position under SP292 to its true position. A vertical well targeting the edge of the upfaulted block would be that far away if sited only from the time-migrated section.

Tutorial 8.3

Purpose: To study the relation between vertical section and time-slice in 3D data.

The accompanying Sheet 1 ([Figure T8.3.1](#)) is a section from a 3D survey (crossline 1879) which shows a sedimentary series dipping south-east with a fault about the middle of the section. A horizontal line on the section marks the intersection of a time-slice at 2,860 ms with the plane of the section. The time-slice is shown in Sheet 2 ([Figure T8.3.2](#)).

1. On Sheet 1, pick out the fault and mark it on the section. Note the fault-drag folds which have developed close to the fault on the down-throw side.

Figure T8.3.1 Seismic data by courtesy of BP

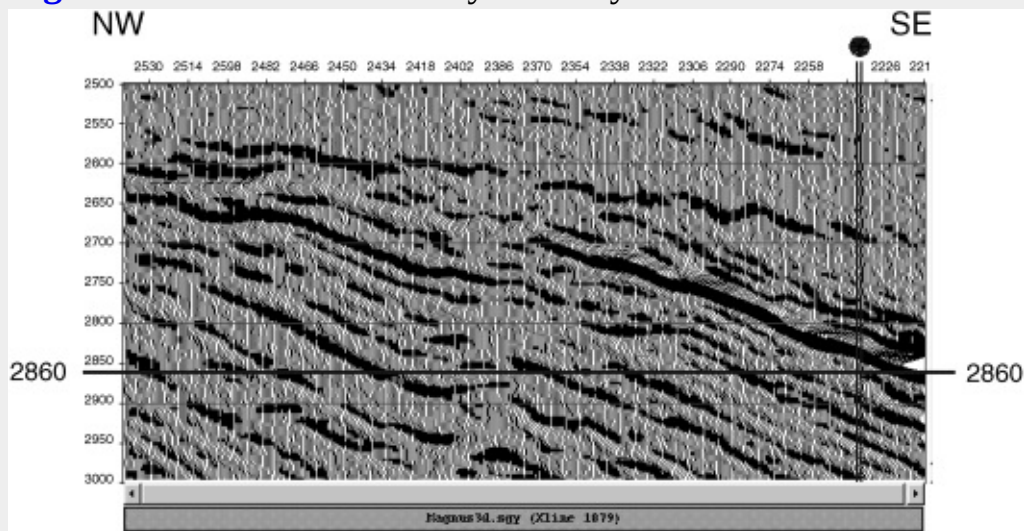
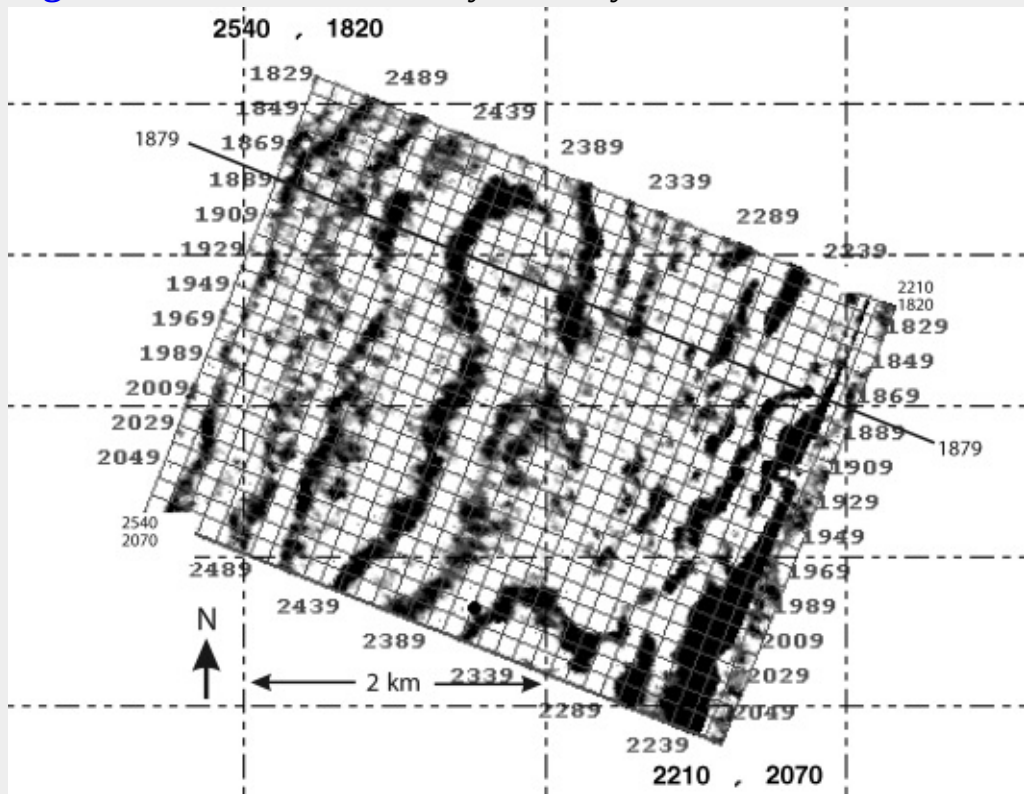


Figure T8.3.2 Seismic data by courtesy of BP.



2. Fold the section along the line of intersection with the time-slice at 2,860 ms and lay it on the time-slice with the folded edge running along the 1879 line on the map.
3. Correlate the black reflection peaks on the section with their 'outcrops' across the time-slice. Carefully note the expression of folds on the section and time-slice close to the fault.
4. Transfer the position of the fault from the section onto the time-slice and study the expression of the fault and the associated drag folds on the outcrop patterns of the time-slice. Mark in the fault all the way across the map area.

Chapter 9

Modifying The Seismic Waveform

9.1 Introduction

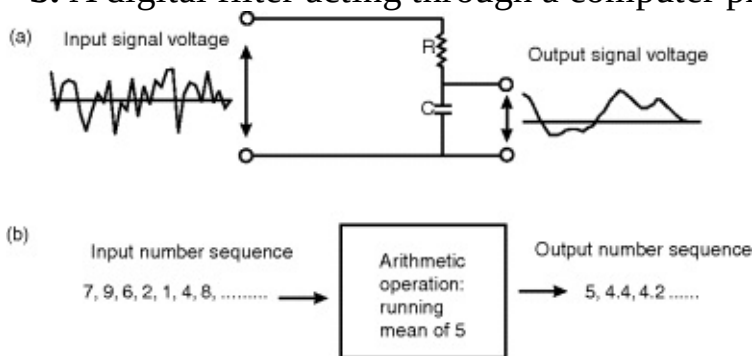
Why should we modify the seismic waveform? If we wish to use the seismic reflections from a reservoir to deduce reservoir properties (e.g. porosity, presence of hydrocarbons), the seismic waveform has to be free from noise. By noise, we mean any parts of the seismic trace that are not simple zero phase wavelets generated from geological interfaces. In Chapter 5, the problem of multiple reflections was highlighted as a principal cause of noise. Other causes include random noise from such sources as traffic or bad weather.

The word 'filter' is used to describe a device or process that modifies a signal passing through it. The name comes from the notion of filtering a fluid through a paper screen to remove dirt. In analogue audio systems, the tone controls are examples of filters that modify the music signal, for example by preferentially stopping high frequencies (treble cut). [Figure 9.1](#) shows a simple form of such a device, in which the capacitor is virtually a short-circuit for high frequencies in the signal so that these frequencies are greatly reduced at the output. In digital systems, a digital filter takes the form of an arithmetical operation carried out on the string of numbers that represents the signal. An everyday example with which most people are familiar is the smoothing of a graph by taking the running means of, say, five adjacent data points. The process acts as a high-cut filter in frequency terms, tending to smooth out high-frequency jitter in the signal ([Figure 9.1](#)). Of course, no new information can be added to a signal by a filtering operation, but information that is already present may become more evident.

Figure 9.1 Different types of filter which cut high frequencies.

a. An electronic filter realized from circuit components: R = resistor, C = capacitor.

b. A digital filter acting through a computer program or human brain.



We study the action of filters not only because they are widely used in data processing, but because the idea of the filter forms a conceptual framework in which we can view the whole reflection seismic process. The earth acts as a filter on the sharp source pulse from dynamite or an airgun, modifying it to the complex and extended seismogram that is finally recorded. Understanding the action of the earth filter allows us to calculate a model seismogram from the sonic log at a well locality, so that we may exactly correlate geological features seen in the well

with the seismic data observed there (see Tutorial 7.1).

Digital filtering is easy – try it for yourself in Tutorial 9.1.

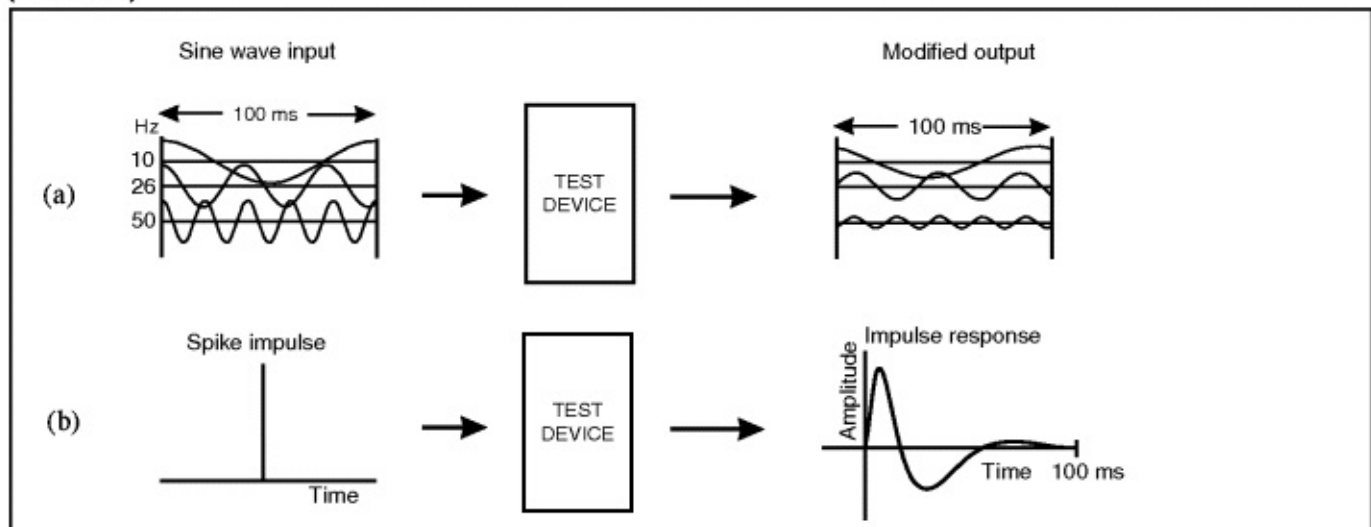
9.2 Testing an Electronic Filter: The Impulse Response

We can investigate the action of an electronic filter experimentally by introducing a selection of sinusoidal oscillations at its input, one by one, and examining how they are modified at the filter output (Figure 9.2a). Each sinusoid might be displayed on an oscilloscope and the amplitude and phase shift of each measured directly on the screen, one after the other. The measurements could be plotted out as spectra, one for amplitude and the other for phase shift relative to the input. Such a plot is called the frequency response of the filter and it tells us exactly what the action of the filter is. It is, of course, a frequency domain description of the filter, describing by how much it modifies the amplitude of the Fourier components and by how much it shifts their phase.

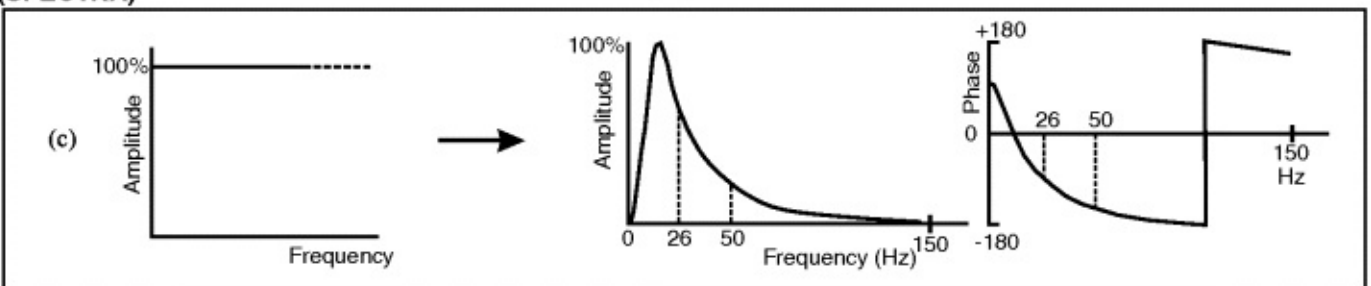
Figure 9.2 Testing the frequency response of an electronic device (geophone, amplifier).

- Measuring the changes in amplitude and phase shift on individual sine waves.
- Recording the impulse response of the device.
- The changes in amplitude and phase imposed by the test device on the spike impulse input.

TIME DOMAIN
(SIGNALS)



FREQUENCY
DOMAIN
(SPECTRA)



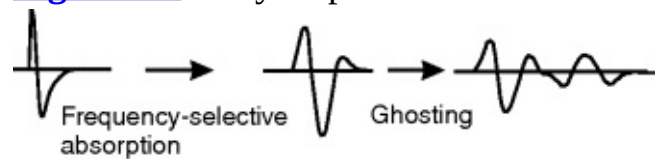
What about a time domain description of the filter? We can assess that by experiment even more quickly by passing a very narrow voltage pulse into the filter (Figure 9.2b). Remember, from Figure 2.9 in Chapter 2, that such a spike waveform is just a zero-phase pulse of very wide

bandwidth – that is, we are firing sinusoids with a wide range of frequencies into the filter all at the same time, with the same amplitude and with no phase shift between them. The time waveform at the output will no longer be a spike but will be delayed, smeared out and made more complex by passage through the filter. It will contain only those frequencies which the filter allows to pass and only those phase shifts which the filter impresses on it, as specified by the frequency response.

The modified pulse is called the ‘impulse response’ of the filter and it is the time-domain equivalent of the frequency response in the frequency domain (Figure 9.2c). In other words, if you take the spectra of the frequency response of Figure 9.2c and use them to construct a pulse waveform, then the waveform will just be the impulse response of Figure 9.2b. Thus, if you measure one response, you can always calculate the other by Fourier transform methods.

Each stage in the passage of a seismic wavelet through the earth results in some modification to the wavelet shape which may be described as the operation of an earth filter. Inevitably, such processes lead to a more complicated wavelet. The list of filters that may affect the initial seismic wavelet is long and it starts with the stages shown in Figure 9.3. Of course, every complication is telling us something about the nature of the earth filter through which the wavelet has passed. Much data processing is directed towards recovering the useful features of the earth filter (primary reflector interfaces) and suppressing some of its more unfortunate features – notably, various forms of multiple reflection.

Figure 9.3 Early steps in the modification of the source wavelet by the earth filter.



9.3 Digital Filters: Convolution

The notion of the impulse response is a useful link to the action of digital filters. We can think of digital signals as a succession of spike impulses, one for each sample of the signal. In this form it is often called a ‘spikogram’, so the impulse response of a filter is a spikogram triggered by inserting a single spike impulse at the input (Figure 9.4). The amplitude of the impulse response will be set by the amplitude of the input spike. If we inject two voltage spikes into a filter with one sample interval between them, they will trigger off two impulse responses of appropriate amplitude and polarity, the second delayed by one sample interval in time (Figure 9.5a and 9.5b). The final output will be the sum of the two impulse responses (Figure 9.5c).

Figure 9.4 A spike impulse of unit amplitude passed through a filter triggers the characteristic impulse response of the filter expressed as a series of digital samples $\{g_0, g_1, g_2, g_3 \dots\}$.

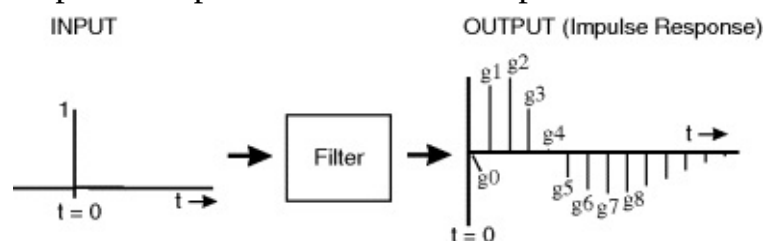
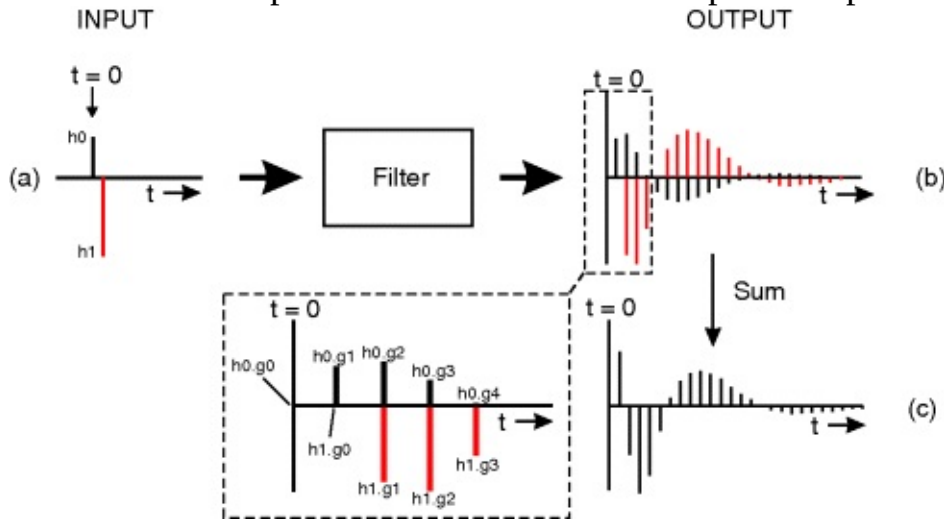


Figure 9.5

- A two-sample signal $\{h_0, h_1\}$ is passed through the same filter as [Figure 9.4](#).
- Each input spike generates a complete impulse response, scaled appropriately.
- The final output is the sum of the two impulse responses.



If we now represent input signal and impulse response as strings of numbers (samples at a regular time interval), we must combine the numbers in a particular way to get the final output.

Suppose we represent the impulse response of the filter to an input spike of amplitude 1 as the time sequence of samples $\{g_t\}$, starting at $t = 0$ as in [Figure 9.4](#):

$$\{g_t\} = \{g_0, g_1, g_2, \dots\}$$

If we use an input of amplitude h_0 at time $t = 0$ ([Figure 9.5a](#)), then the output is scaled up by h_0 times:

$$h_0\{g_t\} = \{h_0g_0, h_0g_1, h_0g_2, \dots\}$$

If we use two inputs of amplitude h_0 and h_1 , separated by 1 sampling interval ([Figure 9.5a](#)), then each input spike will generate a version of the impulse response of the filter, appropriately scaled and delayed by 1 sampling interval ([Figure 9.5b](#)). The net output will be the sum of the two output pulses ([Figure 9.5c](#)). If we call the net output $\{c_t\}$, then:

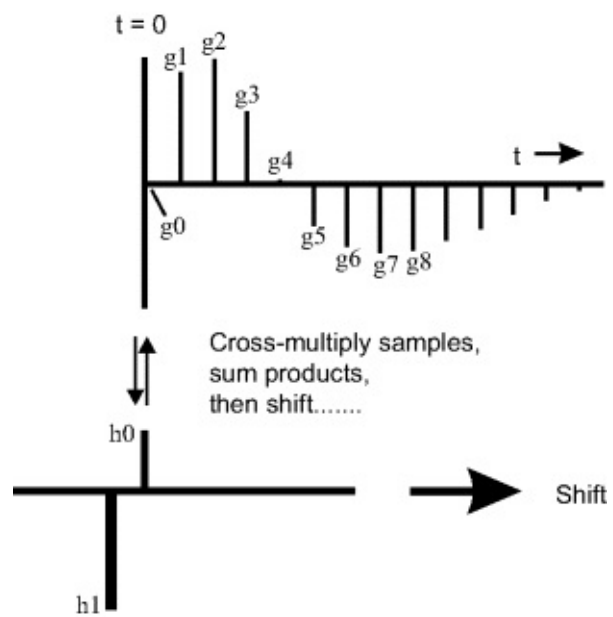
$$\begin{aligned} c_1 &= h_0g_0 \\ c_2 &= h_0g_1 + h_1g_0 \\ c_3 &= h_0g_2 + h_1g_1 \\ c_4 &= h_0g_3 + h_1g_2 \dots \text{etc.} \end{aligned}$$

The operation of cross-multiplication and summation is called convolving the two waveforms, and $\{c_t\}$ is called the convolution of $\{h_t\}$ and $\{g_t\}$, written as:

$$\{c_t\} = \{h_t\} * \{g_t\}$$

An important and extremely useful visualization of the convolution process is provided by the graphical procedure shown in [Figure 9.6](#). One waveform is reversed in time and may be thought of as stepping past the other, one sample interval at a time, stopping at each step to carry out the cross-multiplication and summation of terms that gives rise to one sample of the output. After each output sample is calculated, the signals are mutually displaced by one interval and another cross-multiplication and summation is carried out until one signal has moved completely past the other. We talk of one waveform ‘scanning’ past the other, operating on it to produce the convolved output signal.

Figure 9.6 A useful graphical visualization of the convolution process. One waveform is reversed in time and ‘scans across’ the other. Compare the result with [Figure 9.5](#).



For example, the convolution $\{2, -3, 4\} * \{5, 6, 7\}$ can be represented as:

$$5 \ 6 \ 7 \Rightarrow 4 \ -3 \ 2$$

Scan $\{4 \ -3 \ 2\}$ left to right: cross-multiply terms, sum products, then shift up one interval and repeat.

The successive terms of the output sequence are:

$$\begin{aligned} 5 \times 2 &= 10 \\ (6 \times 2) + (5 \times -3) &= -3 \\ (7 \times 2) + (6 \times -3) + (5 \times 4) &= 16 \\ (7 \times -3) + (6 \times 4) &= 3 \\ 7 \times 4 &= 28 \end{aligned}$$

$$\text{So } \{2, -3, 4\} * \{5, 6, 7\} = \{10, -3, 16, 3, 28\}$$

You will now see that you performed a scanning operation in Tutorial 9.1. You used a five-sample operator which you slid along the signal, stepping along one sample at a time and cross-multiplying five signal samples with five operator samples to get the signal average. What are the numbers in the operator that give the signal average?

Why reverse one waveform? Think of it as entering the filter in time order, i.e. the sample at $t = 0$ goes in first, then the sample at $t = 1, 2, 3 \dots$. The impulse responses are triggered in that order, too, but we plot them in the conventional graphical form, with time increasing from left to right in the final output.

The scanning notion is very useful in practice and allows the properties of several key operations in signal processing to be established in a straightforward way. For example, writing down two number sequences on two slips of paper and scanning one past the other, it becomes obvious that the order in which convolution is carried out is immaterial, i.e.

$$\{h_t\} * \{g_t\} = \{g_t\} * \{h_t\}$$

So you can either think of the filter operator scanning past the signal, generating a modified version as it does so, or the signal entering the filter and coming out the other end in modified form.

If $\{h_t\}$ is an extended series of $n - 1$ terms and $\{g_t\}$ is one of $m - 1$ terms, convolution may be formally written as:

$$C_\tau = S(h_{\tau-s} \cdot g_s)$$

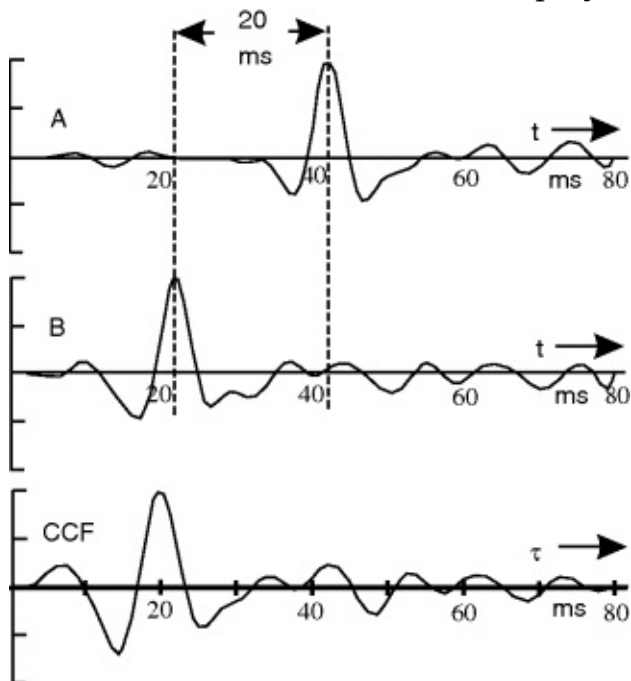
for $s = 0, 1, 2, \dots, m$ and $\tau = 0, 1, 2, \dots, n + m - 1$ (mutual time shift).

9.4 Cross-correlation and Auto-Correlation

The operation of calculating the cross-correlation function (CCF) or correlogram of two signals is again one of 'shift, cross-multiply and sum', but there is no reversal of one signal with respect to the other.

If the two waveforms are similar, but time-shifted (e.g. two seismic traces from adjacent geophones), the CCF will show a large peak when the mutual time shift brings them into coincidence because the cross-products, peak to peak or trough to trough, are then all positive and add up to a large positive number. For example, in [Figure 9.7](#), when signal B has shifted 20 ms past signal A, cross-multiplication of similar peaks and troughs will yield the large positive number at the peak of the CCF ($\tau = 20$ ms).

[Figure 9.7](#) Two similar signals, A and B, and their cross-correlation function (CCF), a function of their mutual time shift τ . Data displayed from program SIGPROC.



The CCF has wide applications in reflection seismology. It is used to measure time-shifts between seismic traces in estimating static corrections, to extract wavelets from seismic traces and to reduce long Vibroseis signals to short wavelets.

If $\{h_t\}$ is an extended series of $n - 1$ terms and $\{g_t\}$ is one of $m - 1$ terms, you can show by the scanning method that:

$$\text{CCF} = \varphi_{hg}(\tau) = \sum (h_{\tau+s} g_s)$$

for $s = 0, 1, 2 \dots m$ and for $\tau = 0, 1, 2 \dots n + m + 1$ (mutual time shift).

The auto-correlation function (ACF) or autocorrelogram is simply the cross-correlation of a signal with itself, φ_{hh} . The peak value will occur when mutual shift $\tau = 0$ and all peaks and troughs cross-multiply to give positive numbers. If you try scanning a signal past itself, you will appreciate that the ACF will be symmetrical about the position of coincidence (maximum ACF), no matter what the shape of the signal is. For that reason, the ACF is normally shown one-sided, plotted from the central peak, the point of coincidence at $\tau = 0$. The amplitude at $\tau = 0$ represents

the sum of the squares of all the signal samples, i.e. the energy of the waveform.

The ACF is widely applied in processing to assess the amount of reverberation that is present in a waveform. When present, reverberation will give rise to large values in ϕ_{hh} at some value of τ other than around $\tau = 0$. Short-term reverberation will give rise to a short oscillatory tail in the central waveform of the ACF beyond the second crossing of the time axis. Long-period reverberation will give rise to high values later in the ACF.

Suppose we regard the ACF as a waveform plotted on a time axis of mutual shift τ and symmetrical about the point $\tau = 0$. Its amplitude and phase spectra can be calculated and it will have a zero phase spectrum. The resultant ‘amplitude’ spectrum is actually an ‘(amplitude)²’ spectrum, because of the cross-multiplication of values in the ACF calculation, and so is the energy spectrum of the waveform.

In the commonest land seismic technique, a long sinusoidal wave train, ranging from low to high seismic frequencies, is passed into the ground by a mechanical vibrator. The recorded seismic traces initially consist of a host of overlapping versions of the sinusoidal wave train – one for each reflection generated in the subsurface. The wave trains are condensed down to wavelets by cross-correlation of the recorded trace with the original sinusoidal wave, as demonstrated in Tutorial 9.2.

Take a look at the remarkable ability of the Vibroseis technique to recover seismic wavelets from noisy data by use of the ACF, in Tutorial 9.2.

9.5 Frequency Filtering by Convolution

Although spikogram diagrams are useful to show the general action of a digital filter, how do we design it to do a specific job? For example, we might want a filter to cut high frequencies above a certain maximum and at a particular rate in db/octave. We must start in the frequency domain by specifying the frequency response of the desired filter, which will be the spectra of the eventual time domain (convolution) operator.

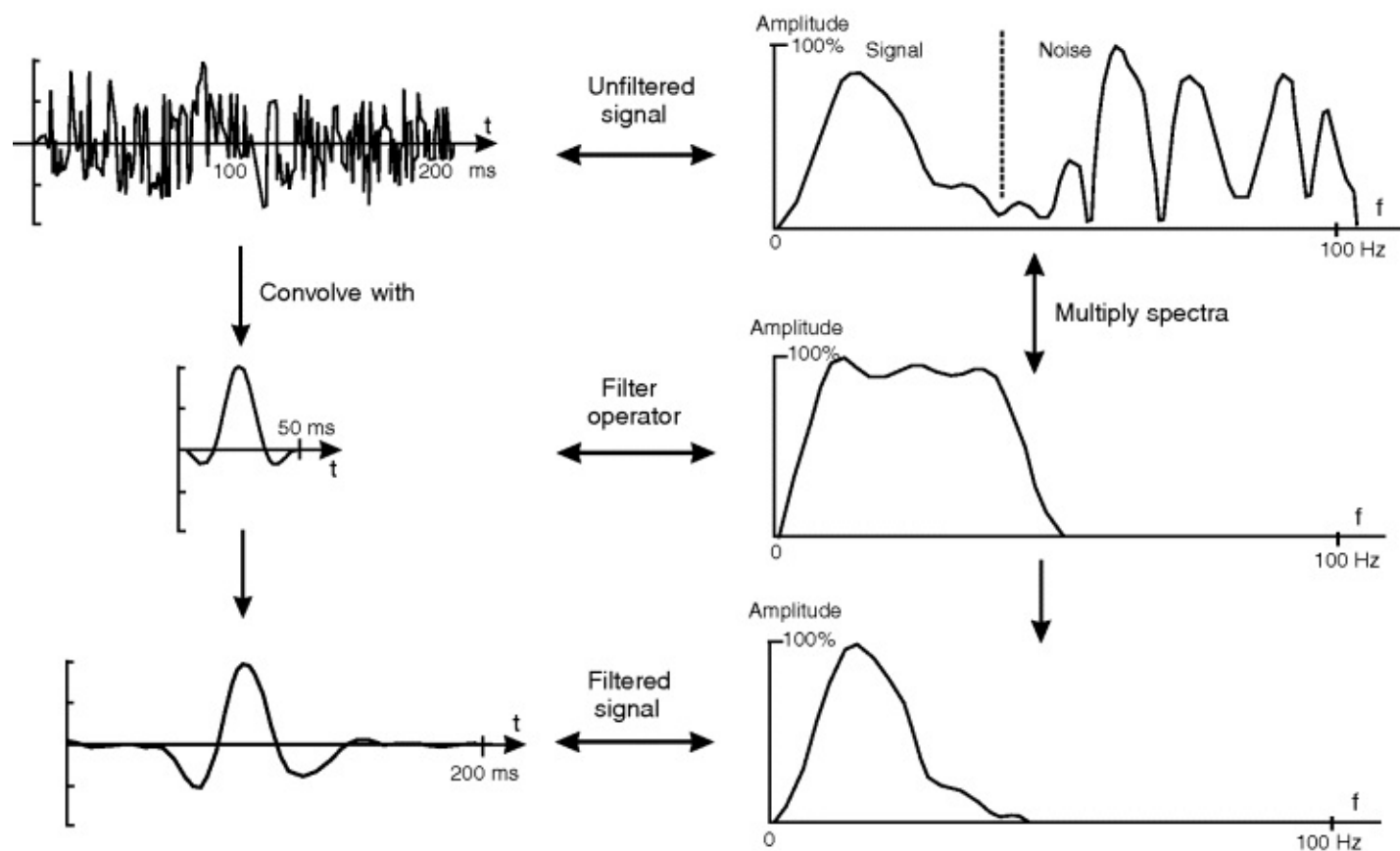
For example, in [Figure 9.8](#), there is a clear division between the desired signal and interfering high-frequency noise, so in this case it is easy to specify a frequency response that will allow the signal to pass while rejecting the noise. In this particular case, we have a high-cut filter, but it is equally possible to design low-cut or band-pass filters of any desired frequency response. Having specified the spectra, we then carry out an inverse Fourier transform to derive the impulse response in the time domain, i.e. the actual convolution operator ([Figure 9.8](#)). Finally, the filter would be applied by convolving the operator with the signal to be filtered.

Figure 9.8 Any filter operation on a signal in the time domain has its equivalent operation on the signal's spectra in the frequency domain. Convolution in the time domain is the equivalent of multiplying amplitude spectra and adding phase spectra (not shown) in the frequency domain.

Figures created from programs SIGPROC and FOURAN.

TIME DOMAIN

FREQUENCY DOMAIN



The specification of the filter's spectrum is generally described in one of two ways. The first is to list the four frequencies that define the part of the spectrum covered by the pass-band. For example, 10–20–50–70 would be interpreted as corner frequencies of 20 and 50 Hz, with zero response at frequencies lower than 10 Hz and higher than 70 Hz. The second method is to define the corner frequencies, together with the rate at which the filter response falls off with frequency in db/octave. For example, if specified as '10/36 – 50/72' the high-frequency corner of the spectrum occurs at 50 Hz and the amplitude falls away at higher frequencies at the rate of 72 db per octave.

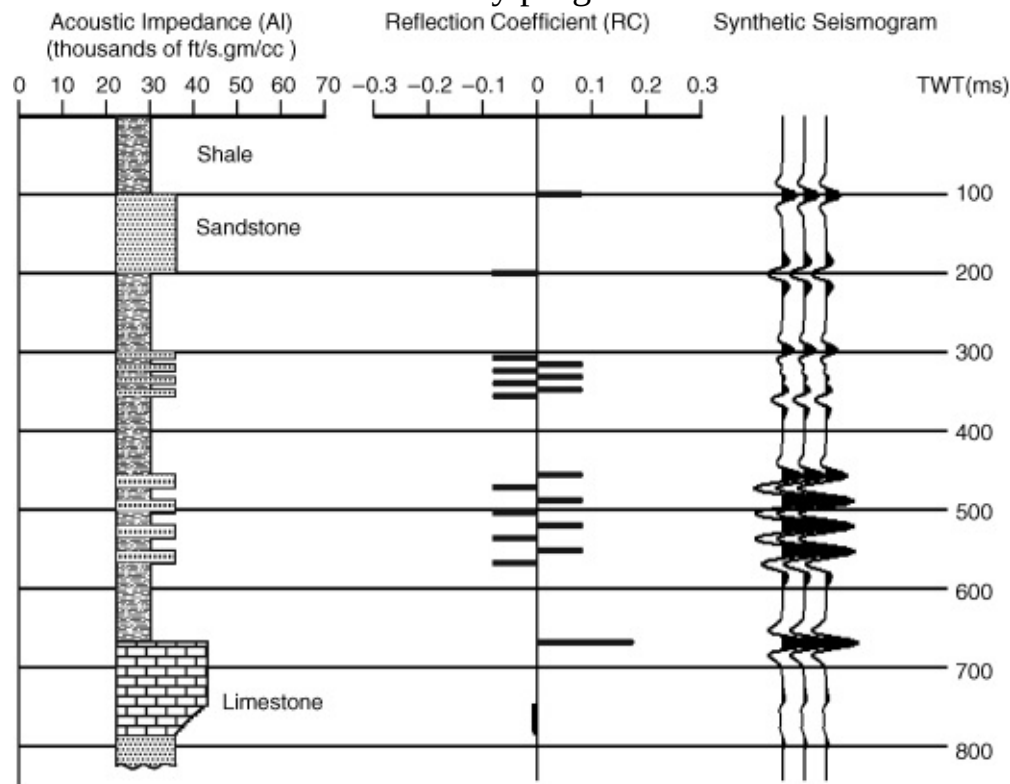
Note that we could carry out the filter operation itself in the frequency domain by operating on the spectrum. We have to multiply the amplitude spectrum of the signal by that of the filter and so chop out the desired pass-band, as shown on the right half of [Figure 9.8](#). The phase spectra should be added together but, since the filter operator is symmetrical, its phase shift is zero, so the phase of the final signal is unaltered. The final step is to transform the new spectra back to the time domain to display the filtered signal. Every filter operation in the time domain has its equivalent in the frequency domain. It is often cheaper to do it like that, so frequency domain processing is widely used in practice.

9.6 The Seismogram As a Convolution

If filtering can be done by a convolution operator and the earth acts as a filter on the simple seismic wavelet, what does the earth operator look like? Referring to [Figure 9.9](#), you can see that the reflection coefficients at lithological interfaces, derived from a log of acoustic impedance in a well, can be plotted as a signal on a TWT axis. Each RC spike on the log represents a reflecting interface and will give rise to a reflection wavelet on the final seismogram. The spike amplitude

will be the reflection coefficient, R , of the interface. The wavelet will be scaled according to the magnitude of the R spike and its polarity will depend on the sign of the R spike. The final seismogram is simply the summation of all these output wavelets, i.e. the convolution of the reflection coefficient series with the basic seismic wavelet. So the earth acts as a filter, with a rather long and complicated impulse response represented initially by the series of reflection coefficients, but then modified by such effects as source wavelet, multiple generation and frequency-selective attenuation to form the raw recorded seismogram. Data processing attempts to remove multiples and broaden bandwidth, leaving a seismogram in which each RC spike is replaced by a basic seismic wavelet.

Figure 9.9 The synthetic seismogram as the convolution of a wavelet with a reflection coefficient series. The outline of the acoustic impedance (AI) log serves as a lithology indicator. 25 Hz Ricker wavelet. Data created by program *SYNTH*.



We can model a seismogram recorded at a well location by convolving the reflection coefficient series calculated from the sonic log with a seismic wavelet, perhaps a theoretical one like a Ricker wavelet, or a wavelet extracted from the data as in Section 9.10 below. Such synthetic seismograms, of the sort illustrated in [Figure 9.9](#), are very useful as a comparison with a seismic section shot through the well. This enables a solid link to be made between the geology in the well and the seismic data, as demonstrated in Tutorial 7.1. Synthetic seismograms are also used widely to model the expected seismic response of a succession of geological strata and so give the interpreter insight into the possible cause of reflection patterns seen in the data (see Tutorial 9.3).

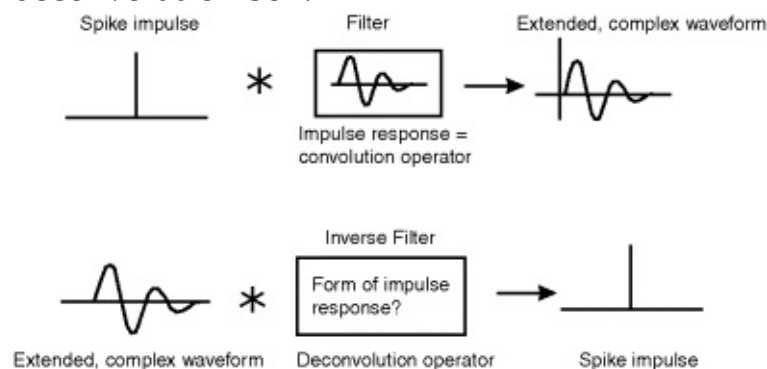
Can you predict what the synthetic seismogram in [Figure 9.9](#) would look like if you were to use a wavelet with a wider bandwidth? Take a moment to test your prediction in Tutorial 9.3.

9.7 Deconvolution

Everything that happens to the simple seismic wavelet as it passes through the rocks tends to

complicate the final waveform. Reverberations, in particular, are major culprits in this respect. It would clearly be of enormous benefit to have a filter which would undo these complications and restore the simple wavelet. Such a filter is called an inverse filter and the process is called deconvolution. We are looking for a numerical operator that we could convolve with the seismic trace to turn complex wavelets into simple ones, perhaps ideal spikes ([Figure 9.10](#)) or some other desired wavelet that we think is present in the data. The question is – how do we unravel the complexities of a convolution?

Figure 9.10 Deconvolution as the inverse of convolution. We have to find the operator within the deconvolution box.



The answer is to use a change of notation – a common ploy of mathematicians when the going gets tough. Suppose we have two wavelets, h_t and g_t , as before, e.g.:

$$\{h_t\} = \{1, -2, 3\}; \{g_t\} = \{2, 3\}$$

You can show by scanning as before that:

$$\{c_t\} = \{h_t\}^* \{g_t\} = \{2, -1, 0, 9\}$$

Now suppose we set up a summation of terms consisting of the powers of a dummy quantity z , where the powers of z increase steadily by 1 (i.e. first a constant term, z^0 , then $z^1, z^2 \dots$) and where each of the z terms is multiplied by a sample of a digital signal. So $\{h_t\}$ is transformed to:

$$h_z = 1 - 2z + 3z^2$$

and $\{g_t\}$ is transformed to:

$$g_z = 2 + 3z$$

The sequence of terms summed together is called the z -transform of the signal. Now multiply the transforms using normal algebraic procedures:

$$\begin{aligned} h_z \cdot g_z &= (1 - 2z + 3z^2) \cdot (2 + 3z) \\ &= 2 + 3z - 4z - 6z^2 + 6z^2 + 9z^3 \\ &= 2 - 1z + 0z^2 + 9z^3 \end{aligned}$$

Note that the multipliers of the z terms of the answer (formally called the coefficients of the z terms) now give the series $\{c_t\}$. The convolution of the two wavelets has been reduced to a simple *multiplication* of two z -transforms, which suggests that deconvolution can be carried out as the *division* of two z -transforms.

Now if the complex wavelet to be deconvolved is $\{p_t\}$ and the inverse filter is $\{f_t\}$, then the deconvolution process to a spike (the desired output) can be written as:

$$\{p_t\}^* \{f_t\} = 1$$

or, in z -transform terms:

$$p_z \cdot f_z = 1$$

Hence:

$$(9.1) \quad f_z = 1/p_z$$

Note that the filter's z -transform is just the inverse of that of the wavelet that is to be deconvolved, hence the name 'inverse filter'. Division of such expressions is readily accomplished (remember long division at primary school?), and the terms of the filter operator are simply the coefficients of the result of the division. For example, the simple reverberating wavelet $\{7, -3, 1\}$ discussed by McQuillin *et al.* (1984) gives rise to the inverse filter z -transform:

$$[1/(7 - 3z + z^2)] = 1/7 + 3z/7^2 + 2z^2/7^3 - 15z^3/7^4 \dots\dots$$

and so the deconvolution operator:

$$\{1/7, 3/7^2, 2/7^3, -15/7^4 \dots\}$$

which is an infinite series of rapidly decreasing terms. You should check by scanning that convolution of this operator with the original wavelet $\{7, -3, 1\}$ very nearly converts it to $\{1, 0, 0, \dots\}$, i.e. a spike.

If the entire seismogram were run through such an inverse filter, each wavelet on the seismogram would be converted to a spike and the output would be identical to the log of reflection coefficients plotted against time like the one shown in [Figure 9.9](#). In good conditions, seismic processing can get part of the way to this goal. However, it will never quite reach it for two reasons:

1. The presence of noise of various sorts detracts from the quality of the data.
2. The seismic data is severely limited in its high frequency content by absorption of energy into the rocks so that the spike is not a realistic desired output.

9.8 Designing Deconvolution Operators

[Equation \(9.1\)](#) indicates that simple division of z -transforms will yield an operator, as explained above. Several problems now arise:

1. With certain input waveforms, where the high amplitudes occur towards the end of the wavelet (maximum-delay waveforms), the coefficients of the deconvolution operator do not converge towards zero but increase without limit, so the whole series is unstable and 'blows up'.
2. The deconvolution operator obtained by polynomial division is an infinite series. When should it be truncated?
3. The wavelet buried in the reverberatory seismogram is not known. How should we estimate its form in order to design the inverse operator?

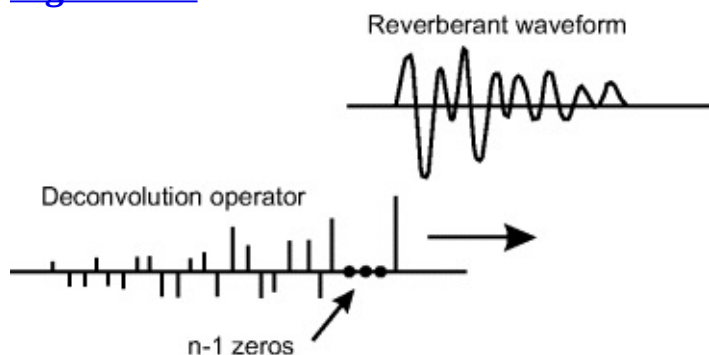
We need not follow out the details of how these problems have been overcome, but the general approach is to find an operator of a chosen fixed length which yields an output as little different from the desired result (spike or whatever) as possible in the least-squares sense, i.e. where the sum of the squares of differences between actual output and desired output is least. Such a filter is called an optimum least-squares inverse filter; it is also known as a Wiener filter, after the mathematician who developed the idea.

9.9 Predictive Deconvolution

The single greatest drawback to spiking deconvolution is the exaggeration of high-frequency noise in the record. Peacock & Treitel (1969) describe the process of predictive deconvolution which has become a standard method in the industry ([Figure 9.11](#)). The effect of the operator may be

visualized in terms of convolution by scanning; the lead spike of the operator scans the early part of the waveform and reproduces it unaltered for n sample intervals. From then on, the reverberant tail generated by the lead spike of the operator is cancelled by the rest of the operator as it works progressively over the whole of the waveform.

Figure 9.11 Predictive deconvolution.



The word 'prediction' is used because the filter's tail, as it scans the early part of the waveform, predicts what the reverberation is going to be and subtracts it from the reverberant waveform generated simultaneously by the lead spike as it traverses the tail of the waveform. If another genuine reflection is lying hidden in the reverberant tail of a waveform, it will not have been predicted and will stand out as a prediction 'error' when the predicted trace is subtracted.

In designing the operator, the prediction distance, n , is generally taken as the second zero-line crossing point on the ACF, which marks the time extent of the basic wavelet. The length of the operator is chosen to extend over the length of the reverberant tail of the ACF. Prediction distance and length of operator are key processing parameters that you will commonly see listed on the labels of time-sections. Note that the shape of the basic wavelet is not affected by this type of deconvolution.

9.10 Wavelet Processing

Wavelet processing is a form of deconvolution where we transform the wavelet into some desirable form – preferably a simpler one, of course. It is a final step in processing and is typically carried out for two reasons:

1. The first reason is that the raw seismic wavelet from an explosive source is generally of minimum-phase type, where most of the energy is concentrated towards the front of the wavelet. This condition is maintained throughout processing, but one of the final steps is to convert the wavelet to zero phase, since that is best for interpretation and for any further processing, such as acoustic impedance inversion.
2. A second reason to carry out wavelet processing is to make sure that the final wavelet shape is the same all over the survey area, independent of variations in conditions of acquisition.

Wavelet processing must start with wavelet extraction, that is the seeking out of the wavelet shape recorded in the actual data. One method depends on an interesting application of the CCF. The seismogram recorded at a well location is cross-correlated with the reflection coefficient series measured down the well from the sonic log. At maximum correlation, each RC spike scans and replicates its matching reflection in the seismogram to form the central waveform of the CCF. The quality of the derived wavelet depends on every RC spike being exactly lined up with its reflection, i.e. an accurately timed RC series is required, tied to check-shots or a VSP survey.

A second method is an application of Wiener filtering. We know that the observed seismogram is the output of a filter which has acted on the RC series as input. The filter operator is the wavelet we are seeking. So, using appropriate software, we design the wavelet to be that least-squares filter operator which will transform the known reflection coefficient series into the ‘desired output’, which is the observed seismogram at the well. Both approaches assume that the observed seismogram at the well is free from noise, multiples or other disturbance.

When the existing wavelet has been extracted, it is transformed by the use of [Equation \(9.1\)](#), where its z-transform takes the place of the p_z term (complex wavelet) on the right hand side and a zero-phase wavelet takes the place of 1 in that equation as the desired output of the inverse filter. The filter can then be applied to the seismic data to transform all wavelets to zero phase form.

9.11 Frequency-domain Processing

So far we have discussed filtering and deconvolution in terms of time domain (convolution) operations. However, bearing in mind the complementary nature of the time and frequency domains mentioned in Chapter 2, it will come as no surprise that every operation in the time-domain has its equivalent in the frequency domain. Extra computation is required to transform to and fro between time signal and spectra but, once in the frequency domain, the operation can often be done much more efficiently in terms of computer time.

We have already skirted around the topic in discussing the design of a band-pass filter ([Figure 9.6 b](#)). It is clear from that diagram that we could simply multiply the amplitude spectrum of the noisy signal by the spectrum of the filter operator, so carving out the desired pass-band. But what about the phase spectra? It turns out that we have to add the two spectra together – in this case adding zero phase from the filter operator, so there is no change to the signal phase within the new, restricted range of frequency. We then do an inverse transform of the modified spectra to create the filtered signal in the time domain.

So, convolution in the time domain is the equivalent of multiplying amplitude spectra and adding phase spectra in the frequency domain – arithmetically much less arduous than convolution. The labour of doing the transforms between the two domains of time and frequency has been reduced by the use of specially designed computer circuits and fast algorithms.

The conversion of a seismogram to its amplitude and frequency spectra is often called one-dimensional Fourier analysis, the dimension being time when in the time domain or frequency when in the frequency domain. It is possible to extend this to the two dimensions (T, X) of an entire seismic section. Time transforms to frequency (f) as before, and the space dimension X transforms to a space-frequency or wavenumber (k), which is the inverse of wavelength along the ground (see Chapter 2, Section 2.8). The resultant spectra are two-dimensional and presented as maps of amplitude or phase shift. One axis of the map is time frequency (f), as before, and the other is space frequency (k). Processes that involve the combination of signals from different seismograms in the same section can often be carried out more efficiently or cheaply in the (f, k) domain.

9.12 Data Processing and the Fragility of Bandwidth

The importance of the three main data processing steps – CMP stacking, deconvolution and

migration – can now be appreciated. These are three ‘make-or-break’ steps, in the sense that if one of them is missed out or done badly, the data are likely to become completely uninterpretable.

However, we might add one more to this group – specialized multiple removal processes. You have already seen, in Chapter 5, the scale of the multiple problem and how deconvolution and CMP stacking do some of the work. Other techniques are also available. One is based on stacking the CMP data along directions other than along the reflection hyperbola (Radon transform methods). Another approach is to model the multiple-generating process, then subtract the modelled multiples from the observed data. Remember the surface-related multiples modelled in Tutorial 5.2?

In any operation where signals are added together, whether in data acquisition or data processing, it is easy to lose the high frequencies of the seismic spectrum and so reduce bandwidth. Consider adding together two signals of 100 Hz. If there is a time shift of as little as 5 ms between the signals, then the peaks of one will coincide with the troughs of the other (a phase shift of 180°) and there will be complete cancellation of energy at that frequency. At 10 Hz, the phase shift is just 18° and the two signals will sum constructively.

The damage starts with data acquisition in the field, when signals from a linear array of geophones or hydrophones are summed electrically and passed to the recorder as a single channel of data. If the shot-receiver offset is small, then the rising reflection wavefront from a deep reflector is almost horizontal, it will strike all geophones in the array almost simultaneously and there is no problem. At large offsets, there will be a small time lag from geophone to geophone as the wavefront runs at an angle across the array, and high frequencies in the waveform may begin to cancel. The time lag is partly NMO and partly move-out caused by dip on the reflector in the direction of shooting. The time lag will be greatest for long arrays, large shot-geophone offsets, shallow reflections, steeply dipping strata and low near-surface velocity.

A second cause of high-frequency loss linked to geological dip may be the binning of data in 3D acquisition. A shot recorded at two close geophone locations within a bin will give seismograms with extra move-out (in addition to NMO) if there is dip on the reflectors in the direction of shooting. This move-out will remain after correction for NMO, and so may cause loss of bandwidth on CMP stacking. It is one constraint on the size of bin. The interpreter has to trust that the geophysicists who designed the survey have allowed for all this, but should be aware that these factors may affect reflection bandwidth.

In the course of processing, NMO stretch on shallow events will reduce bandwidth if the muting schedule is not carefully done. If an incorrect stacking velocity has been chosen, the reflection will not be correctly aligned across the CMP gather and, once again, the high frequencies will suffer. Residual static shifts within the CMP gather are yet another potential cause of high-frequency loss.

Finally, certain geological conditions can preferentially reduce high-frequency components of the signal, in addition to frequency-dependent attenuation. The presence of gas in pore spaces appears to reduce content of high frequencies in the wavelet and may be used as a gas indicator. However, the same effect can be caused by reverberation of the signal in a high-velocity thin-bedded unit, and this was discussed in a classic early paper on the subject (O'Doherty & Anstey, 1971). Study of the impulse response for energy thrown back towards the surface demonstrates that the unit acts as a filter, preferentially throwing back high-frequency energy towards the surface and transmitting low-frequency energy to greater depth. A reflection from a deep

reflector below such a unit would therefore be reduced in bandwidth, which could be a problem in certain types of stratigraphy, such as interbedded lavas (e.g. west of Shetland) or thin limestones interbedded with shales.

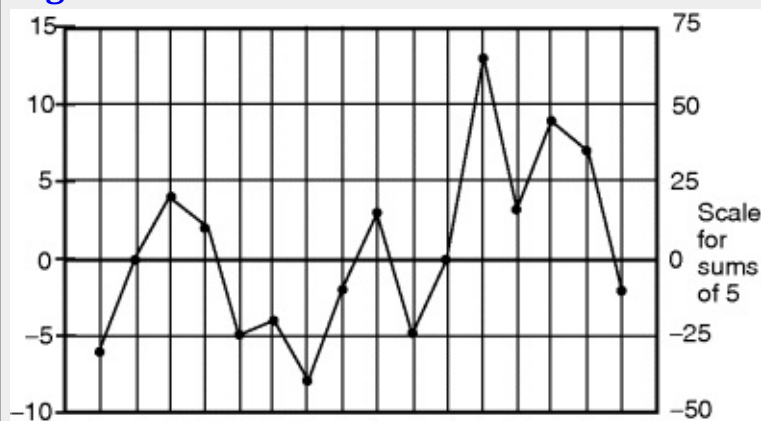
Tutorials for Chapter 9

Tutorial 9.1

Purpose: To demonstrate a simple digital filtering operation by hand

The numbers plotted on [Figure T9.1.1](#) represent a digitally sampled signal that contains a low-frequency component (a general upwards trend to the right) with higher-frequency components superimposed on it. The object of this tutorial is to show how simple numerical operations can separate one component from another.

Figure T9.1.1



Calculate five-point running mean

The basic idea is to take an average value of the signal over five points and plot the average on the graph at the mid-point position of these points. For example, the first group of five numbers is -6, 0, 4, 2, -5; plot the average (-1) at the 3rd sample position. The next group to be averaged is 0, 4, 2, -5, -4; the average (-3/5) is plotted at the 4th sample position. To ease the arithmetic, don't calculate the average, just plot the sum of five against the right hand scale.

Work along the string of sample numbers shown below. To keep you in the correct group of five numbers, make a slot five numbers wide on the edge of a piece of paper and slide it along the string of sample numbers. Not only does this avoid errors, but it has deeper significance – you will see later that you are working along the string with a numerical operator whose length is that of the slot in the paper. Carry on until you get to the end.

Your new graph is the output of a filter operation. How could you describe it in terms of the signal frequencies passed by the filter – a high-pass or a low-pass filter operation?

Sample values = -6 0 4 2 -5 -4 -8 -2 3 -5 0 13 3 9 7 -2

Tutorial 9.2

Purpose: To demonstrate the remarkable power of the Vibroseis technique in recovering signal obscured by noise. If this is the first time you have used the program SIGPROC, check the Help/Quick Start tutorial to see the basic operation.

The Vibroseis Signal and its ACF

1. Start program SIGPROC and on the menu click on configure to set the path to the files copied from CD to disk and OK the default settings under Set Display.
2. Click Signal1/Vibroseis/Parameters and set the following:

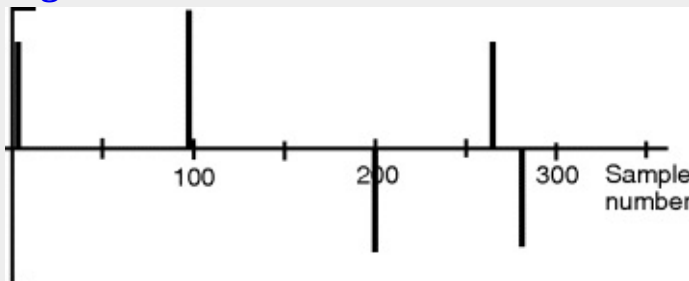
Sweep Length	1200 ms
Sample Interval	2 ms
Low Frequency Limit	5 Hz
High frequency limit	60 Hz
Taper Lengths	300 ms

3. Click on Signal 1/Vibroseis/Display Signal. Note the form of the signal: frequency is swept (continuously variable in linear fashion) from 5 to 60 Hz and the waveform is linearly tapered at each end over 300 ms. It is 600 samples (1,198 ms) long.
4. Click on Signal/Save As and save Signal 1 to your data folder with a suitable file name – perhaps one that records the sweep length and sample interval, e.g. vib12002.sig.
5. Click on Signal 2/Open and Display and open the file you have just saved. Now you have two identical Vibroseis sweeps on the screen.
6. Click on Process/Cross-correlate 1&2 and OK the small message window. The ACF of the sweep will appear as Signal 3.
7. Note that the ACF is:
 - i. Symmetrical about the centre maximum like a zero-phase seismic wavelet.
 - ii. Shows subsidiary oscillation, so-called correlation noise (which might be reduced by better tapering).
8. Signals 1 and 2 are shown in the particular position where cross-correlation (cross-multiplication and summation of products) gives the peak value of the ACF. Imagine signal 2 scanning past signal 1 sample by sample – this is the position where the sum of the products will give a maximum value.

Pulling Vibroseis signals out of noise

9. Still working with *SIGPROC*, click on Signal1/Open and open the file 5reflvibN.sig. This signal is a synthetic Vibroseis field record containing five Vibroseis reflections identical to vib12002.sig that you created in part A. They have variable amplitude and polarity and are obscured by random noise. The goal here is to convert the trace to an interpretable seismogram containing five reflection wavelets by performing cross-correlation with the original Vibroseis sweep.
10. Click on Signal 2/Open and Display and open vib12002.sig. Go to Process/Cross-Correlate 1&2 and view the result in Signal 3.
11. Compare the seismogram with the trace of reflection coefficients from which it was generated in [Figure T9.2.1](#). Do the wavelets have the correct polarity? Do they have the correct relative amplitudes? Are they spaced correctly? Has the signal/noise ratio been improved compared to the raw Vibroseis recording in Signal 1?

Figure T9.2.1



Tutorial 9.3

Purpose: To use a synthetic seismogram to test the seismic response of a geological model

1. Start program *SYNTH*, click configure and enter the path to your data folder on your computer.
2. Click File/Open/Sonic + Density and open longone.sdt. Click File/Open/Wavelet and open Rick4004.sig (a 40 Hz Ricker wavelet sampled at 4 ms). Click Parameters and accept all default values. Click Draw, OK the message and close the subsidiary information window.
3. Compare the synthetic seismogram with that shown (from the same log data) on [Figure 9.9](#). Why the big difference around 300 ms? The lesson for the interpreter might be to beware of using variation in amplitude as an indicator of lithology at this level in the section.

Chapter 10

Refining Reservoir Architecture from Seismic Data

10.1 Introduction: The Reservoir Model

We express our knowledge of a reservoir by building a model in the form of numerical data sets that describe features of the reservoir. For example, there will be at least two surfaces described by (x, y, z) coordinates, one for the top of the reservoir and one for the bottom, both originating as seismic structure maps tied to well control. Within these surfaces, the reservoir may be represented by a large number of cells, each cell possessing a number of properties such as porosity, permeability and fluid saturations (oil, gas, water). It is the task of the petroleum engineer to use this model to predict the flow of reservoir fluids in order to optimize hydrocarbon production.

Seismic data makes two main contributions to the reservoir model:

1. Definition of reservoir architecture (reservoir boundaries, layering, faulting, distribution of sedimentary sequences).
2. Mapping of reservoir properties (presence of hydrocarbons, porosity, lithology) between well control.

The basic delineation of geological structure has already been covered in Chapters 7 and 8. In this chapter, we will survey some additional techniques and processes that may be used to refine the sedimentary environment of the reservoir and its geological structure. The mapping of reservoir properties will be covered in Chapter 11.

The term ‘seismic attribute’ is much employed in connection with reservoir studies. An attribute is any quantity directly measured from a seismic trace or a group of traces or calculated from such measurements. Only amplitude, TWT and signal polarity can be directly measured from seismic data, but a large number of quantities can be calculated from these fundamental measurements. Examples include frequency and phase of the seismic waveform or dip, and direction of dip, measured across a group of traces. In this chapter, attributes that help define sedimentary facies and reservoir structure will be discussed.

10.2 Refining Reservoir Environment: Seismic Stratigraphy and Facies Analysis

Seismic stratigraphy is the study of the distribution, relationships and facies of sedimentary units using all the information available in a seismic reflection survey. Seismic stratigraphic studies may be conducted on large or small scales. Vail, Mitchum and co-workers at Exxon were the first to make use of seismic data in this way on a large scale, and the basic concepts are described in Vail & Mitchum (1977). The whole topic has now been broadened out into sequence stratigraphy, incorporating well-log data and microfossil and radiometric dating in an integrated study of the

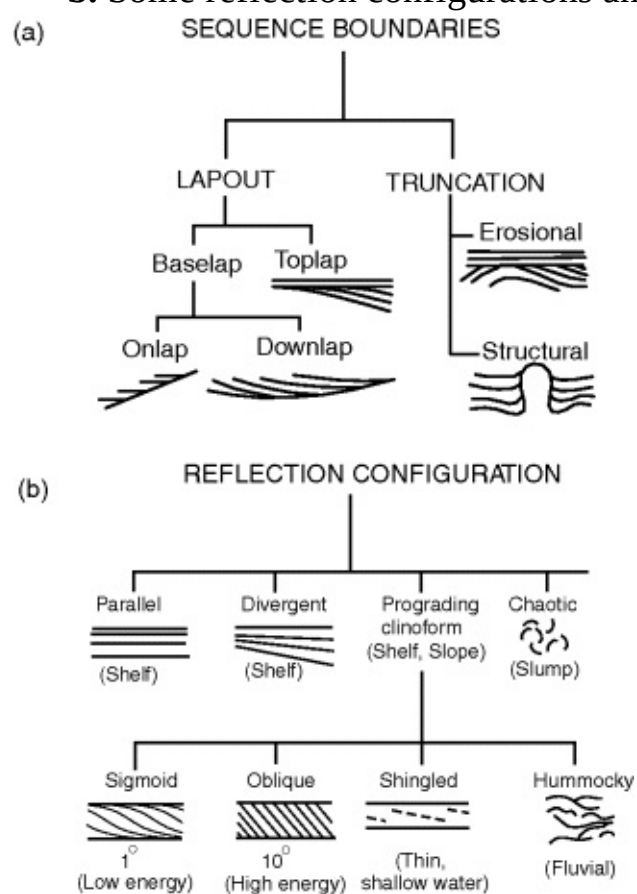
history of basin filling (Myers & Milton, 1996). We will not attempt to cover this huge field here, but will look at the seismic contribution to such studies at the reservoir scale – the delineation of sedimentary sequences and the interpretation of facies within sequences from seismic textural attributes.

10.2.1 Sequences and System Tracts

The basic unit of study is the depositional sequence, described by Mitchum *et al.* (1977) as ‘a stratigraphic unit composed of a relatively conformable succession of genetically related strata and bounded at its top and base by unconformities or their correlative conformities’. The sequence is defined on the seismic section by seismic sequence boundaries, which are recognized by the orderly termination of reflections on surfaces of unconformity. Some of the reflection terminations often observed are illustrated in [Figure 10.1a](#).

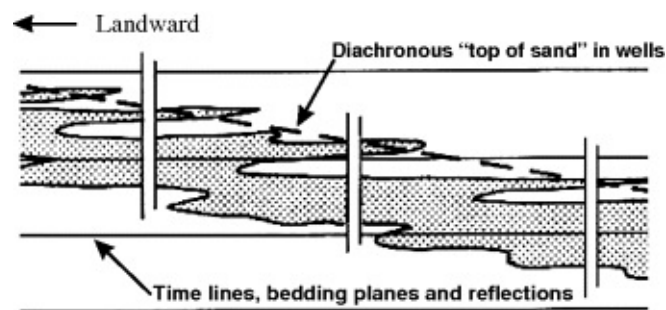
Figure 10.1

- a. Types of sequence boundary defined by reflection terminations.
- b. Some reflection configurations and their interpretation.



An underlying concept is that reflections are parallel to bedding planes and so mark old positions of the water/sediment interface ([Figure 10.2](#)). As a result, they may persist as continuous events through lateral changes in facies, for example in passing from the sandy topset beds of a prograding clastic sequence out into basin shales (Vail & Mitchum, 1977).

[Figure 10.2](#) The relation between reflections from bedding planes and sparsely sampled stratigraphy in wells in the case of rising, oscillating sea level.



Much of the subject has developed around the model of the infilling of a basin by clastic sediments during cycles of relative change of sea level. A series of depositional sequences is formed when a basin margin goes through a fall and rise in relative sea level. The sequences are grouped into system tracts named after the controlling sea level, i.e. low-stand system tract (LST), transgressive system tract (TST) and high-stand system tract (HST) (Bertram & Milton, 1996). Potential reservoirs in the form of sand-prone sequences can be formed in any of the system tracts. Galloway (1998) discusses the occurrence of sands in the context of the three system tracts and shows their typical well-log responses.

10.2.2 Picking Seismic Sequence Boundaries

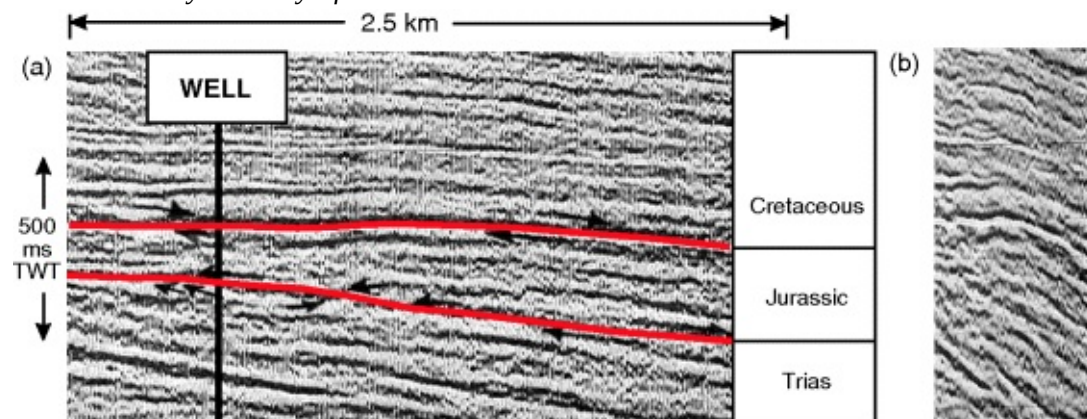
Picking sequence boundaries requires a different outlook and different skills from the interpreter compared to those needed for structural interpretation, and it takes a certain amount of practice before one's eye is attuned to seeking out the evidence. The interpreter is no longer following reflections but is looking for surfaces along which reflections terminate. Quite often, such a surface will also be marked by a reflection, but it need not be.

The technique consists of identifying the reflection terminations, marking them with a small arrow drawn parallel to the reflection and eventually joining up the ends of the arrows with a coloured line to mark the boundary (Figure 10.3a). The boundary can be treated like any other surface, transferred from line to line and mapped across an area.

Figure 10.3

- A time section with two sequence boundaries picked on reflection terminations and confirmed in a well.
- The same section (without labels) compressed horizontally.

Seismic data by courtesy of Western Geco.



Where the terminations are ill-defined, a better approach may be to identify locally conformable sequences on either side of the boundary by picking bundles of conformable events within the seismic data. Exaggerating dips by compressing the horizontal scale (Figure 10.3b) and displaying

the data as the phase attribute (Chapter 11, Section 11.11) will also help to separate out the sequences. Note that sequence boundaries need not be marked by distinct reflections. Also, the same boundary may be defined at one place by terminations from below, and at another by terminations from above. In [Figure 10.3a](#), both sequence boundaries are erosional unconformities. The Jurassic succession onlaps on to an unconformity with the Trias and the Cretaceous downlaps on to an unconformity with the Jurassic (compare [Figure 10.1a](#)).

10.2.3 Seismic Facies Analysis

It was recognized from the beginning of seismic stratigraphy that the characteristics of reflections within a depositional sequence (amplitude, geometry) could be interpreted in terms of sedimentary facies (Mitchum *et al.*, 1977; Sangree & Widmier, 1977). Some examples are shown in [Figure 10.1b](#), together with interpreted sedimentary environments. Facies units were given descriptive codes (High Amplitude Continuous, Transparent) and mapped by hand across an area.

However, this mode of interpretation could only be used to a limited extent because of the limitations of 2D data. Sedimentary units could only be viewed on vertical sections, and the wide spacing between sections often made the correlation and visualization of reservoir-scale units difficult or impossible. In addition, the same unit sectioned on one line could look very different when sectioned in a different direction on another line. As a result, the mapping of sedimentary facies within a potential reservoir interval could be very uncertain.

With the advent of 3D data, not only have much better images of the internal structure of sedimentary units been made available, but two other major advances have become possible:

1. The morphology of individual lithological units can be extracted from the 3D volume.
2. Numerical procedures can be applied to describe the textural reflection attributes of depositional sequences and map them out within a reservoir volume.

As a result, a new area of study called seismic geomorphology has become established. (Latimer, 2007).

10.2.4 Sedimentary Units As 3D Volumes

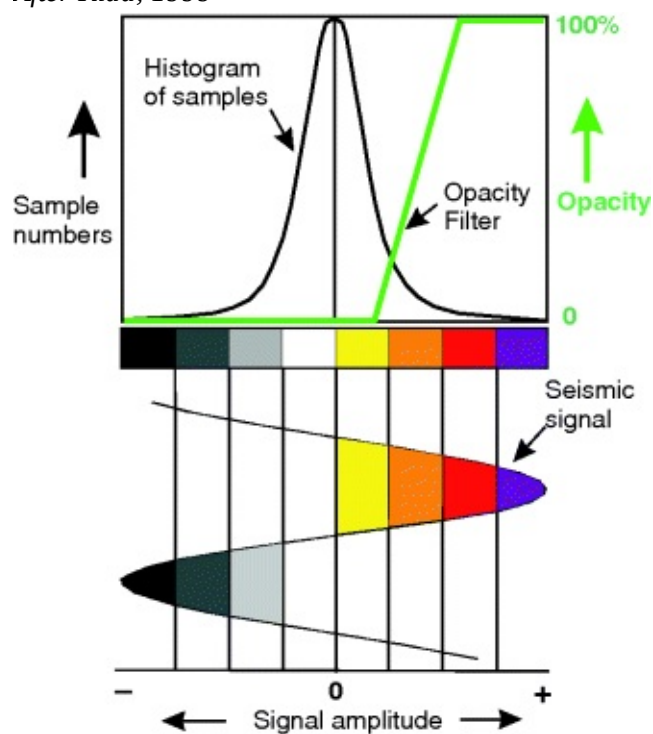
Once again, new technology has driven an advance in our understanding of the subsurface. A key factor has been the development of advanced colour management on computer displays of seismic data. You will recall, from Chapter 3, Section 3.4, that a 2D section can be displayed in colour by assigning a colour patch, a picture element (pixel) to each sample of the seismic trace according to the sample's amplitude. In 3D, the pixel is given a third dimension and becomes a coloured cube – a volume picture element or 'voxel'. On a workstation display, we can choose to show only voxels of a certain limited amplitude range, displayed as a particular colour, with all other samples turned off by reducing their colour intensity (opacity or visibility) to zero. In this way, we have the ability to isolate and display a particular volume of the 3D data.

The colour management system is explained in [Figure 10.4](#). Colours have been assigned to amplitude levels of the seismic signal, ranging from purple (most positive) to black (most negative). The program presents the interpreter with a histogram showing the number of samples plotted against signal amplitude. Typically, the largest number of samples have low amplitudes. The interpreter can choose to display only the high-amplitude positive pixels by setting an opacity filter in the manner shown in [Figure 10.4](#). In a deep-water environment, where the dominant

lithology is shale, high amplitudes are likely to mark reflections from sands, so the voxel display with that filter setting will show the sand bodies in 3D. Since the range of colours can be compressed or expanded, and the opacity filter varied as well, the interpreter has very precise control over what appears in the final display.

Figure 10.4 Colour management in 3D seismic displays. A chosen range of signal amplitudes can be selected for display by setting a suitable opacity (visibility) filter.

After Kidd, 1999

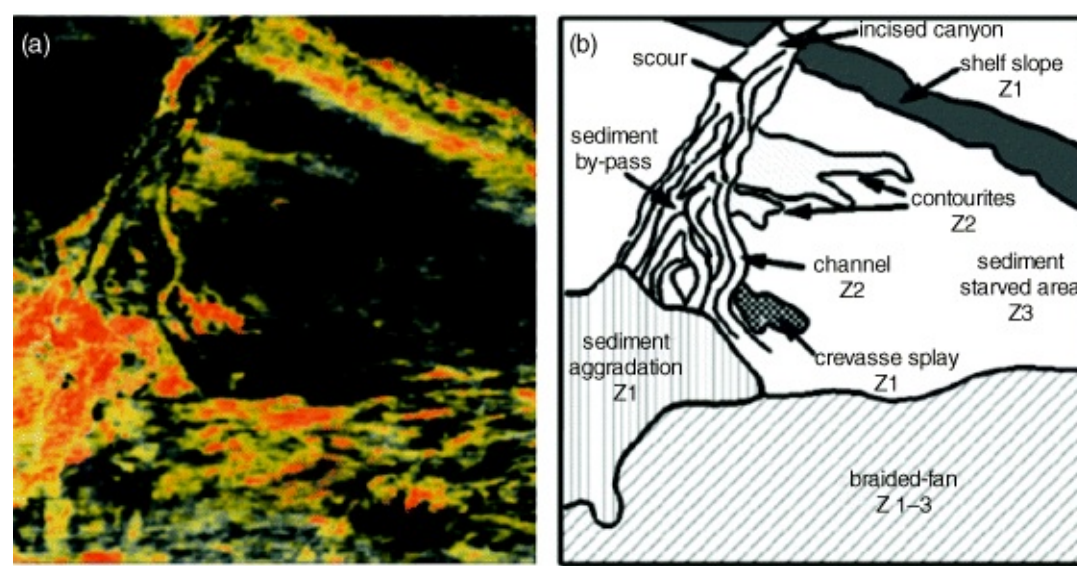


In a key publication, Kidd (1999) explained how volume interpretation should be carried out. Important steps included a review of data scaling, isolation of the objective within a time window or a horizon-defined window (a depositional sequence) and the application of a suitable colour scheme. [Figure 10.5](#) shows the output from the use of an opacity filter similar to that shown in [Figure 10.4](#), together with an interpretation of the resultant voxel volumes in terms of a lowstand channel fan system. Fine tuning of the opacity filter to display a subtle fault system is also demonstrated.

Figure 10.5

- Volume visualization of 3D data, using colours for a restricted range of high amplitudes approximately similar to that defined by the filter shown in [Figure 10.4](#).
- An interpretation of **a** as a lowstand channel fan system. Z1 = high opacity (visibility), Z3 = low opacity.

From Kidd, 1999



A further advantage of this mode of data presentation is that the voxel volume can be rotated on the screen and viewed from any angle. The ultimate display is an immersive environment where 3D volumes and picked horizons, together with well data, are projected on to the walls of a viewing room, giving interpreters the impression of being buried in the data volume and moving through it. Such displays have proved to be powerful tools for integrating a reservoir data set and presenting it to a reservoir team (Hanley, 1999).

10.2.5 Multi-attribute Facies Analysis

The seismic reflection patterns shown in [Figure 10.1b](#) were used as the basis of manual methods of facies analysis and mapping, but the huge increase in data volumes of 3D data have made these methods too slow, while improvements in data quality and information content have made it very worthwhile to adopt numerical methods of analysis.

West *et al.* (2002) give an account of how manual preparation of seismic facies maps has been replaced by a three-stage process:

1. Numerical analysis of the reflection patterns – a textural analysis first used in image processing.
2. Derivation of certain attributes based on that analysis.
3. Combination with other attributes in a semi-automatic assignment of facies throughout a 3D depositional sequence.

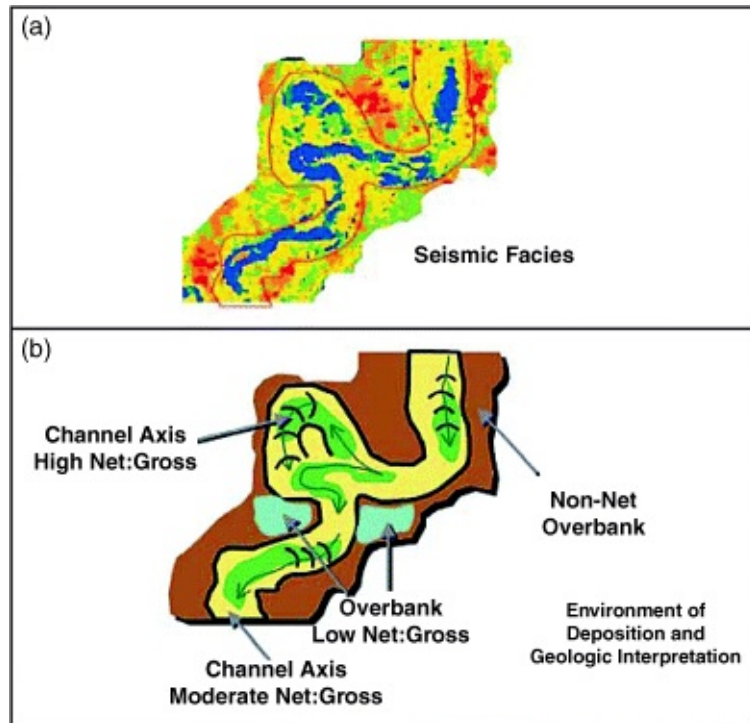
The interpreter is still very much in charge of the process, for example in the selection of an interval of interest defined by picked sequence boundaries and in the choice of key reflection patterns on which to base Stage 1. The assignment of facies in Stage 3 is done by a computer process called a Probabilistic Neural Network (PNN), which has to be trained by providing it with examples (seismic data sets) of typical facies selected visually from the 3D volume by the interpreter. The interpreter conducts quality control of the PNN output by asking the question, ‘Is the computer doing what I would have otherwise done manually, and is it geologically reasonable?’

The final display is a 3D coloured volume of the interval of interest, which the interpreter can examine by displaying horizon slices or by extracting particular voxel volumes. The end product is an integration by the interpreter of the seismic facies data with other attribute and well data, to form a geological depositional model on which a drilling programme can be based ([Figure 10.6](#)).

Figure 10.6

- a. A seismic facies map generated from reflection patterns by neural network methods.
- b. A geological depositional model developed from a.

From West et al., 2002



10.2.6 Analysis of Seismic Facies by Trace Shape

Gao (2004) reported on a completely different approach to texture analysis which avoids the considerable time and effort spent by the interpreter and the computer system in the multi-attribute method. A small piece of seismic data is defined as a model. In its simplest form, it can be a short section of a single trace, perhaps 30 ms long, or it can be a small volume of data. The model searches through the data set trace by trace, sample by sample. At each point, the samples of the model are (conceptually) graphed against the corresponding samples of the seismic data in a scatter plot, and a linear regression analysis is made of the data values against the model values. The gradient of the plot will vary from 1.0 (model and data identical) to 0 (model and data completely different). The gradient is recorded as a new value for that point in the survey volume. In this way, a complete new data volume of 'similarity' values is built up, which can be presented in colour and viewed like any other 3D volume. Sedimentary units with a seismic response similar to that of the reference model should now take the form of voxel volumes which are all coloured the same.

The major piece of interpreter input is now definition of the search model. Gao (2004) reported that, even when using one cycle of a cosine waveform as a model, the method resolved subsurface deep-water channel systems well. A gas deposit in the Gulf of Mexico was clearly detected by using a search model based on a synthetic seismogram from a well that penetrated the gas reservoir interval. It seems possible that the method could be used as a rapid way of searching through a 3D seismic volume for a particular sedimentary facies already drilled elsewhere in a prospect area.

10.2.7 Seismic Facies in Carbonates

Sarg & Schuelke (2003) discussed reasons why the study of seismic facies has been less developed in carbonates than in siliciclastic sediments:

1. Seismic resolution is lower because of higher velocities.
2. Interbedding with siliciclastic sediments may generate strong multiple reflections.
3. Interbedding with mobile evaporites may generate complex structure and steep dips.
4. Depositional dips may be much steeper than in clastics, up to 35° or more.

In addition, seismic textures within units may be chaotic or smeared because:

1. No distinct bedding is present.
2. Karst formation generates a chaotic reflection character.
3. Complex pore systems generate lateral and vertical variations in reflectivity.
4. Raypaths from diffraction points under a thick, high-velocity carbonate will be restricted in their angular scatter when they reach the surface and will give a poor image after migration.

Reef units are fairly distinctive, although not because of textural characteristics. Bubb & Hatlelid (1977) gave several criteria for picking them out on seismic sections including the presence of reflections from the top of the reef (rare), drape of overlying sediments over the reef bulge and loss of continuity of reflections as they are followed into the incoherent events within the reef mass. Quite a lot has been published about the Devonian reefs of western North America (e.g. Brown *et al.*, 1990), but little can be seen of internal seismic textures. Masferro *et al.* (2003), using specially processed 3D data, detected prograding units as important textural features in carbonate build-ups and, in one example, applied a multi-attribute textural analysis to distinguish a lagoonal facies from a marginal facies.

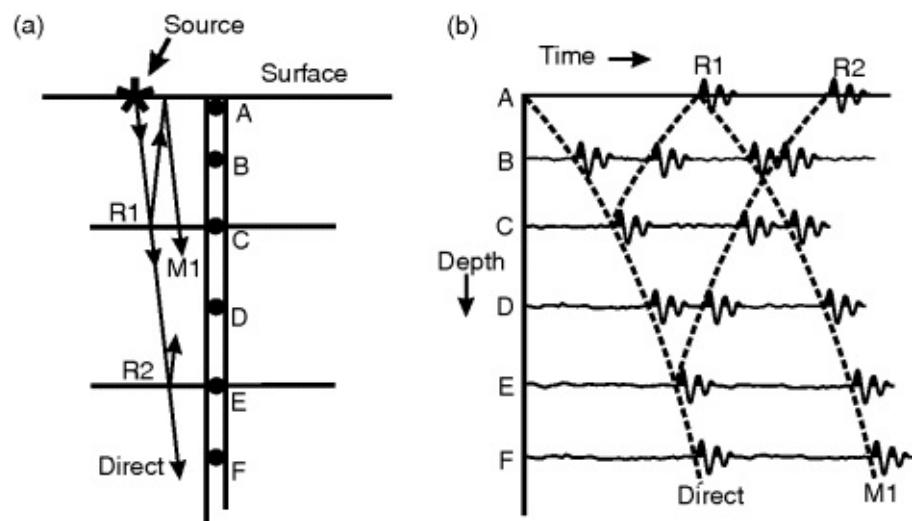
10.3 Refining Reservoir Structure: Vertical Seismic Profiling (VSP)

Vertical seismic profiling is an extension of the well velocity survey described in Chapter 6, Section 6.2. An excellent review of the subject is to be found in Hardage (1985). An array of up to about 50 geophones, typically spaced at 10–20 m, is placed in the well, with the geophones clamped to the side of the well-bore to minimize noise. A shot is fired at the surface and the individual seismograms from each geophone are recorded. The array is then shifted in the well and the process is repeated until the subsurface zone of interest has been adequately covered. Since a full VSP survey takes up expensive rig time and carries the risk of blocking the well if the array becomes stuck, it is only carried out if the surface seismic data is so poor as to prevent a proper well-tie or has failed to resolve some structural problem.

The basic idea can be explained with respect to [Figure 10.7a](#), which shows a simple earth model consisting of two reflectors (R1 and R2) and six of many possible geophone positions, A to F. In practice, no geophone is placed at position A because it would only record the same seismogram as observed at the well location on a normal seismic section.

Figure 10.7

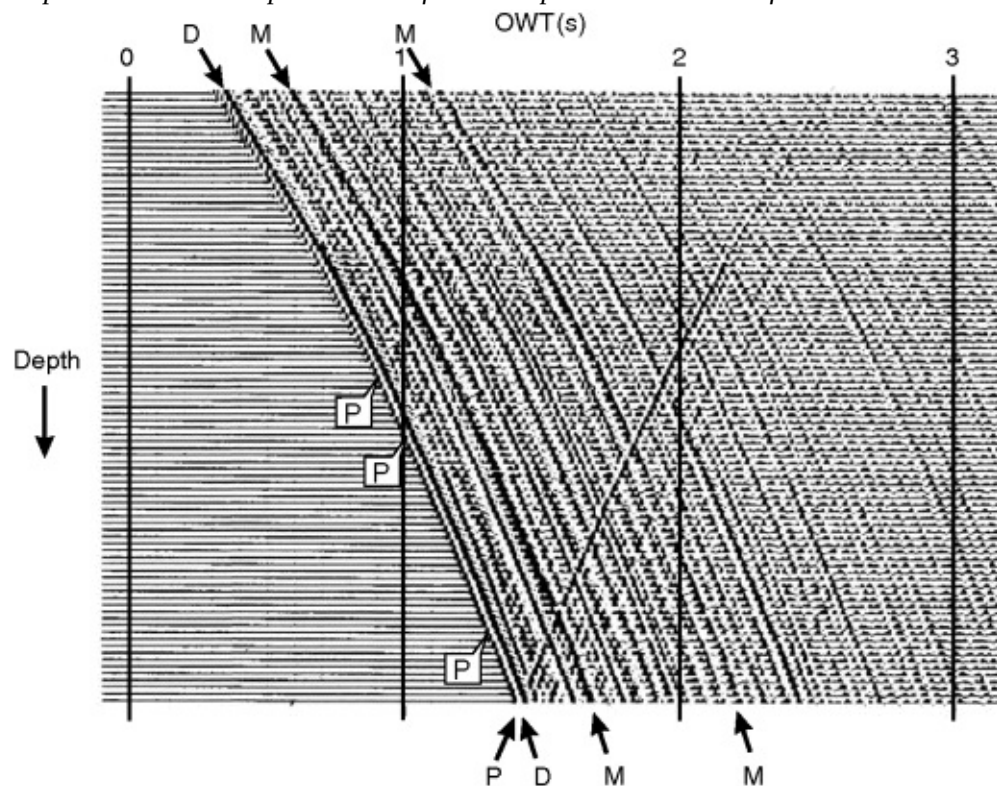
- a. A vertical seismic survey with down-hole geophones A to F and raypaths for two reflections and a surface multiple.
- b. A schematic version of the seismograms recorded at geophones A to F in a.



Consider first the down-travelling direct wave: it passes all geophones and will register as the first arrival on all seismograms at the one-way time (OWT) to that depth (Figures 10.7b Figures 10.8). The travel times will lie on the time-depth curve of the well, which would be a straight line for uniform velocity, but which typically steepens up as velocity increases with depth. Close behind the direct wave, and also travelling downwards, comes the surface multiple (M1) from reflection R1 (Figure 10.7a). It falls on a line parallel to the first arrivals that runs obliquely down through the plot and it lags behind the direct wave by the two-way reflection time to R1 (Figure 10.7b). Multiples are particularly obvious on Figure 10.8, which vividly illustrates the strength of such events in seismic reflection data.

Figure 10.8 VSP field data. D = direct down-going wave, M = down-going multiple reflections, P = up-going primary reflections.

Reproduced with the permission of the European Association of Geoscientists and Engineers (EAGE)



Now consider the upwards-travelling reflection R1, which starts from the interface at geophone C at the time of the direct arrival. As the reflection travels up, it will follow the reverse of the downwards time-depth curve, successively generating a set of reflection events at geophones B and A. In a similar fashion, reflection R2 will start from the direct time at geophone E and pass

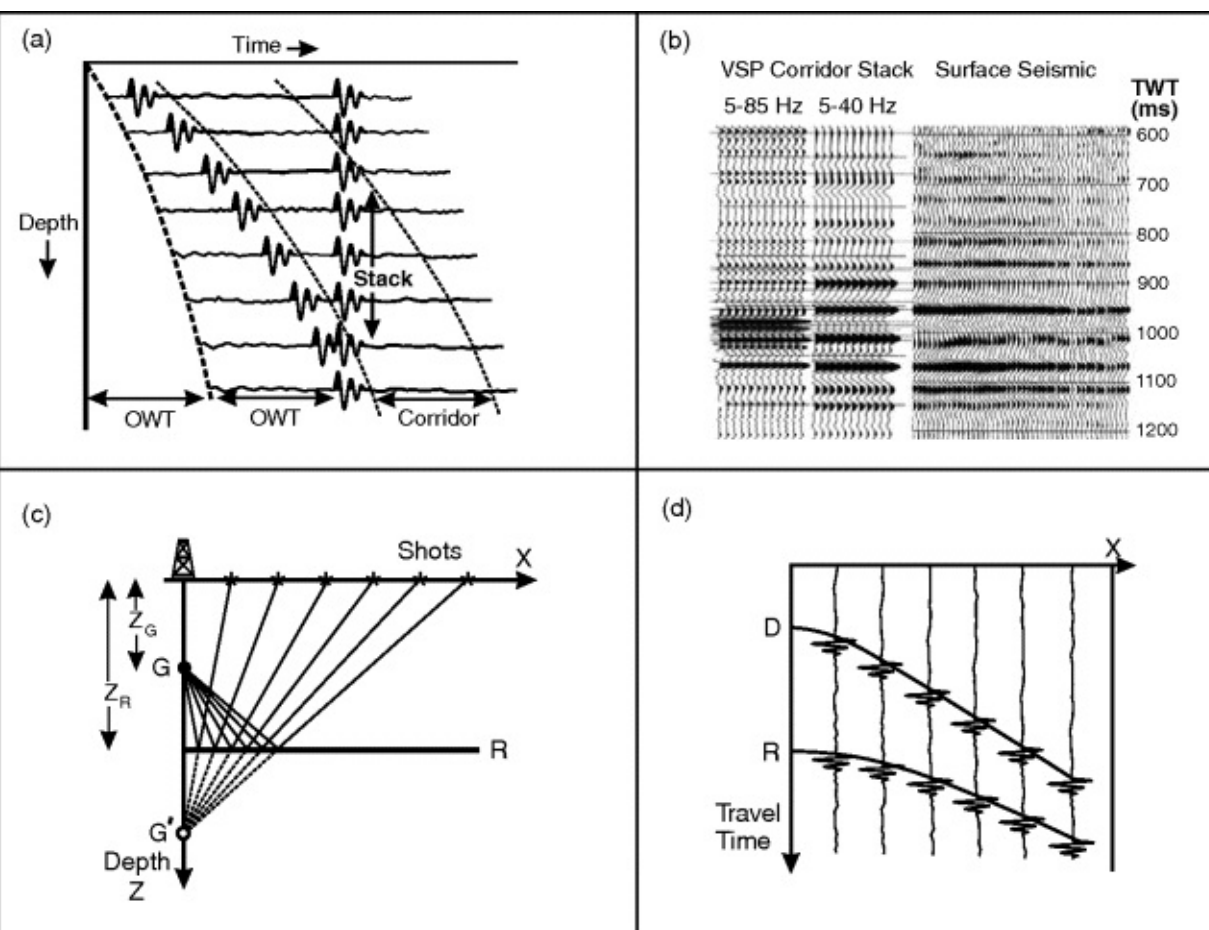
upwards across the recorded traces along a path that is the symmetrical reverse of the down-going direct wave to E. Thus, the display clearly separates downwards-travelling from upwards-travelling seismic energy. In [Figure 10.8](#), an especially strong reflection is easily seen passing upwards through the plot from a time of about 1.35 s on the direct wave, but many more faint reflections can be recognized above it. Reflections from a surface survey observed at the well location (seismogram A in [Figure 10.7b](#)) can be related quite specifically to their generating interfaces at depth on a display of this sort.

10.3.1 VSP Processing and Applications

The first step in processing the data is to apply a Wiener filter to each trace designed to convert the down-going complex wavelet recorded in the first arrivals into a simple zero-phase wavelet. Since all the reflections are versions of the direct wavelet, they will also be converted to zero-phase form. The second step is to apply an f-k filter to the recorded data to separate out the up- and down-going reflections. The process works particularly well with VSP data, because the two wave trains differ so much in their apparent velocity across the data set. A final step is to form a corridor stack, as shown in [Figure 10.9a](#). Each trace is delayed by the time of the direct arrival. Upwards-travelling reflections are thereby aligned across the data set and can be stacked into a composite trace to improve the signal/noise ratio. Stacking is limited to a narrow corridor of data immediately after the first break in order to minimize any multiple interference and to take advantage of the short reflection paths to the down-hole geophones, like that from R2 to geophone D in [Figure 10.7a](#). The process should yield a virtually noise-free seismogram, with every event directly linked to its generating interface in the well. The corridor stack is generally presented as a set of identical traces and is the ideal means with which to tie reflections to their causative geological interfaces in the well ([Figure 10.9b](#)).

Figure 10.9

- a.** VSP traces delayed by the direct arrival time. Up-going primary reflections are brought into alignment and may be stacked within a corridor behind the first arrivals.
- b.** An example of a VSP corridor stack compared to surface seismic. (From Chopra *et al.*, 2004).
- c.** Walkaway VSP for a depth section with one reflector. G = well geophone, G' = well geophone image across the reflector. Direct ray-paths are omitted.
- d.** Model data set recorded from **a**. D = direct arrival, R = reflected arrival.



In addition to exact seismic-to-well ties, VSP provides additional benefits, several of which are discussed and illustrated by Campbell *et al.*, 2005:

1. Possible effects of the presence of hydrocarbons on the down-going wavelet can be estimated by observing the wavelet above and below the formation in the well. This may allow better interpretation of seismic attribute sections in the vicinity of the well.
2. Measurement of amplitude changes in the down-going wave may help to maintain true relative amplitudes in the processing of an associated surface seismic survey.
3. Since the VSP data can be reliably processed to zero phase, the surface seismic data at the well can be compared to it and, if need be, phase adjusted to match.
4. The corridor stack from below the total depth of the well may be processed to give a log of acoustic impedance or velocity at greater depths and so allow some assessment of drilling conditions ahead of the bit – very useful if the well is to be continued. The process can be done especially well, because the velocity log through the drilled portion of the well can be used as a calibration or control on the inversion process.
5. If a corridor stack is made of the VSP data at some time much later than the first break, it will contain a lot of multiple energy and may help in attacking a particular problem with multiples in the surface seismic data (Burton & Lines, 1997).

10.3.2 Walkaway VSP

By offsetting the shots some distance from the well, it is possible to form a seismic section (or seismic volume in 3D) for some distance away from the well location. This may be desirable when the seismic data from a surface survey are of poor quality, so that planning the optimum track of the well bore at the reservoir level is uncertain. A walkaway VSP survey, as the name

implies, is one where a line of shots is made at the surface through the well location, out to a range of several kilometres, and recorded on a geophone array set at a fixed depth down the well ([Figure 10.9c](#)). It is the most common of several possible offset-VSP configurations (Dillon & Thomson, 1984).

The data from a walkaway survey is initially presented as a sort of time-distance section, each trace simply plotted vertically at the shot distance offset from the well ([Figure 10.9d](#)). The travel times of reflections can be modelled as one-way times from a diffractor located at the mirror image of the geophone across the reflector and can be written as:

$$(10.1) \quad (T_X)^2 = (X^2 + K^2)/V^2$$

where T_X is travel time on a trace at offset X from the well, Z_R is the depth of the reflector, Z_G the depth of the geophone, V the velocity down to the reflector and $K = 2Z_R - Z_G$ ([Figure 10.9c](#)). The shape of the reflection is once again a hyperbola ([Figure 10.9d](#)).

The main objective in processing walkaway data is to convert it to a seismic section (or 3D seismic volume) that can be patched into an existing surface seismic section.

Spend a few moments with Tutorial 10.1 to find out the shape and limiting size of the small section obtained from a walkaway VSP.

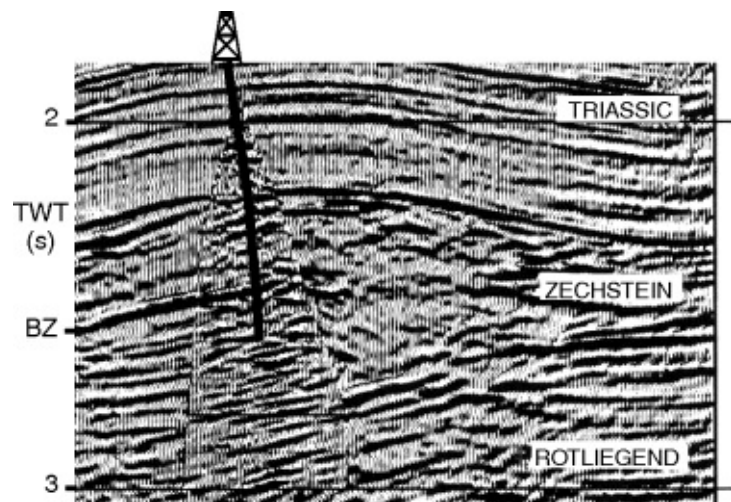
A simple, cheap procedure that gives good results with flattish strata is the VSP-CDP (CMP) transformation (Dillon & Thomson, 1984). The process reforms the recorded walkaway data into normal-incidence traces like CMP traces in a stacked, unmigrated seismic section.

The process is fast and cheap and may be all that is required when the sediments are flat (Chopra *et al.*, 2004). For more complex structures, migration is required. Kirchhoff-style migration has often been employed in VSP work because of its flexibility in handling different source-receiver configurations (Dillon 1985; Wiggins *et al.*, 1986).

A paper by van der Poel & Cassell (1989) illustrated the integration of VSP and surface seismic data. They discussed both VSP-CDP transformation and VSP migration and showed a time-migrated section patched into the migrated surface seismic section ([Figure 10.10](#)). The survey successfully located the up-dip extent of the Base Zechstein reflector where it terminates at a fault. Note the characteristic shape of the limited subsurface coverage from the VSP data (see Tutorial 10.1).

Figure 10.10 A migrated section from a walkaway VSP survey patched into a surface seismic section. BZ = Base Zechstein.

After van der Poel and Cassell, 1989



At sea, the walkaway technique can be extended to a 3D survey by shooting around a spiral path centred on the well. This is especially useful in sub-salt situations or where a gas chimney above the reservoir spoils surface data. In land surveys, problems with access and extra costs make data acquisition of walkaway 3D VSP surveys much more difficult than at sea, but an interesting approach is to take advantage of a surface 3D survey at the time of acquisition by recording the shots down-hole if a suitable well is available within the area of survey (Chopra *et al.*, 2004).

10.4 Refining Reservoir Structure: Seismic Attributes

Recalling that a seismic attribute is any quantity measured or calculated from seismic data, we have already used the attributes of TWT and velocity in a structural context to prepare structure depth maps. Given reasonable data quality, it is normally fairly straightforward to delineate the top and base of the reservoir volume, but an important aspect of reservoir geometry is compartmentalization. This is the degree to which it may be split up by faults into separate compartments, possibly forming separate flow units.

One of the great benefits of 3D surveys has been the accurate delineation of faults, which can now be unequivocally followed across the volume of data. However, delineating numerous faults and placing them accurately in the reservoir model can be a major bottleneck in the interpretive workflow if done manually, section by section. Automatic fault detection is required, and various seismic attributes have been developed to achieve that goal and otherwise facilitate structural interpretation.

Note that data quality becomes much more important in attribute studies than in making maps of basic structure. The expression of a small fault may be easily obscured by noisy data at a place where the gross structural interpretation can be carried through with confidence (Hesthammer, 1999).

10.4.1 Horizon Displays of Dip Magnitude and Azimuth

Faults will be expressed as zones of steep dip and/or variable azimuth of dip on seismic reflections. The first method of automatic fault detection emerged in the 1980s, as the number of 3D surveys grew and computer graphics presentations matured. Shell was one of the companies at the forefront of these developments, and papers by Dalley *et al.* (1989) and Rijks & Jauffred (1991) reported on their use of measurements of dip and azimuth of dip.

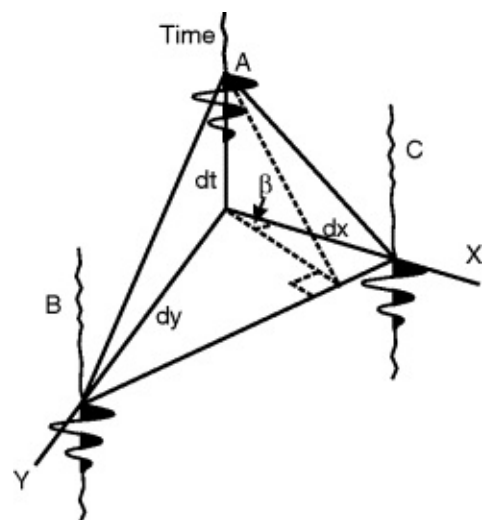
The method depends on picking and timing a particular horizon of interest. Autotracking is

essential in order to pick consistently at the same point on the waveform, and interpolation of times to 1 ms accuracy is necessary to achieve full resolution of detail. A time measurement is available at every trace location, so that the time gradients dt/dx and dt/dy (in s/m) can be measured from a picked reflection on one trace to the same pick on adjacent traces in the x and y directions ([Figure 10.11](#)). From these gradients, amount of dip and azimuth of dip (relative to the x -axis of the survey) can be calculated:

$$(10.2) \text{ Dip (s/m)} = [(dt/dx)^2 + (dt/dy)^2]^{1/2}$$

$$(10.3) \text{ Azimuth (degrees)} = \arctan [(dt/dy)/(dt/dx)]$$

Figure 10.11 Dip and azimuth of dip of a reflection. Time gradients between trace A and traces B and C can be used to calculate the amount of dip (in s/m) and the dip azimuth angle β .



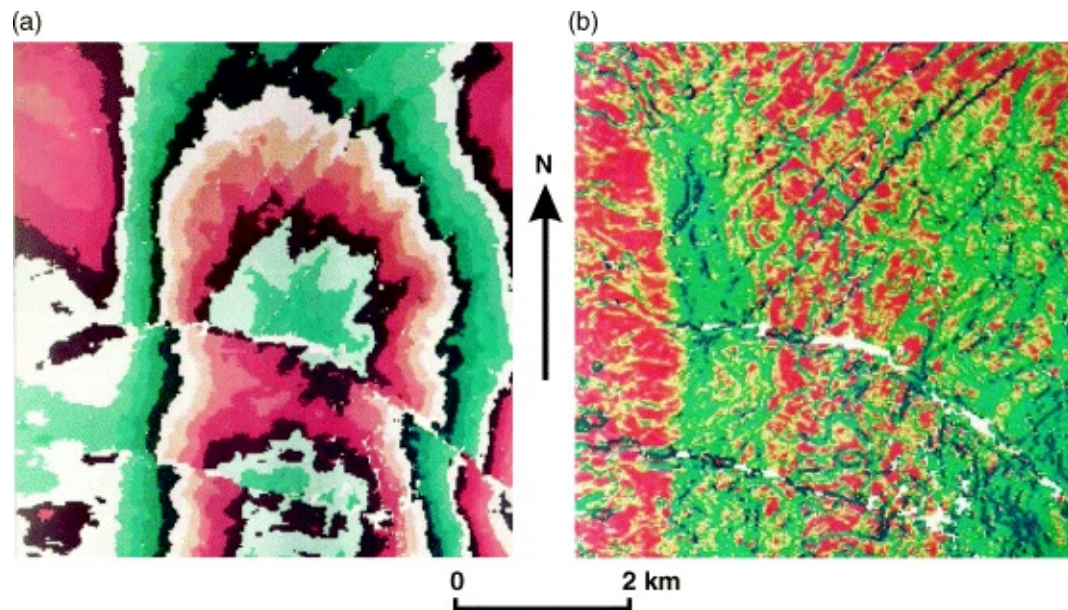
Alternatively, a plane surface is fitted to times on a small number of surrounding traces, dip and azimuth are calculated from that surface and these values are assigned to the location of the central trace (Rijks & Jauffred, 1991).

On map displays of the survey (computer screen or print-out), each trace location is coloured according to the magnitude of dip or the azimuth of dip. Combined displays of both attributes are also possible. Faults will show as narrow zones across the map where there is a sudden colour change marking the steep dips within the fault zone ([Figure 10.12b](#)). The major faults trending approximately E–W in [Figure 10.12a](#) cause clear displacement of the time contours, but the numerous NE–SW trending faults are not so obvious until one sees the dip map ([Figure 10.12b](#)).

Figure 10.12

- A colour-contoured time map of a horizon showing an anticline, overall relief about 300 ms.
- Dip map of the same area as **a**. Red shows flattish areas, green and blue show dips up to 0.3 ms/m.

(Reproduced with the permission of the European Association of Geoscientists and Engineers (EAGE))



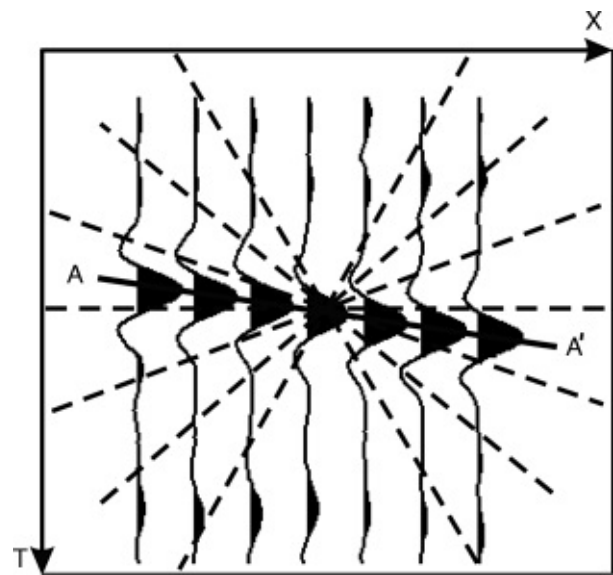
The time surface of the picked horizon may also be presented as a shaded relief surface where one specifies the ‘sun’ position, a direction of illumination across the surface, and calculates the resulting brightness of the surface image at each point. Thus, if illumination is from the north, fault planes will show as bright lines where they trend E–W and downthrow north.

One problem with horizon-based structural attributes is that time has to be spent on picking the horizon and preparing an accurate time map. Moreover, there is no indication of how the structure evolves higher or lower in the section unless further horizons are picked and timed. What is really needed in an attribute that is calculated throughout an entire volume of 3D data – a volume that could be sliced in any direction of interest, just like the 3D seismic data itself, and could show faults at any level. Especially useful would be map displays of faults on time-slices so that the interpreter could short-circuit the traditional process of picking individual faults on vertical sections.

10.4.2 Volumetric Dip Magnitude and Azimuth

To go from dip measurements on a picked horizon to measurements at all data points in a 3D data set means a huge increase in the amount of computation. We can use the ‘slant stack’ method as an example and start with a 2D section taken along the x -axis of the survey. We select a particular time on a particular trace at the centre of a small window of data – perhaps seven traces wide – and stack the traces over a range of trial dips ([Figure 10.13](#)). Semblance can be calculated and used as a measure of the ‘goodness’ of the stacking process as it was in the case of CMP stacking. Of course, the stacking path here is along a straight line through the traces, not along a hyperbola. The dip that gives the highest semblance is assigned to the reference time at the centre trace of the seven. The dip is in the x -direction and so is a measure of dt/dx . The window then moves down one sample to a new time and the process is repeated down to the end of the trace, over all the traces on the section and over all the sections that parallel the x -axis. The process provides a dt/dx value at each sample of the 3D volume.

Figure 10.13 Measuring dip in 2D by stacking data along test alignments and looking for maximum semblance, in this case to be found along A – A'. Can be extended to 3D, but with much more computation.



In the same way, we can work along sections that parallel the y -axis and calculate a dt/dy value at each sample and subsequently the dip and azimuth of dip at each sample from [equations \(10.2\)](#) and [\(10.3\)](#). A lot of computation is involved although, in practice, the process need only be run over a particular volume or zone of interest, such as a reservoir interval.

Chopra & Marfurt (2007a) outline two other methods of calculating volumetric dip and provide an extensive list of references. Although volumetric dip could be displayed as an attribute by itself, its main use is in the proper application of other attributes, such as coherence.

10.4.3 Coherence

Coherence expresses the similarity of a seismic trace to its neighbours. In its earliest version, the cross-correlation function (CCF) of a short windowed portion (<100 ms) of a trace is calculated against neighbouring traces in the in-line and cross-line (say, x and y) directions. If the maxima of the normalized cross-correlation functions are M_x and M_y respectively, then coherence is defined as $(M_x \cdot M_y)^{1/2}$ (Bahorich & Farmer, 1995; Marfurt *et al.*, 1998). The correlation window then moves down the traces one sample and a new value of coherence is calculated. Thus a new coherence trace is calculated sample by sample and, eventually, a whole new 3D coherence volume is built up and can be displayed, like the original seismic data, in sections and time-slices on a 3D workstation.

If traces are similar, coherence will be high. Across a fault zone, traces will be dissimilar and coherence will be low. High coherence is the norm over large areas of a map, so is displayed as a white background on time-slices or sections against which faults show up as thin dark lines of low coherence. The most useful form of presentation is the time-slice or horizon slice. In [Figures 10.14a](#) and [10.14b](#), the circular dark mass left of centre marks the incoherent reflections from the interior of a salt dome. The dark lines radiating out from it are the traces of radial faults. Coherence is also low across the edges of sedimentary features such as channels and slumps. In [Figure 10.14b](#), a network of channels is revealed in the lower right quadrant, marked by thin dark lines of low coherence along the channel edges. The channels show well in this time-slice, but sedimentary features are generally best seen on horizon slices. However, one of the attribute's strengths is that there is no need to spend effort on picking individual horizons before mapping out faults; it can all be done on time-slices.

Figure 10.14 Coherence time-slices calculated by:

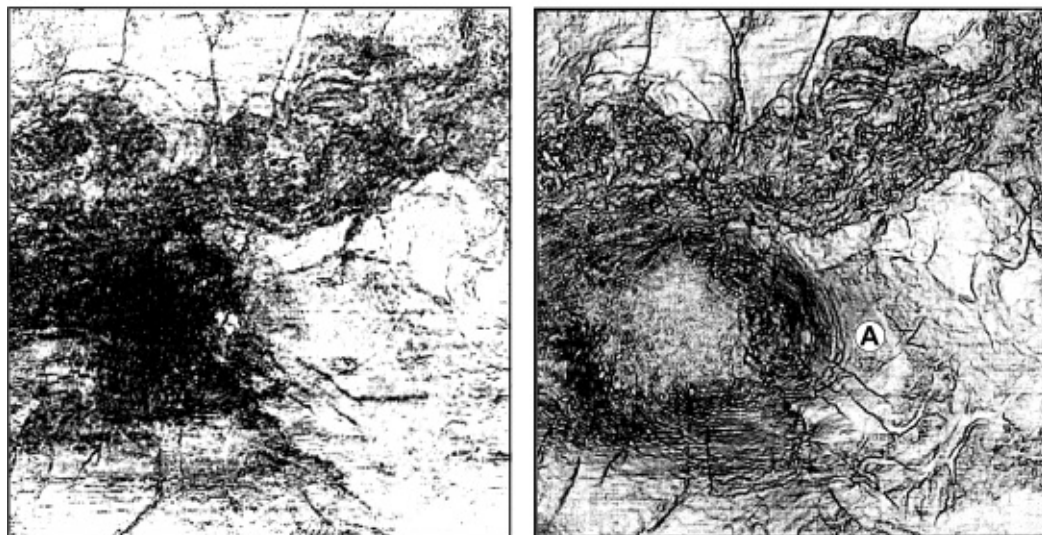
a. cross-correlation;

b. an eigenstructure-based method: point is referred to in text.

(From Gersztenkorn and Marfurt, 1996.)

(a)

(b)



The success of coherence displays stimulated the invention of better ways of calculating trace-to-trace similarity. Marfurt *et al.* (1998) described another measure of coherence based on semblance, the measure of similarity between traces that is widely used in velocity analysis and volumetric dip measurement. As a measure of coherence, semblance is calculated across a group of traces in a small sub-volume of data and is recorded at the central sample of the data volume. If the group of traces straddles a fault, semblance will be low, again marked by a dark feature on the mapped display.

This measure of coherence uses a much shorter time window than cross-correlation, so will give finer depth resolution of sedimentary features. For example, it allows the separation of different sets of channels on different time-slices rather than smearing them all into one fuzzy response. Also, because semblance involves more traces around a central point, it will give a higher signal/noise ratio than the correlation measure. Marfurt *et al.* (1998) provide many examples of the effect of varying the time and spatial dimensions of the semblance volume. However, unlike the cross-correlation measure, it is affected by variation in amplitude between the traces and requires the measurement of volumetric dip. The same analysis can be expressed as a variance attribute, where $\text{variance} = (1 - \text{semblance})$.

The obvious improvement in image quality in [Figure 10.14b](#) compared to [Figure 10.14a](#) is due to the use of a semblance-related calculation, but one that avoids the influence of amplitude variation between traces (eigenstructure-based coherence – Chopra & Marfurt, 2007a). In [Figure 10.14b](#), the shorter time window used in the calculation has preserved the response of the channels in the lower right quadrant, and the higher signal/noise ratio has made all discontinuities stand out much better than in [Figure 10.14a](#).

Of the many interesting details in [Figure 10.14b](#), the curving, narrow lines just left of point A are stratal discontinuities created by steeply-dipping sediments on the flank of the salt dome. Later versions of the calculation avoid this by incorporating measurement of volumetric dip and calculating coherence in the plane of dip. Alternatively, the expensive dip calculation can be avoided by using a slab of data flattened on a prominent reflection (Chopra & Marfurt, 2008).

Coherence has joined dip/azimuth displays as one of the most important of the structural attributes. Its application now goes beyond fault and channel detection to processing quality

control, detection of acquisition footprint and composite displays with other attributes, such as inversion (Chopra, 2002).

10.4.4 Automatic Fault Extraction: Ant-Tracking

Bahorich & Farmer (1995) noted that faults generated surfaces of low coherence within the coherence volume, which could be picked using horizon auto-tracking software adapted to follow the low coherence values present on the fault plane. They showed faults picked in this way and displayed by 3D visualization software. Since then, the topic has received much attention in the industry, both as regards ways of picking the fault planes and ways of handling and displaying the huge numbers of faults that may be picked.

Even with horizon-tracking software, the interpreter has to set off the process on a chosen coherence track for every fault picked. Is there some hands-off process we could use that would search through the data volume and present the interpreter with a collection of extracted fault planes? Consider a process which assigns a large number of seed points at random through the coherence data volume. If a seed point falls on a value of high coherency, then that point is removed. If a seed point falls on a low coherence value, the location is marked and the process continues to look for and mark similar points around it. It continues searching and marking until it runs out of locations with low coherence. At the end of the process, faults will be heavily marked surfaces within the data set.

This process has been compared to the way that ants mark trails to good supplies of food, and so has been called ‘ant-tracking’ (Pedersen *et al.*, 2002). Faults can be classified by orientation and strength of attribute, and logged in a database.

Now we have the second problem – how to handle all the new data. Pedersen *et al.* (2003) described their approach based on a structural analysis of the extracted data. They started with validation of the extracted fault surfaces, ranked according to strength of attribute on the surface and intensity of marking by the ‘ants’ and done interactively with the seismic data. The orientation data can be summarized on a stereogram, and different groups of faults with the same orientation can be extracted and displayed separately in 3D.

Silva *et al.* (2005) used ant-tracking coupled with fault editing to reduce the time spent on a regional fault interpretation from 10 days down to 3 days. Editing of surfaces was done primarily on the basis of size, orientation and vertical extent (they did not mention using the strength of the attribute on the surface). Comparison with manual interpretation showed an excellent match between the faults picked by ant-tracking and by an experienced interpreter.

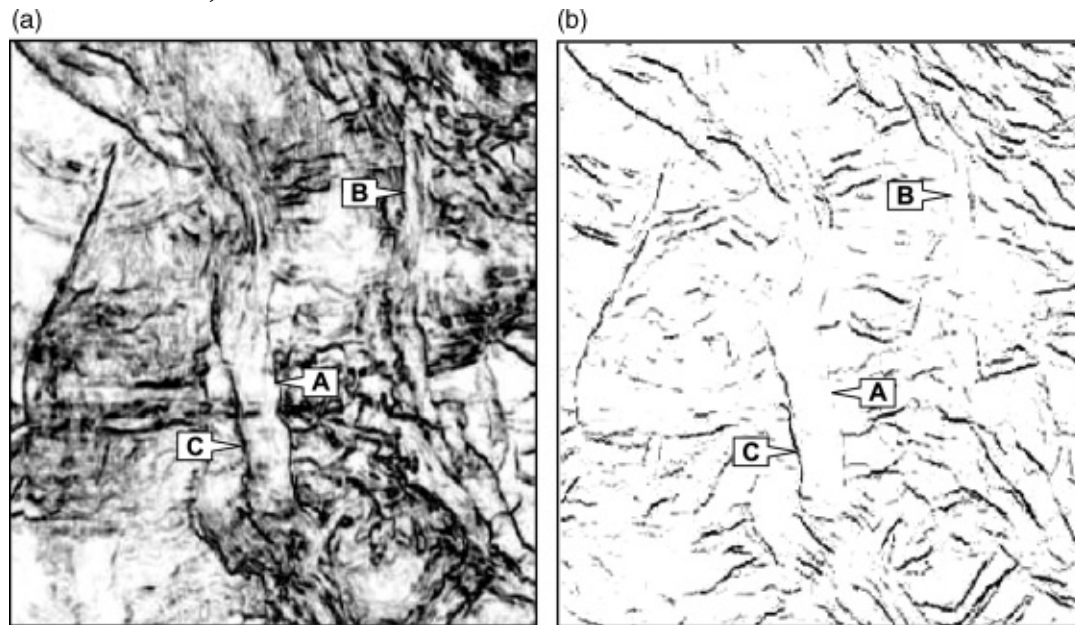
[Figure 10.15](#) shows a map of variance on a time-slice (a measure of coherence) and the same area after fault extraction by ant-tracking. An interesting point is that the margins of the vertically trending features which catch the eye in [Figure 10.15a](#) (such as A and B) are scarcely visible in [10.15b](#), presumably because they are not extensive in depth and so are never heavily marked by the ant-tracking process. They might be interpreted as channel margins. In contrast, the interpreter would expect to see feature C expressed as a fault on sections, because it shows strongly on both displays. Note how the ant-tracking process has also brought clarity to the fault pattern in the top right and bottom right corners of the map.

[Figure 10.15](#)

a. Coherence map.

b. Ant-tracking analysis of **a.** Points A, B and C are referred to in text.

From Silva et al., 2005



10.4.5 Curvature

Curvature is a well-known property of surfaces that has been used in optometry, image processing and terrain analysis since the 1970s. Within the last ten years, it has been applied to seismic interpretation for two main purposes:

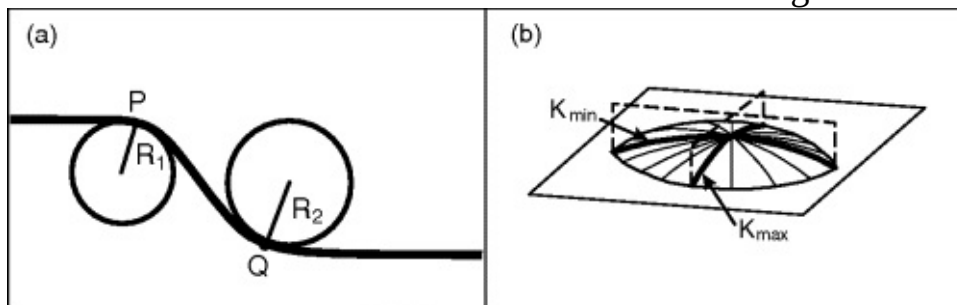
1. To display faults and lineaments across a mapped area.
2. As a means of finding fracture zones – the productive sweet-spots in reservoirs of low permeability.

Curvature, K , at a point on a 2D curve, is described in terms of a circle of radius R which fits the curve locally around the point; curvature is then $1/R$ (Figure 10.16a). Curvature is reckoned as positive for a convex upwards curve and negative for a concave upwards curve. On a 3D surface, a slice is taken through the surface and the curvature is measured on the curve of intersection of slice and surface. Curvature then depends on the direction of the slice through the surface, and we are mostly interested in normal curvatures, where the slice is at right angles to the surface. In Figure 10.16b, two such slices are shown through an ellipsoidal surface. These illustrate the fact that there will always be one slice that shows the maximum curvature (K_{\max}) and one that shows the minimum curvature (K_{\min}) of the surface. Both curvatures are positive in Figure 10.16b, but would be negative for a synclinal surface.

Figure 10.16

a. Definition of curvature along a line. At P curvature is $+(1/R_1)$, at Q $-(1/R_2)$.

b. Maximum and minimum curvature on an elongated dome.



Curvature can be calculated on a single mapped horizon, or at all points within a volume of 3D seismic data. A mapped horizon is available as a set of depths or times (z values) at a grid of points (x, y values) across the mapped area. Curvature at a point is calculated by fitting a quadratic surface to the z values over a small matrix of grid points, typically 3×3 or 5×5 , centred on the point in question. The surface is a best fit in the least-squares sense, so if z' is the value on the fitted surface, then the errors $(z - z')^2$ are kept as small as possible. The z' values on the best-fit surface are described in terms of their (x, y) coordinates by the expression:

$$(10.4) \quad z' = ax^2 + by^2 + cxy + dx + ey + f$$

The coefficients a, b, c, d, e and f can all be calculated (using finite differences) from the differentials (gradients in x and y) of the z' values, for example $a = (d^2z'/dx^2)/2$. From these coefficients, various measures of the curvature of the best-fit surface can be calculated (Roberts, 2001). For example the mean curvature, $K_m = (K_{\max} + K_{\min})/2$ is given by:

$$(10.5) \quad K_m = [a(1 + e^2) + b(1 + d^2) - cde]/(1 + d^2 + e^2)^{1/2}$$

Another important curvature, the Gaussian curvature, K_g , can be calculated in a similar fashion. Neither of these curvatures is of immediate interpretational value, but they provide a route to the calculation of useful curvatures, for example maximum and minimum curvatures from the equations:

$$(10.6) \quad K_{\max} = K_m + (K_m^2 - K_g)^{1/2}$$

$$(10.7) \quad K_{\min} = K_m - (K_m^2 - K_g)^{1/2}$$

K_{\max} is a curvature that proves useful in the detection and display of faults on the mapped horizon (Roberts, 2001). The generation of the least-squares surface causes the sharp step of a fault to be smoothed to a curve, with positive curvature on the upthrow side and negative on the downthrow side ([Figure 10.16a](#)). On a colour-coded map, the fault will show as two adjacent lines of different colour, thus displaying the sense of throw as well as the location of the fault.

Two other curvatures are often used. The most-positive curvature, K_{pos} , is derived from K_{\max} by setting coefficients d and e to zero, in effect removing any planar element in the description of the least-squares surface. The most negative curvature, K_{neg} , is derived in the same way from K_{\min} . The calculation of curvature is carried out at all points on the mapped horizon and the results displayed as colour coded maps in the same fashion as maps of dip and azimuth.

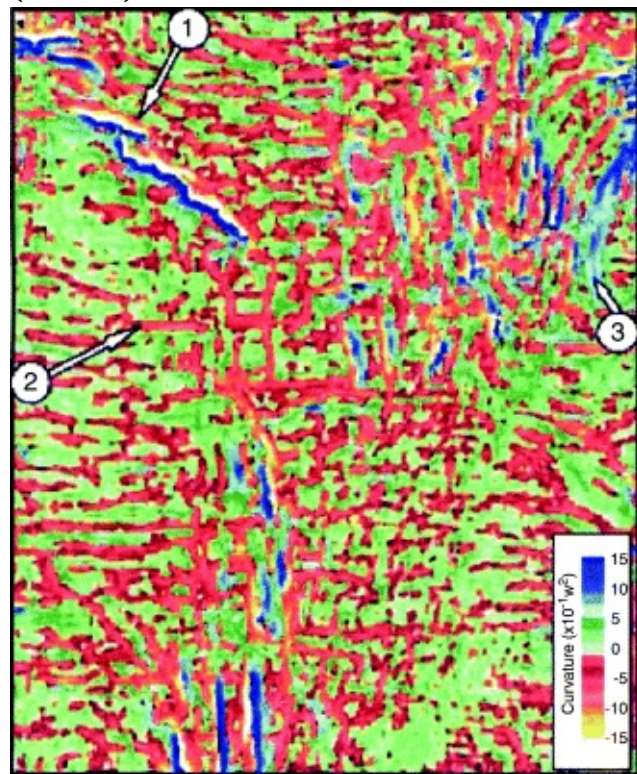
Various other curvatures and related quantities have been defined and used in other fields of study (Roberts, 2001), but it seems from published literature that K_{\max} , K_{pos} and K_{neg} have seen most application in seismic surveys. An important point to consider is the scale of the sampling grid used to establish the best-fit surface ([equation \(10.7\)](#)). Wynn & Stewart (2003) thought that grid spacing of less than 300 m (typically ≈ 50 m) will pick up fault-related curvature, while greater spacing will pick up sedimentary or tectonic-related curvature. Helmore *et al.* (2004) found that Paleocene channels in the northern North Sea basin mapped as lineaments of positive curvature (the result of differential compaction) when curvature was calculated at spacings of several hundred meters.

Curvature was first calculated for picked horizons. However, time gradients can be calculated throughout a volume (Section 10.4.2), which thus allows curvature to be calculated at every sample through a 3D data volume (Helmore *et al.*, 2004, Buck *et al.*, 2007, Chopra & Marfurt, 2007b; 2008).

10.4.6 Applications of Curvature

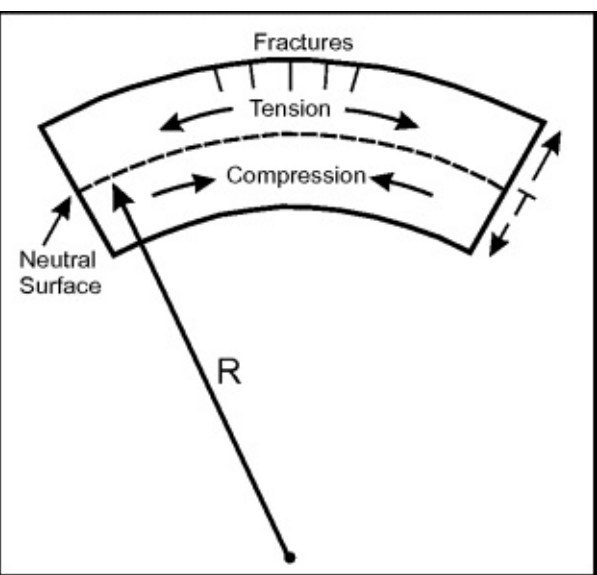
Maximum curvature is a useful attribute for mapping faults, and [Figure 10.17](#) shows their typical expression with positive curvature on the upthrow side, negative on the downthrow. Curvature may extend the expression of a fault as it changes laterally from a distinct break into a monoclinial fold. Chopra & Marfurt (2008) and Blumentritt *et al.* (2006) point out that K_{pos} and K_{neg} curvatures give a less cluttered map of fault lineaments although the sense of throw is lost. These two curvatures also enhance weaker lineaments, providing information in areas that may be virtually blank on coherence maps. However, the result may often be a lattice pattern across the map that requires careful interpretation. Just as with coherence, volumetric curvature should allow tracing of fault planes down through the structure, but so far there seem to be no reports of it being used as an attribute in an ant-tracking type of analysis.

[Figure 10.17](#) Maximum curvature showing the expression of faults (1), ridges (2) and troughs (3). Reproduced with the permission of the European Association of Geoscientists and Engineers (EAGE)



In tight gas reservoirs, fracture zones often form sweet spots where gas production is greatly enhanced (Cooke-Yarborough, 1994). It is well known (Price, 1966) that fractures will form where the rocks are stretched in the upper half of a rock layer folded in an anticline ([Figure 10.18](#)). The tensional stress σ is given by the expression:

[Figure 10.18](#) Fracturing in a bent layer caused by tension at its upper surface.



$$\sigma = ET/2R$$

where E is Young's modulus and T and R are dimensions shown in [Figure 10.18](#). The stress is thus directly proportional to the curvature of the layer.

Such fractures have been observed in experimental deformation of rock units (Handin *et al.*, 1972), so there is a potential link between mapping curvature and detecting fracture zones. However, the link is uncertain; fractures may form and then be closed by later mineralization or by renewed stress in a later phase of tectonism. As is so often in reservoir studies, each field is a special case, and good well control in the form of image logs and flowmeter readings is essential to establish a working relation between production levels, fractures and curvature.

There are some encouraging reports. Hart *et al.* (2002) found a distinct linear zone of curvature on a picked horizon in tight gas-bearing sandstones. The zone ran between two wells, 2.5 km apart, which were not only highly productive but were linked by their drainage histories. Surrounding wells were isolated and were much less productive. Dip azimuth and shaded relief lineaments followed the same trend, and the authors inferred a fracture swarm linking the two wells. Buck *et al.* (2007) created a composite volumetric attribute (PrimeFac) by multiplying K_{pos} with the amplitude in a low-frequency band of the seismic spectrum. The attribute was displayed as narrow coloured bands, which correlated well with faults on both time-slices and sections. The azimuth of vertical fractures imaged in logs in a well corresponded with the orientation of the PrimeFac attribute at the well location.

10.4.7 Structure-oriented Filtering

The process of differentiating a signal generally decreases the signal/noise ratio in the seismic data, especially if the noise has a rather wider bandwidth than signal. Curvature is calculated from signal gradients, so it is easily affected by noise in the signal. Processes in 3D interpretation such as horizon auto-picking are also sensitive to disruption by noise, leading to patchy coverage of a horizon and associated attributes. To counter this, additional processing is commonly performed, which essentially tries to enhance reflection continuity from trace to trace while retaining the expression of faults.

Hocker & Fehmers (2002) detailed the Shell experience of this topic. They pointed out that, as geologists take a greater part in interpretation, it becomes increasingly necessary to stabilize interpretation products and to speed up and simplify interpretation workflows. They outlined a

three-stage process that has been in operation for a number of years within Shell and which may be summarized as the following steps:

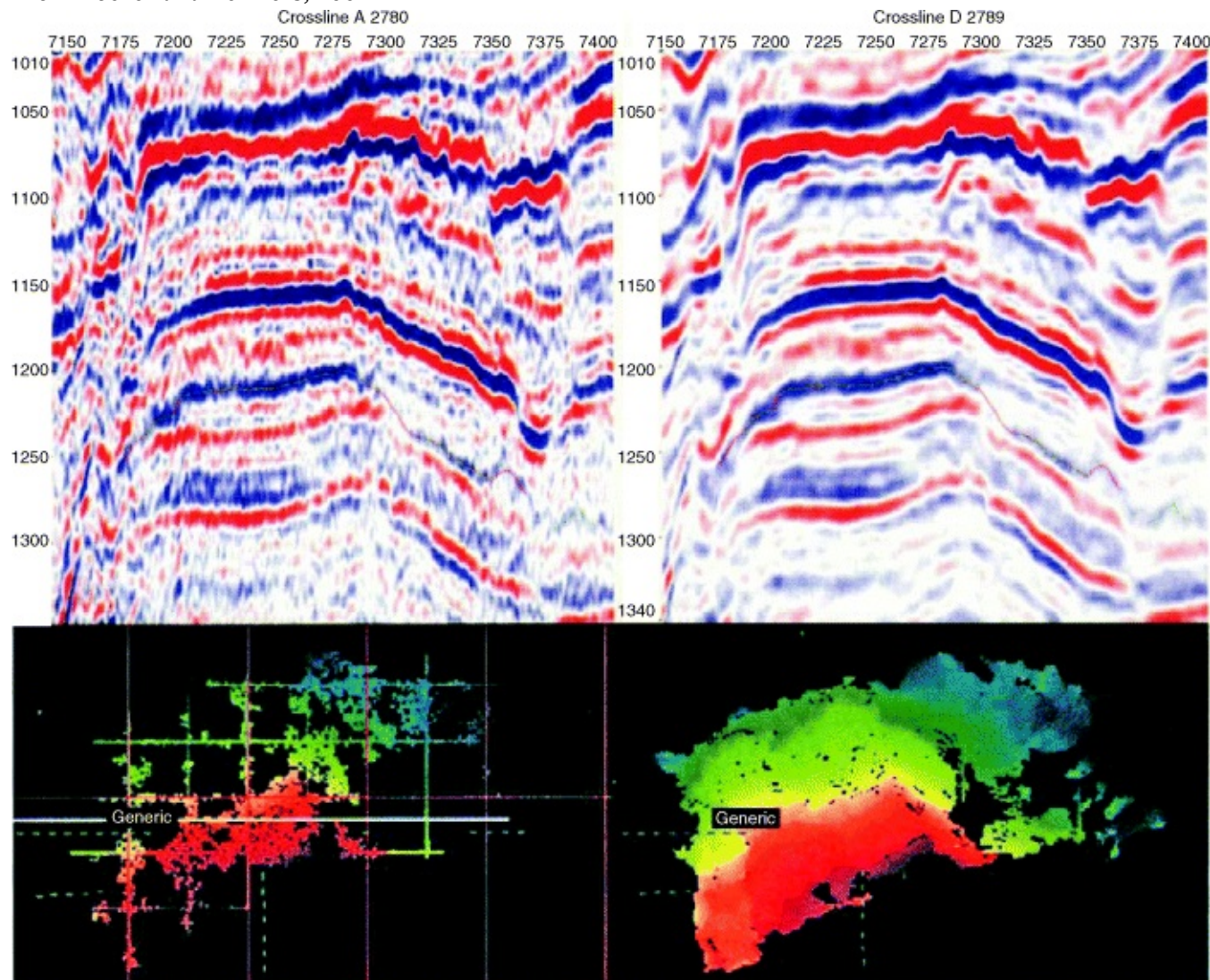
1. Local dip measurement.
2. Edge detection, recognition of faults
3. Smoothing of the data along reflections in the direction of local dip, but not across detected edges.

Their latest approach is to use an anisotropic diffusion technique pioneered in image processing.

The results of such filtering are impressive ([Figure 10.19](#)) and benefit all aspects of structural interpretation from auto-picking horizons to coherence and curvature attributes. Chopra and Marfurt (2007a; 2008) give many examples of data enhancement and discuss alternative ways of filtering the data (for example, trace to trace averaging, median filtering), stressing that the method employed should be tailored to the nature of the noise.

Figure 10.19 A seismic section before (left) and after (right) structure-oriented filtering. At the bottom is a horizon autotracked from the corresponding sections.

From Hocker and Fehmers, 2002



10.5 Seismic Forward Modelling

The numerical model of the reservoir that we build will be derived partly from seismic modelling procedures, which are widely employed at all stages of the work. In forward modelling, we set up

a theoretical model of a geological structure and calculate its seismic expression in the form of one or many seismograms. At the simplest level, working in one dimension, we may generate a one-trace synthetic seismogram from well-logs in order to tie the geology observed at the well location to the reflections on a seismic section through the well (Chapter 7, Tutorials 7.1 and 7.2). In planning a survey, we might wish to test the response of a particular geological scenario to wavelets of different bandwidth in the manner of Tutorial 9.3 (Chapter 9).

Working in two dimensions, the ability to construct seismic sections from hypothetical geological cross-sections can be a big help in testing possibilities in a seismic interpretation. If the model section agrees with the observed section, it may prove nothing for certain (only drilling would do that), but we might proceed further down that interpretive path, seeking other forms of corroboration. Forward modelling may be extended to 3D models and achieved by ray-tracing or by wave-front extrapolation.

Applications of forward modelling make an extensive list:

1. Well ties via synthetic seismograms.
2. Validation of well-to-well correlations of strata.
3. Optimum survey planning – coverage and illumination of structures, resolution of detail in stratigraphy.
4. Construction of velocity models for depth migration.
5. Validation of a structural seismic interpretation – does the interpreted structure generate the observed reflection times?
6. Derivation of travel-time equations and reflection responses to subsurface structure (numerous examples throughout this book).

In inverse modelling (inversion), we do the opposite of forward modelling: we start with the seismogram or data volume and carry out a calculation which generally incorporates some ancillary data. The new calculated values constitute some form of earth model. ‘Inversion’ is a very general term. For example, the process of structural interpretation that yields a depth model of the reservoir is structural inversion. However, in reservoir studies, the term ‘inversion’ is generally used to describe a particular process (discussed in Chapter 11) that yields an earth model expressed as layers of different acoustic impedance (AI). It is commonly applied in reservoir studies because AI is often related to porosity.

10.5.1 One-dimensional Modelling: The Synthetic Seismogram

In this process, we generate only one trace by convolving the series of reflection coefficients observed at a well location with a suitable source wavelet (Chapter 9, Section 9.6). The resultant seismogram may be compared with that observed on a seismic section shot through the well location, and individual reflections can be tied directly to causative geological interfaces in the well (see Chapter 9, [Figure 9.9](#) and Chapter 7, Tutorials 7.1 and 7.2).

The choice of wavelet can be difficult. It should be specified by its amplitude and phase spectra. The amplitude spectrum is generally straightforward to obtain and may be supplied by the processing people or, on a computer, by Fourier analysis of seismic traces near the well with subsequent smoothing of the spectrum. On old paper sections, it may be good enough to use the spectrum of the final band-pass filter listed on the label.

The phase shift spectrum is generally the least well established piece of information about the

wavelet. Look in the processing record of the data for any mention of wavelet processing: generally, an attempt has been made to achieve a zero phase wavelet. Use a zero-phase wavelet initially in the model, but also be prepared to use wavelets with a range of phase lags and leads, e.g. $\pm 30^\circ$ and $\pm 60^\circ$. In a workstation environment, the interpreter will have the opportunity of extracting the wavelet from the seismic data at a well location by the methods explained in Chapter 9, Section 9.10.

Finally, a useful approach which can give good results is to search the well-log for a step-wise change in velocity which should have generated a single, simple wavelet on the section. The wavelet may then be extracted from the section (even on old paper data by manual digitization) and used in the synthetic. In marine data, the water-bottom reflection may provide a simple wavelet from which to extract the phase, but only if the sediment is sufficiently uniform for about the first 40 m under the sea bed.

The final synthetic seismogram is most usefully presented as a triple plot consisting of the AI log, the RC log and the synthetic seismogram. Inclusion of the AI log facilitates precise identification of geological boundaries on the seismic section (Chapter 9, [Figure 9.9](#)). The synthetic is inserted into the seismic section at the well location for direct comparison with the recorded data (Chapter 7, Tutorial 7.2). In the above scheme, primary reflections with true relative amplitudes will be generated in the synthetic trace, but no multiples – a suitable state for comparison with processed data in which multiples have been suppressed.

10.5.2 Mis-match between Synthetic Seismogram and Section

Where both the well data and the seismic data are of good quality, the match between synthetic and observed seismograms can be good (Chapter 7, Tutorials 7.2 and 7.4). However, there are many reasons why the match may be poor:

1. Extra reflections may appear on the synthetic as compared to the section for the following reasons:
 - a. Serious caving of the side of the borehole may have led to a low-amplitude ultrasonic signal in the logging device and late timing on the more distant receiver, so giving unusually long transit times and a false velocity change on the log. To create a reflection, these conditions would have to persist for several tens of feet in the hole. Where caving is suspected to have happened (from inspection of the caliper log), editing of the sonic log may be required.
 - b. The hole may have penetrated a local sand lens about the size of the inner Fresnel zone, so the lens affects the log but is not extensive enough to give rise to a good reflection at the surface.
 - c. Mud filtrate may have invaded the formation deeply enough to affect the transit time.
2. Extra reflections may appear on the seismic section as compared to the synthetic because:
 - a. Multiples are not well suppressed on the section (check against a synthetic generated with multiples if software allows).
 - b. The seismic section was produced with strong AGC, so weak reflections appear on the section which scarcely show on the synthetic (unlikely in modern data).
 - c. A thin overpressured horizon in a shale of low permeability may generate a moderate reflection on the section. However, the horizon may lose pressure around the well upon being penetrated by the drill, and thereby not show on the sonic log or be represented on the

synthetic seismogram.

d. On 2D data, sideswipe may be present, possibly at high amplitude.

3. If most reflections appear to be at about the right time, but there is only poor correspondence of waveform shape and there seem to be time shifts between the two traces, then the phase shift of the synthetic wavelet is probably wrong.

4. Due to mode conversion, there may be considerable variations in amplitude versus offset (AVO) across the CMP gather (see Section 11.4 in Chapter 11). The result may be a change of polarity between synthetic seismogram and seismic data, or a reflection on the synthetic, but nothing on the section.

In a comprehensive review of the factors affecting the fit of synthetic seismograms with observed seismic data, White & Hu (1998) gave several examples of the quality of fit that can be achieved and emphasized the importance of good multiple suppression and migration in processing the seismic data. Careful editing of the sonic and density logs is also very important.

The main application of synthetic seismograms is in correlating well geology to the seismic section, as demonstrated in Chapter 7 in Tutorials 7.1 and 7.2. Synthetic seismograms are also useful as tutorial aids to the interpreter in the study of the seismic response from different geological sequences, e.g. gradational lithological boundaries, effect of hydrocarbons in reservoir rocks, etc. Some simple examples were given in Chapter 9, in [Figure 9.9](#), together with Tutorial 9.3.

The knowledge gained may be used to plan surveys for particular geological targets, or as an aid in interpretation, by demonstrating features of the seismogram that one should look for (or beware of) on the section.

10.5.3 Forward Modelling in Two and Three Dimensions

In two-dimensional modelling, we set up a geological cross-section, assign velocities, densities and depths to the geological units, assign a suitable wavelet and calculate the seismic section that would be observed. The calculation may be done for normal-incidence reflection (stacked, but unmigrated sections) or for migrated sections.

One of the simplest methods is to measure the sequence of reflection coefficients that would be encountered in each of a series of vertical boreholes across the geological section (one for each CMP position) and to calculate a synthetic seismogram at each location. This process simulates an ideal depth-migrated section which has been re-scaled vertically in time. Velocities, densities and depths may vary across the section, so that both structure and facies changes may be modelled. The method is useful as a quick way of modelling lateral stratigraphic variation (Middleton, 1987).

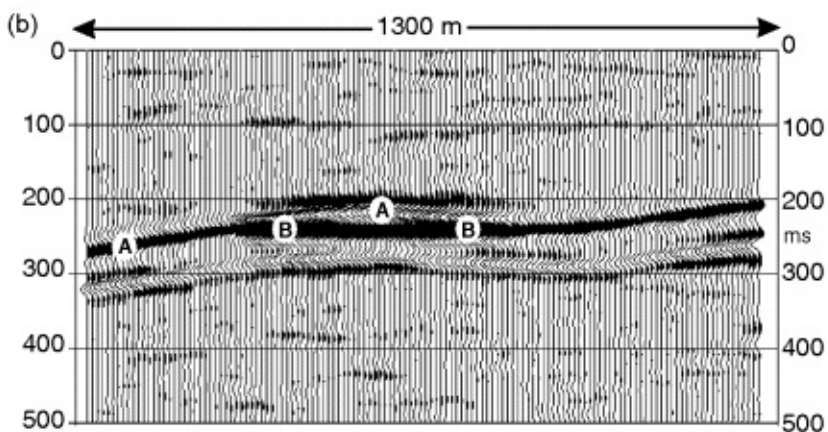
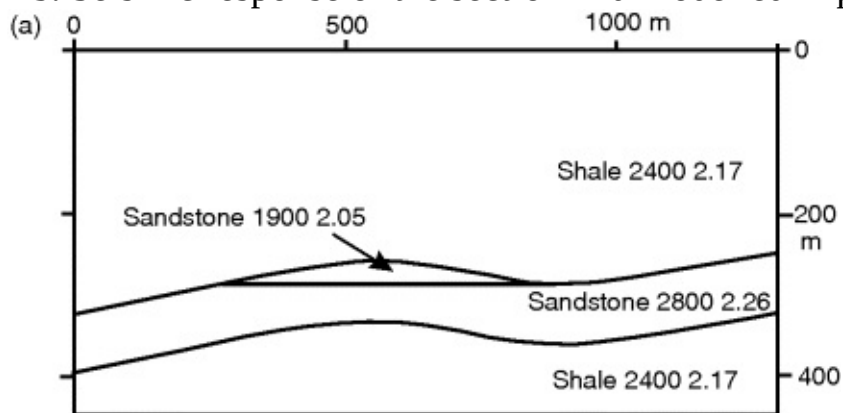
[Figure 10.20](#) shows a geological model and a seismic section derived from it, modelled by this method. It shows some of the key characteristics of a gas bright spot, notably: the reversal in polarity of reflection A over the top; higher amplitudes from tuning at the pinch-outs either side of the flat spot B; and slight push-down of the flat spot, caused by low velocity of the gas-bearing rock above. It is also easy to check out the response of a model to different source wavelets by this technique.

[Figure 10.20](#)

a. A geological model of gas trapped in a minor reversal of dip in a sandstone encased in shale,

labelled with velocities (m/s) and densities (g/cm^3).

b. Seismic response of the section in **a** modelled in program *SYNTHSEC*.



Try your hand at 2D forward modelling of the classic interpretation pitfall called 'fault shadow' with program *SYNTHSEC* in Tutorial 10.2

Forward modelling can also be done in 3D, but the extra dimension makes setting up the model and carrying out the calculations much more arduous and not something that is typically included in an interpretation workflow. It is often used in planning 3D surveys, for example in checking that a particular part of a complex 3D target will be illuminated by the proposed shooting program.

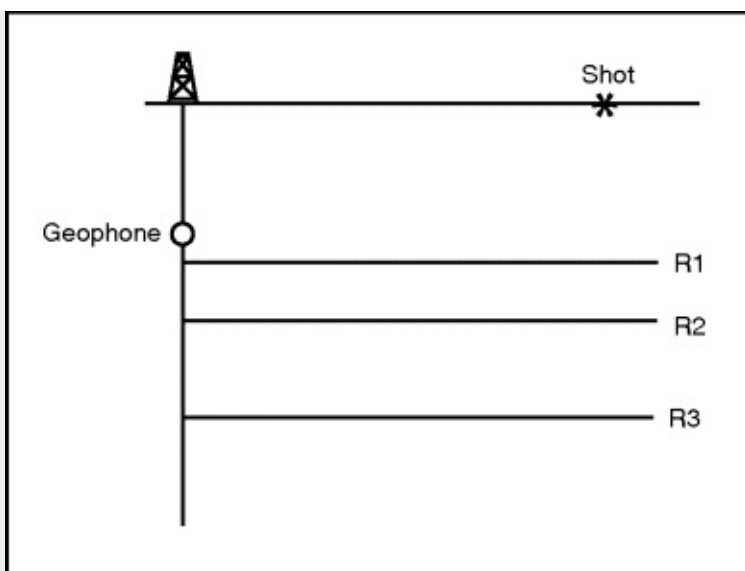
Forward modelling may be used in a variety of other situations, depending on the desired product. For example, we have already seen how, in Kirchhoff prestack migration, the time-surfaces across which data values must be summed to condense diffractions to reflections are established by ray-tracing through a velocity model of the subsurface (Chapter 8, [Figure 8.9](#)). For 3D migration, the modelling has to be done in 3D.

Tutorials for Chapter 10

Tutorial 10.1

Purpose: To demonstrate the limited extent of subsurface coverage from a walkaway VSP survey

[Figure T10.1.1](#)



1. In [Figure T10.1.1](#), find the mirror image of the shot across reflector R1 and draw the (imaginary) ray from there to the well geophone. Note the reflection point where the ray crosses R1. Connect the reflection point back to the shot to show the true raypath.
2. Repeat for reflectors R2 and R3. Assume velocity is constant, so rays are straight lines.
3. Note how the reflection points on the three reflectors lie on a curved path. If the shot position shown is at maximum offset from the well, this curve defines the maximum width of subsurface coverage.

Tutorial 10.2

Purpose: To demonstrate the fault shadow effect by 2D forward modelling.

1. Start program *SYNTHSEC*. If this is the first time you have used it, take a few minutes to check out its basic function in Help/Quickstart.
2. Re-start *SYNTHSEC* and choose Geological Model/Create from the menu.
3. Click on Lithologies/New and for lithologies 1, 2 and 3 enter velocities of 2,000, 3,000 and 3,500 m/s. Give the model a name: Tut10_2 is OK.
4. Click on Section/Open Bitmap and from the data files provided open Tut10_2.bmp. This model shows left-dipping strata with a normal fault in the middle. The top of the 3,500 m/s layer is Top Reservoir.
5. Go on to Calibrate and measure the section using the six control points marked in red. Click twice on measuring points that are circled twice.
6. Complete the calculation of the seismic section and display it in *SEGYP2D* (shades of grey or colours are good). Why has the false anticlinal structure appeared at the Top Reservoir? This is a classic seismic interpretation pitfall, and false structures like this have been drilled in the past. See Fagin (1996).

Chapter 11

Seismic Input to Mapping Reservoir Properties

11.1 Introduction

In this chapter, we will survey some of the methods used to extract information from the seismic data about the properties of the hydrocarbon reservoir. For quantitative estimates of rock properties, it is essential to calibrate the seismic-derived quantities to well data; however, even prior to any drilling, the seismic data can often highlight potential zones of interest. Each reservoir project is, to some extent, a one-off, with a workflow designed for the particular circumstances of the reservoir and the object of the investigation. Geologists, geophysicists and petrophysicists are all involved, and the interpretation becomes a team effort.

Once again we are dealing with seismic attributes – quantities derived from the seismic data which may be related in some way to reservoir properties of interest, such as porosity or hydrocarbon content. Some attributes can be directly linked by physical theory to a rock property; for example, the high amplitudes commonly observed over gas-bearing porous sandstones are linked to the low acoustic impedance of the gas-bearing rocks. Many attributes cannot be directly linked to rock properties through physical theory, but they may still be usefully employed by making the link in a statistical manner. In every case, it is important to remember that the attribute can only be given a certain geological or petrophysical interpretation when calibrated with well data.

Seismic attributes have had a chequered history from the 1970s onwards, but they have become increasingly important with the widespread adoption of 3D seismic techniques through the 1990s to the present day (Barnes, 1999, Chopra & Marfurt, 2005). One key factor in their revival is the facility with which seismic attributes can be displayed in high resolution across a map of a 3D survey. A second factor is the improvement in data quality that follows from the universal use of 3D seismic data in reservoir studies, free from sideswipe, with high spatial resolution and with better multiple elimination. Although a structural interpretation can be forced through even when the data is rather poor, the old adage of ‘garbage in, garbage out’ applies especially to the calculation of seismic attributes.

An important general point is that the mode of presentation of the data is very important in seismic interpretation. Sometimes it may be simply a matter of changing from colour to greyscale, or of adjusting a colour scale to show up a particular range of values in the data, or of transforming the data into another attribute, such as acoustic impedance. These opportunities have grown up with the development of computer graphics technology over the last 30 years. The slow growth of the 3D technique in the 1970s and early 1980s may be partly explained by the difficulty of presenting the data to the interpreter (and to senior management!) in the absence of versatile computer graphics.

Colour displays facilitate the vivid presentation of variations in attributes across a map area, and the image of a section or horizon slice can be enhanced by the techniques applied to digital

images. Integration of extra data sets such as well tracks, well logs or synthetic seismograms is easily done. The interpreter may end up with almost more choice of data displays than he/she knows what to do with, but should always keep a large measure of healthy scepticism about what the ‘pretty pictures’ that appear on the computer screen really say about the subsurface.

11.2 Reflection Amplitude

One of the holy grails in seismic exploration is to detect the presence of oil and gas directly from the seismic data. The digital revolution of the 1960s made it easy to display the true relative amplitude of seismic reflections. For structural interpretation, automatic gain control (AGC) was always used in preparing sections, so that weak but structurally important reflections could be easily seen. However, where AGC was absent, interpreters sometimes noticed sudden flare-ups of amplitude along individual reflections. These were dubbed ‘bright spots’, and in the Gulf of Mexico many were found to be caused by rather shallow gas-bearing sands of low acoustic impedance compared to the surrounding shales. If the reservoir was thick enough, the bright spot might be floored by a ‘flat spot’, the horizontal reflection from the gas/water interface below. These were the first Direct Hydrocarbon Indicators (DHIs). [Figure 10.20](#) in Chapter 10 showed the modelled seismic response of such a gas sand and illustrated several characteristic features, not all of which may be present in every example.

Sadly, it soon became clear that a comparatively small percentage of gas (of no economic interest) was all that was needed to cause a disproportionately impressive bright spot (Domenico, 1974). Even more confusingly, other gas reservoirs showed only as an obscure phase change or a drop in amplitude – a ‘dim-out’. Moreover, lateral facies variation, such as the local development of thin limestones, also caused bright spots. It was therefore soon recognized that a bright spot by itself is not the ‘magic petroleum indicator’ that we would like to have. However, the study of seismic attributes, such as amplitude, frequency, phase and the polarity of the seismogram, received great stimulus as a result. Amplitude is still the most widely applied of all attributes and, in favourable circumstances, it may enable the mapping of the lateral extent of both gas and oil-bearing reservoirs.

Flat spots are much less commonly seen than bright spots, but they are superior as a DHI because of their uniqueness. In favourable circumstances, it may be possible to map the extent of a reservoir by mapping the flat spot from the gas/water interface, thus saving the cost of step-out holes during development of a field (Backus & Chen, 1975).

Dorn *et al.* (1996) described the use of amplitude in mapping porosity across the Pickerill Gas Field in the southern North Sea Basin. Their study was especially interesting in that it showed how many potentially upsetting factors have to be taken into account and investigated in the course of detailed reservoir seismic analysis, and how further processing of the seismic data may be necessary to fine-tune the seismic response. They had found an encouragingly regular relationship between acoustic impedance and porosity in the Rotliegend sandstone interval and a reasonable relation between the amplitude of synthetic seismograms at Top Rotliegend level and reservoir porosity. However, the relationship between amplitude of *observed* data and porosity was poorly defined.

The wavelet extracted from observed data at the wells proved to be far from zero phase (approximately -90° phase), and both amplitude and phase spectra were adjusted accordingly.

Note that if $s(t)$ = seismogram, $w(t)$ = wavelet and $RC(t)$ = reflection coefficient series at the well (all functions of time, t), then:

$$s(t) = w(t) \cdot RC(t)$$

in the time domain. Or, in the frequency domain (f),

$$s(f) = w(f) \cdot RC(f)$$

where $s(f)$, etc. are amplitude spectra. Hence:

$$w(f) = s(f) / RC(f)$$

So the wavelet's spectrum is just the seismogram spectrum divided by that of the reflection coefficient series. This is how Dorn *et al.* (1996) derived a 'compensated' wavelet spectrum. They also designed a filter to change the wavelet's phase from approximately -90° to zero. When the re-processed seismic amplitudes at the well locations were plotted against well porosity, a much tighter relationship was observed, which was confirmed in new wells drilled subsequently. The new porosity-amplitude relationship was used to map porosity all across the field and the results were incorporated in the integrated reservoir model.

This study also demonstrated many other factors that have to be considered in assessing amplitude. Tuning effects between top and base reservoir and between top and base of the overlying anhydrite were considered and judged to be present only as second-order effects. It was noted that the overlying anhydrite had very uniform acoustic impedance across the field, so that amplitude variation would relate only to changes in the underlying Rotliegend sandstone. An image-ray correction ('Hubral correction') was applied to the seismic data to make sure the wells would be compared to the correct observed traces.

11.3 Acoustic Impedance (AI) Inversion

We know that the contrast in acoustic impedance (ρV) across a reflecting interface, expressed as the reflection coefficient (R), determines the reflection amplitude:

$$(11.1) \quad R = (\rho_2 V_2 - \rho_1 V_1) / (\rho_2 V_2 + \rho_1 V_1)$$

where $\rho_1 V_1$ and $\rho_2 V_2$ refer to the acoustic impedance of the layers above and below the interface. Reflections tell us about the interfaces between rock layers, but do not directly tell us about the nature of the layers themselves. Reflections are good for tracing structure, but for reservoir properties we would much rather deal with layer properties (e.g. velocity, density) than interface properties.

An attractive goal is to create an AI log at every seismic trace within a 3D subsurface volume. Porosity is often strongly correlated with AI and, with good well calibration, we could then take full advantage of the seismic data as an interpolator of porosity between well control. Since we start with geophysical measurements (the seismic trace) and directly calculate an earth model, we are dealing here with inverse modelling.

11.3.1 AI Inversion by Recursion and Trace Integration

Suppose that instead of the seismic trace, we have a reflection coefficient series $R(t)$ – a sequence of spikes sampled at regular time intervals. If we start at a layer of known AI = $\rho_1 V_1$, then, by rearranging [equation \(11.1\)](#), we can calculate the AI of the layer below:

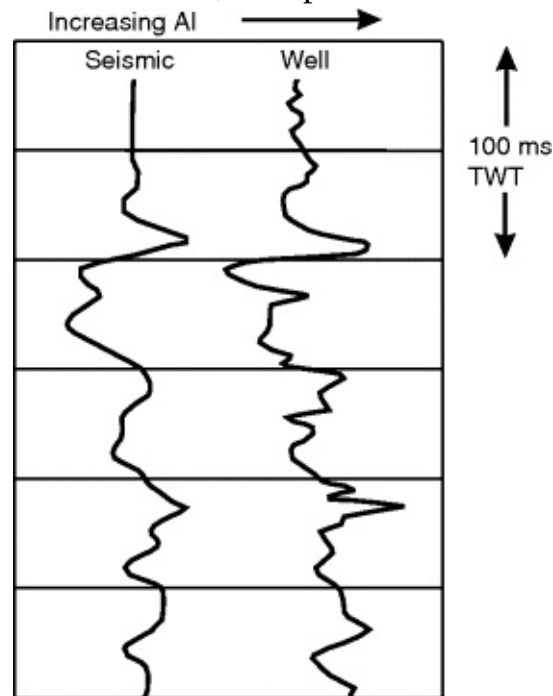
$$(11.2) \quad \rho_2 V_2 = \rho_1 V_1 (1 + R) / (1 - R)$$

and we can use this new value of AI, together with the next $R(t)$ value, to calculate the next AI value down the succession of layers. The calculation can continue, sample by sample, down the series of reflection coefficients, converting each seismic trace to a time-sampled log of acoustic impedance. The calculation is recursive; new values are calculated from previous values.

In reality, we do not have a spiky trace of R values – we simply have a deconvolved seismic trace with as sharp a zero-phase wavelet as we can get. We can scale the trace samples to suitable fractional values as pseudo-reflection coefficients, assume a starting value of $\rho_1 V_1$ in a uniform formation just above the reservoir and carry out the recursive calculation. Inevitably, though, the limitations of the wavelet's spectrum means that the bandwidth of the seismic AI is restricted at both the low and high frequency ends.

In [Figure 11.1](#), the high frequencies are clearly restricted in the seismic version (by absorption in the earth), giving a smoother result. The trend to higher values of AI at depth, evident in the well data in [Figure 11.1](#), is lost in the seismic version, simply because the seismic instruments are unable to record such low-frequency variation. The low frequencies may be added back from filtered well data or detailed velocity analyses, but the high frequencies are lost forever.

Figure 11.1 Acoustic impedance (AI) derived by the recursive method from a seismic trace at a well location, compared to AI calculated from sonic and density logs in the well.



Now what about trace integration? First, we make an approximation of $R(t)$ in [equation \(11.1\)](#) by writing:

$$(\rho_2 V_2 - \rho_1 V_1) = \Delta(\rho V)$$

$$\text{and } (\rho_2 V_2 + \rho_1 V_1) \approx 2\rho V$$

$$\text{so } R(t) = \Delta(\rho V) / 2\rho V$$

If we integrate $R(t)$ with respect to time, i.e. add the values, sample by sample, into an accumulating sum, we create another time-varying quantity:

$$\Sigma R(t) = \Sigma [\Delta(\rho V) / (2\rho V)]$$

Comparing this to the standard integral:

$$\int (1/2x) \cdot dx = 1/2 \cdot \ln x$$

$$\text{we can say } \Sigma R(t) = 1/2 \cdot \ln(\rho V)$$

so $\ln(\rho V) = 2\Sigma R(t)$

(11.3) and $(\rho V)(t) = \exp[2\Sigma R(t)]$

If we again take the amplitudes of the seismic signal to be a measure of the reflection coefficients, then the logarithm of acoustic impedance can be calculated as a function of time by progressively summing (integrating) the reflection trace amplitudes. Substitution of the sum in [equation \(11.3\)](#) gives the acoustic impedance. Finally, for direct comparison with sonic well log data, we might use some relationship between AI and V, such as:

$$V = (AI/0.31)^{0.8}$$

(derived from Gardner's law, AI in m/s.g/cm³, V in m/s). Data created in this way is often called a pseudo-sonic log.

11.3.2 The Good and the Bad of AI Inversion

Convincing comparisons have been made between pseudo-sonic logs and real sonic logs from a well on the seismic line ([Figure 11.1](#); Lavergne & Wilm, 1977; Lindseth, 1979).

The converted traces are displayed side by side and scaled in depth so that, to the geologist, they appear as very closely spaced well logs, enabling detailed correlation of units across the section. Some advantages of such traces over raw seismic data are:

1. The section shows a property of the layers (AI or velocity) rather than a property of the interfaces between layers (reflections).
2. There are no distortions in depth, so correlation and thickness measurements can be made directly.
3. They can be tied in to sonic logs measured in wells along the section, thus enabling the quality of the data to be assessed against the real thing and providing feedback on possible improvements in processing.
4. There is better resolution of thin beds. This was noticed quite early (DeLaplanche *et al.*, 1982), but it is not clear why it should be so.

If the velocity inversion seems to be going wrong (i.e. does not check with sonic data in a well), there are several possible reasons:

1. Deconvolution and wavelet processing has not provided a zero-phase wavelet.
2. Noise is being inverted (multiples, sideswipe in 2D data).
3. Amplitudes may have been boosted or reduced by amplitude variation with offset (AVO) in the CMP stack.
4. True relative amplitudes may not have been preserved through the processing sequence.

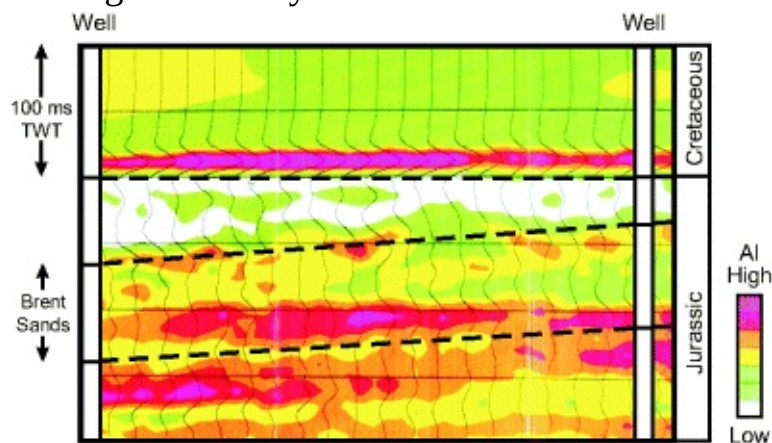
Many pitfalls occur along the way in this procedure:

- The polarity convention used on the section may have to be reversed.
- Deconvolution and wavelet processing to a zero-phase wavelet require special care.
- The initial processing has to be done so as to maintain true relative amplitudes in the seismic data.
- Any noise present (multiples, sideswipe) will be converted to spurious acoustic impedance variations.
- The numbers representing the seismic trace have to be scaled to fractions of the right magnitude to represent reflection coefficients.
- And finally, the process should be started in a uniform formation of known acoustic

impedance above (or below) the reservoir interval of interest.

[Figure 11.2](#) is an example of how conversion to acoustic impedance may throw fresh light on a subsurface interpretation. The seismic data from a Brent Sands reservoir of the northern North Sea Basin were flattened on a prominent base Cretaceous reflection, and inversion was focused on a restricted interval of interest extending over 300 ms TWT. Deconvolution of the data was performed by defining an optimum least-squares filter at each of four wells that would convert the seismic trace at the well to the reflection coefficient series measured in the well. Away from the wells, an average of the filters (weighted inversely as distance to the wells) was applied to the seismic data to deconvolve it to a reflection coefficient series prior to inversion by the recursive calculation. A discordant zone of high impedance lying parallel to the base Cretaceous was revealed in the reservoir all over the study area. In [Figure 11.2](#), this is evident at about 210 ms from the top of the section. From examination of thin sections from core samples, it could be tied to diagenetic alteration of detrital biotite to iron-rich, high-density minerals such as siderite and pyrite, with consequent increase in AI and serious reductions in porosity at that level (Ashcroft & Ridgway, 1996).

[Figure 11.2](#) Seismic image of a diagenetic zone expressed as a discordant zone of high AI within the Brent Sands formation, northern North Sea Basin. Reproduced with the permission of The Geological Society



11.3.3 Sparse-spike, Model-Based and Coloured Inversion

The recursive calculation described above was the first method of AI inversion, but it is not the best because it tends to smooth the data, noise is treated as reflection data, and adding low frequencies of AI from well data or velocity analyses is often problematical. In practice, AI inversion is accomplished by one of three other methods: sparse-spike inversion, model-based inversion or coloured inversion.

Sparse-spike inversion concentrates on getting as near as possible to perfect deconvolution and restoration of the low frequencies without calling on auxiliary data. It takes advantage of the fact that many of the samples in the reflection coefficient series are close to zero, with a few big ones that often dominate the response, as you probably saw from the series used in making the synthetic seismogram in Tutorial 7.1 in Chapter 7. This structure allows the series of reflection coefficients to be treated as a sparse-spike series, which has the remarkable property that we can reconstruct it even if we know only part of its spectrum. The computer procedure is called the Simplex Algorithm; this requires that the sum of the absolute values of the series should be a minimum, favouring series which are mostly close to zero except for a few isolated terms, in

accord with the sparse spike model (Levy & Fullagar, (1981); Oldenburg, 1983). The series of reflection coefficients can then be reliably inverted to acoustic impedance.

In the model-based method, well data is used to construct an approximate AI trace, from which a synthetic seismogram is prepared (the model). Each recorded seismic trace is then compared to the synthetic, and the AI trace is perturbed until it generates a synthetic seismogram that matches the seismic at that location. The AI trace is then assigned to the new AI volume at that location. A very readable overview of the process is given by Hampson (1991). This actually deals with AVO data, where the model is a synthetic CMP gather rather than a single trace, but the principles are the same.

Coloured inversion came later in a paper by Lancaster & Whitcombe (2000). They found from experience with sparse-spike inversion that the process could be replicated in a much simpler way as the operation of a convolution filter operator on the seismic trace. A single operator can be derived on the basis that it transforms the average spectrum of the seismic data over the field to the average spectrum of AI as observed in the wells. That operator can then be applied to all the seismic traces in the area of the field. The adjective 'coloured' comes from the output being strictly limited in bandwidth to that of the seismic data – the analogy is the limited spectrum of coloured light. Lancaster & Whitcombe (2000) reported excellent correspondence between coloured and sparse-spike inversion on a test set of data. They also emphasized its speed and easy implementation within the interpreter's workstation environment, there being no need to offload data to a special processing package.

11.4 Amplitude Variation with Offset (AVO)

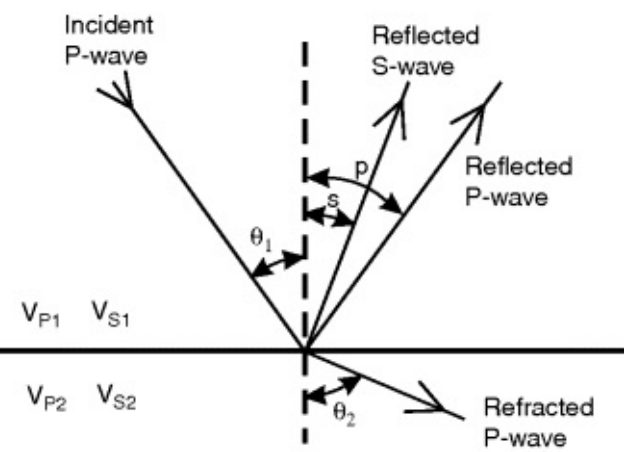
Drilling bright spots is a very expensive way of finding out that they are not all caused by hydrocarbons! To separate hydrocarbon-bearing from water-bearing sands, the industry turned to a seismic phenomenon that was well known from earthquake seismology – the splitting of reflection energy into both P-waves and reflected shear waves (S-waves) when an interface is struck obliquely by P-waves.

The situation is shown in [Figure 11.3](#). P-wave particle motion is along the direction of propagation, so at the interface there is a horizontal component of motion which generates a reflected S-wave in addition to the reflected P-wave. Snell's law applies to the angles of reflection of both wave types, so in [Figure 11.3](#):

$$\sin\theta_i/\sin p = V_{p1}/V_{p1}$$

$$\sin\theta_i/\sin s = V_{p1}/V_{s1}$$

Figure 11.3 Mode conversion. At oblique incidence, a P-wave generates both a reflected P-wave and a reflected S-wave.



Since the incident energy is split between the two waveforms, the process is often known as energy partitioning. Another term applied to the phenomenon is mode conversion.

The amplitude of the P-wave reflected at angle θ is not constant; it may increase or decrease, or even change polarity, as θ increases, depending on the lithological contrast and also (especially important) depending on the nature of the pore fluids above and below the interface. We acquire abundant seismic data with variable angle of incidence in the CMP gather, where θ increases from 0° at the zero offset trace (normal incidence reflection) up to about 40° at large offsets. At greater offsets, traces are truncated to avoid excessive NMO stretch. Thus, the basis of the method is to study the amplitude variation with offset (AVO) of reflections across CMP gathers, in the hope of distinguishing hydrocarbon-saturated rocks from water-saturated rocks.

It is important to calculate the theoretical change in amplitude with offset for a reservoir interface for two reasons:

1. To test by forward modelling whether the lithologies present in and around the reservoir will give rise to observable AVO effects.
2. To design methods of data processing and display that will reliably show the presence of hydrocarbons in the subsurface.

The amplitude is defined by the reflection coefficient $R(\theta)$ of the interface, which depends not only on θ , the angle of incidence on the interface, but also on the contrast in P-wave velocity, S-wave velocity and density across the interface. The fundamental equations were derived early in the 20th century by Zoeppritz (see the account in Sheriff & Geldart, 1995, Chap. 3), but they have been expressed in various simplified versions for AVO interpretation. Among the simplifications are the following, referring to [Figure 11.3](#):

Average P-wave velocity, $V_p = (V_{p2} + V_{p1})/2$

Contrast in P-wave velocity, $\Delta V_p = V_{p2} - V_{p1}$

Normal incidence reflection coefficient, P-wave,

$$R_p = (\rho_2 V_{p2} - \rho_1 V_{p1}) / (\rho_2 V_{p2} + \rho_1 V_{p1})$$

$$\approx \frac{1}{2} (\Delta V_p / V_p + \Delta \rho / \rho)$$

And similarly, for S-wave reflection coefficient,

$$R_s \approx \frac{1}{2} (\Delta V_s / V_s + \Delta \rho / \rho)$$

Contrast in density, $\Delta \rho = \rho_2 - \rho_1$

Average density, $\rho = (\rho_2 + \rho_1) / 2$

Density reflection coefficient,

$$R_d = \Delta \rho / \rho$$

$$\theta = (\theta_1 + \theta_2) / 2$$

Only small reflection coefficients are valid, and the angle of incidence should be not more than

about 30°.

The starting-point for expressions of $R(\theta)$ is an equation given by Aki & Richards (1981) and rearranged by different authors to bring out particular relationships. Fatti *et al.* (1994) expressed it as the sum of three terms, each one being a modified version of a normal-incidence reflection coefficient:

$$R(\theta) = c_1 \cdot R_p + c_2 R_s + c_3 \cdot R_d$$

and

$$c_1 = 1 + \tan^2 \theta$$

$$c_2 = -8\gamma^2 \sin^2 \theta$$

$$c_3 = 2\gamma^2 \sin^2 \theta - \frac{1}{2} \tan^2 \theta$$

(11.4) $\gamma = V_s/V_p$

Calculating the reflection response of the interface between top reservoir and its seal in this way is an essential first step in AVO studies. Alternative lithological combinations that are likely to occur in that part of the basin may also be modelled for comparison. Note that the modelling is really for Amplitude Variation with Angle (AVA). From the seismic data, we measure AVO across a CMP gather, but we can convert measured offset to angle of incidence at depth, provided we know the velocity structure down to the reflector. Although strictly AVA, the whole method of analysis is generally labelled as AVO.

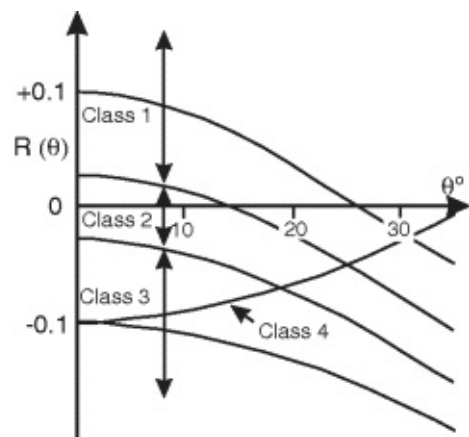
Spreadsheets make AVO calculations easy, and you can see the results instantly as a graph. Take a look at some of the remarkable variations in R in Tutorial 11.1, which has an *Excel* spreadsheet all set up.

Rutherford & Williams (1989) made a study of AVO in gas sands under a shale seal and were able to explain the puzzling variations observed in bright spots. They established a three-fold classification which is widely used ([Figure 11.4](#)):

- Class 1 sands are deep ($\approx 14,000$ ft), well-indurated and show a positive reflection, which dies away and may even reverse polarity at far offsets. This behaviour is illustrated as the initial set-up in Tutorial 11.1.
- Class 2 sands are shallower (≈ 9000 ft) and less indurated. They may show as a weak reflection of either polarity at near offsets. If the reflection has positive polarity, it may die away to nothing at mid-offsets, then change polarity and increase in (negative) amplitude at far offsets (a phase reversal of 180°).
- Class 3 sands are shallowest (≈ 4000 ft), the least indurated, and cause the classic bright spot where the reflection is of negative polarity at all offsets and increases in amplitude with offset, as demonstrated in Tutorial 11.1.

Hilterman (2001) discusses and illustrates seismic sections with examples of all three classes. A Class 4 was later added (Castagna & Swan, 1997). It shows a bright spot with a strong negative reflection, which becomes weaker with offset.

Figure 11.4 Variation of reflection coefficient $R(\theta)$ with angle of incidence on the reflector (θ) showing four classes of reflection response. After Rutherford & Williams (1989) and Castagna & Swan (1997).



It is worth noting that shale/gas sand reflections intermediate between Classes 1 and 2 could well show positive polarity on the near-offset stack and negative on the far-offset stack. On the total stack, the reflection might then cancel out completely and so lead to a mis-tie when compared to a synthetic seismogram based on well data and simulating a zero-offset response.

11.4.1 AVO and Poisson's Ratio

Alternative expressions for $R(\theta)$ incorporate V_s through the quantity Poisson's ratio, generally labelled σ (Greek sigma) and related to V_p/V_s as:

$$(11.5) \sigma = [(V_p/V_s)^2 - 2] / 2[(V_p/V_s)^2 - 1]$$

Poisson's ratio is a measure of the plasticity of a substance. Suppose a cube of material, free to distort, is squeezed along one axis, say the x -axis. It will shorten along the x direction and lengthen equally along the y and z directions (if it is isotropic). If the change in length along the three axes is δx , δy and δz , then Poisson's ratio is defined as:

$$\sigma = \delta y / \delta x = \delta z / \delta x$$

If the material is a liquid (incompressible), there will be no resistance to the deformation, the volume will remain the same before and after deformation and it is easily shown that $\sigma = 0.5$, its maximum value. If the material is a solid, it resists deformation through possessing shear strength, so δy and δz are smaller than in a liquid for a given δx , and σ is less than 0.5 and may range down to about 0.1. Typical values of σ range from about 0.17 for sandstone up to about 0.32 for dolomite (Domenico, 1984).

Poisson's ratio will be affected by lithology as a primary control, but it will also vary with other factors such as clay content, cementation or porosity. Its magnitude will depend on how these factors affect V_s and V_p . Change in the nature of the pore fluids alone does not affect shear strength or V_s , but may still change Poisson's ratio because of a change in V_p . Hence, a sandstone will have a lower σ when gas-bearing than when water-bearing.

Poisson's ratio occupies a key position in AVO studies. In most early calculations of the variation of reflection coefficient at oblique incidence, it was assumed that σ was the same for rocks above and below the interface, in which case AVO effects are negligible. However, Koefoed (1955) found that one result from older work showed a clear AVO effect and he spotted the reason: σ changed a lot across the interface. He carried out enough calculations to establish that AVO effects could be large and important if σ changed, easily doubling or halving the amplitude of reflections within incident angles of 0 to 30 degrees. At the end, he stated: '... in a more remote future it may become possible to draw conclusions concerning the lithological nature of rock

strata from the shapes of the reflection coefficient curves ...'. Thirty years later he was to be proved right.

11.4.2 AVO Methodology

How should we set about getting information on AVO from the observed seismic data? Ostrander (1984) set out the basic methodology and showed the industry that it was quite feasible to use variations in amplitude with offset to differentiate between different types of bright spots.

Using reliable values of Poisson's ratio that had been published in the 1970s, Ostrander (1984) set up a model of a gas-bearing sand in which the displacement of water by gas caused Poisson's ratio to drop from 0.4 to 0.1. He showed that the reflection coefficient at the gas/brine contact could completely change polarity, from -0.1 to $+0.2$, as the incident angle changed from 0 to 40 degrees.

Ostrander established the basic method:

1. Use the variation in amplitude across a CMP gather as the primary measurement.
2. Sum CMP traces over a small number of adjacent CMP locations and a small range of offsets to improve signal/noise ratio. This set of data is commonly called a super-gather.
3. Compensate for other variations in recorded amplitude with offset caused by factors such as array attenuation and spherical divergence.
4. Use the known velocity structure to convert offset across the gather to equivalent angle of incidence at depth.

In data recorded from a proven gas bright spot, he was able to demonstrate a clear increase in amplitude of about 300 per cent at an incidence angle of about 35° . This compared with a clear decrease in amplitude from a bright spot known to be caused by a basaltic lava flow.

How can we be sure that the variation we see in the seismic data is a genuine AVO effect? Careful processing is essential, and Yu (1985) discussed the processing steps necessary to control amplitude variations in the CMP gather caused by non-geological factors. The most important are as follows:

1. Variations caused by cross-cutting multiples (suppressed by f-k filtering of the gather).
2. Variations that are offset-dependent but not caused by energy partitioning at the interface (e.g. array attenuation, tuning effects). This was compensated for by measuring the average decay of amplitude as a function of time and offset across the data.
3. Variations caused by near-surface effects such as shot and receiver coupling to the earth and location-dependent attenuation of the seismic energy, which can be assessed in a similar way to surface-dependent static corrections. In marine data, such effects are negligible compared to land data.
4. Most importantly, Yu (1985) stressed the need for careful equalization of the trace amplitudes, using a scalar derived from the average amplitude of all traces within a CMP gather rather than any form of trace-by-trace equalization.

The final AVO plot in Yu's study successfully differentiated between a shale/gas bright spot and a shale/(gas plus oil) bright spot.

11.4.3 Angle Stacks

An angle stack is one of the simplest ways of presenting and using AVO data. It is made by

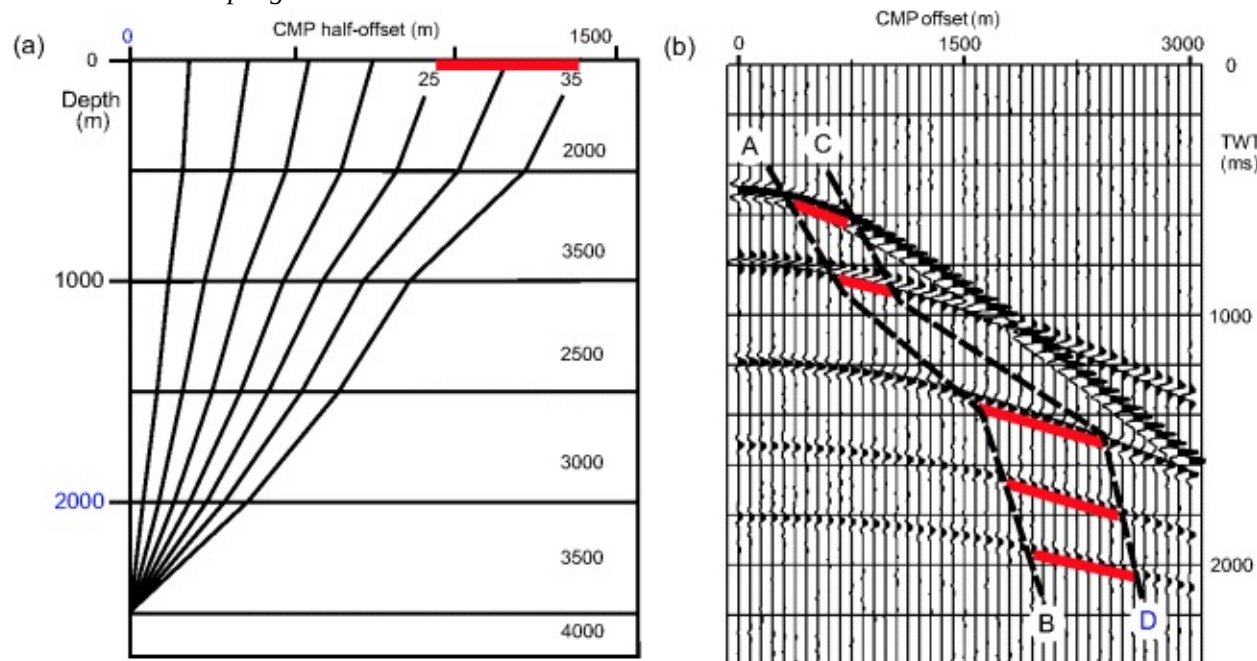
choosing a set of traces from the CMP gather containing data which is all reflected at about the same incident angle. It may be sufficient to make only two sets of stacked data – one of the near-offset traces and one of the far-offset traces. Choosing the traces to take out of the CMP gathers is easy for the near and far offsets, but to choose traces for a specific angle of incidence may require ray-tracing if layers with unusually high or low velocity are present.

[Figure 11.5a](#) shows an example of a section in which the second layer from the surface is of high velocity, so that the required data for the deeper reflections are thrown off to unusually large offsets. The red line marks rays incident between 25 and 35° on the deepest reflector. In [Figure 11.5b](#), data between lines A – B and C – D can be corrected for NMO and stacked to form a 25–35° angle stack trace.

Figure 11.5

- An earth model with raypaths drawn (for half a CMP gather) to the deepest reflector at increments of 5° in angle of incidence.
- CMP gather for the model shown in a.

Data modelled in program CMPGATHER



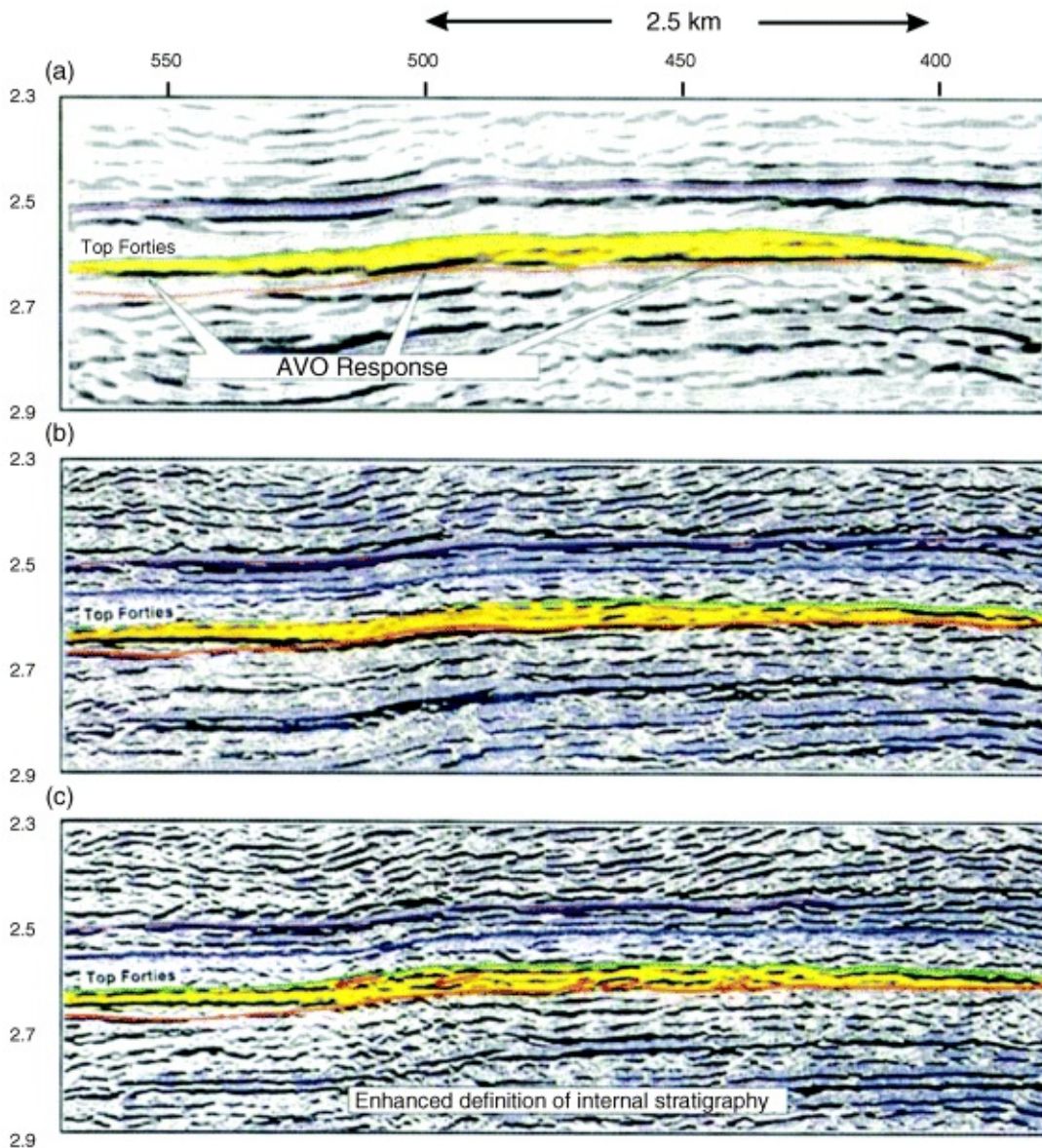
A particularly good example of the use of angle stacks is provided by Barrett *et al.* (1995), who describe a marked AVO effect in the seismic data from the Everest Field, UK North Sea, where gas condensate is stratigraphically trapped in submarine fan sandstones. [Figure 11.6](#) shows the result of forming sections from near- and far-offset stacks. The far-offset stack shows a marked AVO anomaly with a high-amplitude event, following the base reservoir sand in the east (right) and continuing as a flat spot along the condensate/water contact to the west (left), where the base reservoir dips below it. In contrast, the near-offset stack shows little response at base reservoir. The top reservoir (Top Forties) shows a clear polarity reversal on both field-recorded and modelled CMP gathers, which ties with its very different expression on the two different angle stacks. In support of this interpretation, much effort went into detailed modelling of the expected AVO variation across CMP gathers and comparison with recorded gathers.

Figure 11.6

- Far-offset stacks (reverse polarity).
- Full-offset stacks.

c. Near-offset stacks.

(Reproduced with the permission of The Geological Society).



11.5 AVO Intercept and Gradient

Shuey (1985) put AVO interpretation on a more quantitative footing by establishing the first of what are now several AVO attributes. He simplified the equation of Aki & Richards (1981) and rearranged it to bring out the dependence of $R(\theta)$ on angle of incidence θ :

$$(11.6) \quad R(\theta) = A + B \sin^2\theta$$

Where $R(\theta)$ = reflection coefficient at angle of incidence θ , A = P-wave reflection coefficient at normal incidence (R_p) and B is the (linear) gradient of a plot of $R(\theta)$ versus $\sin^2\theta$. The equation is correct for angles of incidence up to about 30° . Tutorial 11.1 shows that a plot of $R(\theta)$ versus $\sin^2\theta$ is, indeed, a straight line out to an angle of about 30° .

The quantity B contains the AVO information, but still in a rather complex fashion. It is defined by changes in Poisson's ratio and the changes in P-wave velocity and density across the interface. Shuey (1985) showed that by assuming a generalized value of Poisson's ratio, it was possible to calculate the quantity $\Delta\sigma$, i.e. the change in Poisson's ratio across the interface. If the analysis were carried out at many CMP locations, a profile of changes in Poisson's ratio along a horizon

could be calculated and interpreted in terms of presence or otherwise of gas.

How are values of A and B acquired from the seismic data? At every CMP location, the variation of amplitude across the NMO-corrected CMP gather is measured trace by trace at a particular time sample within the time window of interest. Each sample is the result of reflection at a different angle of incidence which is known from the velocity structure ([Figure 11.5](#)). The data is plotted (conceptually) against $\sin^2\theta$, a least-squares best line is fitted and this yields a value for A and for B . The process is then repeated for the next time sample down the CMP gather, to the end of the interval of interest. The result is two new traces at the CMP, one of A and one of B . The results are presented as time-sections that look rather like ordinary seismic sections, or as new data volumes in the case of 3D surveys.

The intercepts are measures of R_p , so the volume of R_p values should be a good estimate of normal-incidence reflectivity – better than a conventional CMP-stacked section, which contains any AVO effects that may be present on far-offset data. A section of R_p should look like a near-trace stacked section. The gradient section will show bright spots over strata where there is a conspicuous AVO effect. To highlight zones of AVO activity, the quantity (A/B) may be displayed.

11.5.1 Intercept-gradient Cross-Plots

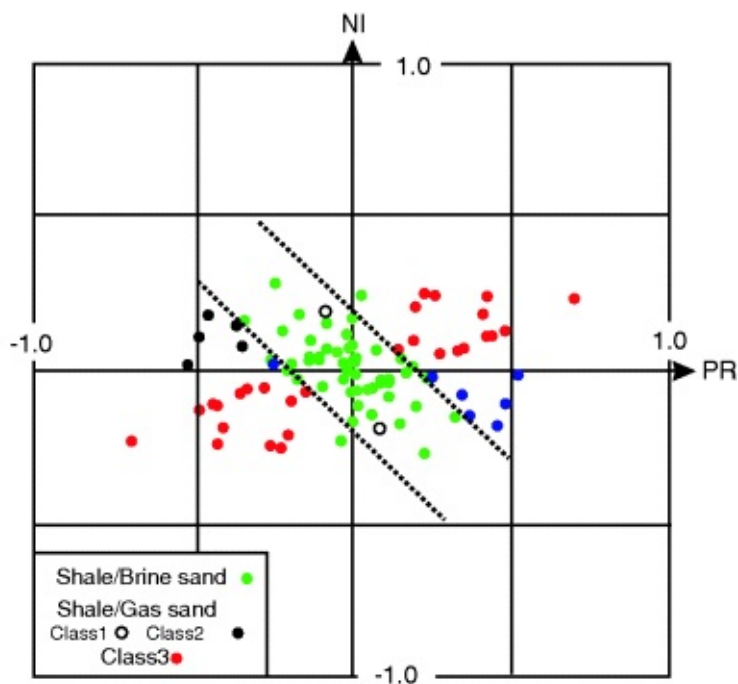
Rutherford & Williams (1989) explained the puzzling features of bright spots in terms of the three classes, but how can we identify shale/gas sands from shale/water sands or shale/shale reflections? How label them rapidly on a section or within a huge 3D volume? Verm & Hiltermann (1995) simplified Shuey's equation for $R(\theta)$ to:

$$(11.7) \quad R(\theta) = NI\cos^2\theta + PR\sin^2\theta$$

NI is the normal incidence reflection amplitude, expressed as A in [equation \(11.6\)](#) or R_p in [equation \(11.4\)](#), while PR is the Poisson Reflectivity, $\Delta\sigma/(1 - \sigma)^2$. Verm & Hiltermann pointed out that there was a wide and overlapping range of reflection coefficients at shale/sand interfaces, such that only Class 3 sands could be reliably identified from NI alone, but by cross-plotting NI against PR , a second dimension was provided with which to separate out the three classes.

Castagna & Smith (1994) published well and laboratory measurements of V_p , V_s and ρ conducted on 25 sets of shales, water sands and gas sands that were in close proximity *in situ*. A cross-plot of NI and PR made from these measurements is shown in [Figure 11.7](#), which illustrates the separating ability of such a plot very well. The amplitudes from shale/water sand and shale/gas sand reflections overlap completely along the NI dimension, but they are well separated on the PR dimension of the combined plot. The class of the reflections shown on [Figure 11.7](#) was decided by entering the data for each of the 25 sets of measurements in the spreadsheet of Tutorial 11.1 and inspecting the $R(\theta)$ response. A clear AVO response was demonstrated by all but five of the shale/gas sands responses.

[Figure 11.7](#) Cross-plot of NI against PR showing separation of shale/gas sands from shale/brine sands. Data from 25 sets of measurement listed in Castagna & Smith (1994)



NI and PR values were calculated from that set of data for the case of shale over sand (top reservoir) and from the same data, sand over shale (base reservoir), which gives the same NI and PR values, but of opposite sign. The final spread of values is what might be observed in a real sequence of sands and shales, showing both top reservoir and base reservoir reflections. Taking the NI axis as North in [Figure 11.7](#), reflections between layers of water-bearing sediment will always be distributed along a NW–SE central strip as described by Castagna *et al.* (1998). This distribution is described as a background variation generated by wet sands and shales, and is always present in any set of AVO measurements from a CMP gather. If the data is taken from a restricted time interval over which the V_p/V_s ratio is fairly constant, the points will tend to plot along a straight line, otherwise (as in [Figure 11.7](#)) they will be more scattered. Reflections from shale against Class 3 sands spread along a NE–SW strip and shale against Class 2 sands along a WNW–ESE strip close to the horizontal axis.

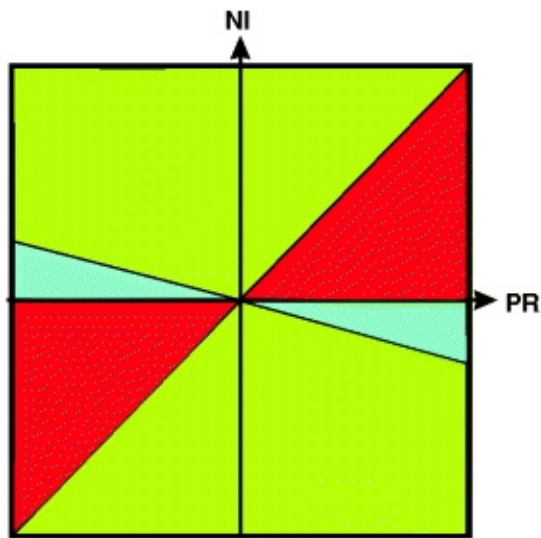
A plot of this type can be produced at every CMP for a time interval of interest encompassing a reservoir. When the cross-plot is prepared from seismic data, there will be many more dots – one for each time down the CMP gather at which the AVO was measured and NI and PR values were calculated. As amplitude waxes and wanes with time down the wavelet in the CMP gather, the plotted points will move to and fro along the characteristic strip of the plot – for example along the NW/SE strip, as the process goes down through a sequence of shale/water sand reflections.

How can this information be transferred back into the seismic volume for display and integration with other exploration data? Verm & Hilterman (1995) assigned colours to these characteristic areas, as shown conceptually in [Figure 11.8](#). At each time down the stacked trace, a colour can be assigned from the plot and applied to the stacked reflection, thereby differentiating Class 2 and Class 3 reflections within the seismic volume. [Figure 11.9](#) shows the results of such an analysis over a proven gas accumulation, where the colour red indicates Class 3 sand.

Castagna & Swan (1997) stressed the importance of analysing AVO data on AB crossplots. They showed a plot similar to [Figures 11.7](#) and [11.8](#) (allowing for the swapping of axes) and including Class 4 sands. Sands in Classes 2 and 3 give data points that fall well off the background line, but classes 1 and 4 will plot in the north-west and south-east quadrants and so may be more difficult to distinguish from the background trend of wet sediment reflections.

Figure 11.8 General areas into which shale/sand reflections fall in a NI vs. PR plot.

(After Verm and Hilterman, 1995)






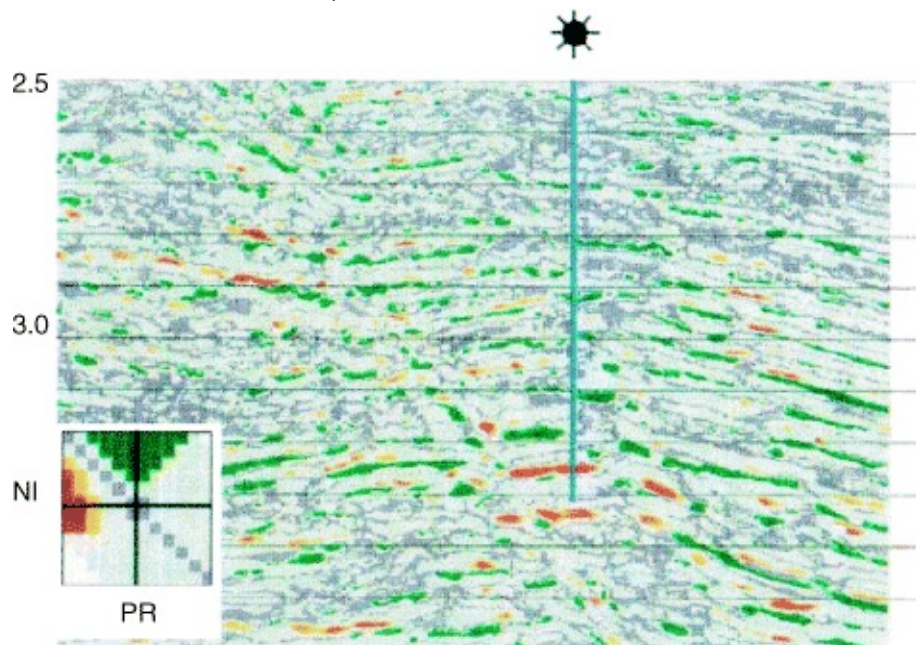
Class1  Class2  Class3 

Figure 11.9 A seismic section coloured according to where the reflections fall on the associated NI-PR plot (red = Class 3 reflection).

From Verm and Hilterman, 1995



11.6 Fluid Factor

A very different approach to treating AVO data was taken by Smith & Gidlow (1987). They described how a trace of $\Delta V_p/V_p$ can be obtained by simply stacking the NMO-corrected CMP gather after weighting the samples in a certain way according to travel time and offset within the gather. In the same way, a trace of $\Delta V_s/V_s$ can also be generated by stacking the gather, but with a different set of weights. The quantity $\Delta V_p/V_p$ is, of course, close to R_p (see Section 11.4), and the density term can be added by invoking some suitable relation between density and V_p , such as Gardner's Law, which can be expressed as:

$$\Delta\rho/\rho = (\Delta V_p/V_p)/4$$

so that a zero-offset section can be prepared once more.

However, the novel concept that Smith & Gidlow (1987) introduced was that of a fluid factor – an AVO attribute which would be virtually zero over most of a seismic section where the pore fluid was water, but which would appear as a seismic event where the pore fluid was gas – the perfect DHI. To see how this works, we should start with the remarkable finding reported by Castagna *et al.* (1985), who found that, over a wide range of measured samples of water-saturated shales and siltstones, V_p and V_s were related as:

$$(11.8) \quad V_p = 1.16V_s + 1360$$

(velocities in m/s), so that V_p plotted against V_s forms a straight line plot of gradient 1.16 and intercept 1,360, often called the ‘mudrock line’. Water-saturated sandstones plot close to this line, but with slightly lower V_p values. Taking finite differences of this equation, we can say:

$$\Delta V_p = 1.16\Delta V_s$$

$$\text{so} \quad \Delta V_p/V_p = 1.16\Delta V_s/V_p$$

and after multiplying the right hand side by V_s/V_p , we have:

$$(11.9) \quad \Delta V_p/V_p - 1.16(V_s/V_p)(\Delta V_s/V_s) = 0$$

This quantity is defined as the fluid factor:

$$(11.10) \quad \Delta F = \Delta V_p/V_p - 1.16(V_s/V_p)(\Delta V_s/V_s)$$

It should be close to zero for rocks that are water-saturated and lie on the mudrock line.

A complete section of ΔF can be made by multiplying each sample of the $\Delta V_s/V_s$ section by $1.16(V_s/V_p)$ and subtracting it, sample by sample, from the $\Delta V_p/V_p$ section. For a particular area, a particular version of [equation \(11.8\)](#) would have to be established from well data with a gradient that might be different from 1.16. Since the variation of V_p with time will be known, the variation of V_s/V_p with time can be obtained from [equation \(11.8\)](#).

The ΔF section so formed should be everywhere close to zero, so long as the pore fluid is water. Where ΔF seriously differs from zero, the pore fluid is likely to be hydrocarbon, or there is a lithological change from sand/shale. One of the attractions of the fluid factor approach is as a reconnaissance method. The fluid factor can be rapidly calculated and a volume of 3D data can be quickly searched for anomalous fluid factor values to pinpoint locations for further investigation.

Fatti *et al.* (1994) published an interesting case history from a gas field on the southern continental shelf of South Africa. They showed maps of fluid factor that in general agreed much better with the field boundaries than did a conventional amplitude map.

11.7 AVO Inversion to Rock Properties $\lambda\rho$ and $\mu\rho$

We have already met μ (μ), a symbol for the shear modulus, mentioned in Chapter 4, Section 4.2, which is a measure of a solid's shear strength, and ρ (ρ) is the familiar symbol for density. But what about λ (λ)? It is commonly used to signify wavelength, but here it is used to mean an elastic constant called Lamé's constant.

You will recall from Chapter 4 that the P- and S-wave velocities are defined in terms of bulk modulus (k) and shear modulus (μ):

$$(V_p)^2 = [k + (4/3)\mu]/\rho \quad \text{and} \quad (V_s)^2 = \mu/\rho$$

But V_p can also be written in terms of Lamé's constant, λ :

$$(11.11) \quad (V_p)^2 = (\lambda + 2\mu)/\rho$$

$$\text{so } (\lambda + 2\mu)/\rho = [k + (4/3)\mu]/\rho$$

$$(11.12) \quad \text{and } \lambda = k - (2/3)\mu$$

(Sherriff & Geldart, 1995).

What is the nature of λ ? One way to view it is to note that, in a liquid where $\mu = 0$, from [equation \(11.12\)](#), $\lambda = k$, so we may think of λ as a fluid incompressibility.

Goodway *et al.* (1997) pointed out that the fundamental description of the seismic wave involved only the elastic moduli, and they proposed that changes in those quantities should be used as rock property indicators rather than changes in mixed parameters like velocities or Poisson's ratio. It is straightforward to calculate λ and μ from P and S sonic logs and the density log:

$$(11.13a) \quad \mu = \rho(V_s)^2$$

$$(11.13b) \quad \lambda = \rho(V_p)^2 - 2\rho(V_s)^2$$

(from [equation \(11.11\)](#) and the expression for μ).

Goodway *et al.* (1997) calculated, from well log data, the percentage change in various indicator quantities between shale and gas sand in typical bright spot conditions. For Poisson's ratio, the change is 55 per cent, but for the λ/μ ratio it is 110 per cent. This is encouraging, but how do we calculate λ and μ for rock layers from seismic traces? We notice that if we multiply equations 11.13 all through by ρ , we get:

$$\mu\rho = (\rho V_s)^2 \quad \text{and} \quad \lambda\rho = (\rho V_p)^2 - 2(\rho V_s)^2$$

$$(11.14) \quad \text{or} \quad \mu\rho = Z_s^2 \quad \text{and} \quad \lambda\rho = Z_p^2 - 2Z_s^2$$

where Z_p = P-wave impedance and Z_s = S-wave impedance.

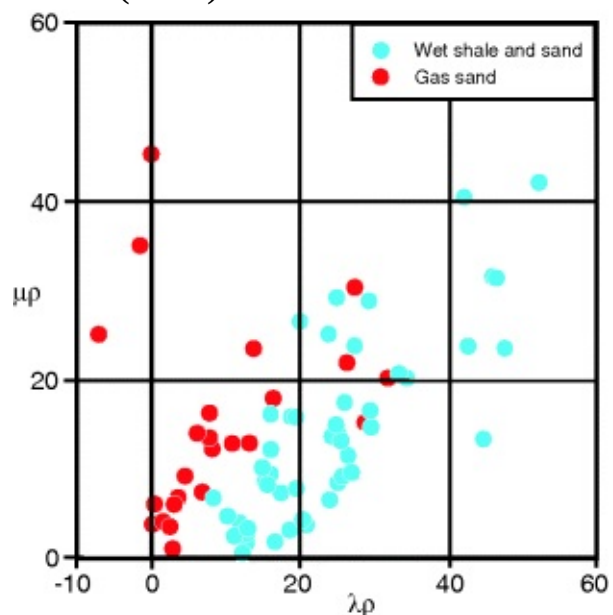
How can we obtain impedances from seismic data? Remember that we can convert a seismic trace of P-wave reflectivity into a trace of P-wave impedance by the process of AI inversion (Section 11.3). [Equation \(11.4\)](#) tells us that the AVO measured across the CMP gather, $R(\theta)$, contains within it the P- and S-wave reflectivities R_p and R_s . If we can extract these reflectivities, we can carry out inversion to P-wave and S-wave impedances, Z_p and Z_s . We extract R_p and R_s by fitting a least-squares best curve to [equation \(11.4\)](#) using the amplitudes, $R(\theta)$ measured from the CMP gather at known values of θ and a V_s/V_p ratio for that part of the succession, taken from well logs.

The process goes on through these steps:

1. At a particular time, measure the AVO across a NMO- corrected CMP gather.
2. Fit the best curve to the AVO data by least squares adjustment of the reflectivities R_p and R_s , using just the first two terms of [equation \(11.4\)](#). A V_s/V_p value has to be estimated for the interval of interest to calculate c_2 .
3. Repeat at all times down the gather within the interval of interest to build traces of reflectivities R_p and R_s .
4. Repeat for all CDPs to form two sections (or 3D volumes) – one of R_p and the other of R_s .
5. Transform the traces of reflectivities into traces of impedance by carrying out impedance inversion.
6. Calculate $\mu\rho$ and $\lambda\rho$ from equations 11.14 as sections or complete volumes of data.

Interpretation of the results is done by cross-plotting $\lambda\rho$ against $\mu\rho$, identifying data that fall in an area of low $\lambda\rho$ and flagging up those data points on the seismic section or in the 3D seismic volume. [Figure 11.10](#) shows such a plot, made from data published by Castagna & Smith (1994) described in Section 11.5.1 above. The gas sands fall into a distinct field of the plot with low $\lambda\rho$ values. More typically, the sands will also show high $\mu\rho$ values because matrix strength is higher in sandstones than in shales.

Figure 11.10 Cross-plot of $\lambda\rho$ against $\mu\rho$ from 25 sets of measurements listed in Castagna & Smith (1994).



A study of AVO responses in a Tertiary basin offshore of Trinidad by Young & Tatham (2007) used $\lambda\rho$ and $\mu\rho$ to distinguish between gas and non-gas bright spots. The workflow comprised three stages:

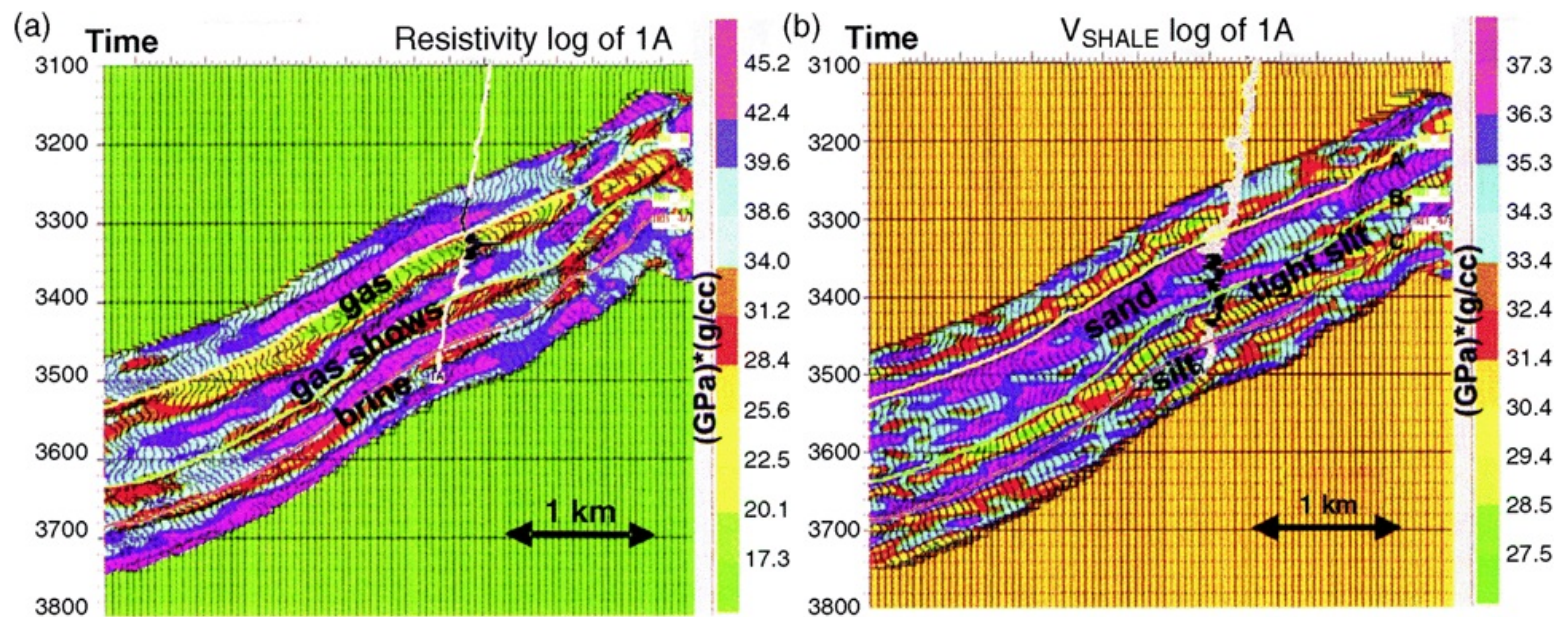
- The first stage was a feasibility study from well data in the basin to see if it was possible to separate brine sand from gas sand using simple cross-plots such as V_p versus V_s .
- The second stage was data pre-conditioning by the formation of super-gathers and adjustment of small time differences to improve the flatness of reflections across the CMP gather.
- The third stage was the extraction of reflectivities R_p and R_s and their inversion to P- and S-impedances, followed by calculation of $\mu\rho$ and $\lambda\rho$.

[Figure 11.11](#) shows a section of $\lambda\rho$ and $\mu\rho$ traces in a restricted interval of interest containing three target horizons. Only the topmost horizon shows a clear zone of low $\lambda\rho$ and high $\mu\rho$, consistent with a gas-sand interpretation and confirmed by drilling. The same report demonstrates an alternative display to highlight the gas-bearing zone, where points identified from the low $\lambda\rho$ + high $\mu\rho$ area of a crossplot are transferred back on to the seismic data as a colour patch.

Figure 11.11

- Low $\lambda\rho$ values pick out a gas-bearing sand in Tertiary sediments.
- High values of $\mu\rho$ pick out sandy lithologies. Only seismic data within a zone of interest is displayed.

(From Young and Tatham, 2007).



11.8 AVO Inversion to P- and S-Wave Impedance

The AVO method was used mostly as a reconnaissance tool for 15 years after its inception but, with the great improvements in seismic data quality (3D migrated gathers, better multiple elimination) and the facility of plotting maps of properties on horizon slices, there are now attempts to extract quantified reservoir properties from the AVO data.

Russell *et al.* (2006) reported a study in which they produced maps of porosity, sand percentage and water saturation based on extraction of P-wave and S-wave impedances and density from seismic data. They started with the version of the AVO equation previously shown as [equation \(11.4\)](#):

$$R(\theta) = c_1 \cdot R_p + c_2 R_s + c_3 \cdot R_d$$

where R_p , R_s and R_d are P-wave, S-wave and density reflectivities respectively, and the c constants are given above in Section 11.4:

The three reflectivities were extracted for every time down the CMP gather by fitting a least-squares curve to the recorded variation in amplitude across the gather. Finally, the reflectivities were converted to impedances by a model-based inversion. This process is similar to that described in Section 11.3.3 to invert a stacked seismic trace to a trace of acoustic impedance, but with two major differences. The first is that all three initial traces (Z_p , Z_s and ρ) are perturbed at once, hence the title of 'simultaneous inversion'. The second difference is that a synthetic CMP gather is generated, for comparison with a recorded gather, instead of a synthetic seismogram for comparison with a seismic trace. Russell *et al.* (2006) reported that about 20 iterations were required to achieve a match. The result was a trace of each of Z_p , Z_s and ρ at each CMP location across the survey area for the reservoir interval of interest.

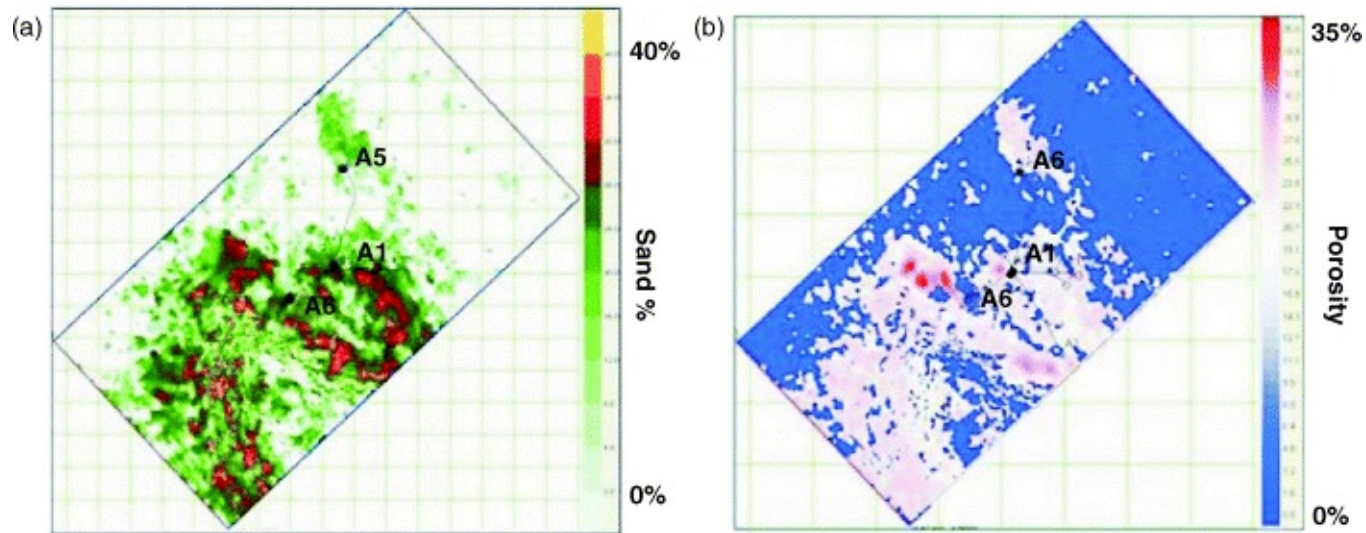
Russell *et al.* (2006) showed maps of Z_p , Z_s and ρ across the survey area. Three wells were available – two with gas and one with water. They used well data to cross-plot shale volume against density, establish a threshold of density to separate sand-prone from shale-prone areas and then establish a map of sand distribution. Well data also provided a cross-plot of porosity against Z_p , which showed two distinct trends – one for gas and one for water – and allowed a map of porosity to be made. It is notable that the two maps, sand and porosity, show very similar

distributions even though prepared from two different data sets, one from seismic-derived density and the other from seismic-derived impedance ([Figure 11.12](#)). Finally, a map of water saturation was calculated from density, porosity and the known densities of gas, water and rock matrix. The map was in accord with the well data.

Figure 11.12

- a. Map of sand distribution prepared from AVO-derived density measurements.
- b. Map of porosity prepared from AVO-derived acoustic impedance.

(Reproduced with the permission of The Canadian Society of Exploration Geophysicists (CSEG))



11.9 Elastic Impedance: AVO Made Easy?

[Equation \(11.4\)](#) for the reflection coefficient at oblique incidence, $R(\theta)$, is a complicated affair when compared to the simplicity of the normal-incidence reflection coefficient, R_p , in [equation \(11.1\)](#), which can be written simply as:

$$R_p = (AI_2 - AI_1)/(AI_1 + AI_2)$$

where AI is acoustic impedance and 1, 2 refer to the layers above and below the interface.

We use the term ‘acoustic impedance’ because it applies to P-wave motion, identical to sound waves and able to travel in solids, liquids or gases. Elastic waves incorporate shear wave motion and only travel in solids. So is it possible to devise an elastic impedance (EI) that gives a similar equation:

$$(11.15) \quad R(\theta) = (EI_2 - EI_1)/(EI_1 + EI_2)$$

and would it make using the property of AVO easier? In addition to containing V_p and ρ , as in acoustic impedance, we might expect elastic impedance also to depend on V_s and angle of incidence θ .

Connolly (1999) reported that it was indeed possible to set up EI defined as:

$$(11.16) \quad EI = V_p^{(a)} \cdot V_s^{(b)} \cdot \rho^{(c)}$$

where $a = \tan^2 \theta$
 $b = -8\gamma^2 \sin 2\theta$
 $c = 1 - 4\gamma^2 \sin^2 \theta$
 and $\gamma = V_s/V_p$

Where wells have been logged for V_p , V_s and ρ , an EI well-log can be calculated assuming some angle of incidence θ – perhaps 30° , a typical angle of incidence for far-offset angle stacks. Where

the rocks are water wet and AVO effects are negligible, a suitably scaled EI log should be much the same as the AI log; but where hydrocarbons are present, it will deviate to lower values. Connolly (1999) showed several examples from the Atlantic margin West of Shetland and from the Gulf of Mexico in which EI logs ($\theta = 30^\circ$) clearly picked out not only gas sands from wet sands, but also oil sands. In the same wells, AI logs from these sands showed either a subdued response or none at all.

So much for logs, but what about EI and seismic data? Once you have an EI log, synthetic seismograms can readily be made just as they are from an AI log – that is the worth of [equation \(11.15\)](#) above. The synthetic seismogram must then be compared to an angle stack made for the same angle of incidence. Connolly (1999) showed an excellent tie between a synthetic seismogram calculated from a 30° EI log and a 30° angle stack from the West of Shetlands area.

The angle-stack seismic data can also be inverted to an EI volume, just as normal-incidence data can be inverted to an AI volume. At the Foinaven field, west of Shetland, low values of the 30° EI inverted data were found to be strongly correlated to hydrocarbon pore volume and were used to guide the trajectories of horizontal wells through reservoir sands. Elastic impedance has been further developed into ‘extended elastic impedance’ by substituting a factor $\tan \chi$ for $\sin^2 \theta$ (χ is Greek chi) (Whitcombe, 2002; Whitcombe *et al.*, 2002).

11.10 Best Fluid Indicator?

Which detects fluid content better – λ - μ - ρ or fluid factor? Smith & Gidlow (2000) reviewed the state of the game. They took the 25 sets of measurements reported by Castagna & Smith (1994) and calculated various AVO indicators for reflections from shale/brine, shale/gas and gas/brine interfaces directly from the measured values. They also created reflectivity curves from the data and extracted indicators from these for comparison. The fluid factor scored high in showing a quiet background and reflectivity-derived values which tracked the direct calculations well. However, an indicator based on λ and μ was virtually identical so, within this limited set of data, either approach worked well.

Ross (2002) tested six different approaches to using AVO data on a model seismic volume generated over two thin (11 m maximum) sands, one gas-filled the other wet. Results were judged on how well the areal extent of the sands was determined and how well the gas fill was resolved in a section. Of the methods discussed so far, elastic impedance and $\lambda\rho/\mu\rho$ did best. Best of all was a neural network prediction based on three inputs – AVO intercept and gradient and the stacked seismic trace. Interesting though this is, however, the test model was rather limited in having such very thin sands, and it is possible that different results might have been obtained with a different reservoir model.

It seems that, with so many variables affecting a reservoir (lithology, thickness, depth, pore fluids, diagenesis), no single method of AVO analysis is always going to be preferred. Furthermore, factors other than just simple technical efficiency may be important. For example, Whitcombe (2002) made an important point about BP's experience in the west of Shetland area, where, by using the EI approach through logs, far-offset synthetics and inverted seismic volumes, the AVO phenomena could be made more readily understandable and useful to a multidisciplinary team.

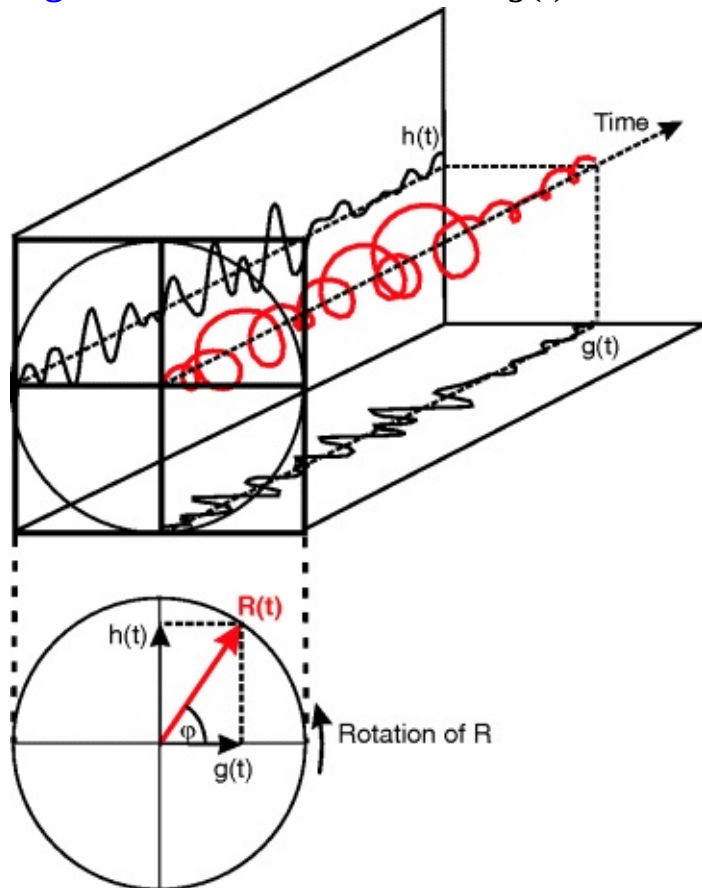
11.11 Instantaneous Seismic Attributes

So far in these final two chapters, we have dealt with seismic attributes that relate in a deterministic way to conditions in the subsurface. For example, coherence is an expression of the jump in depth across a fault, while the $\lambda\rho$ measure is an expression of the AVO phenomenon. Quantitative interpretation can go ahead in a deterministic way, e.g. to extract impedances and calculate reservoir properties. Now we will look, rather briefly, at a different species of attribute and a different mode of utilization.

The first seismic attributes to be named as such were derived from a complex-number description of the seismic trace (Taner & Sheriff, 1977; Taner *et al.*, 1979). The recorded seismic trace $g(t)$ is transformed to another trace, $h(t)$, by a mathematical operation – the Hilbert transform, which gives a 90° phase shift to all frequencies. The two are combined as the real and imaginary parts of a time-varying complex number, $R(t)$ (Figure 11.13). As time goes on, $R(t)$ varies in length and rotates at varying speed, tracing out a spiral in the complex number-time space of the diagram. The projection of $R(t)$ on the horizontal plane is the recorded seismic trace and the projection on the vertical plane is $h(t)$. This description allows the definition of new attributes:

1. Reflection strength, $R(t) = [g(t)^2 + h(t)^2]^{1/2}$
2. Instantaneous frequency = $d\phi/dt$
3. Instantaneous phase angle, $\phi(t) = \arctan[h(t)/g(t)]$
4. Polarity, defined as the sign of the seismic signal at maximum $R(t)$.

Figure 11.13 The seismic trace $g(t)$ as the real part of a time-varying rotating vector.



Note how this description of a seismic trace differs from the Fourier description. Instead of amplitude and phase spectra that refer to the whole trace, we now have a new set of numbers for

each time sample, which vary with time down the seismic trace, forming new traces of the attributes. Each attribute gives a new 3D volume to be displayed as time-slices or vertical sections in some appropriate set of colours. Since there is an attribute value for every time sample, they are often termed instantaneous attributes.

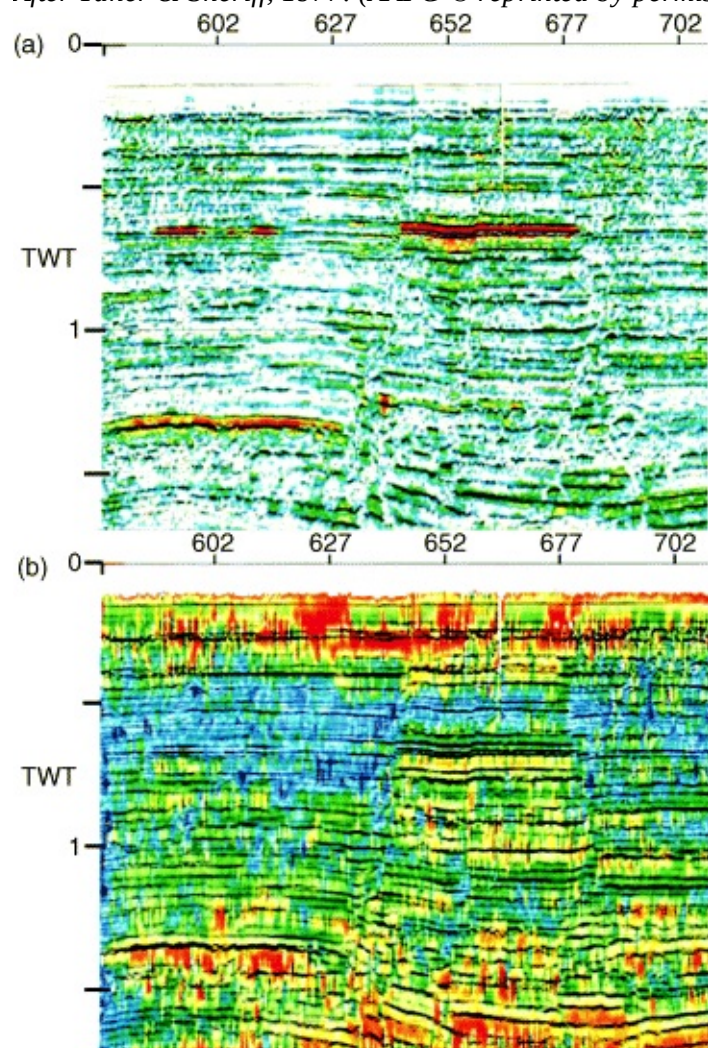
Reflection strength $R(t)$ is the magnitude of the envelope of the seismic trace. It is plotted as a colour on top of the original seismic data as a grey background and it brings out bright spots by highlighting them (e.g. in red) on the section ([Figure 11.14a](#)). Instantaneous frequency is a measure of how fast the vector R is rotating ([Figure 11.13](#)) and will be large when the seismic trace is oscillating rapidly. It may be an indicator of gas where it shows a drop to low values under a bright spot ([Figure 11.14b](#)).

Figure 11.14

a. Reflection strength (red high, blue low).

b. Average weighted frequency (red low, blue high).

After Taner & Sheriff, 1977. (AAPG © reprinted by permission of the AAPG whose permission is required for further use)



Instantaneous phase angle $\phi(t)$ cycles through 0 to 360° each time the vector R rotates about the reference circle, so it creates cyclical colour bands along each reflection. It emphasizes reflection continuity, so weak reflections show just as well as strong reflections, a property that may help in picking seismic stratigraphic boundaries. Conversely, discontinuities in reflections such as faults are made more conspicuous by the phase attribute. Polarity may be useful in distinguishing between hydrocarbon and lithological bright spots.

As always, the interpreter has to be sceptical. Tuning effects can artificially blow up trace

amplitudes (check Tutorial 9.3) and may dominate the instantaneous frequency response in thin beds (Robertson & Nogami, 1984).

The frequency drop under known gas sands is an intriguing phenomenon which stimulated interest in low frequency analysis of seismic data. The data are analyzed by a process of spectral decomposition. A key publication is that by Partyka *et al.* (1999). They described a process in which a short window 100 ms long moves down a seismic trace sample by sample. At each data point, a Fourier analysis is carried out on the data within the window and the amplitude of the spectrum at some chosen frequency is measured and assigned to the time at the centre of the window. In this way, a new data trace (and eventually a whole volume) is built up, expressing the variation in amplitude at a particular frequency. Further processing is required to remove the wavelet overprint and leave variation caused by geology. In thin-bedded sandstones, case histories indicate that the presence of oil or gas will give an amplitude bright spot at low frequencies of 10–20 Hz (Goloshubin *et al.*, 2006; Harilal *et al.*, 2009).

11.12 Usage of Seismic Attributes

The invention of instantaneous attributes and the introduction of colour plots spurred the development of seismic attributes generally. With the growth in workstation interpretation, many other attributes were invented or brought in from image processing. Chen & Sidney (1997) list no less than 63 attributes and give a short description and the applicability of each.

It is important to realize that the instantaneous attributes stem from the mathematics of signal description, not from the physics of wave propagation. With the exception of reflection strength, which is another expression of reflection amplitude, the attributes' links to subsurface geology are not as direct as those considered so far. The industry has never really made much use of instantaneous attributes, because most only give qualitative indications of variation and cannot be tied in a quantitative sense to reservoir geology.

Barnes (1999; 2001) covers the history of attributes and includes a telling quote from Robertson & Fisher (1988): 'The mix of meaningful and meaningless values is probably the major factor that has frustrated interpreters looking for physical significance in the actual numbers on attribute sections'. In a later paper, Barnes (2006) shows, by cross-plotting one attribute against another, that four of them are essentially the same, just calculated in different ways.

However, it is always possible that, although we cannot trace the exact path by which some attribute is linked to the geology, there actually is such a link. We shall see in the next section that reliable information about the subsurface can be gained by combining several attributes in a statistical analysis.

11.13 Predicting Log Properties from Seismic Attributes

Schultz *et al.* (1994), Russell *et al.* (1997) and Hampson *et al.* (2001) have given accounts of how to make use of seismic attributes to convert seismic traces to well-log data by using a statistical approach rather than a deterministic one. The starting position is that a number of wells (ideally ten or more) have already been drilled and logged in the survey area, and the seismic data is used to interpolate some log property such as porosity between the wells. One method uses multi-attribute linear regression and the other uses a neural network.

Linear regression in its simplest form is the fitting of a straight line $y = a + bx$ to a set of n points (x_i, y_i) in such a way that the mean squared error E^2 between actual data points y_i and the y values $(a + bx_i)$ predicted on the straight line is minimized. E is called the prediction error. So:

$$E^2 = (1/n)\sum_n [y_i - (a + bx_i)]^2$$

is minimized, where $i = 1, 2, 3 \dots n$.

The best values of a and b in the equation for y fall out of the minimization process and the line is generally called the least-squares best-fit line.

Suppose we have a well-log $L(t)$ sampled in time t and three attributes determined from an average of seismic traces close around the well location – perhaps the nine nearest traces. The attributes are also sampled in time, $A_1(t)$, $A_2(t)$ and $A_3(t)$, then for a particular time t' we have:

$$L(t') = w_0 + w_1A_1(t') + w_2A_2(t') + w_3A_3(t')$$

L is now a function of the three A variables. The weights w take the place of a and b in the straight line equation.

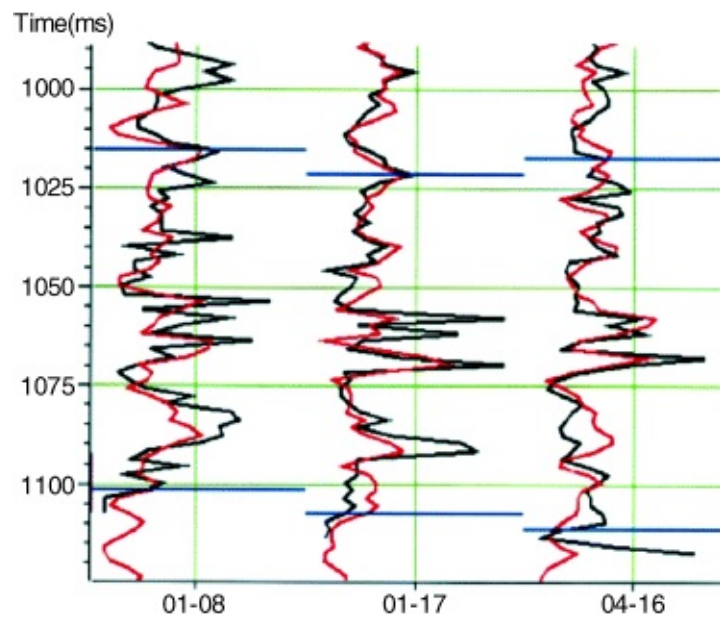
If we sample the well-log and the attribute traces at a succession of times through some interval of interest in all the wells available, we will have a large number of such equations with which to calculate the optimum weights. Once again, the constraint on the calculation of weights is to minimize the mean-squared error between the actual log values and the calculated log values. In the end, we should have an expression for $L(t)$ which will convert seismic traces close to wells to the chosen well log, perhaps a log of porosity. We may then use the same expression across the whole of the survey area to convert the entire seismic data set to the chosen log.

Crucial steps in the process are the choice of attributes and the validation of the process. The prediction error decreases as the number of attributes used increases, but the validation process may show that only three or four are effective in reducing the prediction error, and the error may even rise as more attributes are used.

The published results are impressive. [Figure 11.15](#) from Hampson *et al.* (2001) shows original porosity logs from three wells, with predicted porosity logs superimposed. In each case, the well had been left out of the training group, thereby simulating drilling after the prediction. Significantly better results were obtained with the neural network method, especially in the thin-bedded part of the sequence.

Figure 11.15 Measured porosity logs (black) compared to porosity logs calculated from seismic attributes (red).

From Hampson et al., (2001)



Schultz *et al.* (1994) discuss the philosophy behind this approach to estimating reservoir properties. They point out that it is a data-driven process, so each transform will be unique to the reservoir for which it was derived. They stress that the attributes must be wholly seismic-based, without any reliance on well data, so traces inverted to pseudo-AI by trace integration could be used, but not if inverted by model-based inversion.

The question of how many wells are required is an interesting one. Kalkomey (1997) concludes that best results will be obtained by maximizing the number of wells and minimizing the number of attributes. Good Figures are about ten wells and five attributes. As always, the quality of the results will only be as good as the generating seismic data, so any significant noise in the calibrating seismic traces will be faithfully rendered as spurious porosity.

11.14 4C and 4D Surveys

Shear waves (S-waves) were introduced in Chapter 4, Section 4.5, where various reasons were mentioned as to why S-waves have traditionally been ignored in routine petroleum seismology. However, in the 1980s there was some interest in shear waves in land surveys, in the hope that they might provide more information on subsurface physical properties. Interpretation of the data followed two paths: studies of lithology based on the V_p/V_s ratio; and studies of fracture orientation based on shear wave polarization. However, problems with reliably generating shear waves and accounting for static corrections in very low-velocity near-surface deposits, together with a perception of only limited added value, prevented wide adoption. Despite this, since the 1990s there has been a revival of interest, albeit in special areas of application.

Starting in the early 1990s, ocean bottom cables (OBC) have been deployed, which rest on the sea bed and incorporate geophones as well as hydrophones. Each geophone consists of three separate coils, whose axes are mutually at right angles so that the full ground motion, P-wave or S-wave, can be recorded. In addition to these three components of ground velocity, a pressure hydrophone is also installed at each receiver location, hence the 'four components' (4C) name.

The objective is to record waves which have travelled down to the reflector as P-waves, have been converted to S-waves by mode conversion at the reflector and have travelled back up to the sea bed as S-waves. They are commonly called converted waves (C-waves). Unlikely as it may seem, enough energy is available from this mechanism to create a C-wave reflection volume.

When interpreted in combination with the P-wave section, valuable new information is provided.

Three immediate advantages of employing sea-bed receivers, compared to conventional surface hydrophones, are:

1. Better signal/noise ratio.
2. Recording of shear wave motion without conversion back to P-waves at the sea bed (which must happen with surface recording).
3. Cancellation of reverberations thrown down from the sea surface which give signals of opposite polarity in the geophone and hydrophone.

In an excellent review paper, Caldwell (1999) was able to make the following general points:

- Surveys have been carried out in most of the important offshore exploration areas, worldwide.
- Data quality has been good and unaffected by geographical area.
- Mode conversion takes place at depth on the reflectors, not at the sea floor under the shot.

Applications are of three types:

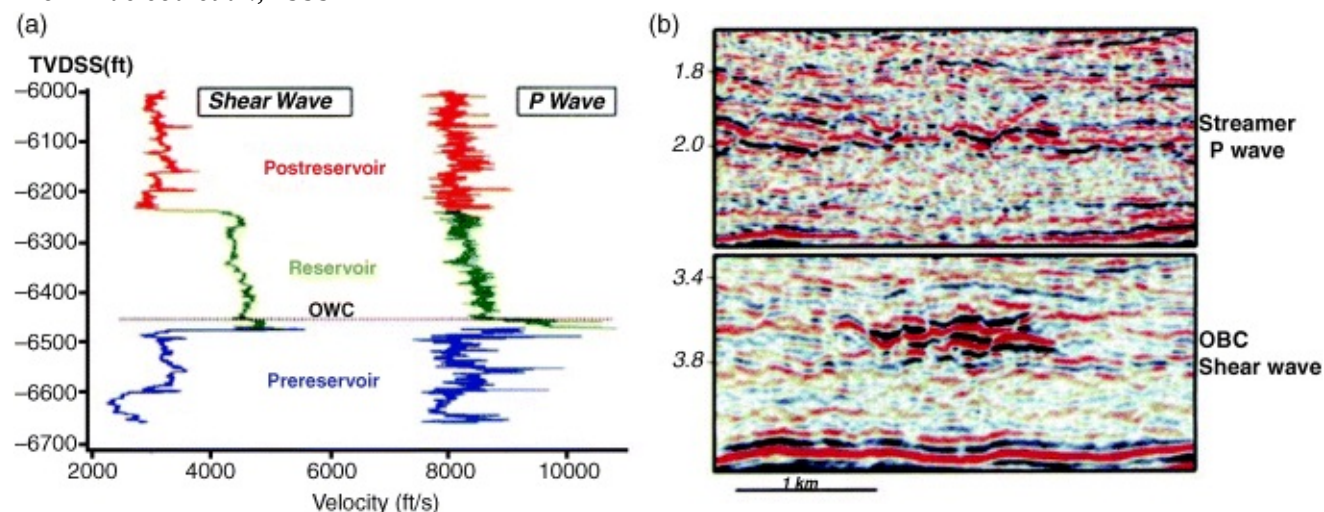
1. Better imaging through gas columns (because the S-wave is unaffected by pore fluids), or where reservoir sands and sealing shales have no P-wave impedance contrast but strong S-wave contrast.
2. Better bright spot discrimination. Lithological interfaces will show on both P-wave and C-wave data, but pore fluid interfaces will show only on P-wave data.
3. Mapping hydrocarbon saturation.

An outstanding application of the technique is described by Macleod *et al.* (1999) concerning the results from the 3D 4C survey of the Alba Field, central North Sea. In [Figure 11.16a](#), well-log data shows very clearly the lack of good P-wave velocity contrast between the reservoir and surrounding rocks compared to the good contrast evident in the S-wave data. The seismic sections in [Figure 11.16b](#) show a dramatic difference in reflection response, with the S-wave (C-wave) section providing a proper image of the reservoir, but the P-wave section showing only a fragment of it.

Figure 11.16 Data from the Alba Field, North Sea Basin.

- a. P-wave and S-wave velocity logs.
- b. S-wave section compared to P-wave section.

From Macleod *et al.*, 1999



One of the constant problems with using P-wave and C-wave data together is matching reflections in one set of data to reflections from the same interface in the other. Two-way time to the same reflection will always be greater in the C-wave data, because of the lower S-wave velocity, perhaps only a half or a third of the P-wave velocity in the same section.

In an informative paper, Nahm & Duhon (2003) described a survey conducted over a gas field in the Gulf of Mexico, where gas pervading the sedimentary column caused serious deterioration in the P-wave seismic quality. Initial attempts to match the two sets of data by compressing the C-wave sections in time were unsuccessful, and matching was eventually achieved by measuring times to corresponding fault intersections on the P-wave and C-wave sections, so generating a conversion function. The C-wave data not only gave very clear views of the structure, but amplitude studies showed that the Class III gas sands of the area gave bright spots on P-wave and dim spots on C-wave data, thereby providing a means of distinguishing gas sand reflections from lithological bright spots. One might say of S-waves, as of certain other seismic topics such as velocity anisotropy and walkaway VSP – when you need it, nothing else will do.

The term '4D' stands for '4 dimensions' and is applied to successive 3D surveys conducted over a producing field at intervals ranging from six months to a few years, in order to monitor the changing fluid contents of the reservoir. The fourth dimension of time is thus added to the three dimensions of survey space.

4D surveys as commercial undertakings emerged from experimental work in the late 1990s (Whitcombe *et al.*, 2001). To begin with, they were simply conventional 3D surveys, typically marine and conducted with conventional surface sources and streamers, as many still are. However, it is clearly essential to have every possible difference of technique eliminated between two such surveys, so that the only cause of a change in the data sets is a change in the subsurface conditions in the field. The biggest difficulty is ensuring that the receivers occupy the same positions, shot for shot, between the two surveys, and the ultimate solution is a fixed sea-bottom receiver cable as employed in 4C surveys.

BP have been prominent in the development of 4D work (Foster *et al.*, 2008). In 2003, the company installed a large-scale permanent cable system on the Valhall Field in the North Sea (van Gestel *et al.*, 2008). The recording cable was laid in parallel lines covering 70 per cent of the field area, buried in a trench in the sea bed to a depth of 1 m and equipped with 4C receivers.

Shots are made at the surface to a positional accuracy of 4–5 m and surveys have been made approximately every six months since 2003. The field is in a very porous chalk reservoir, which is subject to variable compaction as reservoir pressure drops, and the seismic data have been important in assessing geomechanical conditions to optimize well paths, as well as monitoring fluid movement during depletion of the field.

Tutorials for Chapter 11

Tutorial 11.1

Purpose: To calculate the amplitude variation with offset (AVO) for some important lithological interfaces. The tutorial requires the use of the program Microsoft *Excel*.

1. Load the file *tut11_1.xls* into *Excel*. This spreadsheet is set up to calculate the variation of amplitude with offset for the case of an interface between an upper layer (1) and a lower layer (2).
2. Note that the model data for the upper layer (1) is held in columns A – C of row 6 and is labelled:

V_{p1} = P-wave velocity, upper layer, m/s
 V_{s1} = S-wave velocity, upper layer, m/s
 ρ_1 = density, upper layer, g/cm³

and similarly for the data for the lower layer (2) in columns D to F.

Figures in the other columns are all calculated from this input data, including Poisson's ratio σ . The final R_0 values appears in column G, rows 10–19. Note the space for calculation of V_s at bottom left.

3. Initial values for the model data are taken from Hilterman (2001), [Figure 11.4](#) B.2, and are similar to those in Rutherford & Williams (1989) for a Class 1 gas sand under a shale seal. The sand is typically rather deep ($\approx 4,000$ m) and well indurated, with a low V_p/V_s ratio and low σ . Note the high contrast in σ values with the shale above. The accompanying graph shows that the reflection in a CMP gather will be of moderate amplitude and positive polarity at short offsets, but will fade away and even change to negative polarity at long offsets. What might then happen to the reflection on the full stack?

4. The classic bright spot of the Gulf of Mexico (Class 3 of Rutherford & Williams, 1989) is easily modelled by making the following changes (data again from Hilterman, 2001):

V_{p1} to 2,191 m/s (click on cell A6, type 2191 and Enter).

V_{s1} to 818 m/s

r_1 to 2.16 g/cm³

V_{p2} to 1,542 m/s

V_{s2} to 901 m/s

r_2 to 1.88 g/cm³

Note how the reflection is now of negative polarity and gets stronger as offset increases.

5. Will a sandstone/limestone bright spot show AVO? Choose suitable V_p and ρ values from [Figure 4.2](#) in Chapter 4 for a mid-range sandstone and enter them on the spreadsheet (columns A and C, row 6). Do the same for a mid-range limestone and enter the values in columns D and F. Calculate V_s values (bottom of the spreadsheet) for $\sigma = 0.2$ for sandstone and 0.3 for limestone (Domenico, 1984). Enter these V_s values in columns B and E of row 6 and note the changes in the graph of R_0 . Now you can see a strong positive reflection at all offsets, with only a modest AVO effect at 30° angle offset – probably undetectable in real data.

Tutorial Answers

Tutorial 2.1

- a. Period 0.05 sec, frequency 20 Hz, phase -65°
- b. Period 0.017 sec, frequency 59 Hz, phase 38°

Tutorial 2.3

- 7 $T = 0.0625$ sec
- 8 $T = 0.125$ sec
- 9 T tends to infinity

Tutorial 4.2

- 1 $V = 2,292$ m/s
- 2 Reflector depth = 573 m

Tutorial 4.4

- 4 Chalk/marl, $R = -0.176$
- 5 Marl/sandstone, $R = -0.043$

Tutorial 5.1

- 1 The hyperbola is flatter and its summit time is greater.
- 2 The hyperbola is asymmetrical; times on the left are less than on the right.

Tutorial 5.2

- 7 The drop in AI from limestone to shale gives a negative reflection.
- 9 Each multiple is reversed in polarity by reflection down from the sea surface.

Tutorial 6.1

- 1 Interval velocities (m/s): Tertiary 1,779, Cretaceous 3,110, Triassic 3,626, Permian 4,698
- 2–4 Velocities (m/s) referred to interfaces in the order Top Cretaceous, Top Trias, Top Permian, Top Carboniferous:
 - V_a : 1,779, 2,472, 2,680, 3,005
 - V_{rms} : 1,779, 2,560, 2,783, 3,170

V_{stack} : 1,779, 2,610, 2,825, 3,210

Tutorial 8.2

Horizontal shift to true migrated position = 560 m SW

True vertical depth = 2,690 m

References

- Aki, K. & Richards, P.G. (1981) *Quantitative Seismology*. WH Freeman and Co., San Francisco, CA.
- Albertin, U., Woodward, M., Kapoor, J., Charles, S., Nichols, D., Kitchenside, P. & Mao, W. (2001) Depth imaging examples and methodology in the Gulf of Mexico. *The Leading Edge* **20**, 498–513.
- Alkhalifah, T. & Tsvankin, I. (1995) Velocity analysis for transversely isotropic media. *Geophysics* **60**, 1550–1566.
- Alkhalifah, T., Tsvankin, I., Larner, K. & Toldi, J. (1996) Velocity analysis and imaging in transversely isotropic media: methodology and case study. *The Leading Edge* **15**, 371–378.
- Al-Yahya, K. (1989) Velocity analysis by iterative profile migration. *Geophysics* **54**, 718–729.
- Anstey, N.A. (1982) *Simple Seismics*. International Human Resources Development Corporation, Boston, MA.
- Ashcroft, W.A. & Ridgway, M.S. (1996) Early discordant diagenesis in the Brent Group, Murchison Field, UK North Sea, detected in high values of seismic-derived acoustic impedance. *Petroleum Geoscience* **2**, 75–81.
- Backus, M.M. & Chen, R.L. (1975) Flat spot exploration. *Geophysical Prospecting* **23**, 533–577.
- Bacon, M., Simm, R., & Redshaw, T. (2003) *3-D Seismic Interpretation*. Cambridge University Press, Cambridge, UK.
- Bahorich, M. & Farmer, S. (1995) 3-D seismic discontinuity for faults and stratigraphic features. *The Leading Edge* **14**, 1053–1058.
- Barnes, A.E. (1999) Seismic attributes, past, present and future. *Society of Exploration Geophysicists Expanded Abstracts* **18**, 892–895.
- Barnes, A.E. (2001) Seismic attributes in your facies. *CSEG Recorder* **26**, 41–47.
- Barnes, A.E. (2006) Redundant and useless seismic attributes. *Society of Exploration Geophysicists Expanded Abstracts* **25**, 978–982.
- Barrett, R.F., Margesson, R.W. & D'Angelo, R.M. (1995) Use of rock properties and AVO in the Everest Field development, UKCS. *Petroleum Geoscience* **1**, 311–317.
- Bee, M.F., Bearden, J.M., Herkenhoff, E.F., Supiyanto, H. & Koestoer, B. (1994) Efficient 3-D seismic surveys in a jungle environment. *First Break* **12**, 253–259.
- Bertram, G.T. & Milton, N.J. (1996) Seismic Stratigraphy. In: Emery, D. & Myers, K. (eds), *Sequence Stratigraphy*, 45–60. Blackwell Science Ltd., Oxford.
- Birch, F. (1961) The velocity of compressional waves in rocks to 10 kilobars part II. *Journal of Geophysical Research* **66**, 2199–2224.
- Blumentritt, C.H., Marfurt, K. & Sullivan, E.C. (2006) Volume-based curvature computations illuminate fracture orientations – Early to Mid-Palaeozoic, Central Basin Platform, west Texas. *Geophysics*, **71**, B159–B166.
- Brown, A.R. (2004) *Interpretation of Three-Dimensional Seismic Data*. 6th edition. American Association of Petroleum Geologists, Tulsa, OK.

- Brown, A.R., Dahm, C.G. & Graebner, R.J. (1981) A stratigraphic case history using three-dimensional seismic data in the Gulf of Thailand. *Geophysical Prospecting* **29**, 327–349.
- Brown, R.J., Anderson, N.L. & Hills, L.V. (1990) Seismic interpretation of Upper Elk Point (Givetian) carbonate reservoirs of Western Canada. *Geophysical Prospecting* **38**, 719–736.
- Bubb, J.N. & Hatlelid, W.G. (1977) Seismic stratigraphy and global changes in sea level. Part 10. Seismic recognition of carbonate build-ups. In: Peyton, C.E. (ed), *AAPG Memoir 26. Seismic Stratigraphy – applications to hydrocarbon exploration*, 185–204. American Association of Petroleum Geologists, Tulsa, OK.
- Buck, D.M., Alam, A. & Taylor, J.D. (2007) Fractured reservoir prediction from 3D seismic volumetric curvature and low-frequency imaging. *Society of Exploration Geophysicists Expanded Abstracts* **26**, 422–426.
- Burton, A. & Lines, L. (1997) VSP detection of interbed multiples using inside-outside corridor stacking. *Geophysics* **62**, 1628–1635.
- Caldwell, J. (1999) Marine multi-component seismology. *The Leading Edge*, **18**, 1274–1282.
- Campbell, A., Fryer, A. & Wakeman, S. (2005) Vertical seismic profiles – more than just a corridor stack. *The Leading Edge* **24**, 694–697.
- Castagna, J.P. & Smith, S.W. (1994) Comparison of AVO indicators: a modeling study. *Geophysics* **59**, 1849–1855.
- Castagna, J.P. & Swan, H.W. (1997) Principles of AVO crossplotting. *The Leading Edge* **16**, 337–344.
- Castagna, J.P., Batzle, M.L. & Eastwood, R.L. (1985) Relationships between compressional-wave and shear-wave velocities in clastic silicate rocks. *Geophysics* **50**, 571–581.
- Castagna, J.P., Swan, H.W. & Foster, D.J. (1998) Framework for AVO gradient and intercept interpretation. *Geophysics* **63**, 948–956.
- Chen, Q. & Sidney, S. (1997) Seismic attribute technology for reservoir forecasting and monitoring. *The Leading Edge* **16**, 445–448.
- Chopra, S. (2002) Coherence cube and beyond. *First Break* **20**, 27–33.
- Chopra, S. & Marfurt, K.J. (2005) Seismic attributes – a historical perspective. *Geophysics* **70**, 3S0–28S0.
- Chopra, S. & Marfurt, K.J. (2007a) *Seismic attributes for prospect identification and reservoir characterization*. Society of Exploration Geophysicists, Tulsa, OK.
- Chopra, S. & Marfurt, K. (2007b) Volumetric curvature attributes add value to 3D seismic data interpretation. *The Leading Edge* **26**, 856–867.
- Chopra, S. & Marfurt, K. (2008) Gleaning meaningful information from seismic attributes. *First Break* **26**, 43–53.
- Chopra, S., Alexeev, V., Manerikar, A. & Kryzan, A. (2004) Processing/integration of simultaneously acquired 3D surface seismic and 3D VSP data. *The Leading Edge* **23**, 422–430.
- Claerbout, J.F. (1985) *Imaging the earth's interior*. Blackwell, Oxford.
- Connolly, P. (1999) Elastic impedance. *The Leading Edge* **18**, 438–452.
- Cooke-Yarborough, P. (1994) Analysis of fractures yields improved gas production from

- Zechstein carbonates, Hewitt Field, UKCS. *First Break* **12**, 243–252.
- Dalley, R.M., Gevers, E.C.A., Stampfli, G.M., Davies, D.J., Gastaldi, C.N., Ruijtenberg, P.A. & Vermeer, G.J.O. (1989) Dip and azimuth displays for 3-D seismic interpretation. *First Break* **7**, 86–95.
- Delaplanche, J., Lafet, Y., Sineriz, B.G. & Remon Gil, M.A. (1982) Seismic reflection applied to sedimentology and gas discovery in the Gulf of Cadiz. *Geophysical Prospecting* **30**, 1–24.
- Deregowski, S.M. (1982) Dip-Moveout and reflector point dispersal. *Geophysical Prospecting* **30**, 318–322.
- Deregowski, S.M. (1986) What is DMO? *First Break* **4**, 7–24.
- Dillon, P.B. (1985) VSP migration using the Kirchhoff integral. *55th Annual International Meeting, Society of Exploration Geophysicists, Expanded Abstracts*. **4**, 19–21.
- Dillon, P.B. & Thomson, R.C. (1984) Offset source VSP surveys and their image reconstruction. *Geophysical Prospecting* **32**, 790–811.
- Dix, C.H. (1955) Seismic velocities from surface measurements. *Geophysics* **20**, 68–86.
- Domenico, S.N. (1974) Effect of water saturation on seismic reflectivity of sand reservoirs encased in shale. *Geophysics* **39**, 759–769.
- Domenico, S.N. (1984) Rock lithology and porosity determination from shear and compressional wave velocity. *Geophysics* **49**, 1188–1195.
- Dorn, G., Tubman, K., Cooke, D. & O'Connor, R. (1996) Geophysical reservoir characterisation of Pickerill Field, North Sea, using 3-D seismic and well data. In: Weimer, P. & Davis, T.L. (eds), *Applications of 3-D seismic data to exploration and production*, 107–122. AAPG and SEG, Tulsa, OK.
- Dragoset, W. (2005) A historical reflection on reflections. *The Leading Edge (supplement SEG@75)* **24**(S1), S46–S70.
- Fagin, S. (1996) The fault shadow problem: its nature and elimination. *The Leading Edge* **15**, 1005–1013.
- Fatti, J.L., Smith, G.C., Vail, P.J., Strauss, P.J. & Levitt, P.R. (1994) Detection of gas in sandstone reservoirs using AVO analysis: a 3D seismic case history using the Geostack technique. *Geophysics* **59**, 1362–1376.
- Faust, L.Y. (1952) Seismic velocity as a function of depth and geologic time. *Geophysics* **17**, 192–206.
- Faust, L.Y. (1953) A velocity function including lithologic variations. *Geophysics* **18**, 271–288.
- Fliedner, M.M., Crawley, S., Bevc, D. & Popovici, A.M. (2002) Velocity model building by wavefield-continuation imaging in the deepwater Gulf of Mexico. *The Leading Edge* **21**, 1232–1236.
- Foster, D., Fowler, S., McGarrity, J., Riviere, M., Robinson, N., Seaborne, R. & Watson, P. (2008) Building on BP's large-scale monitoring experience – the Clair and Chirag-Azeri projects. *The Leading Edge* **27**, 1632–1637.
- Galloway, W.E. (1998) Clastic depositional systems and sequences: application to reservoir prediction, delineation and characterization. *The Leading Edge* **17**, 173–180.
- Gao, D. (2004) Texture model regression for effective feature discrimination: application to

- seismic facies visualization and interpretation. *Geophysics* **69**, P958–P967.
- Gardner, G.H.F., Gardner, L.W. & Gregory, A.R. (1974a) Formation velocity and density – the diagnostic basics for stratigraphic traps. *Geophysics* **39**, 770–780.
- Gardner, G.H.F., French, W.S. & Matzuk, T. (1974b) Elements of migration and velocity analysis. *Geophysics* **39**, 811–825.
- Gersztenkorn, A. & Marfurt, K.J. (1996) Eigenstructure based coherence computations. *Society of Exploration Geophysicists, Expanded Abstracts* **15**, 328–331.
- Goloshubin, G., VanSchuyver, C., Korneev, V., Silin, D. & Vingalov, V. (2006) Reservoir imaging using low frequencies of seismic reflections. *The Leading Edge* **25**, 527–531.
- Goodway, W., Chen, T. & Downton, J. (1997) Improved AVO fluid detection and lithology discrimination using Lamé petrophysical parameters; “ $\lambda\rho$ ”, “ $\mu\rho$ ” and “ λ/μ fluid stack”, from P and S inversions. *Society of Exploration Geophysicists, Expanded Abstracts* **16**, 183–186.
- Gray, S.H. (1986) Efficient travel time calculations for Kirchhoff migration. *Geophysics* **51**, 1685–1688.
- Hampson, D. (1991) AVO inversion, theory and practice. *The Leading Edge* **10**, 39–42.
- Hampson, D.P., Schuelke, J.S. & Quirein, J.A. (2001) Use of multiattribute transforms to predict log properties from seismic data. *Geophysics* **66**, 229–236.
- Handin, J., Friedman, M., Logan, J.M., Pattison, L.J. & Swolfs, H.S. (1972) Experimental folding of rocks under confining pressure: buckling of single-layer rock beams. In: Heard, H.C., Borg, I.Y., Carter, N.L. & Raleigh, C. B. (eds) *Flow and fracture of rocks, Geophysical Monograph 16*, 1–28. American Geophysical Union, Washington, DC.
- Hanley, S. (1999) Analyzing real data in a virtual world. *The Leading Edge* **18**, 710–712.
- Hardage, B.A. (1985) *Vertical seismic profiling*. Geophysical Press, London.
- Harding, T.P. (1985) Seismic characteristics and identification of negative flower structures, positive flower structures and positive structural inversion. *Bulletin American Association of Petroleum Geologists* **69**, 582–600.
- Harilal, Rao, C.G., Saxena, R.C.P., Nangia, J.L., Sood, A. & Gupta, S.K. (2009) Mapping thin sandstone reservoirs: application of 3D visualization and spectral decomposition techniques. *The Leading Edge* **28**, 156–167.
- Hart, R.S., Pearson, R. & Rawling, G.C. (2002) 3-D seismic horizon-based approaches to fracture swarm sweet-spot definition in tight-gas reservoirs. *The Leading Edge* **21**, 28–35.
- Hawkins, K., Leggott, R., Williams, G. & Kat, H. (2001) Addressing anisotropy in 3-D prestack depth migration: a case study from the Southern North Sea. *The Leading Edge* **20**, 528–535.
- Hecht, E. (1987) *Optics*. Addison-Wesley, Reading, MA.
- Helmore, S., Plumley, A. & Humberstone, I. (2004) A 3D seismic volume curvature attribute aids structural and stratigraphic interpretation. *Petroleum Exploration Society of Great Britain, Petex 2004, Extended Abstracts, Well Placement Section*.
- Herron, D.A. (2000) Horizon autopicking. *The Leading Edge* **19**, 491–492.
- Hesthammer, J. (1999) Improving seismic data for structural interpretation. *The Leading Edge* **18**, 226–247.
- Hilterman, F.J. (1970) Three-dimensional seismic modelling. *Geophysics* **35**, 1020–1037.

- Hilterman, F.J. (2001) *Seismic amplitude interpretation*. 2001 Distinguished Instructor Short Course Series No. 4, sponsored by the Society of Exploration Geophysicists, European Assoc. of Geoscientists and Engineers, Houston, TX.
- Hocker, C. & Fehmers, G. (2002) Fast structural interpretation with structure-oriented filtering. *The Leading Edge* **21**, 238–243.
- Hudson, J.D. & Trewin, N.H. (2002) Jurassic. In: Trewin, N.H. (ed), *The Geology of Scotland*, 323–350. The Geological Society, London.
- Jones, I.F., Sugrue, M.J. & Hardy, P.B. (2007) Hybrid gridded tomography. *First Break* **25**, 35–41.
- Kalkomey, C.T. (1997) Potential risks when using seismic attributes as predictors of reservoir properties. *The Leading Edge* **16**, 247–251.
- Kaufman, H. (1953) Velocity functions in seismic prospecting. *Geophysics* **18**, 289–297.
- Kearey, P., Brooks, M. & Hill, I. (2002) *An Introduction to Geophysical Exploration*. 3rd edition. Blackwell Science Ltd., Oxford.
- Kennet, P., Ireson, R.L. & Conn, P.J. (1980) Vertical seismic profiles: their applications in exploration geophysics. *Geophysical Prospecting* **28**, 676–699.
- Kidd, G.D. (1999) Fundamentals of 3-D seismic volume visualization. *The Leading Edge* **18**, 702–709.
- Kleyn, A.H. (1983) *Seismic reflection interpretation*. Applied Science Publishers, Barking, UK.
- Koefoed, O. (1955) On the effect of Poisson's ratios of rock strata on the reflection coefficients of plane waves. *Geophysical Prospecting* **3**, 381–387.
- Lancaster, S. & Whitcombe, D. (2000) Fast-track coloured inversion. *Society of Exploration Geophysicists, Expanded Abstracts* **19**, 1572–1575.
- Latimer, R. (2007) Introduction to this special section: Sequence stratigraphy utilizing seismic. *The Leading Edge* **26**, 869.
- Latimer, R.B., Davison, R. & van Riel, P. (2000) An interpreter's guide to understanding and working with seismic-derived acoustic impedance data. *The Leading Edge* **19**, 242–256.
- Lavergne, M. & Wilm, C. (1977) Inversion of seismograms and pseudo velocity logs. *Geophysical Prospecting* **25**, 231–250.
- Lawyer, L.C., Bates, C.C. & Rice, R.B. (2001) *Geophysics in the affairs of mankind*. Society of Exploration Geophysicists, Tulsa, OK.
- Levy, S. & Fulagar, P.K. (1981) Reconstruction of a sparse spike train from a portion of its spectrum and application to high resolution deconvolution. *Geophysics* **46**, 1235–1243.
- Linari, V. (2004) A practical approach to well-seismic data calibration. *The Leading Edge* **23**, 774–775.
- Lindseth, R.O. (1979) Synthetic sonic logs –a process for stratigraphic interpretation. *Geophysics* **44**, 3–26.
- Lindsey, J.P. (1989) The Fresnel zone and its interpretive significance. *The Leading Edge* **8**, 33–39.
- Lines, L. (1993) Ambiguity in analysis of velocity and depth. *Geophysics* **58**, 596–597.
- Lines, L.R. & Newrick, R.T. (2004) *Fundamentals of geophysical interpretation*. Society of Exploration Geophysicists, Tulsa, OK.

- MacLeod, M.K., Hanson, R.A. & Bell, C.R. (1999) The Alba Field ocean bottom cable seismic survey: impact on development. *The Leading Edge* **18**, 1306–1312.
- Marfurt, K.L., Kirilin, R.L., Farmer, S.L. & Bahorich, M.S. (1998) 3-D seismic attributes using a semblance-based coherency algorithm. *Geophysics* **63**, 1150–1165.
- Marsden, D., Bush, M.D. & Johng, D.S. (1995) Analytic velocity functions. *The Leading Edge* **14**, 775–782.
- Masaferro, J.L., Bourne, R. & Jauffred, J-C. (2003) 3D visualization of carbonate reservoirs. *The Leading Edge* **22**, 18–25.
- Mayne, W.H. (1962) Common reflection point horizontal data stacking techniques. *Geophysics* **27**, 927–938.
- McQuillin, R., Bacon, M & Barclay, W. (1984) *An introduction to seismic interpretation*. Graham and Trotman Ltd, London.
- Middleton, M.F. (1987) Seismic stratigraphy of Devonian reef complexes, northern Canning Basin, Western Australia. *Bulletin American Association Petroleum Geologists* **71**, 1488–1498.
- Millar, N.S. (1998) *Effects of velocity variation on interval velocity*. Unpublished MSc final report, University of Aberdeen.
- Mitchum, R.M., Vail, P.R. & Sangree, J.B. (1977) Seismic stratigraphy and global changes of sea level. Part 6. Stratigraphic interpretation of seismic reflection patterns in depositional sequences. In: Peyton, C.E. (ed), *AAPG Memoir 26. Seismic stratigraphy – applications to hydrocarbon exploration*, 117–133. American Association of Petroleum Geologists, Tulsa, OK.
- Myers, K.J. & Milton, N.J. (1996) Concepts and principles of sequence stratigraphy. In: Emery, D. & Myers, K. (eds), *Sequence Stratigraphy*, 11–41. Blackwell Science Ltd., Oxford.
- Nafe, J.E. & Drake, C.L. (1963) Physical properties of marine sediments. In: Hill, M.N. (ed), *The Sea* Vol. 3, pp. 794–815. Interscience, New York.
- Nahm, J.W. & Duhon, M.P. (2003) Interpretation and practical applications of 4C-3D seismic data, East Cameron gas fields, Gulf of Mexico. *The Leading Edge* **22**, 300–309.
- Neidell, N.S. & Taner, M.T. (1971) Semblance and other coherency measures for multichannel data. *Geophysics* **36**, 482–497.
- Nestvold, E.O. (1991) 3–D seismic: is the promise fulfilled? *Society of Exploration Geophysicists Expanded Abstracts*, **10**, 717–720.
- Newman, P. (1973) Divergence effects in a layered earth. *Geophysics* **38**, 481–488.
- Newman, P. (1990) Amplitude and phase properties of a digital migration process. *First Break* **8**, 397–403.
- O'Brien, P.N.S. (1969) Experiments concerning the primary seismic pulse. *Geophysical Prospecting* **17**, 511–547.
- O'Brien, P.N.S. (1974) Aspects of seismic research in the oil industry. *Geoexploration* **12**, 76–96.
- O'Doherty, R.F. & Anstey, N.A. (1971) Reflections on amplitudes. *Geophysical Prospecting* **19**, 430–458.
- Oldenberg, D.W., Scheur, T. & Levy, S. (1983) Recovery of the acoustic impedance from reflection seismograms. *Geophysics* **48**, 1318–1337.

- Ostrander, W.J. (1984) Plane-wave reflection coefficients for gas sands at nonnormal angles of incidence. *Geophysics* **49**, 1637–1648.
- Partyka, G., Gridley, J. & Lopez, J. (1999) Interpretational applications of spectral decomposition in reservoir characterization. *The Leading Edge* **18**, 353–360.
- Peacock, K.L. & Treitel, S. (1969) Predictive deconvolution: Theory and practice. *Geophysics* **34**, 155–159.
- Pedersen, S.I., Randen, T., Sonneland, L. & Steen, O. (2002) Automatic fault extraction using artificial ants. *Society of Exploration Geophysicists, Expanded Abstracts* **21**, 512–515.
- Pedersen, S.I., Skov, T., Hetlelid, A., Fayemendy, P., Randen, T. & Sonneland, L. (2003) New paradigm of fault interpretation. *Society of Exploration Geophysicists, Expanded Abstracts* **22**, 350–353.
- Peng, C. & Steenson, K.E. (2001) 3-D prestack depth migration in anisotropic media: a case study at the Lodgepole Reef play in North Dakota. *The Leading Edge* **20**, 524–527.
- Pharez, S., Jones, N., Dirks, V., Zimine, S., Prigent, H., Ibbotson, K. & Gruffeille, J-P. (2005) Prestack wave-equation migration as a routine production tool. *The Leading Edge* **24**, 608–613.
- Price, N.J. (1966) *Fault and joint development in brittle and semi-brittle rock*. Pergamon Press, London.
- Ratcliff, D.W., Jacewitz, C.A. & Gray, S.H. (1994) Subsalt imaging via target-oriented 3-D prestack depth migration. *The Leading Edge* **13**, 163–170.
- Ricker, N. (1953) The form and laws of propagation of seismic wavelets. *Geophysics* **18**, 10–40.
- Rider, M. (1996) *The Geological Interpretation of Well Logs*. Whittles Publishing, Caithness.
- Rijks, E.J.H. & Jauffred, J.C.E.M. (1991) Attribute extraction: an important application in any 3-D interpretation study. *The Leading Edge* **10**, 11–19.
- Roberts, A. (2001) Curvature attributes and their application to 3D interpreted horizons. *First Break* **19**, 85–100.
- Robertson, J.D. & Fisher, D.A. (1988) Complex seismic trace attributes. *The Leading Edge* **7**, 22–26.
- Robertson, J.D. & Nogami, H.H. (1984) Complex seismic trace analysis of thin beds. *Geophysics* **49**, 344–352.
- Rockwell, D.W. (1967) The digital computer's role in the enhancement and interpretation of North Sea seismic data. *Geophysics* **32**, 259–281.
- Ross, C.P. (2002) Comparison of popular AVO attributes, AVO inversion and calibrated AVO prediction. *The Leading Edge* **21**, 244–252.
- Russell, B., Hampson, D., Schulke, J. & Quirein, J. (1997) Multiattribute seismic analysis. *The Leading Edge* **16**, 1439–1443.
- Russell, B., Hampson, D. & Bankhead, B. (2006) An inversion primer. *CSEG Recorder* **31** (Special Edition), 97–103.
- Rutherford, S.R. & Williams, R.H. (1989) Amplitude-versus-offset variations in gas sands. *Geophysics* **54**, 680–688.
- Sangree, J.B. & Widmier, J.M. (1977) Seismic stratigraphy and global changes of sea level. Part 9. Seismic interpretation of clastic depositional facies. In: Peyton, C.E. (ed), *AAPG Memoir* **26**.

- Seismic stratigraphy – applications to hydrocarbon exploration*, 165–184. American Association of Petroleum Geologists, Tulsa, OK.
- Sarg, J.F. & Schuelke, J.S. (2003) Integrated seismic analysis of carbonate reservoirs: from the framework to the volume attributes. *The Leading Edge* **22**, 640–645.
- Schneider, W.A. (1978) Integral formulation for migration in two and three dimensions. *Geophysics* **43**, 49–76.
- Schoenberger, M. (1974) Resolution comparison of minimum phase and zero-phase signals. *Geophysics* **39**, 826–833.
- Schultz, P.S., Ronen, S., Hattori, M. & Corbett, C. (1994) Seismic-guided estimation of log properties. Part I. *The Leading Edge* **13**, 305–310, 315.
- Sheriff, R.E. (2002) *Encyclopedic dictionary of exploration geophysics*. 4th edition. Society of Exploration Geophysicists, Tulsa, OK.
- Sheriff, R.E. & Geldart, L.P. (1995) *Exploration Seismology*. Cambridge University Press, Cambridge, UK.
- Shuey, R.T. (1985) A simplification of the Zoeppritz equations. *Geophysics* **50**, 609–614.
- Silva, C.C., Marcolino, C.S. & Lima, F.D. (2005) Automatic fault extraction using ant-tracking algorithm in the Marlin South Field, Campos Basin. *Society of Exploration Geophysicists, Expanded Abstracts* **24**, 857–861.
- Smith, P.E. & Gidlow, P.M. (1987) Weighted stacking for rock property estimation and detection of gas. *Geophysical Prospecting* **35**, 993–1014.
- Smith, G.C. & Gidlow, M. (2000) A comparison of the fluid factor with λ and μ in AVO analysis. *Society of Exploration Geophysicists, Expanded abstracts* **19**, 122–125.
- Taner, M.T. & Koehler, F. (1969) Velocity spectra – digital computer derivation and application. *Geophysics* **34**, 859–881.
- Taner, M.T. & Sheriff, R.E. (1977) Application of amplitude, frequency and other attributes to stratigraphic and hydrocarbon determination. In: Peyton, C.E. (ed), *AAPG Memoir 26. Seismic stratigraphy – applications to hydrocarbon exploration*, 301–327. American Association of Petroleum Geologists, Tulsa, OK.
- Taner, M.T., Koehler, F. & Sheriff, R.E. (1979) Complex seismic trace analysis. *Geophysics* **44**, 1041–1063.
- Thomsen, L. (1986) Weak elastic anisotropy. *Geophysics* **51**, 1954–1966.
- Thomsen, L. (2002) *2002 Distinguished Instructor Short Course. Understanding seismic anisotropy in exploration and exploitation*. Society of Exploration Geophysicists, Tulsa, OK.
- Tucker, P.M. (1988) Seismic contouring: a unique skill. *Geophysics* **53**, 741–749.
- van der Poel, N.J. & Cassell, B.R. (1989) Borehole seismic surveys for fault delineation in the Dutch North Sea. *Geophysics* **54**, 1091–1100.
- van Gestel, J.-P., Kommedal, J.H., Barkved, O.I., Mundal, I., Bakke, R. & Best, K. D. (2008) Continuous seismic surveillance of Valhall Field. *The Leading Edge* **27**, 1616–1621.
- Vail, P.R. & Mitchum, R.M. (1977) Seismic stratigraphy and global changes of sea level. Part 1: Overview. In: Peyton, C. E. (ed), *AAPG Memoir 26. Seismic stratigraphy – applications to hydrocarbon exploration*, 51–52. American Association of Petroleum Geologists, Tulsa, OK.

- Verm, R. & Hilterman, F. (1995) Lithology color-coded seismic sections: the calibration of AVO cross-plotting to rock properties. *The Leading Edge* **14**, 847–853.
- Walton, G.G. (1972) Three-dimensional seismic method. *Geophysics* **37**, 417–430.
- Wang, Z. (2002) Seismic anisotropy in sedimentary rocks, part 2: laboratory data. *Geophysics* **67**, 1423–1440.
- West, B.P., May, S.R., Eastwood, J.E. & Rossen, C. (2002) Interactive seismic facies classification using textural attributes and neural networks. *The Leading Edge* **21**, 1042–1049.
- Whitcombe, D.N. (2002) Elastic impedance normalization. *Geophysics* **67**, 60–62.
- Whitcombe, D.N., Marsh, J.M., Bagley, G., Lewis, A.J., McGarrity, J.P., Nash, T., Parr, R.S. & Saxby, I.P. (2001) Systematic application of 4D in BP's NW Europe operations. *Society of Exploration Geophysicists Expanded Abstracts* **20**, 1608–1611.
- Whitcombe, D.N., Connolly, P.A., Reagan, R.L. & Redshaw, T.C. (2002) Extended elastic impedance for fluid and lithology prediction. *Geophysics* **67**, 63–67.
- White, R.E. & Hu, T. (1998) How accurate can a well-tie be? *The Leading Edge* **17**, 1065–1071.
- Whitfield, P., Dazley, M., Santos-Luis, B., Nieuwland, F. & Lemaitre, L. (2008) Building velocity models for depth imaging in the presence of short-wavelength velocity variations: a North-Sea case study. *First Break* **26**, 45–50.
- Widess, M.B. (1973) How thin is a thin bed? *Geophysics* **38**, 1176–1180.
- Wiggins, W., Ng, P. & Manzur, A. (1986) The relation between the VSP-CDP transformation and VSP migration. *Society of Exploration Geophysicists, Expanded Abstracts* **5**, 565–568.
- Wyllie, M.R.J., Gregory, A.R. & Gardner, G.H.F. (1958) An experimental investigation of factors affecting elastic wave velocities in porous media. *Geophysics* **23**, 459–493.
- Wynn, T.J. & Stewart, S.A. (2003) The role of spectral curvature mapping in characterizing subsurface strain distributions. In: Ameen, M. (ed), *Fracture and in-stress characterization of hydrocarbon reservoirs. Special Publications* **209**, 127–143. The Geological Society, London.
- Yilmaz, O. (2001) *Seismic Data Analysis*. 2nd edition. Society of Exploration Geophysicists, Tulsa, OK.
- Yilmaz, O. & Claerbout, J.F. (1980) Prestack partial migration. *Geophysics* **45**, 1753–1779.
- Young, K.T. & Tatham, R.H. (2007) Fluid discrimination of post-stack ‘bright spots’ in the Columbus Basin, offshore Trinidad. *The Leading Edge* **26**, 1508–1515.
- Yu, G. (1985) Offset-amplitude variation and controlled-amplitude processing. *Geophysics* **50**, 2697–2708.

Index

- 2D seismic surveys
 - acquisition
 - interpretation
- 3D seismic surveys
 - acquisition
 - usage, growth, impact
 - interpretation
- 4D surveys
- 4C surveys
- AC (alternating current)
- A/D convertor
- AGC (automatic gain control)
- AI (acoustic impedance)
 - inversion
 - examples
- airgun
- alias signal
- amplifier
- amplitude
 - spectrum
- analogue
- angular frequency
- anisotropy
- ant-tracking
- anti-alias filter
- antithetic fault
- array
- AVA (amplitude variation with angle)
- AVO (amplitude variation with offset)
 - and Poisson's ratio
 - and elastic impedance
 - angle stacks
 - examples
 - fluid factor
 - intercept and gradient
 - inversion to impedance

lambda-rho, mu-rho
methodology
ACF (auto-correlation function)
auto-picking, -tracking
bandwidth
fragility
binary numbers
bins, binning
bow-tie
bright spot
buried focus
bubble pulse
bulk modulus
C (converted) waves
channel
character
Cheops pyramid
class 1, 2, 3, 4 sands
class 1, class 3 sands
CMP (common mid-point)
CMP stacking
colour displays
coloured inversion
common offset gather
common offset section
common receiver gather
common shot gather
compartmentalisation
composite log
contouring
convolution
operator
corner frequency
correlation
corridor stack
CRP (common reflection point)
CCF (cross-correlation function)
cross-line data
cross-plotting
cycle-skipping

data quality
DC (direct current)
decibel scale
deconvolution
depositional sequence
depth map
depth ties
DHI (direct hydrocarbon indicator)
diagenesis
diffraction
 and reflections
 and faults
 hyperbola
diffraction curve
digitization
digital recording
dim-out (dim spot)
direct wave
diversity stack
DMO (dip move-out)
downward continuation
DT log
dynamite
earth filter
EI (elastic impedance)
EI well-log
EI synthetic seismogram
EI inversion
far-offset stack
fault
 pattern
 connection
 shadow
 auto-tracking
filter
 digital
 electronic
 inverse
 operator
 spectrum
 structure-oriented

finite difference
first arrival
f-k processing
f-k migration
flat spot
fluid indicators
fold
Fourier analysis
Fourier series
Fourier synthesis
Fourier transform
fracture zones
frequency
frequency domain
frequency filtering
frequency response
Fresnel zone
 and faults
fundamental

Gardner's Law
gas sand
gas column
gathers
geophone
geophone spread
ghosting
GPS (global positioning system)
growth fault

harmonics
head wave
Hertz
Hilbert transform
horizon slice
Huyghen's principle
hydrophone
hydrophone streamer, cable
hyperboloid

IFT (inverse Fourier transform)
IFZ (inner Fresnel zone)
image gather

- image ray
- image ray tracing
- image source
- impedance
 - acoustic (see AI)
 - elastic (see EI)
 - S-wave
 - inversion from AVO
- impulse response
- incompressibility
- inline data
- instantaneous attributes
- instantaneous frequency
- instantaneous phase
- inversion
 - simultaneous
- isochrons
- key reflections
- Kirchhoff
- Lame's constant
- lambda-rho, mu-rho
- layered earth model
- low frequencies
- LVL (low velocity layer)
- map migration
- maximum curvature
- migration
 - 3D
 - and Fresnel zone
 - aperture
 - example
 - future
 - Kirchhoff
 - pre-stack time (PSTM)
 - pre-stack depth (PSDM)
 - ray-tracing
 - smiles
 - wave equation
- mirror image
- mode conversion

- modelling
 - forward
 - inverse
- model-based inversion
- monocline
- most-positive curvature
- most-negative curvature
- mudrock line
- multiples
 - suppression of
 - sea-bed
- multiplexing
- muting
- near-offset stack
- neural network
- NMO (normal move-out)
 - NMO stretch
- noise
- normal faults
- normal-incidence reflection
- Nyquist frequency
- OBC (ocean bottom cable)
- offset
- offset VSP
- opacity
- over-pressure
- OWT (one-way time)
- P-wave
 - waveform
 - attenuation
 - transmission
- paravane
- particle displacement
- particle velocity
- peg-leg multiple
- period
- phase angle
- phase lag
- phase lead
- phase shift

zero
linear
phase spectrum
pixel
Poisson's ratio
Poisson reflectivity
polarity
polarization
polar anisotropy
porosity
power spectrum
predictive deconvolution
proprietary survey
Radon transform
Rayleigh wave
raypath
 curvature
 zero-offset, far-offset
ray tracing
RC (reflection coefficient)
RC series, sequence
recording instruments
recursion
reflected wave
reflection point dispersal
reflection strength
reflectivity (RC)
refracted wave
refraction survey
reservoir model
reverberation
ripple
RMO (residual move-out)
S (shear) wave
S-wave section
sampling frequency
sampling interval
sand distribution
secondary source
seed lines
SEG-Y file

seismic attributes

prediction of well-logs

coherence

curvature

dip magnitude, azimuth

horizon-based

instantaneous

usage

volumetric

seismic data acquisition

seismic facies

analysis

seismic geomorphology

seismic modelling

forward

inverse modelling to AI

seismic receivers

seismic reflection

amplitude

and diffraction

continuity

facies

history

industry

picking

polarity

primary

principle

resolution

sequence

terminations

water-bottom

seismic resolution

seismic sequences

seismic sources

seismic stratigraphy

seismogram

semblance

sequence boundary

shear modulus

sideswipe

signals
S/N (signal/noise ratio)
Snell's Law
sonic log
 digitization
space frequency
sparse-spike inversion
spectrum
speculative survey
spherical spreading
spike waveform, spikogram
static corrections
stratigraphic markers
streamer
super gather
surface waves
surface multiple
survey datum
synthetic seismogram

TWT (two-way time)
TWT maps
telemetry
thin beds
time contouring
time-depth conversion
 examples
time domain
time section
time series
time shift, lag
time slice
tomography
trace shape
trace integration
transit time
tuning thickness

uphole time

variance
velocity (P-wave)
 analysis

and density
and depth conversion
and lithology
and porosity
and pore pressure
anisotropy
average
Faustian
from well data
interval (layer)
linear function of depth
spectrum
 V_{rms} (root-mean-square)
 V_{stack} (stacking)
 V_{nmo} (normal move-out)
variation
velocity-depth models
velocity pull-up, push-down
vertical stacking
velocity survey
vibrator
vibroseis
volumetric dip
voxel
VSP (vertical seismic
profiling)
VSP-CMP transform
VTI (vertical transverse isotropy)

water gun
water multiples
water saturation
waveform
 amplitude
 cosine
 frequency
 periodic
 phase
 scanning
 truncation
walkaway VSP
wave equation

wavefront

wavelet

 extraction

 processing

 Ricker

 zero phase

wavenumber

weathered layer

weighted stacking

West Sole Field

Wiener filter

wiggle-trace

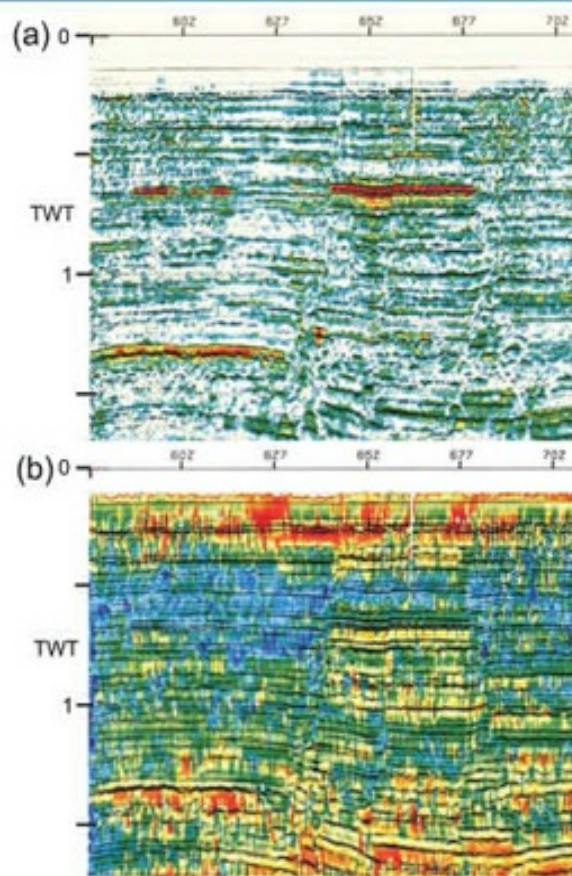
workstation

Wyllie equation

Zoeppritz

z-transform

A Petroleum Geologist's Guide to Seismic Reflection



William Ashcroft

 WILEY-BLACKWELL